



HAL
open science

Collective contact guidance of cell monolayers : polar laning and crisscross bilayering

Mathilde Lacroix

► **To cite this version:**

Mathilde Lacroix. Collective contact guidance of cell monolayers : polar laning and crisscross bilayering. Cellular Biology. Université Paris sciences et lettres, 2022. English. NNT : 2022UPSLS027 . tel-04605773

HAL Id: tel-04605773

<https://pastel.hal.science/tel-04605773>

Submitted on 8 Jun 2024

HAL is a multi-disciplinary open access archive for the deposit and dissemination of scientific research documents, whether they are published or not. The documents may come from teaching and research institutions in France or abroad, or from public or private research centers.

L'archive ouverte pluridisciplinaire **HAL**, est destinée au dépôt et à la diffusion de documents scientifiques de niveau recherche, publiés ou non, émanant des établissements d'enseignement et de recherche français ou étrangers, des laboratoires publics ou privés.



THÈSE DE DOCTORAT
DE L'UNIVERSITÉ PSL

Préparée à Institut Curie

**Collective contact guidance of cell monolayers:
polar laning and crisscross bilayering**

**Guidage par contact collectif de monocouches cellulaires :
migration en bandes polaires
et formation de bicouches orthogonales**

Soutenue par

Mathilde LACROIX

Le 30 mai 2022

Ecole doctorale n° 564

Physique en Île-de-France

Spécialité

Physique

Composition du jury :

Abdul, BARAKAT Directeur de recherche CNRS, Ecole polytechnique	<i>Président</i>
Karine, ANSELME Directrice de recherche CNRS, Université de Haute-Alsace	<i>Rapportrice</i>
Sylvain, GABRIELE Associate professor with tenure, Université de Mons	<i>Rapporteur</i>
Salima, RAFAI Chargée de recherche CNRS, Université Grenoble Alpes	<i>Examinatrice</i>
Raphaël, VOITURIEZ Directeur de recherche CNRS, Sorbonne Université	<i>Examineur</i>
Pascal, SILBERZAN Directeur de recherche CNRS, Institut Curie	<i>Directeur de thèse</i>

Remerciements

La thèse a été pour moi une grande aventure de travail et de vie très formatrice pendant laquelle j'ai eu la chance de côtoyer des personnes formidables. Je souhaite remercier ici toutes ces personnes qui m'ont soutenu dans cette épreuve et qui, de près ou de loin, ont été impliquées dans le travail présenté dans mon manuscrit de thèse.

Tout d'abord, je remercie les membres de mon jury de thèse, Abdul Barakat, Karine Anselme, Sylvain Gabriele, Salima Rafai et Raphaël Voituriez, pour avoir accepté d'évaluer mon travail et pour le riche échange que nous avons eu lors de la soutenance. Je remercie également chaleureusement Karine Guevorkian et Raphaël Voituriez qui ont suivi mon travail lors des comités de thèse.

Je remercie mon directeur de thèse Pascal Silberzan pour son encadrement, en particulier pour m'avoir introduit aux sujets passionnants que sont la matière active et la physique des tissus cellulaires, pour la confiance qu'il m'a accordé, pour son intuition scientifique qui a accompagné mes choix expérimentaux et pour tous ses précieux conseils de mises en valeur des résultats scientifiques.

I would like to thank my collaborators Bart, Carles, Sam, and Jacques whose numerical and theoretical contributions were crucial in the present work and from whom I learned a lot in the past few years. I always enjoyed our discussions which surely helped the projects move forward.

I also thank the former and current members of the "Biology-inspired Physics at Mesoscales" team: Thibault, Isabelle, Axel, Sylvie, Hsiang, Artem, Caroline, Xingming, Brice, Flavia, Pauline, Sarah, Nastassia, Trinish, Pascal, Pierre, Thomas, and Victor. I am particularly grateful for the scientific discussions, for all the experimental tips and for the great moments that we shared in the lab and outside, and that often revealed a strong shared interest for worldwide gastronomy. I would like to specifically thank Thibault for having trained me in experimental technics when I arrived four years ago, Trinish my office mate for being that thoughtful, and Caroline for having brought a new energy to the team and sharing with me the eager to make research more sustainable.

I was glad to be part of the Physico Chimie Curie unit during the last years. Thanks to the energy and investment of wonderful people, it is a great place to work in. I would like to thank all the unit members for the shared moments that have always brightened my days in the lab whether it was a quick discussion in the corridor, a useful scientific input, a cell culture time with fun music in L2, or all the warm events such as bar trials, pétanque tournaments, lab retreat, and so many other gatherings.

Au cours de cette thèse, plusieurs membres de l'Institut Curie et de l'IPGG m'ont fourni une aide précieuse, et je les en remercie chaleureusement :

- les membres de la plateforme BMBC, notamment Aude et Fanny pour leur aide en culture et biologie cellulaire et pour leur bonne humeur qui fait du L2 un endroit agréable où travailler, et John pour son aide avec les Western blots entre autres.
- Guillaume, Olivier, Nawel et Kévin de la plateforme technologique de l'IPGG pour leur aide avec les équipements de micro-fabrication.
- les membres de la plateforme PICT-IBISA pour leur accompagnement en imagerie confocale.
- Laurence, Thuy, Nathanaële et Brigitte, pour leur précieux travail et pour leur aide bienveillante au quotidien.

Je souhaite remercier également les auteurices de contenus audios qui ont accompagné de leurs histoires et de leurs idées mes longues séances au microscope, en salle blanche et en salle de culture, dans le désordre : Victoire Tuillon, Matthieu Ricard, Léa Salamé et ses femmes puissantes, Christophe Hondelatte, Jean-Marc Jancovici, Bon pote, Mathieu Vidard et les autres que j'oublie ...

En parallèle de ma thèse, j'ai eu la chance de travailler en mission doctorale à la Cité des Sciences et de l'Industrie. Je remercie les médiatrices et médiateurs scientifiques, Marlène, Lisa, Graziella, Agathe, Nadège, et les autres, avec qui j'ai passé d'excellents moments de partage et auprès de qui j'ai beaucoup appris.

Je tiens enfin à remercier toutes les personnes qui m'ont entouré tout au long de ma thèse, ces proches avec qui j'ai partagé au quotidien mes interrogations, mes progrès, mes déceptions, mes petites et grandes victoires, ... ! Je remercie ma famille et en particulier mes parents et ma sœur qui depuis toujours me supportent au sens anglais (et parfois français) du terme, et qui pendant cette thèse ont su m'écouter avec bienveillance et être présents dans les moments importants. Je remercie Artiom pour son soutien, sa patience et sa présence sans faille à mes côtés pendant cette dernière année. Je remercie mes amis merveilleux, avec qui j'ai passé tant de moments inoubliables au fil de ces années et sur qui j'ai toujours pu compter. Je ne les liste pas mais ils se reconnaîtront dans tous ces événements et rituels qui ont joyeusement ponctué mes années de thèse à Paris : les fêtes et brunch à la coloc' rue du Douanier Rousseau, les bièrecredis, les picnics à Montsouris, les soirées d'anniversaire et autres pendaisons de crémaillère, la zumba, le pilate, la course et autres défis sportifs, les raclettes mensuelles, les après-midi jeux de société, les verres au 2bis, au corse, au Gobelet d'argent ou au Louissette, les vacances et week-ends passés ensemble, et tant d'autres ! Je remercie enfin Nastassia, ma collègue de laboratoire mais surtout l'amie avec qui j'ai tant partagé, pour son écoute, son soutien, sa persévérance, sa joie de vivre, et ses métaphores souvent loufoques mais toujours éclairantes.

List of abbreviations

B

BM = Basement Membrane
BMBC platform = Biochemistry, Molecular
Biology and Cells platform
BrdU = Bromodeoxyuridine

C

CCD = Charged Coupled Device
CG = Contact Guidance
CIL = Contact Inhibition of Locomotion

D

DMEM = Dulbecco's Modified Eagle's Medium
DMSO = Dimethyl Sulfoxide
DNA = Desoxyribonucleic Acid

E

ECM = Extra Cellular Matrix
EHL = Embryonic Human Lung

F

FA = Focal Adhesion
FBS = Fetal Bovine Serum
FFT = Fast Fourier Transform
FOV = Field of View

H

HBEC = Human Bronchial Epithelial Cell

I

IPGG = Institut Pierre-Gilles de Gennes

K

KD = Knock Down

L

LIC = Line Integral Convolution
LSM = Laser Scanning Microscope

M

MDCK = Madin-Darby Canine Kidney
mRNA = messenger RNA
 μ PG = micro-Pattern Generator

N

NRK = Normal Rat Kidney
nt = nucleotide

P

PBS = Phosphate Buffer Saline
PDMS = Polydimethylsiloxane
PEG = Polyethylene Glycol
PIV = Particle Image Velocimetry
p-nblebb = para-nitroblebbistatin

R

RPE1 = Retinal Pigment Epithelial 1
RNA = Ribonucleic Acid

S

shRNA = short hairpin RNA
sCMOS = scientific Complementary Metal-
Oxide-Semiconductor

U

UV = UltraViolet

W

WT = Wild Type

Foreword

The ability of cells to migrate collectively is crucial in many biological processes such as morphogenesis, wound healing, or cancer progression. *In vivo*, cells are often guided by oriented surrounding structures, such as bundles of extra cellular matrix. Such anisotropic fibers can be mimicked *in vitro* by topographical structures such as grooves and ridges. Although the “contact guidance” of individual cells on such textured substrates has been thoroughly studied, less is known on the cell collective response to these cues. Better understanding and controlling collective cell behaviors on textured substrates could lead to important advances for example in the tissue engineering field.

From a physics perspective, collective cell migration is a typical example of collective behavior that can emerge in active matter systems. Such collective behaviors have been studied in a large range of living and non-living active systems at different scales, from biofilament assemblies to robot or animal herds. Recently, an important effort has been made to identify universal rules controlling the emergence of such collective behaviors. It is then of interest, both from a biological and a physics point of view, to study collective migration phenomena in cell monolayers.

This manuscript contains the main parts of the work I did during my PhD under the supervision of Pascal Silberzan in the lab Physico Chimie Curie (UMR 168) at Institut Curie. In our team named “Biology-inspired Physics at Mesoscales”, we use a physical approach to study collective behaviors that emerge in cell populations. We are also convinced that biological systems such as cell monolayers can inspire new physics and are well-suited to test non equilibrium physics model. In this context, I studied during my PhD collective behaviors that emerge in confluent cell monolayers on well-controlled micro-textured substrates. To do that, I used several microfabrication, cell biology and microscopy techniques. The images were quantified using image analysis tools including Particle Image Velocimetry (PIV). The experimental results were interpreted in the framework of active matter physics and lead to collaborations with theory groups.

The manuscript is divided in four chapters:

- The first chapter is a general introduction that gives the context of this work and introduces useful biological and physical concepts. More specific introductions and motivations of the two projects presented in this manuscript are found at the beginning of Chapter 3 and Chapter 4.
- The second chapter describes the material and methods that have been used to perform and analyze the experiments presented in Chapter 3 and Chapter 4. Details on the protocols and methods can be found in Annex 6.1 and 6.2.
- The third chapter presents the results obtained when chaotic epithelial cells are guided by microgrooves in their substrates. I show that the confluent monolayers adopt spontaneously a large-scale polar laning pattern in which the cells organize into wide (\sim mm) alternating lanes that migrate in antiparallel directions. Our results are well-captured by a hydrodynamic

description developed in the context of this project by Carles Blanch-Mercader, Samuel Bell and Jacques Prost from the team “Physical approach of biological problems” at Physico Chimie Curie. This continuum approach is complemented by particle-based simulations performed by Bart Smeets from the “BIOSYST-MeBioS” group at KU Leuven.

- The fourth chapter focuses on the formation of perpendicularly stacked layers of muscle cells. I present a strategy based on topographical contact guidance to trigger the self-formation of such structures at large scale with C2C12 myoblasts and investigate the underlying mechanism. This project also led to a collaboration with Carles Blanch-Mercader, Samuel Bell and Jacques Prost that gave new insights on the active nematic description of C2C12 myoblasts.

Mathilde Lacroix,

April 8, 2022

Content

1. Introduction	1
1.1. From single to collective cell migration	3
1.2. Active nematic and polar fluids.....	12
1.3. From single to collective contact guidance	27
2. Materials and methods.....	35
2.1. Substrates micro-fabrication.....	37
2.2. Cell biology.....	39
2.3. Microscopy.....	43
2.4. Image analysis	44
2.5. Statistics.....	50
3. Collective contact guidance drives polar laning of chaotic epithelial cells	51
3.1. Motivations: impact of contact guidance on collective cell dynamics	53
3.2. Experimental results.....	59
3.3. Discussion	77
3.4. Continuum theory of an active polar fluid with anisotropic friction	80
3.5. Self-propelled particle-based simulations	85
3.6. Conclusion and perspectives.....	92
4. Crisscross bilayering of myoblasts controlled by collective contact guidance	95
4.1. Motivations: between 2D and 3D, multilayering in cell populations.....	97
4.2. Orthogonal bilayering at a perpendicular interface	107
4.3. Impact of the orientation mismatch at the interface.....	120
4.4. Discussion	123
4.5. Active nematic fluid description	128
4.6. Conclusion and perspectives.....	139
5. Conclusion.....	143

6. Annexes	145
6.1. Materials and detailed protocols	147
6.2. Robustness of PIV measurements to parameters change	157
6.3. Continuum theory of an active polar fluid with anisotropic friction	161
6.4. Equations for self-propelled particle-based simulations.....	169
6.5. Impact of surface chemistry on bilayering.....	172
7. Bibliography	177

1. Introduction

1.1. From single to collective cell migration	3
1.1.1. Single cell self-propulsion on a substrate.....	3
1.1.2. Definition and examples of collective cell migration	4
1.1.2.1. <i>Definition</i>	4
1.1.2.2. <i>In vivo collective cell migration</i>	5
1.1.2.3. <i>In vitro strategies to trigger and study collective cell migration</i>	6
1.1.3. Impact of cell-cell interactions on collective migration	8
1.1.3.1. <i>Cell-cell adhesion</i>	8
1.1.3.2. <i>Contact inhibition of locomotion</i>	9
1.1.4. Classification of interactions involved in collective cell migration.....	10
1.2. Active nematic and polar fluids.....	12
1.2.1. Definition and examples of active matter systems	12
1.2.2. Classification of active systems regarding symmetries	13
1.2.3. Quasi-long-range order and topological defects in liquid crystals.....	14
1.2.4. Active nematic hydrodynamics	16
1.2.4.1. <i>Active gel theory for a system with nematic symmetry</i>	16
1.2.4.2. <i>Splay and bend instabilities in contractile and extensile active nematics</i>	18
1.2.4.3. <i>Defect motion and active turbulence</i>	19
1.2.4.4. <i>Spontaneous flows in confined active cellular nematics</i>	20
1.2.5. Polar active systems	21
1.2.5.1. <i>Emergence of flocking in polar active systems</i>	21
1.2.5.2. <i>Classical theoretical models describing a flocking transition</i>	22
1.2.5.3. <i>Continuum description of cell monolayers as an active polar gel</i>	24
1.2.5.4. <i>Particle-based simulations of cell monolayers</i>	25
1.3. From single to collective contact guidance	27
1.3.1. <i>In vivo</i> guidance of cells by the ECM and larger anatomic structures	27
1.3.2. <i>In vitro</i> single cell contact guidance	29
1.3.3. <i>In vitro</i> collective contact guidance.....	32

The aim of my PhD project is to trigger and study, from a physics point of view, collective migration phenomena in confluent monolayers of cells guided by microscale topographical cues. In this first chapter, I give the general context of this work and introduce useful biological and physical concepts. More specific introductions and motivations of the two projects presented in this manuscript are found at the beginning of Chapter 3 and Chapter 4.

In this general overview, I first highlight the importance of collective cell migration in several biological processes such as morphogenesis, wound healing, and cancer invasion and present how this phenomenon arises from the combination of cell self-propulsion and cell-substrate and cell-cell interactions. For the present study, collective behaviors that emerge in experimental cellular systems are investigated using concepts from the active matter theory. In the second section, I define and present various examples and models of active matter, particularly emphasizing the differences between polar and nematic active systems. I show how this framework has already been used to understand collective behaviors in cellular systems. The third section deals with the strategy of contact guidance to orient and guide cells by topographical structures.

1.1. From single to collective cell migration

1.1.1. Single cell self-propulsion on a substrate

The cell is the fundamental structural and functional unit of all living organisms. To maintain their shape and internal organization, cells rely on their cytoskeleton: a meshwork of biofilaments such as actin in the cytoplasm. At the cell membrane, the cytoskeleton links the cell to its environment, through adhesions with the substrate and junctions with other cells. It is a highly dynamic structure, constantly remodeled by polymerization and branching processes. This flexibility and its mechanical properties support the cell in performing its force-related functions such as division or migration.

On a substrate, cells can break symmetry and self-propel through the following three steps repeated process^{1,2} (Figure 1.1.A) that relies on a variety of actin structures (Figure 1.1.B):

- 1) At the front of the crawling cell, actin polymerization at the lamellipodium exerts a pushing force deforming the membrane and extends it in the direction of migration. Filopodia are also created and dynamically probe the environment.
- 2) New unstable adhesion complexes are created between protrusions and the substrate. Some of them mature into stable integrin and vinculin-rich focal adhesions, creating strong anchoring points of the actin stress fibers to the substrate.
- 3) At the rear of the cells, actin fibers are contracted by the action of myosin motors. These active contractile forces are transmitted to the substrate through the focal adhesions. This leads to a net displacement of the nucleus and the cytoplasm, a retraction of the rear of the cell and a detachment of the focal adhesions at the rear of the cell.

1. Introduction

The direction corresponding to the rear-front axis of the cell defines its in-plane polarity \mathbf{p} (alternatively named “polarization”). In the case of spindle-shaped cells, polarization often coincides with cell orientation. Cell locomotion thus results from active traction forces exerted by the cell on the underlying substrate in the direction of its polarity. These active traction forces are balanced by cell-substrate friction forces, resulting from the complex binding-unbinding proteins dynamics at focal adhesions. In absence of external cue, cells move randomly on their substrates and their velocities \mathbf{v} align with their polarities \mathbf{p} .

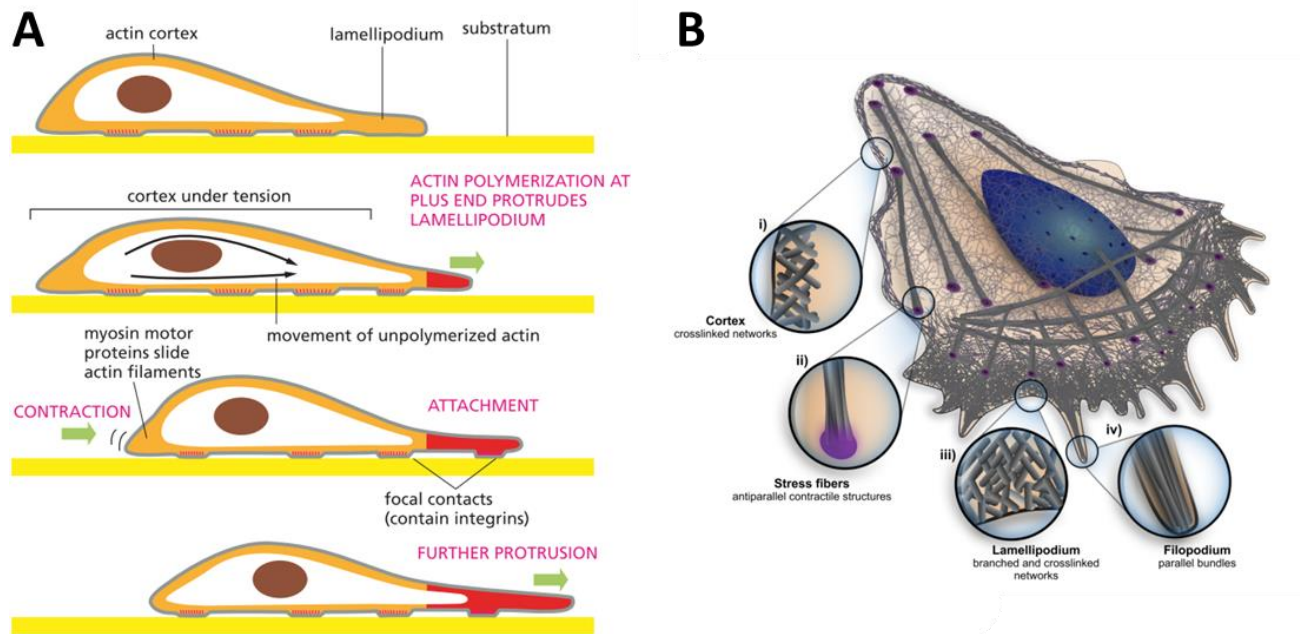


Figure 1.1 : Single cell migration on a substrate.

a. Schematic explaining the different steps of the mechanism supporting single cell migration ¹

b. Schematic presenting the different actin structures involved in cell migration: in particular, the front of the cell consists of a lamellipodium characterized by a branched actin network and retraction of the rear of the cell is supported by actin stress fibers contraction ³.

1.1.2. Definition and examples of collective cell migration

In vivo, cells are usually not isolated. They interact with complex environments and with other cells. To remodel and shape organs and eventually ensure tissue functions, cells often coordinate. Such coordination leads to the emergence of collective behaviors including collective cell migration.

1.1.2.1. Definition

Collective cell migration is defined as the coordinated active migration of a group of cells on a 2D substrate or through a 3D scaffold. It needs to be distinguished from other kinds of collective behaviors ⁴. A group of cells experiences collective migration if:

- It moves in the referential of its substrate (its underlying Extra Cellular Matrix (ECM) for example). Embryonic tissue folding or invagination by supracellular constriction is thus not considered as collective migration.

- Cells migrate on the underlying substrate via active processes. The displacement can't only be the result of coordinated neighbor exchanges (intercalation), or passive translocation of cells pushed by proliferation events (expansive growth of a tumor for example).
- Cells inside the moving group cooperate and coordinate by affecting the behavior of one another⁵. The independent migration of a large number of cells in a chemotactic gradient is thus excluded.

Collective cell migration has been widely studied and several reviews gather *in vivo* and *in vitro* examples as well as its biological and physical current understanding⁴⁻⁹. Here, through the presentation of *in vivo* examples, I highlight the central role of collective cell migration in several biological processes. I then introduce *in vitro* experiments designed to investigate the mechanisms underlying the emergence of such collective migration.

1.1.2.2. *In vivo* collective cell migration

Collective cell migration is a key feature for the normal development of an embryo and is involved in numerous stages of the development. For example, during gastrulation in zebra fish and xenopus embryos, mesendoderm cells internalize and migrate as a cohesive group (the precordial plate) underneath the ectoderm blastocoel roof toward the anterior part in both the dorsal and ventral hemispheres¹⁰⁻¹² (Figure 1.2.A-B).

Collective cell migration is also essential in the context of wound healing¹³. During the inflammation step immediately after tissue damage, phagocytes and platelets are recruited to the site to prevent infections and form a scab on the surface of the wound to restore a provisional barrier. The new tissue formation happens about 2 to 10 days after injury by collective migration of the 2D epithelial cell sheet underneath the scab to close the wound. This process is called the "re epithelization".

Collective cell migration is thus at stake in normal biological situations (embryogenesis and regeneration) but also in pathological ones. Although cancer progression has historically been associated to single cell invasion, it is now recognized that collective migration is involved in metastasis. Typically two types of collective invasion from a primary tumor were distinguished: the diffuse type in which the collective invading mass has an irregular shape, and the strands type in which invading cells form well-organized cell strands¹⁴ (Figure 1.2.C). Invasive tumor cell clusters, independent from the primary tumor they originate from, have also been identified *in vivo*^{4,15}. These clusters in which cells migrate collectively can adopt various shapes that are presented in Figure 1.2.D.

To conclude, a large variety of collective cell migration patterns are involved in normal and pathological *in vivo* processes. To bypass the complexity of these *in vivo* situations, and to investigate the universal mechanisms underlying collective cell migration, *in vitro* strategies have been developed.

1. Introduction

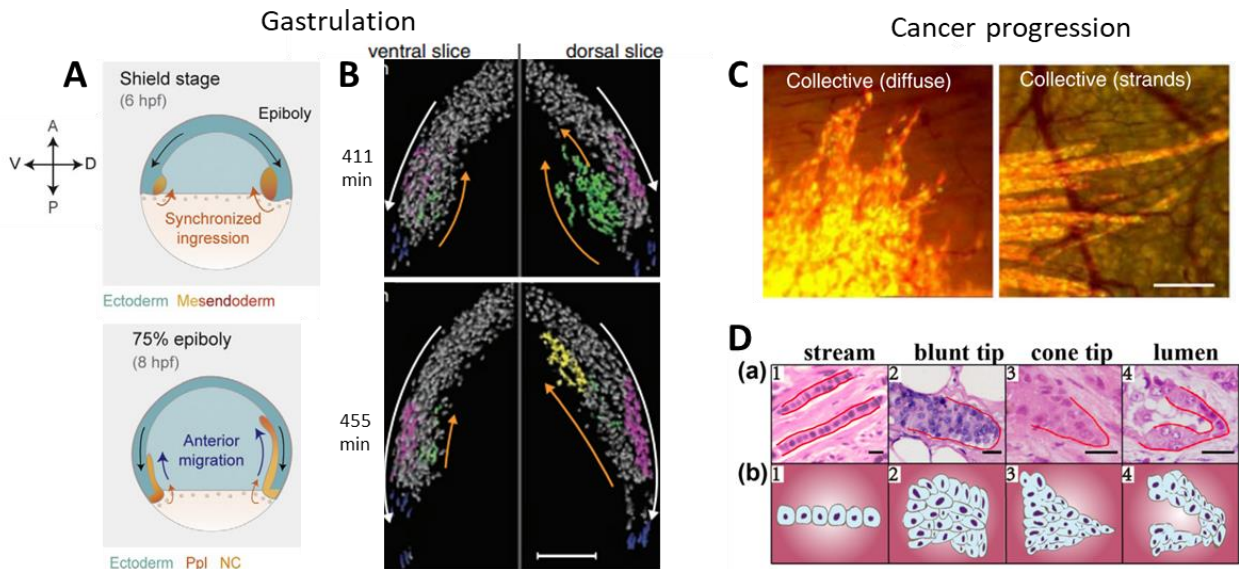


Figure 1.2 : Examples of collective cell migration *in vivo*.

A: Schematic representation of mesendoderm internalization during zebrafish gastrulation. hpf: hours post-fertilization; A: Anterior; P: Posterior; D: Dorsal; V: Ventral; Ppl: Prechordal plate; NC: Notochord (adapted from ¹¹).

B: Lateral view of nuclei during mesendoderm internalization and migration in dorsal and ventral hemispheres of a zebrafish embryo. Orange and white arrows indicate hypoblast and epiblast cell movements. Scale bar: 100 μm (adapted from ¹²).

C: Different invasion modes of fibrosarcoma HT1080 cells from a tumor in a mouse. Left: the cell mass invading from the tumor has an irregular shape which corresponds to a diffuse collective invasion. Right: the invading cells organize in regular compact strands. Scale bar: 250 μm (adapted from ¹⁴).

D: Categorization of invasive tumor cell clusters in four types of collective migration patterns: stream (1), blunt tip (2), cone tip (3) and lumen (4). (a) shows images of pathological slices of breast cancers and (b) the corresponding cartoons (adapted from ¹⁵).

1.1.2.3. *In vitro* strategies to trigger and study collective cell migration

To study collective cell migration, performing minimal and well-controlled *in vitro* experiments is a useful strategy. Indeed, this approach implies that we lose the complexity of *in vivo* processes but gain control on specific factors to investigate their impact on collective migration phenomena. I focus here on 2D *in vitro* systems which do not recapitulate all features of normal physiological migration but provide a controlled minimal environment that can be easily tuned. This approach has widely spread thanks to the progress made in microfabrication techniques.

To quantify collective migration in such well-controlled 2D environment, several physical values can be measured from the experiments. In particular, it is of interest to extract the velocity field $\mathbf{v}(\mathbf{r}, t)$ in cell monolayers from phase contrast movies. This can be done using Particle Image Velocimetry (PIV). This technique was used in the two projects presented in Chapter 3 and Chapter 4 and is presented in 2.4.3. Basically, it is based on the computation of correlation between images taken at two successive time points. From this velocity field one can compute the velocity-velocity correlation function and the corresponding correlation length, which characterizes the typical distance over which cell movements are correlated in the monolayer.

Collective motion of cells can be observed directly in confluent monolayers seeded on 2D substrates. The velocity correlation length, which depends on the cell type, is typically in the range between a few dozen to a few hundred micrometers¹⁶ (Figure 1.3.A). However, to trigger larger scale directed collective migration, other strategies have been developed.

The classic *in vitro* model to study collective cell migration is the so-called “barrier assay” based on the “wound-healing” assay. Typically, cells are seeded in micro stencils and grown to confluence in these limited spaces. At the beginning of the experiment, the stencils are removed to create free space at the edges of the monolayer, which triggers the collective migration of cells toward available free space¹⁷ (Figure 1.3.B).

Collective migration has also been induced *in vitro* by confining cells in mesoscale adhesive patterns (stripes, squares, or disks). In this configuration, collective migration arises due to boundary effect. This is the case for MDCK cells confined in disks. If the disk diameter is smaller or comparable to the velocity correlation length, cells collectively rotate as a solid body. If the diameter is increased further, the global rotation is lost and several local swirls appear¹⁸ (Figure 1.3.C).

These *in vitro* well-controlled strategies can then be used to investigate the role of cellular mechanisms such as cell-cell interactions in the emergence of collective cell migration.

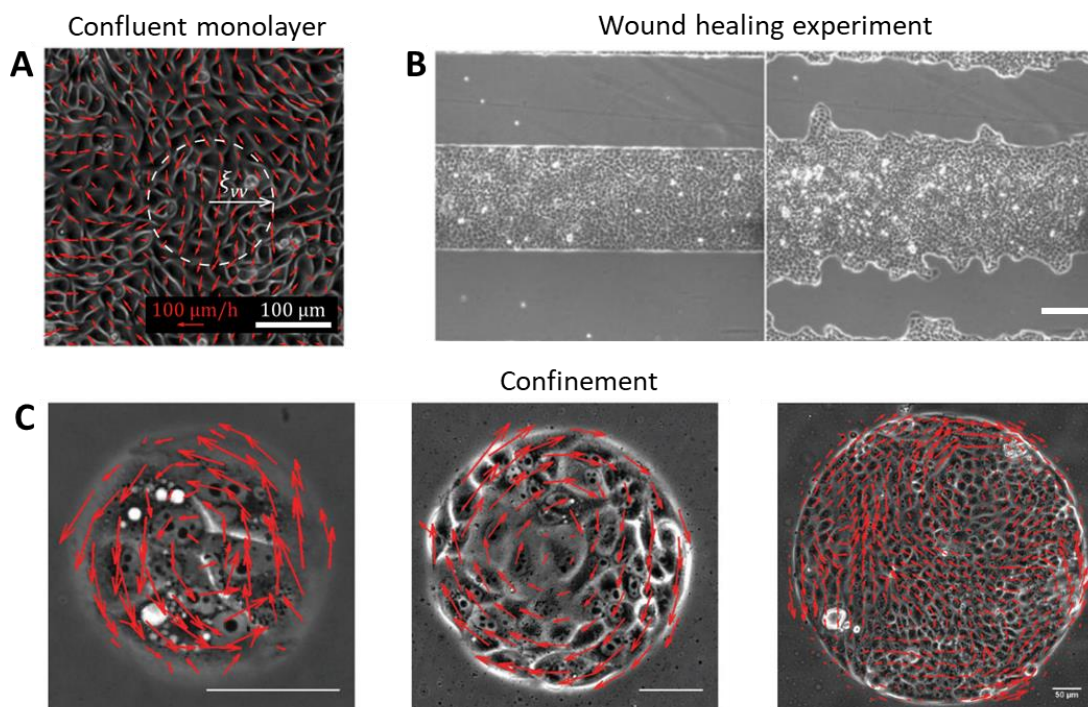


Figure 1.3 : Examples of collective cell migration *in vitro*.

A: In HBEC monolayers, the displacements are typically correlated in domains of radius ξ_w (dashed circle). ξ_w is the correlation length and is of the order 100 μm. Phase contrast image of the monolayer is overlaid with the velocity field¹⁶.
 B: In wound healing experiments, MDCK cells collectively invade available free space to eventually close the wound and form a confluent monolayer. The two images are taken at $t=1.5h$ (left) and $t=12h$ (right) after removing the barrier. Scale bar: 200 μm¹⁷.

C: MDCK cells confined in adhesive circular patterns develop a well-defined collective rotation if the pattern diameter is lower than 200 μm. The images of MDCK cells at confluence on circular patterns of diameter 100, 200 and 500 μm are overlaid with the velocity fields. Scale bar: 50 μm (adapted from¹⁸).

1. Introduction

1.1.3. Impact of cell-cell interactions on collective migration

Cell-cell interaction is a critical parameter controlling collective cell migration. In the following, two types of cell-cell interactions impacting collective cell migration are detailed.

1.1.3.1. Cell-cell adhesion

During gastrulation in zebra fish and *Xenopus* embryos (Figure 1.2.A-B), mesendoderm cells maintain cohesiveness through adhesion proteins C-cadherin in *Xenopus*¹⁹ and E-cadherin in zebrafish²⁰. Moreover, cancerous cells invading fibrillar collagen in the form of collective strands also maintain strong cadherin based cell-cell junctions²¹ (Figure 1.4.A). These strong adhesions allow force transmission from cell-to-cell over large distances^{22,23}. Consequently, epithelial MDCK cells with strong cell-cell adhesions show more spatial correlation in their displacement than independent fibroblast-like NRK cells during a wound healing assay²⁴ (Figure 1.4.C). Furthermore, perturbing cell-cell junctions can lead to the loss of collective migration patterns. For instance, HaCaT keratinocyte cells experience collective oscillations when confined in square patterns, but when cell-cell junctions are impaired by downregulating α -catenin, a protein linking cadherins to the actin cytoskeleton, this collective behavior is lost²⁵ (Figure 1.4.B). Thus, the emergence of collective migration is dependent on cadherin-based cell-cell adhesion.

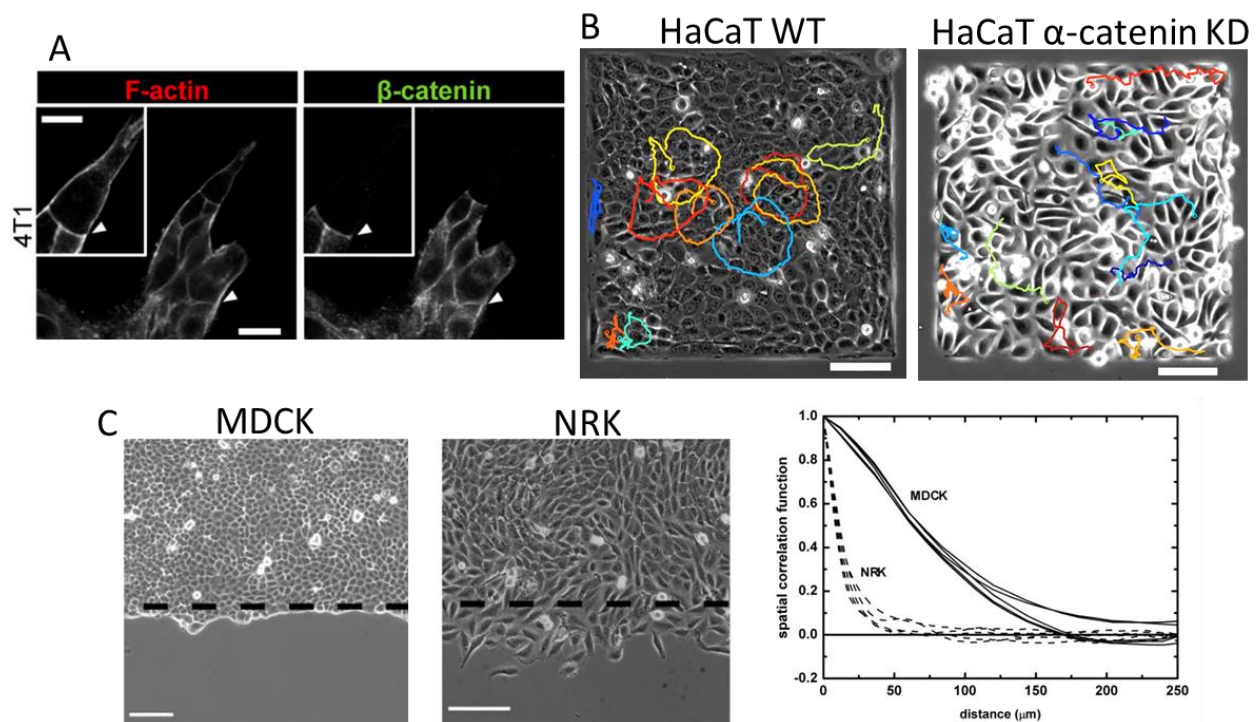


Figure 1.4 : Collective cell migration supported by cell-cell adhesion.

A: β -Catenin, a subunit of the cadherin protein complex, localizes at cell-cell junctions in collective strands of 4T1 metastatic breast cancer cells invading 3D fibrillar collagen. Arrowheads: cell-cell junctions. Scale bar: 20 μm (adapted from²¹).

B: Coordinated oscillations of confined HaCaT keratinocyte cells (left) are lost in confined α -catenin knocked-down cells that experience disordered displacements. Representative trajectories of single cells are drawn in colors. Scale bar: 100 μm (adapted from²⁵).

C: Epithelial (MDCK) and fibroblastic (NRK) tissues wound healing assays (left) show that spatial correlation is larger in epithelial cells with strong cell-cell adhesion compared to fibroblastic cells during free space invasion (right). Scale bar: 100 μm (adapted from ²⁴)

1.1.3.2. Contact inhibition of locomotion

Contact inhibition of locomotion (CIL) is a mechanism at play in collective cell migration of non-adhesive cells. CIL is the process by which cells repolarize away from cell-cell contact after a “collision” through the four steps detailed in Figure 1.5.A. From a physical point of view, this effective avoidance mediated by RhoGTPases can be modelled by a repulsive interaction impacting cell polarization. It has been shown that, even if counterintuitive at first sight, CIL can trigger collective motion. For example, cells confined in thin stripes experience CIL. The result of these repulsive interactions is the formation of cellular trains in which cells all go in the same direction ²⁶ (Figure 1.5.B).

This process is also involved in *in vivo* situations. At late gastrulation stages in vertebrates' development, neural crest cells delaminate from the neural plate and migrate dorsoventrally in loose clusters to reach their final locations where they differentiate into many different cell types (Figure 1.5.D). Inside each cluster, cells do not maintain strong contact but coordinate their motions by repeated CIL ²⁷. This mode of collective migration is referred to as “streaming” (Figure 1.5.C).

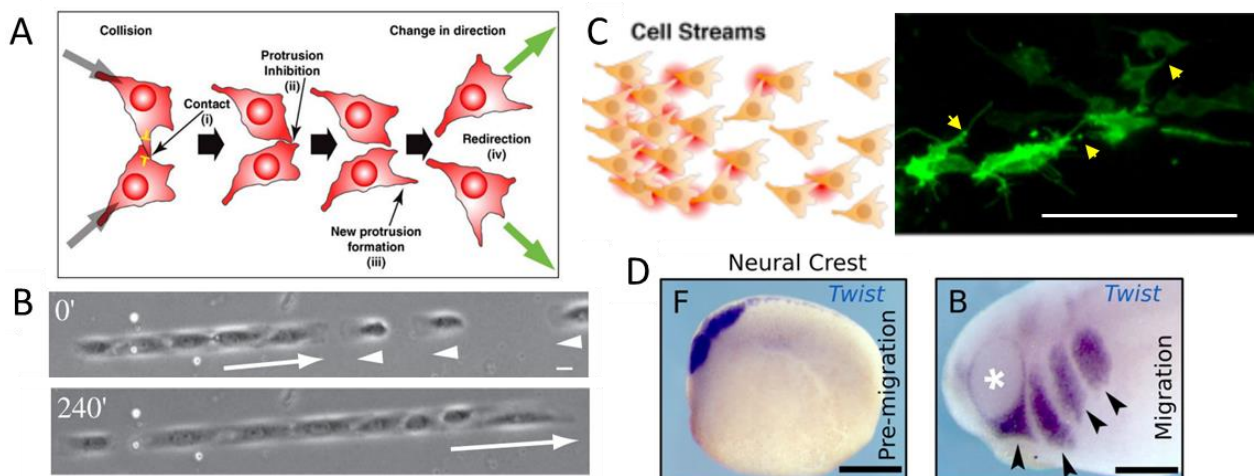


Figure 1.5 : Collective cell migration induced by CIL.

- A: Schematic of a “collision” between two single cells leading to their reorientation via CIL (adapted from ²⁸).
- B: Collective trains of cells emerge from CIL between cells. Arrows indicate direction of train migration, and arrowheads indicate direction of single cell migration at $t=0$ min. Scale bar: 25 μm (adapted from ²⁶).
- C: Left: schematic representation of cell streaming via repeated CIL. Right: Avian neural crest migrating in a stream via repeated CIL; yellow arrowheads show localized protrusion formation. Scale bar: 100 μm (adapted from ^{28,29}).
- D: Lateral views of *Xenopus laevis* embryo show neural crest cells position (purple marker) before (left) and during migration (right). Arrowheads indicate NC streams, * marks the eye/optic vesicle; scale bars: 300 μm (adapted from ³⁰).

Thus, collective migration is a central feature in development, regeneration, and cancer progression. It relies on the cell ability to self-propel and can emerge from strong attractive interactions such as cadherin-based cell-cell adhesion but also in loose clusters of cells without stable cell-cell junctions through transient repulsive interactions such as CIL. However, other interactions can be at stake in collective migration. Next, I present a classification of these interactions that has been recently proposed by Alert and Trepat in a review article ⁹.

1.1.4. Classification of interactions involved in collective cell migration

Even though I insisted on two specific examples, cell-cell adhesion and CIL, other types of interactions can be involved in regulating collective cell migration. A recent review ⁹ has proposed a classification of the different interactions that can be at stake in a monolayer of migrating cells. Classically, authors distinguish cell-cell and cell-substrate interactions, but they also introduce a distinction between interactions that directly impact cell position (i.e. cell velocity \mathbf{v}) and interactions that impact cell polarization \mathbf{p} . This classification is presented in Table 1.1 and a subset of these interactions is sketched in Figure 1.6. Notably in a migrating cell monolayer, interactions with other cells or with the substrate can directly influence the cell polarity \mathbf{p} or the cell velocity \mathbf{v} . It implies that \mathbf{v} and \mathbf{p} are not necessarily well-aligned in confluent monolayers (Figure 1.6.b).

	Positional interactions	Orientalional interactions
Cell-substrate	<ul style="list-style-type: none"> • Active traction forces • Cell-substrate friction forces 	<ul style="list-style-type: none"> • Polarity-velocity alignment <i>(Discussed in 1.2.5.3 and Chapter 3)</i> • Substrate-induced polarization <i>(Ex: durotaxis in which cells migrate toward stiffer regions)</i>
Cell-cell	<ul style="list-style-type: none"> • Cell-cell adhesion • Cell-cell friction • Cell-cell repulsion <i>(Ex: excluded volume interactions)</i> • Active cell-cell forces 	<ul style="list-style-type: none"> • Polarity alignment <i>(Between neighbors, discussed in 1.2.5.2)</i> • Contact regulation of locomotion <i>(ex: CIL)</i> • Polarity-flow alignment <i>(Ex: cells reorient in shear, discussed in 1.2.4)</i> • Polarity-shape alignment

Table 1.1 : Classification of forces and interactions in a migrating cell population ⁹. Some of these forces and interactions are sketched in Figure 1.6.

To conclude, cell monolayers are systems composed of a large number of cells developing complex interactions with their neighbors and their underlying substrates that can lead to collective migration. They belong to a larger class of physical systems namely active matter systems. In the next section, I present the framework of active matter theory that provides concepts and tools to understand the emergence of collective behavior in these complex systems.

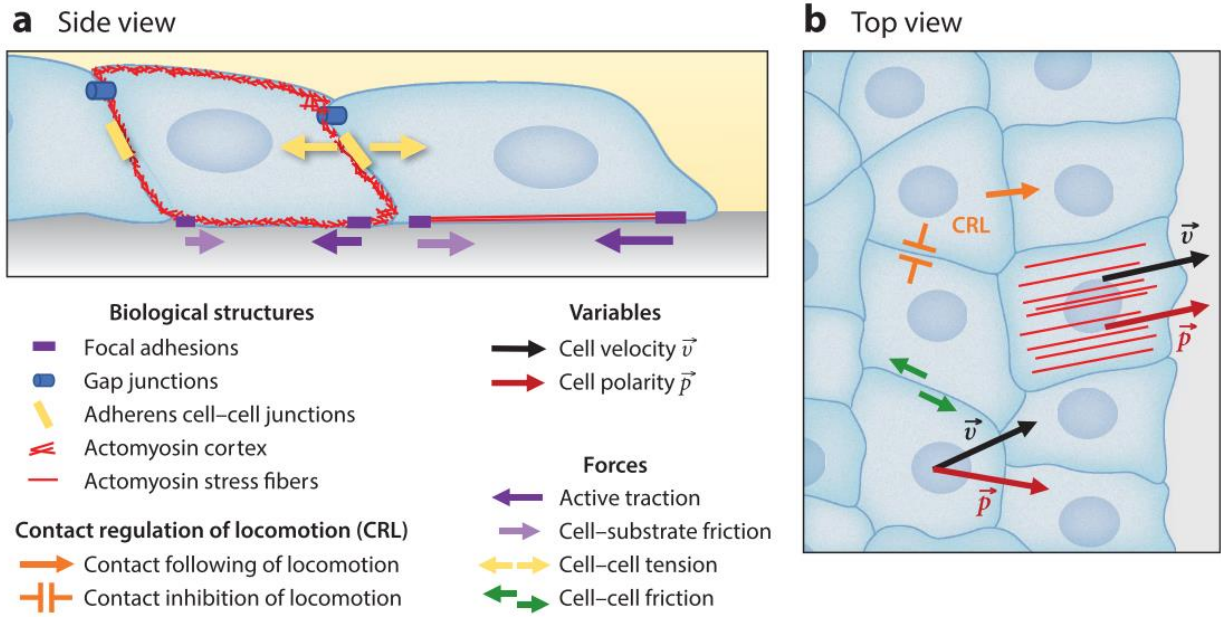


Figure 1.6 : Forces and interactions in a migrating epithelial monolayer ⁹.

Collective behavior is described by cell velocity \vec{v} and cell polarity \vec{p} . The forces and interactions are supported by a variety of biological structures.

1.2. Active nematic and polar fluids

1.2.1. Definition and examples of active matter systems

Active matter is the science of assemblies of objects able to self-propel or to exert forces on their surroundings. It refers to systems composed of a large number of units, each of them locally consuming energy to produce forces. This is a class of non-equilibrium systems in which energy input and dissipation take place locally and are homogeneously distributed in the whole system. They have to be distinguished from usual non-equilibrium systems, such as sheared fluid, in which the energy input is driven by external cues. In these active matter systems, the local interactions with the surrounding medium (fluid, substratum) and between particles give rise to collective behaviors such as correlated collective motion at large length scales and sustained for long time scales.

The active matter framework has successfully been used to describe complex collective behaviors that arise in various living and non-living systems composed of elementary units with a characteristic size ranging from nanometers to meters (Figure 1.7): animal groups, cell monolayers, assemblies of colloids or robots, bacterial colonies, suspensions of bio filaments mixed with associated motor proteins (acto-myosin or microtubule-kinesin systems), etc. Macroscopic properties of active systems are universal in the sense that they are similar for systems very different in terms of detailed microscopic interactions and length scales.

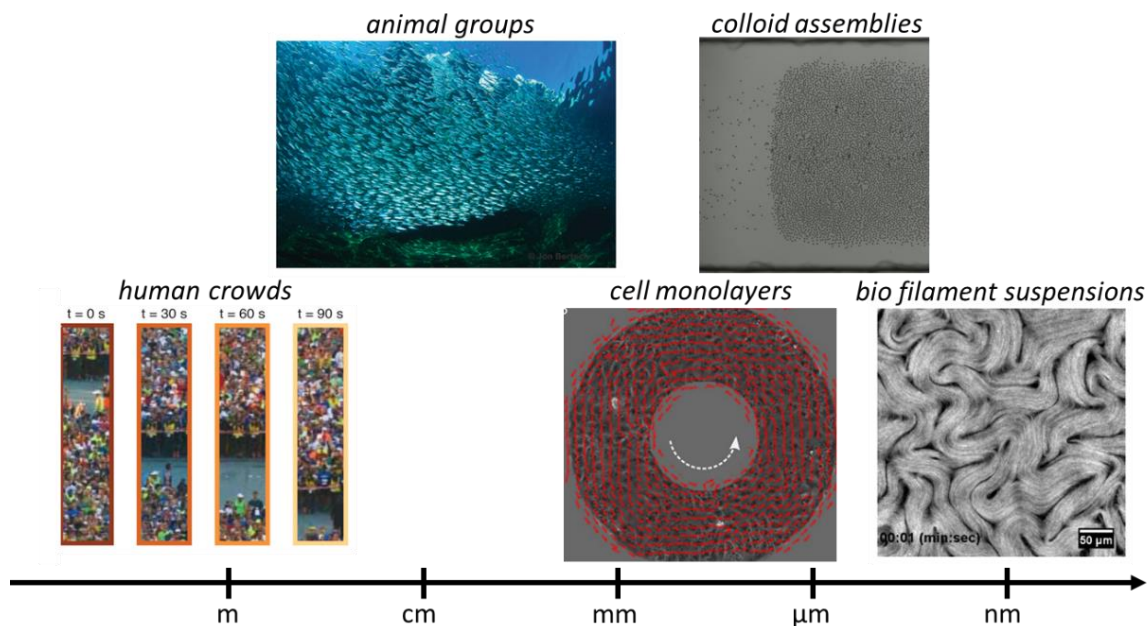


Figure 1.7 : Examples of active matter systems across scales.

From left to right: human crowd polar motion at the Chicago marathon ³¹ (human size: 1.7 m); Polar order in a sardine school ³² (fish size: 20 cm); Collective cell rotation in a ring pattern of width 200 μm ³³ (cell diameter: 20 μm); Flock of motile colloids ³⁴ (colloid radius: 2.4 μm); Active turbulence in a microtubule-kinesin system ³⁵ (microtubule diameter: 25 nm).

The variety of active systems' collective behaviors and theoretical models developed to understand them are gathered in the following reviews ^{32,36–39}. Here, I introduce the most relevant notions and examples for the understanding of the present thesis, highlighting the differences between nematic and polar systems and with an emphasis on cellular assemblies.

1.2.2. Classification of active systems regarding symmetries

Active systems can be classified regarding the symmetry of their individual components and of their aligning interactions presented Figure 1.8. Elementary units composing active systems are often anisotropic: they can be polar with distinct head and tail (Figure 1.8.a) or apolar but elongated (Figure 1.8.b). Apolar particles can have an apolar dynamics if they exert a force dipole on their surroundings (Figure 1.8.b) or a polar dynamics if they are self-propelled (Figure 1.8.c).

Their interactions can be:

- Isotropic if the particles do not tend to align with each other
- Polar if the particles have a polar dynamic and tend to align their polarization (Figure 1.8.d)
- Nematic if the particles tend to align regardless of their direction: it is the case either if the particles are elongated but apolar (Figure 1.8.e) or polar but cannot distinguish between parallel and antiparallel alignment (Figure 1.8.f).

The combination of these symmetry rules fixes the organization of the system: for example, polar particles can adopt a polar or a nematic order depending on the alignment rule (Figure 1.8.d, f).

A nematic liquid crystal is characterized by no positional order and long range orientational order, which is an intermediate state between solid and liquid. At scales much larger than a particle size, a liquid crystal in the nematic state is described with a continuum director field $\mathbf{p}(\mathbf{r})$ obtained by coarse-graining particles' orientation. It is invariant for $\mathbf{p} \rightarrow -\mathbf{p}$. Conversely, polar order is described by a vector director field \mathbf{p} and is characterized by a non-zero averaged polarization in the ordered phase.

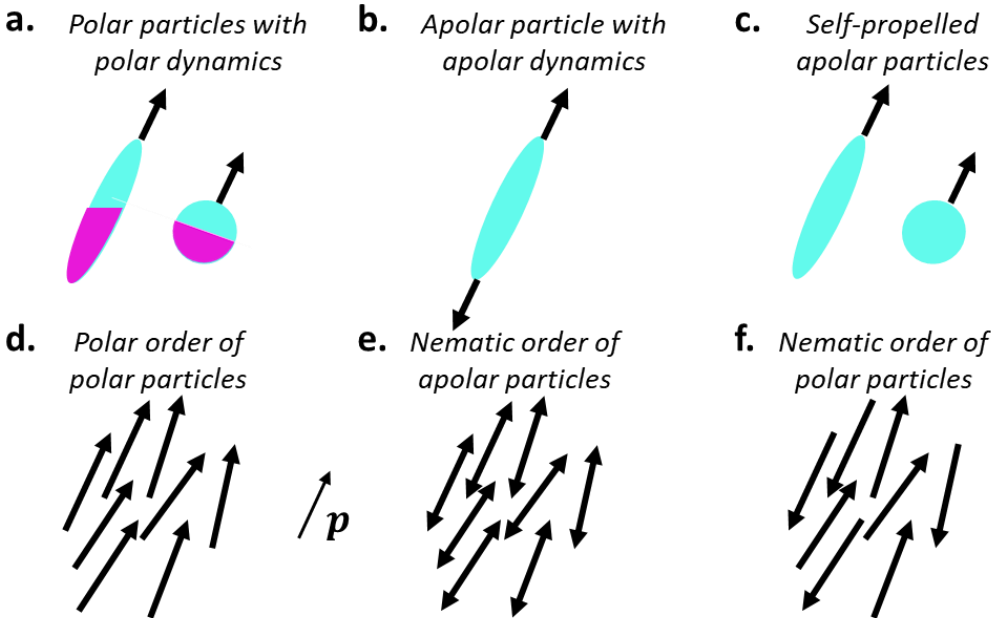


Figure 1.8 : Schematic of the various types of active particles symmetries and ordered states. Inspired by ³².

1.2.3. Quasi-long-range order and topological defects in liquid crystals

Liquid crystals are composed of polar or apolar particles that tend to align with each other. In the ordered phase, distortions of the director field such as splay, twist or bend can appear due to boundary conditions or external perturbations (Figure 1.9.A). In the nematic phase, these continuous variations in the director field are associated with an energy cost described by the Frank-Oseen free energy^{40,41}:

$$F_p = \int dr \left\{ \frac{K_s}{2} (\nabla \cdot \mathbf{p})^2 + \frac{K_t}{2} [\mathbf{p} \cdot (\nabla \times \mathbf{p})]^2 + \frac{K_b}{2} (\mathbf{p} \times (\nabla \times \mathbf{p}))^2 \right\} \quad (1.1)$$

where K_s , K_t and K_b are the Frank elastic constants and are respectively associated with the splay, twist, and bend distortions of the nematic field (Figure 1.9.A). Note that twist distortions can only be found in 3D systems, so the K_t term is always equal to zero for 2D systems such as cell monolayers. The classic one constant approximation assumes $K_s = K_t = K_b = K$. In that case, the Frank-Oseen free energy reduces to:

$$F_p = \int dr \left\{ \frac{K}{2} (\nabla \mathbf{p})^2 \right\} \quad (1.2)$$

The equilibrium state in the absence of an external field or intrinsic activity is predicted by minimizing this free energy and corresponds to the perfectly aligned state. However, due to specific boundary conditions, history of the system or activity induced fluctuations, points where \mathbf{p} is discontinuous appear. They are called topological defects. These singularities are stable: they can be annihilated only by merging with another defect or by moving to a boundary.

A defect is characterized by its topological charge m calculated by measuring the angle change of the director field along a closed loop around the core of the defect. Mathematically, m is given by: $m = \frac{1}{2\pi} \oint \frac{\partial \theta}{\partial l} dl$, where l is the path along the loop and θ is the local director angle. There are four possible charges: $m = \pm 1/2$ or $m = \pm 1$ (Figure 1.9.B). In 2D nematic liquid crystals, ± 1 defects are transient structures that split into two $\pm 1/2$ defects that have a lower energy cost. In population of spindle shaped cells exhibiting quasi long range orientational order⁴², $\pm 1/2$ defects are found between large domains in which cells share the same orientation⁴³ (Figure 1.9.C, D). This implies that population of such elongated cells are in a nematic liquid crystal phase. Polar liquid crystals don't share the $\mathbf{p} \rightarrow -\mathbf{p}$ invariance, and arrows describing the direction of polarization should be added to the lines representing the orientation in the topological defects sketch. In polar systems, half integer defects force a discontinuity in polarization direction along a line and have a high energy cost. Thus, integer defects have a lower energy cost and are found in polar systems such as the gels of microtubules associated with motor proteins shown in Figure 1.9.E⁴⁴.

To conclude, the types of defects can help identifying the polar or nematic nature of a system, at least in the passive state. In this thesis, we are interested in the dynamics of active cell monolayers that locally consume energy. In the following, I introduce the consequences of activity on the dynamics of nematic and polar systems, with an emphasis on experimental realizations in cell monolayers.

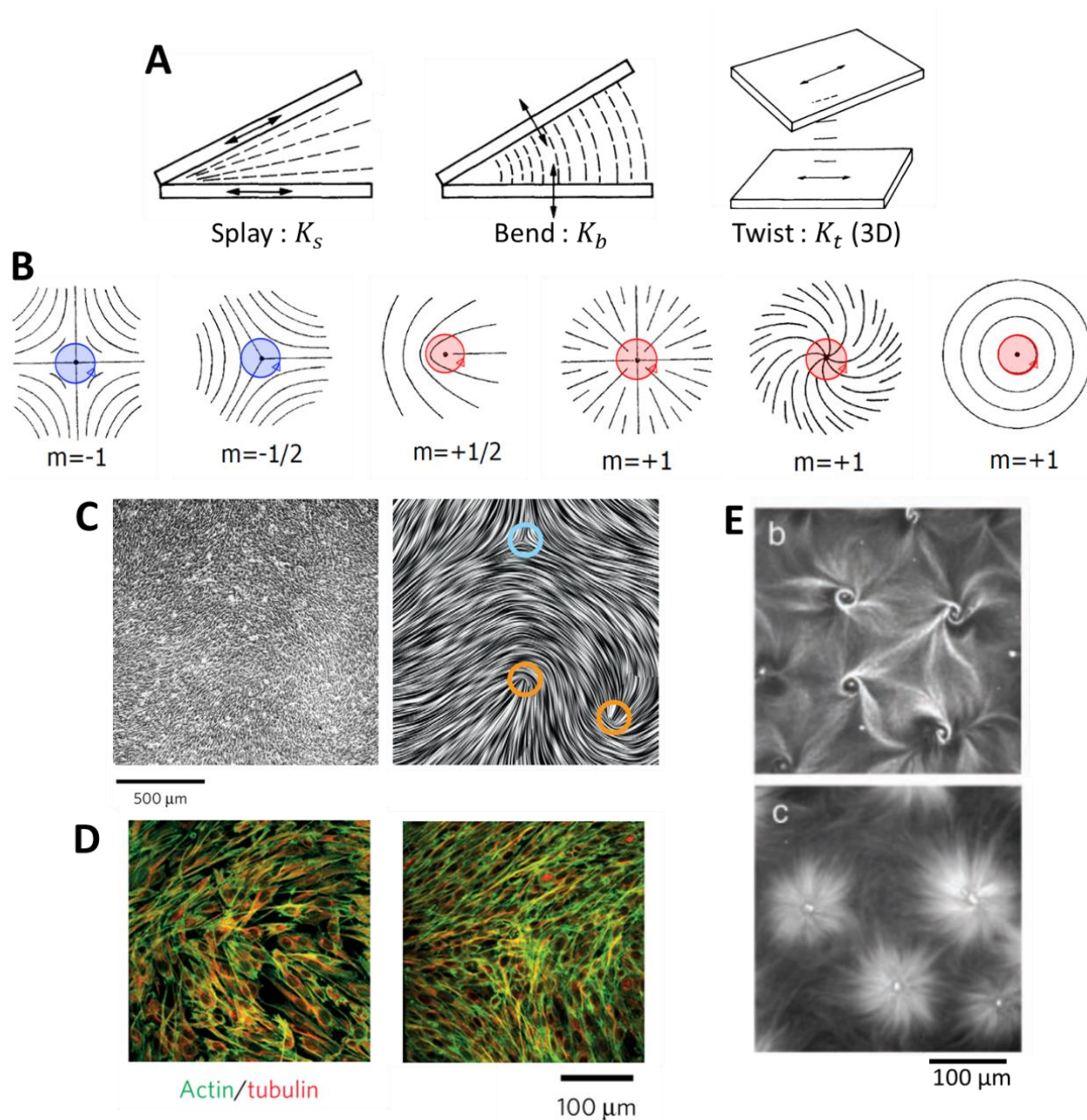


Figure 1.9 : Distortions and topological defects in liquid crystals.

A: Splay, bend and twist distortions of the director field in a nematic liquid crystal (adapted from ⁴⁰). Dashed lines represent the orientation field. Double-headed arrows represent the alignment rules at the boundaries. Note that twist distortions are found only in 3D systems.

B: Six types of topological defects found in 2D liquid crystals. Black lines represent the orientation of the particles. (adapted from ⁴¹ in ⁴⁵).

C: In NIH-3T3 elongated fibroblast monolayers, half-integer defects, characteristic of nematic liquid crystals, are found between large domains in which cells share the same orientation. Left: Phase contrast image 40h post-confluence. Right: Line integral convolution (LIC) representation showing the field lines of the orientation field. Defects are outlined with colored circles ($-1/2$ = cyan, $+1/2$ = orange) (adapted from ⁴³).

D: Zoom on a $+1/2$ (left) and a $-1/2$ (right) defect found in NIH-3T3 monolayers (adapted from ⁴³).

E: integer defects, characteristic of polar liquid crystals, are found in gels composed of microtubules and associated kinesin motors. The two images correspond to different motor concentrations (adapted from ⁴⁴).

1. Introduction

1.2.4. Active nematic hydrodynamics

To describe the dynamics of active matter system, one needs to consider local input of energy in the system. Here I describe a continuum theory of active gels based on generalized hydrodynamic equations driving the system dynamics. I then present the consequences of activity that are observed in experimental systems with nematic symmetry.

1.2.4.1. Active gel theory for a system with nematic symmetry

Active gel theory was initially developed to model active systems of mixed bio filaments and associated motors. However, the theory is based on symmetry consideration and does not rely on microscopic details. It is then well-suited to describe other active systems which share the same symmetries such as cell monolayers. Here, I present the steps for deriving constitutive and conservation equations following the approach of the review “Hydrodynamics of soft active matter”³². Detailed calculations can be found in^{32,46,47}.

In this model, the identified slow hydrodynamic variables are the density ρ , the polarization \mathbf{p} and the momentum density $\mathbf{g} = \rho m \mathbf{v}$, where \mathbf{v} is the local velocity and m is the effective mass of the particles. In the linear Onsager theory approach for deriving generalized hydrodynamic equations, the first step is to express the entropy production rate in the system, that is related to the time derivative of the free energy $T\dot{S} = -\frac{dF}{dt}$, where in our case the temperature T is constant. As in a passive system, entropy production is related to variation of density, polarization, and kinetic energy. Additionally, the local energy input due to energy source consumption must be included in the free energy. The rate of change of free energy per unit volume is $-r\Delta\mu$ where $\Delta\mu$ is the energy gain per unit of energy source consumed and r is the reaction rate. Enforcing conservation laws of the material and performing mathematical rearrangements lead to the following expression of the entropy production rate:

$$T\dot{S} = \int d\mathbf{r} \{ \sigma_{\alpha\beta} v_{\alpha\beta} + P_{\alpha} h_{\alpha} + r\Delta\mu \} \quad (1.3)$$

This form allows identifying fluxes and associated forces (Table 1.2) that control the entropy production in the system.

Flux	Force	Force signature under time reversal
$\sigma_{\alpha\beta}$: symmetric deviatoric stress tensor	$v_{\alpha\beta}$: strain-rate tensor $v_{\alpha\beta} = \frac{1}{2}(\partial_{\alpha}v_{\beta} + \partial_{\beta}v_{\alpha})$	-1
P_{α} : commoving and corotational derivative of the polarization $P_{\alpha} = \frac{Dp_{\alpha}}{Dt} = \frac{\partial p_{\alpha}}{\partial t} + v_{\beta}\partial_{\beta}p_{\alpha} + \omega_{\alpha\beta}p_{\beta}$, where $\omega_{\alpha\beta} = \frac{1}{2}(\partial_{\alpha}v_{\beta} - \partial_{\beta}v_{\alpha})$ is the vorticity	h_{α} : molecular field $h_{\alpha} = -\frac{\partial F_p}{\partial p_{\alpha}}$, where F_p is the polarization free energy	+1
r : reaction rate	$\Delta\mu$: energy gain per unit of energy source consumed	+1

Table 1.2 : Fluxes and forces controlling entropy production in an active gel, and forces time symmetry

The central idea of the linear generalized hydrodynamic theory approach is to write the most general linear relations between forces and fluxes that respect the symmetries of the system. The spatial symmetries regard invariance by translation and rotation of the polarization vector \mathbf{p} and the nematic tensor $q_{\alpha\beta} = p_\alpha p_\beta - \frac{1}{3}\delta_{\alpha\beta}$. For nematic systems, the invariance $\mathbf{p} \rightarrow -\mathbf{p}$ must be enforced. To respect the time-reversal symmetry, the fluxes are separated into a reactive component (time signature opposite to the conjugated force) and a dissipative component (same time signature as the conjugated force). Reactive and dissipative fluxes are then linearly coupled with forces of the same time signature through phenomenological coefficients. Total fluxes are obtained by summing the reactive and dissipative parts. Eventually, assumptions depending on the problem can be made to reduce the number of terms (incompressibility, isotropic viscosity, conserved modulus of \mathbf{p} , etc.). For example, for a nematic incompressible active fluid in a bulk, the constitutive equations for the stress tensor and the polarization evolution read ³²:

$$\begin{aligned} \sigma_{\alpha\beta} &= \sigma_{\alpha\beta}^{passive} + \sigma_{\alpha\beta}^{active}, \\ \text{with } \sigma_{\alpha\beta}^{passive} &= 2\eta \left(v_{\alpha\beta} - \frac{1}{3}v_{\gamma\gamma}\delta_{\alpha\beta} \right) + \frac{\nu}{2}(p_\alpha h_\beta + p_\beta h_\alpha - \frac{2}{3}p_\gamma h_\gamma \delta_{\alpha\beta}) \\ \text{and } \sigma_{\alpha\beta}^{active} &= -\zeta\Delta\mu q_{\alpha\beta} \end{aligned} \quad (1.4)$$

$$\frac{\partial p_\alpha}{\partial t} + v_\beta \partial_\beta p_\alpha + \omega_{\alpha\beta} p_\beta = \frac{1}{\gamma} h_\alpha - \nu v_{\alpha\beta} p_\beta \quad (1.5)$$

Classical coupling parameters already present in the passive description of nematic fluids are the viscosity η that couples stress and velocity, the rotational viscosity γ that controls the relaxation of the polarization field and the flow-alignment coefficient ν that accounts for the passive effect of particle alignment in shear flows. The activity effects are encapsulated in the active stress $\sigma_{\alpha\beta}^{active} = -\zeta\Delta\mu q_{\alpha\beta}$, that comes from the local consumption of an energy source transformed into mechanical energy. The consequences of this active term are discussed in the next subsection.

NB: In the present work, we study cell monolayers that are 2D systems. In order to describe cell monolayers within the framework of the active gel theory, a thin-film approximation gives the 2D version of the constitutive equations for the height-averaged stress ⁴⁸. Furthermore, to fully describe the dynamic of the system, the constitutive equations must be complemented by a force balance equation. In cell monolayers, cells are in contact with a substrate. Thus, friction with the substrate is usually included in the force balance ⁴⁹.

These constitutive equations show that polarization, flows, and activity are coupled by phenomenological parameters (viscosities, friction, activity, etc.). These intrinsic couplings have consequences on the dynamics of active nematic systems. In the following, I detail the hydrodynamic consequences of activity that are the most relevant in the context of the present work. For more details, the characteristic features of active nematic hydrodynamics have been reviewed in ³⁷.

1. Introduction

1.2.4.2. Splay and bend instabilities in contractile and extensile active nematics

Active gel theory derivation reveals the existence of an active stress $\sigma_{\alpha\beta}^{active} = -\zeta\Delta\mu q_{\alpha\beta}$. It means that active systems are constantly submitted to anisotropic stresses because of the local injection of energy. The sign of the activity coefficient ζ is controlled by the nature of the force dipole that active particles exert on their surroundings. The force dipole along the long axis of the particles is composed of inward forces for contractile particles ($\zeta < 0$) or outward forces for extensile particles ($\zeta > 0$) (Figure 1.10.A). In a perfectly ordered system, the stresses generated locally average to zero and no net flow develops (Figure 1.10.B). However, a gradient of orientation leads to local net forces which ultimately generate flows. The direction of the flow is determined by the contractile or extensile nature of the system (column 1 of Figure 1.10.C). Additionally, orientation is intrinsically coupled with flow gradients through the coefficient ν , which may enhance the distortions of the director field. Both effects concur to amplify small distortions in the director field. More specifically in a contractile system, a small splay distortion creates a flow that amplifies the distortion which increases flows through positive feedback. The same mechanism is at stake at small bend distortions in extensile systems. The splay instability in contractile systems and the bend instability in extensile systems is depicted graphically in column 2 of Figure 1.10.C.

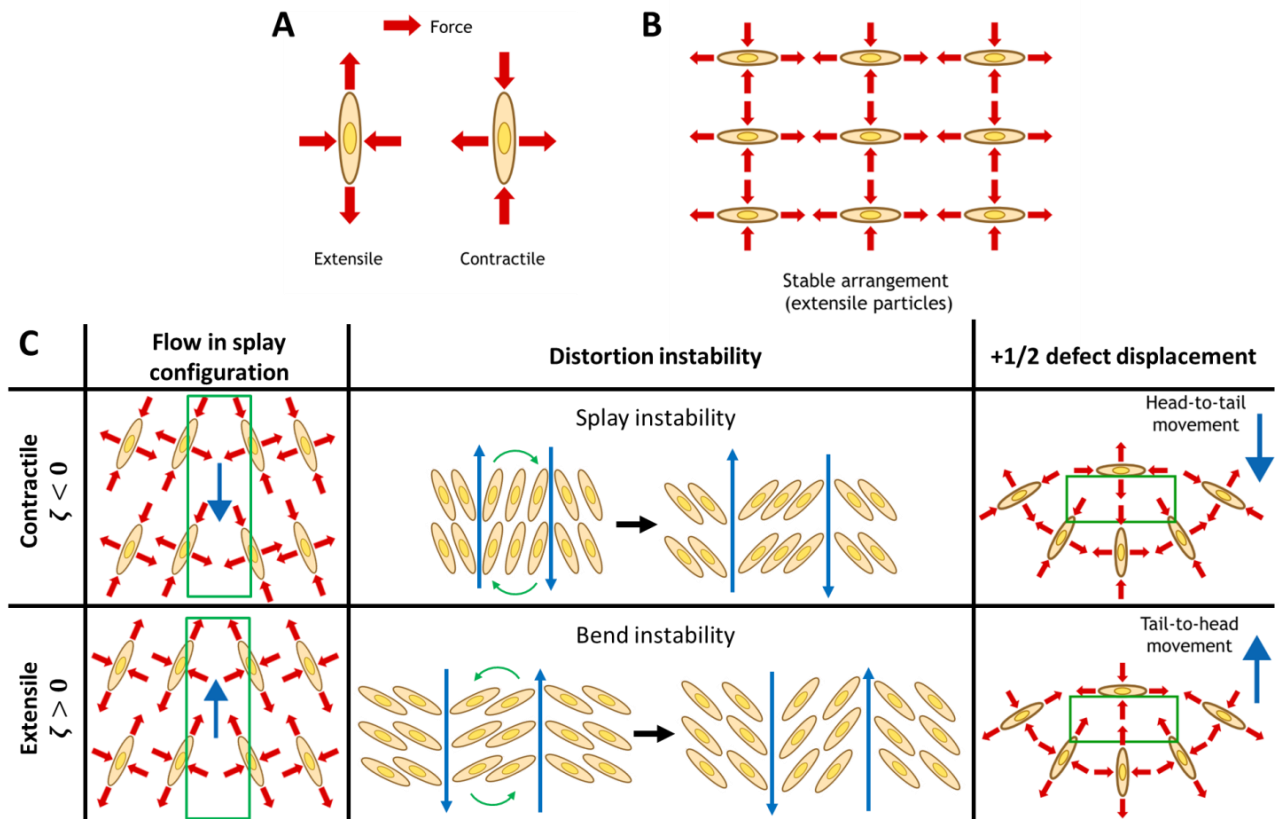


Figure 1.10 : Flows triggered by gradients of orientation in contractile vs extensile active nematic systems, adapted from

36,50

A: Dipolar forces exerted by extensile or contractile cells on their surroundings.

B: In a well-aligned domain, cellular forces are locally balanced, and the arrangement is stable.

C: Instabilities induced by orientational gradient for contractile (top) and extensile (bottom) systems.

Column 1: At a splay distortion, cellular forces do not average to zero locally (in the green box) which leads to a net force and ultimately to flow in the direction of the blue arrow.

Column 2: Sketch of the distortion instability due to the combined effect of flows induced by small distortions (blue arrows) and particle reorientation in flow gradients (green arrows). This instability leads to splay amplification in contractile systems and bend amplification in extensile systems.

Column 3: At the core of +1/2 defects, cellular forces do not average to zero locally (in the green boxes) which leads to a net force and ultimately to +1/2 defect displacement. Contractile +1/2 defects move tail first and extensile +1/2 defects move head first.

Distortion instabilities imply that the ordered state is not stable: small fluctuations grow and amplify distortions. The typical size of well-aligned domains is the active length $l_a \propto \sqrt{\frac{K}{\zeta}}$ and results from a competition between the Frank energy (K) that tends to preserve order and activity (ζ) that tends to destroy it. Ultimately, if activity is large enough, topological defects are created in pairs in the system. Next, I focus on the dynamics of defects and explain how this dynamics can sustain a chaotic state called active turbulence⁵¹.

1.2.4.3. Defect motion and active turbulence

Activity in the system can lead to the creation of pairs of defects (+1/2; -1/2) in the orientation field. At the core of +1/2 defects, the specific orientation field implies that cellular forces do not average to zero locally. Thus, a net force appears at the core of +1/2 defects which leads to +1/2 defect self-propulsion in active nematic systems (column 3 of Figure 1.10.C). Note that +1/2 defects migrate in opposite directions in contractile vs extensile active nematic systems. The direction of +1/2 defect motion thus allows to distinguish between contractile and extensile systems. Interestingly, both behaviors have been experimentally observed in cell monolayers. In HBEC epithelial monolayers, +1/2 defects migrate head first which is a signature of extensile systems⁵² (Figure 1.11.A) whereas in NIH 3T3 fibroblast and C2C12 myoblast monolayers, +1/2 defects migrate tail first which is a signature of contractile systems^{43,53} (Figure 1.11.B-C). Due to their 3-fold symmetry, -1/2 defects are not able to self-propel (Figure 1.11.C). This dynamics at topological defects leads to transition from 2D monolayers to 3D patterns in several systems. This aspect will be further detailed at the beginning of Chapter 4.

Topological defects are spontaneously created and migrate due to activity. +1/2 defects can annihilate with -1/2 defects. At high activity, the system reaches an active turbulent state associated with short-range nematic order, sustained creation and annihilation of defects, and a chaotic flow field. Experimentally, such a state has been observed in a wide range of systems such as microtubule-kinesin 2D suspensions and non-living self-propelled particle assemblies⁵¹. Friction with the substrate is high in cell monolayers and tends to dampen flows over the screening length defined by $l \propto \sqrt{\frac{\eta}{\xi}}$ where ξ is the friction with the substrate and η is the viscosity. However, active turbulence is observed in HBECs monolayers⁵². In Chapter 3, I come back in more details on the active turbulence of HBECs and present a way to regularize such chaotic flows in HBEC monolayers.

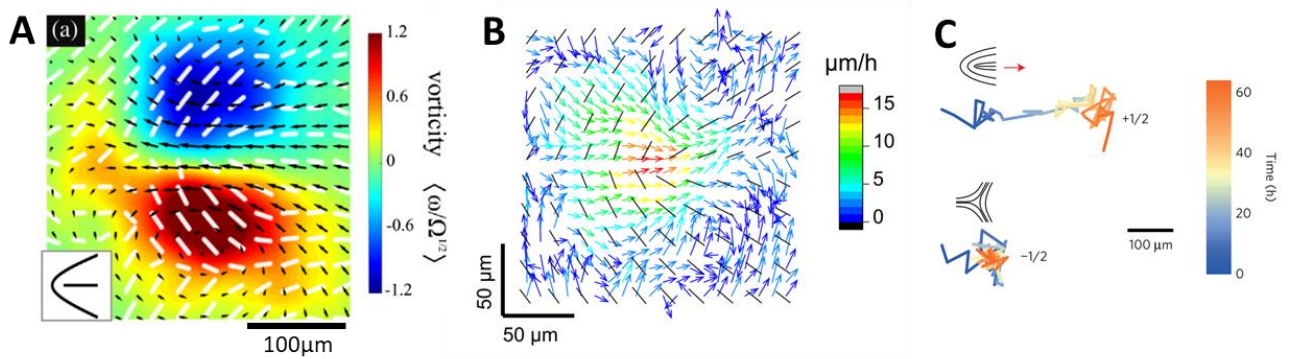


Figure 1.11 : Flows around +1/2 defects in cell monolayers.

- A: The vorticity map and the velocity field around a +1/2 defect in a HBEC monolayer show that the defect moves head first which is a signature of an extensile system; white lines: orientation field, black arrows: velocity field ⁵².
- B: The velocity field around a +1/2 defect in a C2C12 myoblast monolayer shows that the defect moves tail first which is a signature of a contractile system; black lines: orientation field ⁵³.
- C : In a NIH 3T3 fibroblasts monolayer, +1/2 defects move head first while -1/2 defects diffuse around their initial position without net motion ⁴³.

Here, I focused on flows around topological defects that are distortions spontaneously generated and thus not controlled in space and time. Next, I describe the flows that can develop in active cellular nematics confined in controlled geometries.

1.2.4.4. Spontaneous flows in confined active cellular nematics

Recent work showed that when confined in stripes larger than a critical length L_c , C2C12 myoblasts or RPE1 epithelial cells orient at a finite angle with respect to the direction of the stripe. This gradient of orientation leads to a spontaneous shear flow at the boundaries of the stripe ⁴⁹ (Figure 1.12.B). For stripes thinner than L_c , no net flow is measured. This transition has been predicted theoretically more than fifteen years ago using the theory of active gels ⁵⁴ (Figure 1.12.A) and is another example of the generation of flows resulting from a gradient of orientation. Note that the gradient of orientation imposed by the stripe geometry is continuous and flows appear here in the absence of topological defects. However, for more active cells such as HT1080 fibrosarcoma cells, the long-range order is lost and cells present a turbulent behavior ⁵⁵ (Figure 1.12.C).

Here, I would like to stress that the tilt angle and the shear direction of C2C12 confined in stripes correspond to what is expected for an extensile system. However, defect motion in C2C12 monolayers is typical of contractile systems (Figure 1.10.C, Figure 1.11). Although it was not our initial motivation, some experiments presented in Chapter 4, as well as the proposed theoretical description, give new insight about this apparent contradiction.

To conclude, numerous flow patterns observed in cell monolayers are well described by the framework of active nematic systems. In an active nematic system, the interplay between orientation gradients and activity of the elongated apolar particles results in the emergence of net forces and

flows. This idea is at the core of the project presented in Chapter 4 in which a gradient of orientation is imposed to C2C12 myoblasts to induce flows and ultimately trigger the formation of well-controlled 3D cellular structures.

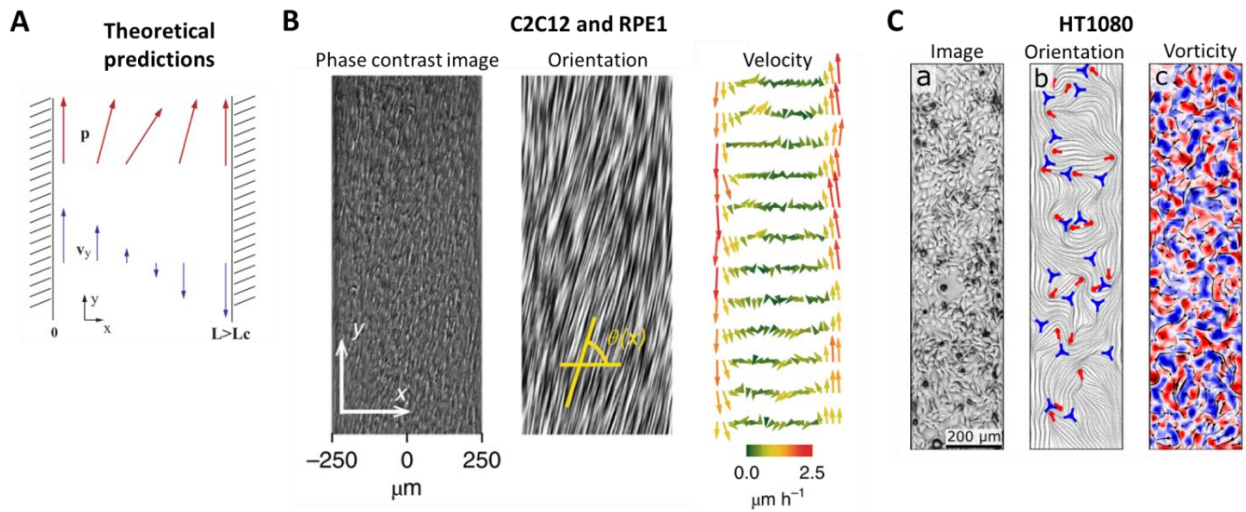


Figure 1.12 : Flows in confined active cellular nematics.

A: Theoretical description of an active gel confined in a stripe predicts the emergence of a shear flow at the boundaries ⁵⁴.

B: RPE1 cells confined in stripes present a tilted orientation in the middle and a shear flow at the boundaries, as predicted by the active gel theory. Additionally, note that convergent flows toward the stripe center emerge in the system. Similar orientation and velocity fields are found in C2C12 monolayers ⁴⁹.

C: HT1080 fibrosarcoma cells are more active than RPE1 and C2C12 and are turbulent in stripe patterns ⁵⁵.

Even though active nematic systems present local polar displacements due to orientation gradients and activity, no global net motion can emerge at the system scale because of their symmetry. However, in situations such as the ones described in 1.1.2.3, cells can break symmetry to self-propel and ultimately sustain a net collective motion in the whole system. To describe these situations in cellular assemblies, one needs to adopt a polar description in which the system is characterized not only by a local orientation but by a local direction. Such polar systems with broken rotational symmetry can indeed transit to a flocking state. In the following, I present experimental realizations of polar flocks and introduce theoretical and numerical models developed to capture their behaviors.

1.2.5. Polar active systems

1.2.5.1. Emergence of flocking in polar active systems

Polar systems are described by a polarization vector that defines locally a direction rather than an orientation. These systems can undergo a flocking transition toward a state in which all the particles align and move in the same direction. Thus, net motion can develop in polar systems. This is the case in bird flocks, animal herds or fish shoals but also in synthetic active matter systems.

For example, colloidal rollers are apolar particles that can be engineered so that, in the presence of an electric field, they self-propel on their substrate. In the absence of interaction, they

travel in random directions (Figure 1.13.A.1). When confined in a microfluidic channel, these self-propelled colloidal rollers experience a transition from a disordered (Figure 1.13.A.1) to an ordered phase (Figure 1.13.A.2) as the density of rollers is increased³⁴. The ordered phase consists in a polar fluid with a non-zero net motion through the channel. In this state, all the particles select a preferred velocity (Figure 1.13.A.2 bottom). More quantitatively, the polarization order parameter Π_0 , being the modulus of the time and ensemble average of the particle velocity direction, varies from 0 to 1 as the fraction area of the rollers increases (Figure 1.13.A.3). This experimental non-living system is a good example of a polar phase emerging in assemblies of interacting apolar self-propelled particles.

Similarly, cells that are able to break symmetry can self-propel in the direction of their polarization (see 1.1.1). For such cells, similar polar phase can emerge at density sufficient to allow interactions. For instance, a density mediated flocking transition has been observed with fish epidermal keratocyte cells. When the density is high enough, the cells align their velocity and migrate collectively⁵⁶ (Figure 1.13.B (f)). As mentioned above (see 1.1.2.3), cell monolayers confined in mesoscale patterns are also able to experience collective migration with a net motion. It is for example the case for MDCK cells confined in rings of different width³³ (Figure 1.13.C). Altogether, cells that are able to self-propel can organize in a polar phase at confluence and experience collective net motion.

1.2.5.2. Classical theoretical models describing a flocking transition

Classically, the flocking transition in polar system has been described by the Vicsek model⁵⁷. It is a particle-based description built on the idea that particles tend to align their movement with the movement of their neighbors. More specifically, each particle is modeled as a point moving at a constant speed v_0 . The direction θ_i of each particle i evolves through a simple alignment rule: between each time point, the direction of the particle is adjusted by averaging the direction of its neighbors:

$$\theta_i(t + \delta t) = \langle \theta(t) \rangle_r + \Delta\theta \quad (1.6)$$

where $\langle \theta(t) \rangle_r$ is the average of the direction of all the particles present in a circular area of radius r around the particle i and $\Delta\theta$ is a noise. Remarkably, the model predicts a transition toward flocking at high density, the flocking state being characterized by the selection of a preferred velocity.

This model includes an explicit alignment rule between neighboring particles. However, cells interact via direct contact and experience a wide variety of short-range interactions. Thus, more elaborated particle-based models without explicit alignment but encapsulating more realistic interactions have been developed and are presented in 1.2.5.4.

A coarse-grained continuum version of the Vicsek model has been proposed by Toner and Tu through a phenomenological description based on symmetry arguments^{58,59}. They proposed hydrodynamic equations on the density field $\rho(r, t)$ and the polarization field $\mathbf{p}(r, t)$. These equations account for the emergence of flocks and for density and velocity wave propagation in compressible polar fluids.

This model assumes that particle velocity is aligned with its polarity. However, in systems with complex interactions such as migrating cell monolayers, particle polarity does not always align with its velocity (see 1.1.4). Indeed, it has been shown experimentally that cell velocity and traction forces

might not share the same orientation in cases of collective migration^{60,61}. Thus, a description distinguishing $\mathbf{p}(\mathbf{r}, t)$ and $\mathbf{v}(\mathbf{r}, t)$ is required for properly describing the collective migration of polar cells. In the next subsection, I explain how the active gel theory presented in 1.2.4.1 can be adapted to describe such situations.

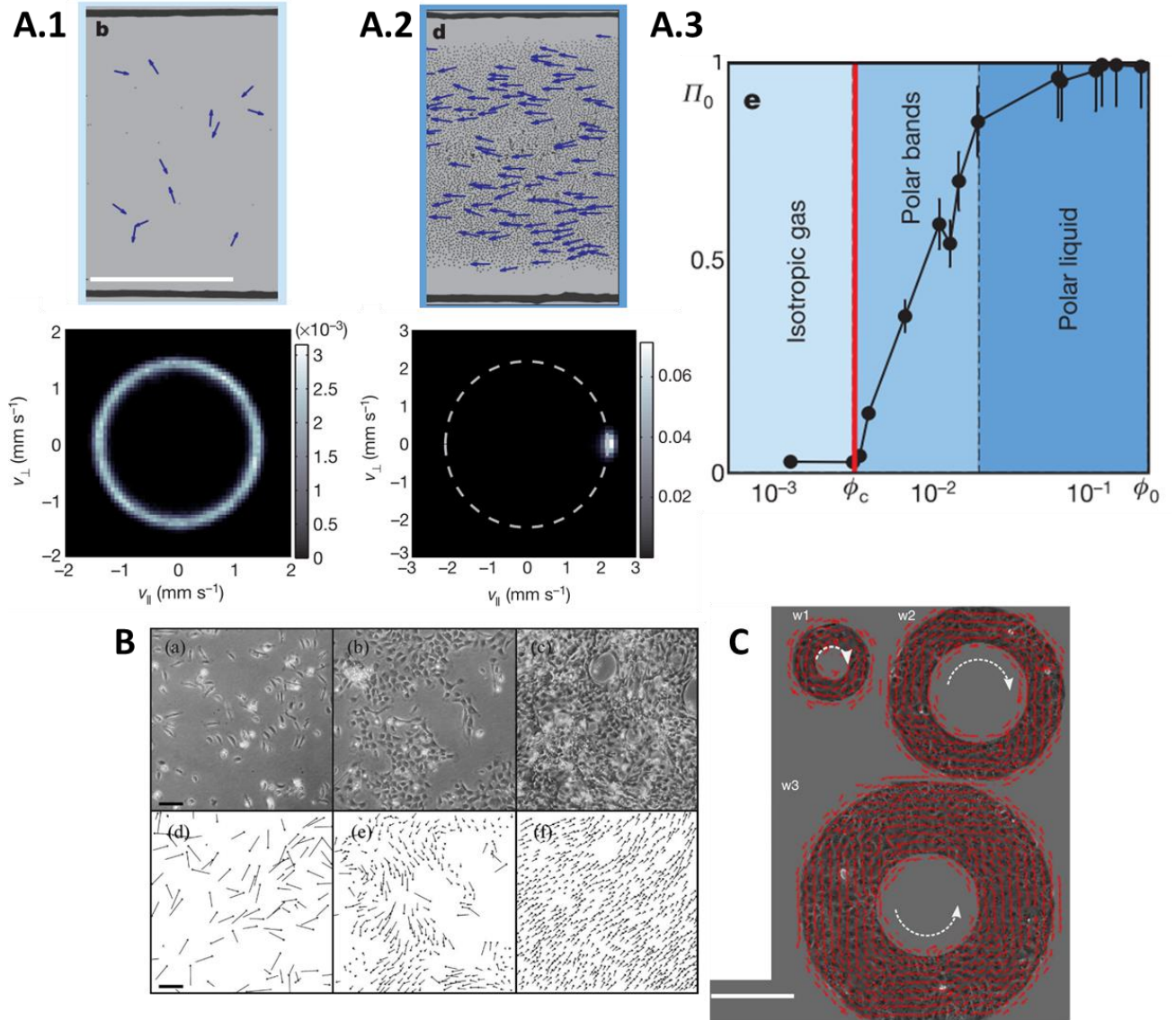


Figure 1.13 : Flocking transition in polar active systems.

A: Flocking transition of self-propelled colloidal rollers confined in a racetrack. While increasing the fraction area of rollers, the system goes from an isotropic gas state (A.1 top) characterized by isotropic velocity distribution (A.1 bottom) to a polar liquid state (A.2 top) in which the particles select a preferred velocity (A.2 bottom). The order parameter Π_0 , defined as the modulus of the time and ensemble average of the particle velocity direction, thus increases from 0 to 1 with the fraction area Φ_0 (A.3). A.1, 2 top: Dark-field pictures of roller populations in a racetrack, scale bar: 500 μm . The blue arrows show the velocity of some rollers in the system. A.1, 2 bottom: probability distribution of the roller's velocity vector $(v_{\parallel}, v_{\perp})$. v_{\parallel} corresponds to the projection of the velocity on the direction tangent to the racetrack; v_{\perp} is normal to v_{\parallel} . Adapted from³⁴.

B: Flocking transition of keratocytes is mediated by cell density that increases from left to right. Top panels show the phase contrast images (scale bar: 200 μm) and bottom panels show the corresponding cells velocities (scale bar: 50 $\mu\text{m}/\text{min}$)⁵⁶.

C: Collective rotation of confluent MDCK cells in ring patterns of different width. Scale bar: 200 μm ³³.

1.2.5.3. Continuum description of cell monolayers as an active polar gel

At the linear order at which the constitutive equations of active gels are derived (see 1.2.4.1), they are invariant under $\mathbf{p} \rightarrow -\mathbf{p}$ without neglecting polar terms that are higher order. Thus, these equations hold for a polar active gel³². The continuum description of migrating cell monolayers based on active polar gel constitutive equations and taking into account compressibility effects can be found in⁹.

Close to the flocking transition, the polarization is a critical variable, and the free energy must include the Landau expansion on the polarization modulus: in the case of incompressible fluid, the free energy then reads:

$$F_p = \int dr \left\{ \frac{a}{2} |\mathbf{p}|^2 + \frac{b}{4} |\mathbf{p}|^4 + \frac{K}{2} (\nabla \mathbf{p})^2 \right\} \quad (1.7)$$

The first two terms correspond to a potential controlling $|\mathbf{p}|$ in which $b > 0$ for stability reason. If $a < 0$, it corresponds to a classical Mexican hat potential. In that case, $|\mathbf{p}|$ tends to be constant and the system is at least locally ordered. If $a > 0$, the preferred bulk equilibrium state is $|\mathbf{p}| = 0$ which corresponds to a disordered state. The last term corresponds to the Frank free energy already described (see 1.2.3) and penalizes distortions of the polarization field.

To describe assemblies of polar cells that self-propel on a substrate, one can use the 2D version of the constitutive equations of active fluids (see 1.2.4.1) and complement it with a force balance including both a friction term $\xi \mathbf{v}$ and an active polar traction term $T_0 \mathbf{p}$:

$$\nabla \cdot \sigma^{tot} = \xi \mathbf{v} - T_0 \mathbf{p} \quad (1.8)$$

With this approach, equations take into account both cell contractility with the active stress in the constitutive equations, and individual polar cell migration through the active traction force in the force balance⁶². This continuum approach has been used notably to investigate specific features observed during the spreading of epithelial monolayers: fingering instability, wetting transition, waves propagation⁹.

Additionally, in polar active systems in contact with a substrate, polarization can reorient not only in flow gradients but also in uniform flows^{63,64}. Thus, polar particles can align their polarization with their velocity. It is the case for cells crawling on a surface: they have been shown to align their self-propulsion direction with the traction force they exert on the substrate²⁵. To describe this effect, a polarization-velocity coupling is usually introduced in the right-hand side of the polarization evolution equation (1.5) presented in 1.2.4.1 which then reads:

$$\frac{Dp_\alpha}{Dt} = \frac{1}{\gamma} h_\alpha - v v_{\alpha\beta} p_\beta + k v_\alpha \quad (1.9)$$

where the first and second terms have been described in 1.2.4.1 and correspond respectively to the relaxation of polarization distortions and to the passive reorientation of particles in flow gradients. The third term is a polar term coupling the polarization to uniform flows with the phenomenological coefficient that we note k in this manuscript. This coupling might capture the tendency of cells to align their velocity and polarization. However, this coupling has not been yet included in continuum models

of collective cell migration ⁹. In Chapter 3, we show that this coupling is essential for describing the HBECs collective behavior triggered by collective contact guidance.

This continuum approach provides a powerful framework to propose analytical predictions of collective migration phenomena of confluent group of cells without knowledge of the microscopic details. Cell-substrate and cell-cell interactions are thus captured in phenomenological parameters. However, these phenomenological parameters can't easily be related to specific cellular processes. Moreover, this approach is based on a linear expansion of fluxes in terms of forces (see 1.2.4.1). Thus, it describes systems close to equilibrium and neglects nonlinearities that can be relevant far from equilibrium.

A different approach models the microscopic interactions between particles. This is the strategy of particle-based models that I introduce in the next subsection. These models are used to simulate the evolution of particle assemblies and eventually to identify which types of interactions can trigger an experimentally observed macroscopic behavior. Here, I focus on simulation models of 2D systems in contact with a substrate.

1.2.5.4. Particle-based simulations of cell monolayers

In particle-based simulations, each particle i is controlled by evolution equations of the velocity \mathbf{v}_i and the polarization \mathbf{p}_i . Forces are balanced on each particle. These forces include active traction force $T_0\mathbf{p}_i$, friction with the substrate $\xi\mathbf{v}_i$, and forces due to positional interactions with neighboring cells. They are sketch in the case of cells confined in a line pattern in Figure 1.14.a. Interaction forces are modeled via an interparticle potential V accounting for short range repulsion due to excluded volume interactions and mid-range attraction due to cell-cell adhesion. Interaction forces can also include friction between cells. This family of models is well-adapted for polar systems as particles are self-propelled along their polarization by the active traction force. Moreover, it is well-adapted to describe systems at different densities. For the particle i with contacting nearest neighbor cells j , and neglecting cell-cell friction, the force balance on particle i reads:

$$T_0\mathbf{p}_i = \xi\mathbf{v}_i + \sum_j \nabla V(|\mathbf{r}_i - \mathbf{r}_j|) \quad (1.10)$$

By tuning the interaction potential, these models allow to describe both monolayers of cells with strong cell-cell adhesion or with weak and transient cell-cell contacts. An example of interparticle potential is presented Figure 1.14.a.

The orientational interactions such as polarity-velocity alignment or CIL are encapsulated in a polarization evolution equation whose precise expression depends on the interactions investigated by the specific model. For example, it has been shown with particle-based models that short range forces combined with polarity velocity alignment can lead to flocking ^{56,65} without the need to explicitly implement Vicsek velocity alignment rules (see 1.2.5.2). Thus, the tendency of cells to align their traction force to their velocity can itself explain the emergence of collective cell migration.

1. Introduction

Interactions such as CIL that are by nature discontinuous and difficult to model with phenomenological parameters in continuum models have been successfully investigated with particle-based simulations^{66,67}. Typically, at each simulation step, the particle polarization \mathbf{p}_i evolves to align with the direction \mathbf{p}_i^{CIL} defined by the direction away from contacts with other particles (Figure 1.14.b-left). This repulsive interaction can by itself lead to collective cell migration in simulations of group of particles (Figure 1.14.b-right) as suggested by experimental results (see 1.1.3.2).

Thus, particle-based simulations are useful to validate the importance of specific microscopic interactions for the emergence of macroscopic patterns in a system. Such a strategy is presented in Chapter 3 to investigate the microscopic interactions that can sustain the large-scale collective behavior that we observe in HBEC monolayers on textured substrate.

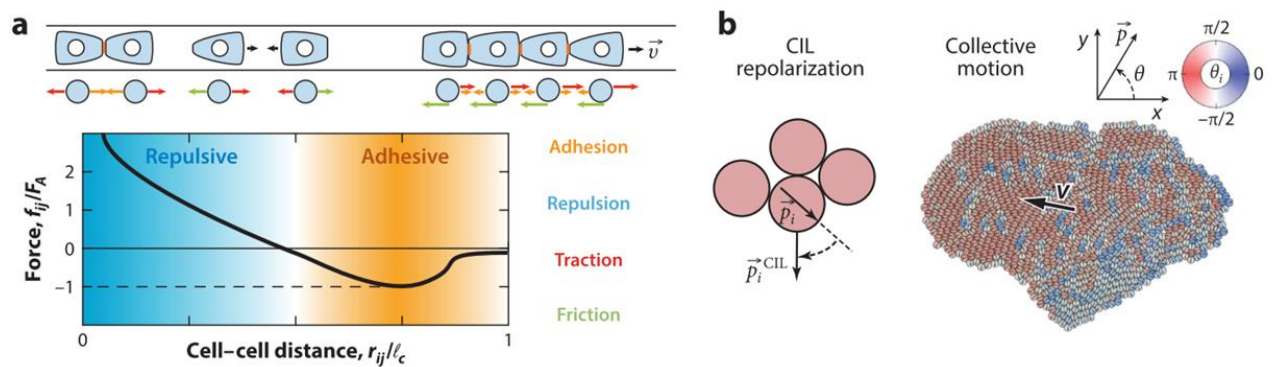


Figure 1.14 : Particle-based models confirm that CIL can trigger collective motion⁹.

a: Schematic representation of forces in particle-based models and typical interparticle potential (adapted from⁶⁶).

b: In particle-based simulations encapsulating CIL interactions, a cell cluster can spontaneously polarize and migrate collectively (right). In the simulations, CIL is modeled by imposing that each particle tends to align its polarization in the direction away from cell-cell contacts (left). The color codes for the cell polarity angle (adapted from⁶⁷).

In conclusion, the active matter framework is well-adapted to describe collective cell migration. Flows induced by gradients of orientation are typical of nematic systems and the flocking transition is a feature characteristic of polar systems. Continuum or particle-based models give insights into the mechanisms triggering collective behaviors. In the present work, the polar continuum theory and particle-based simulations have been used in a complementary way to explain the collective behavior observed in HBEC monolayers and described in Chapter 3. The framework of active nematic fluid has given insight to understand and tune the emergence of flows and well-defined 3D structures in C2C12 monolayers presented in Chapter 4.

The aim of the present work is to study the emergence of collective migration triggered by imposing a fixed orientation of the polarization or well-defined gradients of orientation in confluent cell monolayers. *In vivo*, imposed cell polarization is observed in response to anisotropic topographical cues. In this work, we use the same strategy to control cell migration (Chapter 3) or cell orientation (Chapter 4). In the rest of this introduction, I present how cells are guided, both individually and collectively by the topography of their environment *in vivo* and *in vitro*.

1.3. From single to collective contact guidance

The impact of geometric constraints on cell shape and migration is known since the very beginning of cell culture. Indeed, Harrison described in 1914 that fibers present in the cellular environment influence the shape and migration of cells⁶⁸. A similar phenomenon of elongation and active movement of cells along fibers was observed again by Paul Weiss and collaborators in the forties' and named "contact guidance"⁶⁹. Contact guidance embraces all situations in which cells are oriented or guided by anisotropic topographical features in their substrates and is at play in numerous *in vivo* situations.

1.3.1. *In vivo* guidance of cells by the ECM and larger anatomic structures

In vivo, cells are guided by their microenvironment that provides signaling cues including topographical heterogeneities at different scales⁷⁰⁻⁷². For instance, cells are usually surrounded by fibrillar collagen networks or oriented bundles of collagen fibrils. Collagen fibrils are usually few dozen to few hundred nanometers in diameter, a bundle of collagen fibrils (a collagen fiber) reaches the micrometer scale (1-20 μm in diameter). Cells can also be guided by larger anatomic structures present in many tissues including blood vessels, nerve tracks, muscle fibers⁷³ and other cellular tissue topographies⁷⁴ (cues at a scale around a few dozen of micrometers).

This guidance by cell environment has been particularly observed in the pathological context of cancer^{70,72}. Schematics and images of the various anisotropic structures found in the tumor microenvironment are presented Figure 1.15.A-B. Cancerous cells can degrade the tumor basement membrane (BM) and realign stromal collagen fibers perpendicularly to the tumor⁷². This particular organization of collagen is correlated with poor patient survival⁷⁵ as cells can then use those collagen bundles as 'highways' for efficiently directing their migration in the stroma away from the tumor⁷⁶ (Figure 1.15.C). Stromal cells such as cancer-associated fibroblasts can secrete fibronectin-rich anisotropic ECM fibers which support efficient and directional cancer cell migration⁷⁷. Cancer cells can also use larger structures such as blood vessels to direct their collective migration⁷³ (Figure 1.15.D). ECM alignment or anisotropic environment is thought to promote efficient collective cancer cell invasion whereas loose isotropic fibrillar collagen is associated to single cell invasion^{72,76}.

Moreover, ECM topography plays a role in directing collective cell migration during developmental events^{78,79}. For instance during zebrafish and amphibian gastrulation, mesodermal cells migrate toward the anterior part on oriented ECM fibrils^{80,81}. The inhibition of fibronectin fibrils assembly impairs the directional collective migration of the mesoderm.

Drosophila egg chamber elongation provides a powerful model to investigate how ECM remodeling can direct and promote morphogenesis events (Figure 1.15.E). During oogenesis, the egg chamber exhibits an active rotation of the follicle cell layer over a surrounding static BM (Figure 1.15.E (a), (b), (d)). Cells' directed migration orient the BM collagen IV fibrils in the direction of migration. Follicle cells then migrate over fibrils previously oriented by neighbors that enhance their directed

1. Introduction

migration and orient their basal actin structures (Figure 1.15.E (c)). The polarized fibrillar BM and basal actin bundles eventually act as a ‘molecular corset’ that controls tissue elongation. In this example, BM is remodeled by directed migration and, with a feedback mechanism, the BM anisotropic topography enhances the collective migration and supports tissue elongation. *Drosophila* mutants lacking collagen IV or integrin fail to rotate and elongate which reveals the importance of coordination between the follicular epithelium and the basement membrane topography⁸².

Thus, contact guidance by topographical cues is crucial in different contexts *in vivo*, such as organism’s development and cancer progression, to support collective directed cell migration. *In vitro*, synthetic structured substrates have been used to mimic anisotropic features found *in vivo* in the cell environment to investigate this contact guidance effect in well-controlled condition.

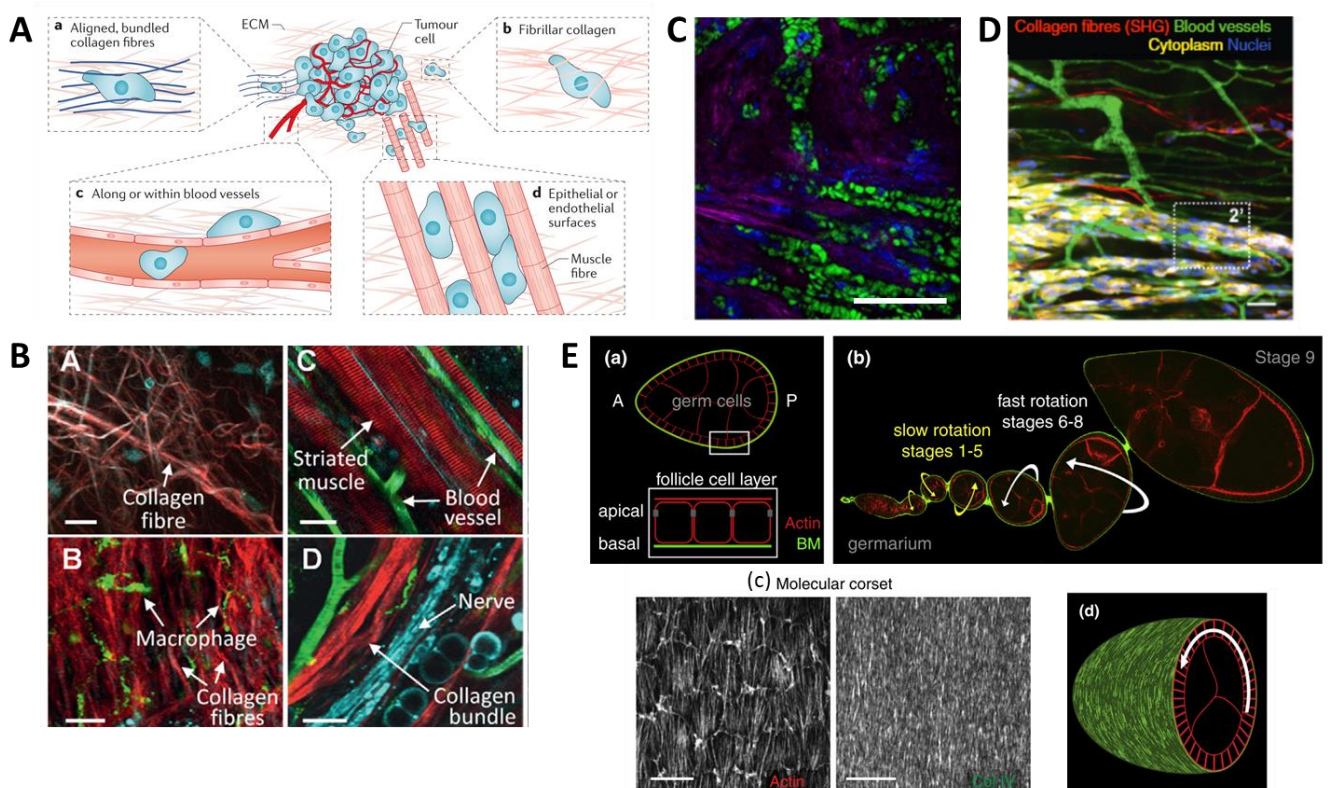


Figure 1.15 : *In vivo* cell guidance by anisotropic nano-to-micro scale structures.

A: Schematic representation of the variety of guiding cues in the microenvironment surrounding a tumor⁸³.

B: Diversity of the connective tissue microstructures in the mouse dermis: collagen-rich loose (A) and dense (B) interstitial tissue, myofibers and blood vessels (C) and collagen bundles and nerves (D); scale bar: 50 μm ⁷³.

C: Cancer cells collectively invade stroma as strands and small clusters along aligned collagen fibers (ex vivo mouse intestinal tumour slice, blue: stromal cells, pink: collagen I, green: nuclei of tumor cells, scale bar: 100 μm)⁷⁶.

D: Collective migration of tumor cells in the mouse dermis is guided by blood vessels. Scale bar: 50 μm (adapted from⁷³).

E: Interplay between egg chamber rotation and BM organization during *drosophila* egg chamber elongation. (a) The egg chamber is composed of a layer of germ cells surrounded by a BM; (b) image of a developmental array of egg chambers shows that the egg chamber begins to rotate before it elongates; (c) the molecular corset consists of parallel arrays of actin bundles at the basal epithelial surface (left, stage nine) and fibril-like structures in the adjacent BM (right, stage seven), scale bar: 10 μm ; (d) the schematic of a transverse section through an egg chamber shows that rotation occurs within the surrounding aligned static BM (adapted from^{84,85}).

1.3.2. *In vitro* single cell contact guidance

Since the first *in vitro* observation by Harrison⁶⁸ and Weiss⁶⁹, single cell contact guidance has been widely investigated. Recent reviews gather the knowledge in the field^{86,87}. Even though various type of micro-fabricated topographies have been shown to guide cells (pits, pillars, wrinkles, fibrous scaffolds, etc.⁸⁸), I focus here on cell response to continuous unidirectional topographies. The main example of such topographies is grooved substrates (or 'gratings'). They are composed by alternating rectangular or sinusoidal grooves and ridges whose widths range typically from 100 nm to 20 μ m and aim to mimic aligned nano-to-microscopic cues found in the natural cell environment.

In a wide range of groove depth and width, most cells have been shown to be guided by a grooved topography. Elongated cells that orient randomly on a flat substrate tend to orient with the grooves when seeded on gratings⁸⁹ (Figure 1.16.A). Moreover, cells that are usually rounded tend to elongate in the direction of substrate anisotropy⁹⁰ (Figure 1.16.B). Grooves geometry defined by the width, spacing, depth and aspect ratio of the grooves is critical for cell response. The optimal geometry maximizing elongation and alignment is cell type dependent. However, most studies report that increasing groove depth (usually from tens of nanometers up to several microns) increases contact guidance^{86,87}.

Topographical cues direct single cell migration for a large variety of cells. Compared to an almost random direction of migration on flat substrate, cells usually migrate along the substrate anisotropy on grooved substrates (Figure 1.16.C). In addition, a typical feature of contact guided cells is the increase of cell speed and cell persistence on grooved substrates^{91,92}. Note that contact guidance guides the cells along the grooves but does not provide a direction for the cell migration: cells migrate along the grooves rightward or leftward with equal probability. Contact guidance is thus a perfect example of cell-substrate interaction impacting the orientation of cell polarization but not its direction. It is interesting to note that guidance has also been observed for cells seeded on alternating lines of fibronectin and cell repellent⁹³.

Even though single cell contact guidance has been extensively studied, the mechanism by which topographical cues can align and guide cells is not fully understood⁹⁴. Several mechanisms have been proposed and depend particularly on the migration mechanism of the cell type studied. Here, I leave aside amoeboid cells and neurons to focus on cells which exhibit mesenchymal migration relying on cell protrusions, actin stress fibers and cell substrate adhesions (see 1.1.1). The organization of these subcellular structures is generally affected by the topography and is involved in possible mechanisms of contact guidance discussed recently in⁹⁴.

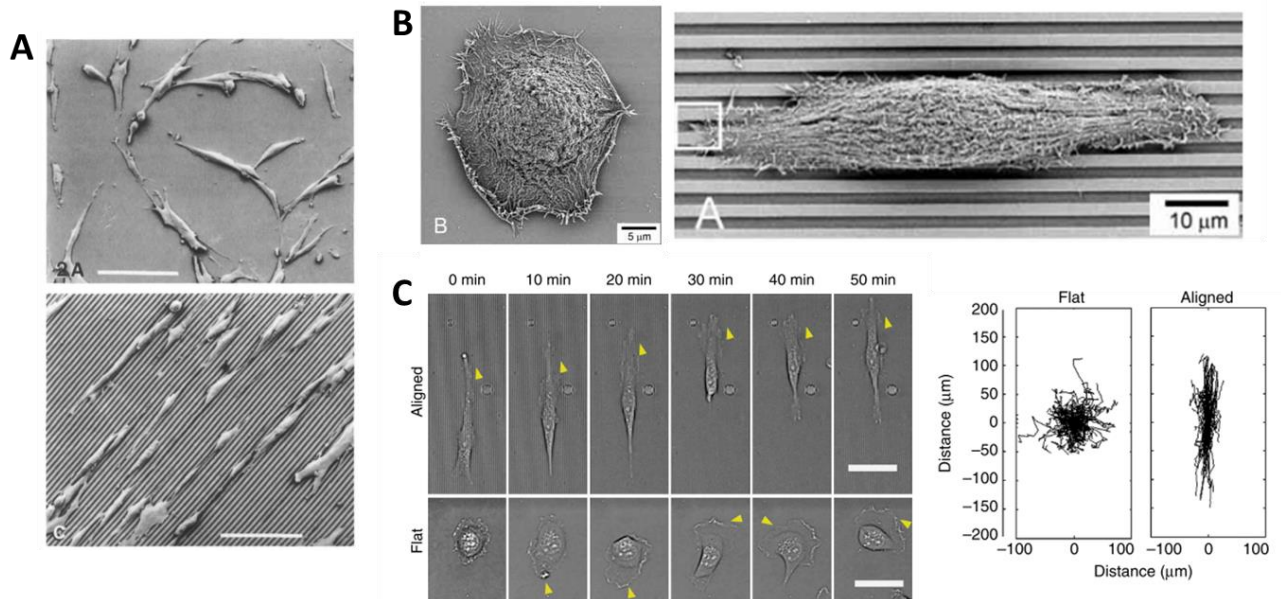


Figure 1.16 : In vitro single cell contact guidance.

A: BHK fibroblast cells orient randomly on a planar substrate (top) and align with substrate anisotropy on grooves (bottom).

Groove and ridge width: 3 μm , groove depth: 2 μm . Scale bar: 120 μm (adapted from ⁸⁹).

B: Human corneal epithelial cells are rounded on a flat substrate (left) and elongated on a grooved substrate (right). Groove

and ridge width $\sim 2 \mu\text{m}$ (adapted from ⁹⁰).

C: MDA-MB-231 human breast adenocarcinoma cells migrate randomly on a flat substrate (bottom) and directionally on

grooves (top). Arrowheads highlight protrusion position: protrusions are stable in one direction on grooves while they

change their direction frequently on flat substrate. Typical trajectories of cells on flat and textured substrates can be found

in the plot at the right of the image sequences. Scale bar: 50 μm . Groove and ridge width: 800 nm, groove depth: 600 nm

(adapted from ⁹¹).

The most accepted model of contact guidance named the “FA-based model” (FA for Focal Adhesions) involves several mechanisms and is explained schematically Figure 1.17.A ⁹⁴. Anisotropic topographical cues guide and stabilize protrusions (lamellipodia and filopodia) in the direction of the topography and prevent them from extending in the perpendicular direction ^{90,91} (Figure 1.16.C and Figure 1.17.C). FAs that mature are confined on grooves and ridges, and thus orient in the parallel direction due to lateral confinement (Figure 1.17.B). Cytoskeletal stress fibers that attach to FAs consequently align with the grooves (Figure 1.17.B). This leads to anisotropic contractile forces generation and ultimately to cell elongation and migration along the grooves.

This mechanism relies on FAs confinement, and thus does not explain contact guidance on grooves and ridges wider than 1-2 μm , or the positive correlation between groove depth and contact guidance. Moreover, contact guidance has been observed under actomyosin perturbation with drugs ⁹⁵ which suggests that local alignment of protrusions and cytoskeleton might be sufficient to contact guidance.

An alternative mechanism could be at play for geometries that do not constrain FAs orientation and in which cells are able to engulf in the grooves: the membrane deformation mechanism ^{94,96} (Figure 1.17.D left). Topographies in which cells can engulf induce high membrane curvature at grooves or

ridges' edges inducing curvature sensitive proteins to be recruited and accumulated specifically at these locations. Focal adhesion and stress fibers are assembled at topography sharp edges^{97,98}, which leads to stress fibers oriented along edges and thus elongation and migration along the grooves⁹⁷ (Figure 1.17.D right). Increasing groove aspect ratio is expected to amplify cell membrane deformation as cells send protrusions into deeper grooves and thus to enhance contact guidance.

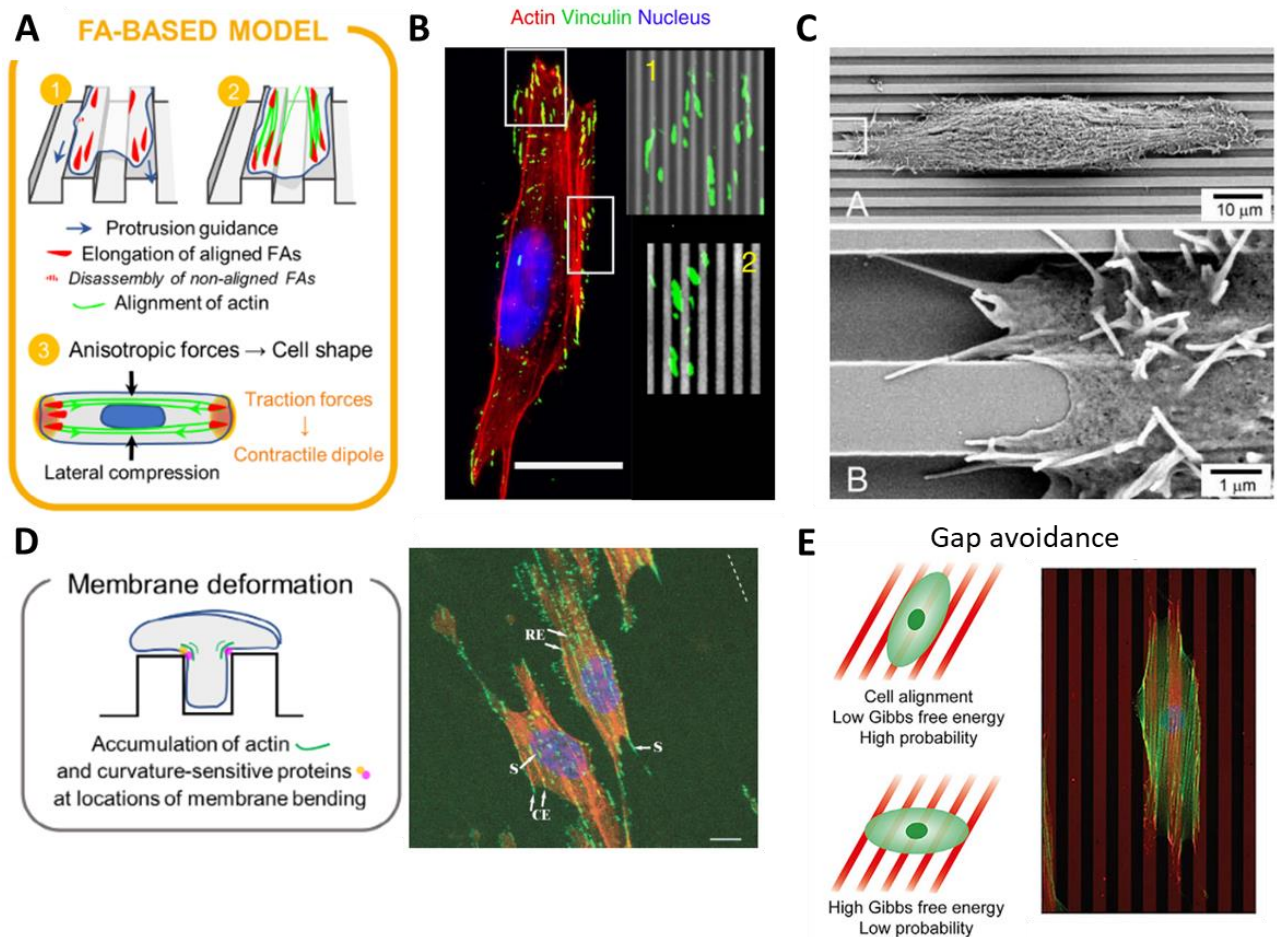


Figure 1.17: Mechanisms of single cell contact guidance.

A: Schematic explaining the FA-based model⁹⁴

B: MDA-MB-231 cell aligns on a nanopatterned substrate. In the lamellipodium, FAs align in the anisotropy direction and are confined in grooves and ridges. Actin fibers also align along the nanogrooves. Magnified regions: FAs overlaid on the nanopatterns bright field image (black: ridges). Scale bar: 20 μm ⁹¹.

C: Human corneal epithelial cell aligns on a micro-grooved substrate (top). The zoomed image (bottom) shows that the cell lamellipodium and filopodia extend along the grooves. Groove and ridge width : ~2 μm ⁹⁰.

D: Schematic of the membrane deformation mechanism⁹⁴ (left) and overlay confocal microscopy image of endothelial cells on grooves (right). The white arrows show that focal adhesions are localized along the groove edges (CE), along the sidewalls of the groove (S), and along the ridge edges (RE). The dashed line denotes the orientation of grooves. Scale bar is 10 μm . Groove depth: 1 μm , groove and ridge width: ~ 3.5 μm ⁹⁷.

E: In the gap avoidance mechanism, the most probable cell alignment is obtained by minimizing area on non-adhesive zones (left). Myofibroblast aligns on parallel lines of fibronectin (red) of width 10 μm spaced by 10 μm (right). FAs: magenta, actin: green, nucleus: blue. (adapted from⁹³).

Another elegant mechanism named “gap avoidance” has been proposed for wider topographies (a few microns up to a cell size). Cells seeded on parallel lines of fibronectin wider than 2 μm orient in the line direction, even if FAs orientation is not constrained (Figure 1.17.E right). The proposed mechanism relies on the minimization of cell cytoskeletal free energy with the constraint that adhesions are forbidden on non-adhesive gaps between fibronectin lines. This minimization is achieved when cells orient parallel to the underlying pattern anisotropy (Figure 1.17.E left)⁹³. This mechanism could also be at play on micro-scale ridges when cells can't engulf in the grooves, because in this case the formation of FAs is prevented in the grooves as it was prevented on non-adhesive area of chemical anisotropic patterns.

Thus, contact guidance is the result of a combination of mechanisms involving FAs adhesion and maturation, extension of protrusions in the anisotropy direction and cytoskeletal components alignment. These mechanisms can be synergetic and adapted for specific topography types.

1.3.3. *In vitro* collective contact guidance

In vivo, cells are usually not isolated and cell-cell interactions can either compete or cooperate with guiding cues. On shallow or thin sinusoidal grooves, C2C12 cells orient randomly when isolated but align with the grooves after confluence⁹⁹ (Figure 1.18.A). Conversely, MDCK elongate in the groove direction when isolated but recover their usual aspect ratio in a dense group of cells¹⁰⁰ (Figure 1.18.B).

Although the dynamics of single cells guided by nano-to-micro topographical cues has been thoroughly investigated, less is known on the contact guidance of ensemble of cells. Most of the dynamical studies focus on situations of free space invasion. In wound healing experiments, a grooved topography is known to increase monolayer progression efficiency^{101,102}: after removing a barrier, a MDCK monolayer front progresses faster on grooves oriented perpendicularly to the frontier versus on flat substrates (Figure 1.18.C). The same effect is observed in cell droplet dispersion assay. A high-density cell droplet is seeded on a substrate and the cell sheet expansion is monitored over time. On isotropic substrate, the expansion is isotropic, whereas on grooved substrates, the droplet expands in the groove direction in an ellipsoidal shape cell sheet^{103,104}. Indeed, the migration of the cell sheet is enhanced parallel and inhibited perpendicular to the grooves (Figure 1.18.D). Thus, anisotropic topography can guide the directed collective migration of epithelial cell sheet.

An interesting dynamical feature appears also in the bulk of a growing MDCK island on top of a substrate made of aligned collagen fibers. Whereas on flat substrates cells coordinate their motion in small patches with random direction of migration, cells on a grooved substrate migrate in the direction of the grooves in much larger coordinated domains¹⁰⁵. These coordinated domains are lanes migrating in antiparallel direction. At later time, these domains get larger and in the FOV observed by the authors, all cells go in the same direction. (Figure 1.18.E). Altogether, these studies suggest that cell coordination is increased along the grooves.

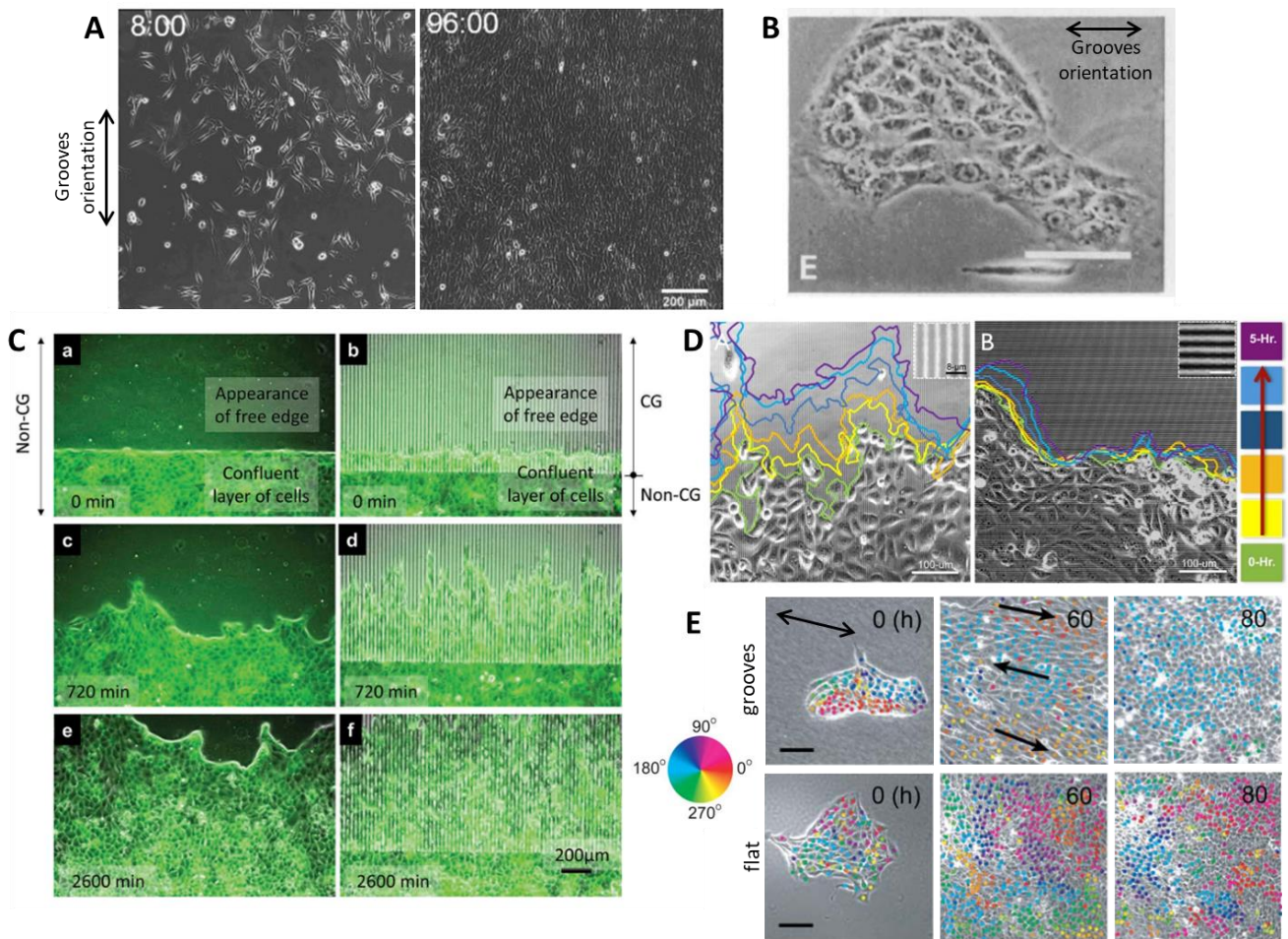


Figure 1.18 : In vitro collective contact guidance.

- A:** Cell density dependent C2C12 alignment on grooves: cells orient randomly when sparsely seeded but align with the grooves when they reach confluence. Groove and ridge width: 400 nm, groove depth: 100 nm ⁹⁹.
- B:** MDCK colony and single cell on grooves: the single cell in the bottom of the image elongates along the grooves, while they recover their normal aspect ratio in a group of cells. Groove and ridge width: 130nm groove depth: 210 nm. Scale bar: 30 μm ¹⁰⁰.
- C:** MDCK cell sheet invasion on flat versus grooved substrates: grooves perpendicular to the initial barrier enhances free space invasion of the monolayer. Groove and ridge width: 5 μm , groove depth: 2 μm ¹⁰².
- D:** human corneal-limbal epithelial cells droplet expansion is enhanced in the direction parallel (D) and inhibited in the direction perpendicular (B) to the grooves. Color codes for cell front position at different time points. Groove and ridge width: 2 μm , groove depth: 1.5 μm ¹⁰⁴.
- E:** MDCK island expansion shows that cells coordinate their migration on aligned collagen fibers (top) at much larger scale compared to cells on a glass substrate (bottom). Color codes for the orientation of migration. Double-headed arrows show the orientation of collagen fibers. Arrows in the image at 60 h represent the direction of massive antiparallel cell streams. Scale bar 100 μm ¹⁰⁵.

Up to now, contact guidance has been mostly studied on single cell migration or collective free space invasion. However, little is known about cell collective response to topographical cues in confluent cell monolayers and no universal interpretation or model has been proposed yet. How cells respond collectively to topographical cues in confluent cell monolayers without free space is the central question of this PhD work. In particular in Chapter 3, we focus on the collective dynamics of chaotic HBECs on grooved topographies.

2. Materials and methods

2.1. Substrates micro-fabrication.....	37
2.1.1. PDMS micro-grooved substrates.....	37
2.1.2. Chemically micro- or meso-patterned substrates.....	38
2.2. Cell biology.....	39
2.2.1. Cell lines.....	39
2.2.2. Cell culture conditions.....	40
2.2.3. Cell seeding for experiments.....	41
2.2.4. Drugs inhibition	41
2.2.5. E-cadherin knock-down in HBECs.....	42
2.2.6. Immunostaining.....	42
2.3. Microscopy.....	43
2.3.1. Time-lapse microscopy.....	43
2.3.2. Confocal microscopy	43
2.4. Image analysis	44
2.4.1. Image pretreatment	44
2.4.2. Local orientation measurement.....	45
2.4.3. Particle Image Velocimetry (PIV).....	46
2.4.3.1. PIV principle.....	47
2.4.3.2. Algorithm implementation	47
2.4.4. Cell tracking.....	49
2.5. Statistics.....	50

In this chapter, I detail microfabrication techniques for fabricating specific cell substrates, cell lines chosen to conduct the projects and cell biology procedures that have been used to perform the experiments presented in Chapter 3 and 4. I then present the details of image acquisition and processing. The list of products, materials, and equipment as well as the detailed protocols can be found in Annex 6.1.

2.1. Substrates micro-fabrication

For the two projects presented in the following chapters, cells are guided by anisotropic microscale cues in their substrates. In this section, I present microfabrication techniques I optimized and used for fabricating such cell substrates. Detailed experimental protocols are provided in Annex 6.1. Substrates' fabrication was done either in the Physico Chimie Curie lab clean room or in the IPGG technological platform clean room, ensuring a particle free environment.

2.1.1. PDMS micro-grooved substrates

In most of the experiments performed for this PhD work, cells were seeded on micro-grooved PDMS substrates. The preparation of these substrates requires the fabrication of micro-structured wafers that are used as molds for the PDMS. The fabrication of these wafers is performed using classical photolithography protocols that rely on the use of a negative photoresist, a resin that reticulates when it is illuminated. The resin is deposited on the wafer, illuminated with the desired pattern, and further developed so that non-illuminated parts are dissolved. The substrate fabrication steps are sketched in Figure 2.1.A and further detailed below.

First, SU-8 negative photoresist was spin coated on a silicon wafer. To ensure proper adhesion of this resin, a thin layer of Omnicoat was deposited on the wafer beforehand (Figure 2.1.A step 1). The height of the photoresist layer was tuned by optimizing spin coating speed or photoresist solution concentration. Tuning the concentration is achieved by using different versions of commercial SU-8 (SU-8 2002 or 2005) or by mixing SU-8 and a thinner solution with different relative proportions. The photoresist was then illuminated with specific patterns designed on the Clewin software (Figure 2.1.A step 2). It was done either by direct laser writing with a μ PG 101 Pattern Generator or by UV illumination through a chromium mask with a mask aligner. Chromium masks were either ordered from the company Compugraphics or homemade with direct writing photolithography following the protocol detailed in Annex 6.1.2. The photoresist was developed in SU-8 developer or in PGMEA in which non-illuminated resin was dissolved (Figure 2.1.A step 3, Figure 2.1.B). The height of the deposited photoresist layer was measured with a contact profilometer, and the obtained pattern geometry checked with a light reflective microscope (Figure 2.1.C). To facilitate PDMS detachment, wafers were silanized in vacuum with a vapor of silane for 2 hours.

Wafers were ultimately used as molds to fabricate PDMS substrates. Liquid PDMS (10:1 mixture of monomers and cross-linking agents) was spin coated on the wafer and reticulated overnight at 65°C (Figure 2.1.A step 4). After detachment from the wafer and 30 seconds of plasma cleaning,

2. Materials and methods

grooved or flat PDMS pieces were put in the bottom of the wells of a glass bottom 12-well plate (Figure 2.1.A step 5) and coated with a fibronectin solution at 10 $\mu\text{g}/\text{mL}$ for 1 hour. The textured areas of the wafer and consequently of the PDMS substrates were 13 mm X 13 mm (Figure 2.1.B). Grooves and ridges were 4 μm wide and their depth ranged from 0 to 2.5 μm .

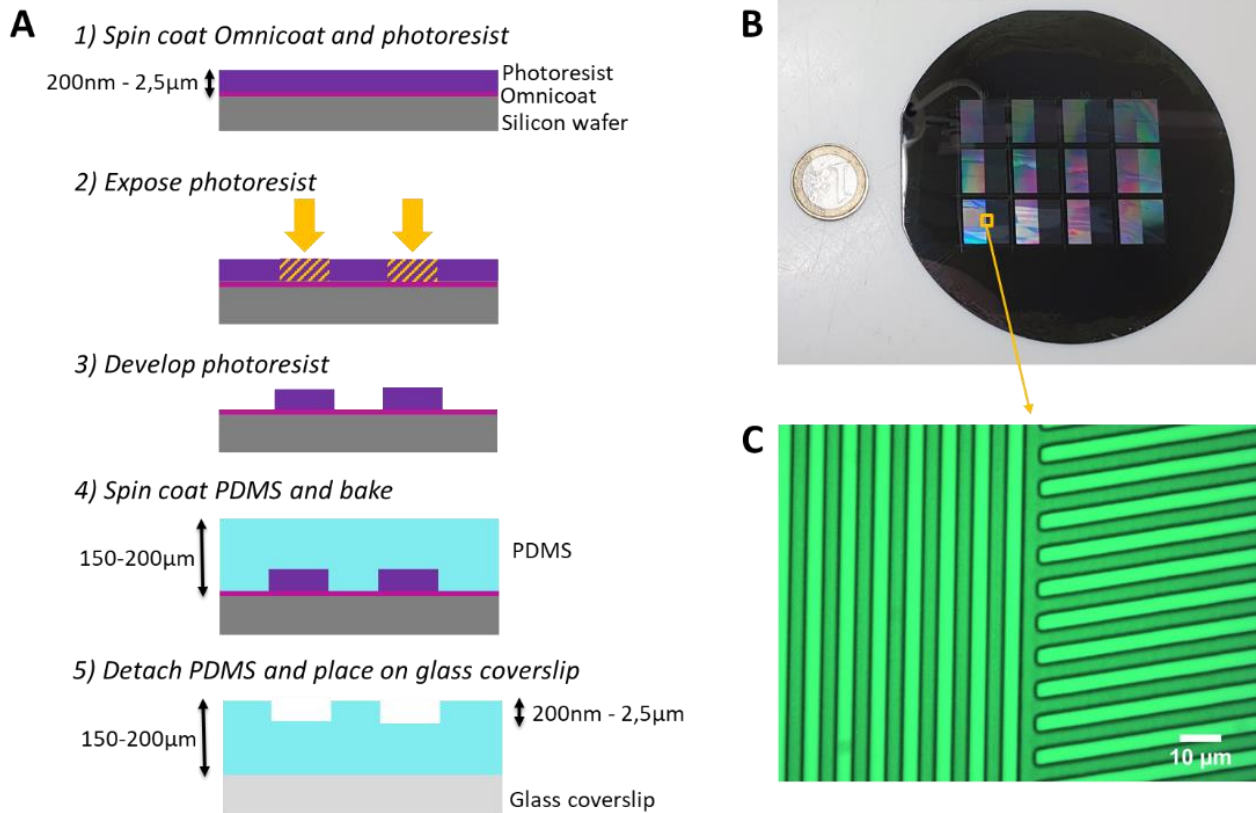


Figure 2.1 : Micro-grooved PDMS substrates fabrication.

A: Photolithography steps for micro-structured substrates fabrication. The detailed protocols can be found in Annex 6.1.3 and 6.1.4

B: Typical wafer obtained after development with 12 micro-grooved parts of 13 mm X 13 mm. Grooved parts are colored due to light diffraction on the microstructures, continuous differences in color are due to small changes in resin height, sharp color changes happen at the interface between grooved zones with different direction. 1-euro coin is used as scale.

C: Image of the wafer at the interface between grooved zones with different orientation. Grooves and ridges are 4 μm wide.

2.1.2. Chemically micro- or meso-patterned substrates

Alternatively, cells were seeded on chemically micro-patterned substrates made of alternating 4 μm wide lines of PEG and fibronectin, or confined in mesoscale zones surrounded by PEG coating, PEG being a cell repellent. These substrates were fabricated with photolithography-based patterning techniques previously optimized in the team¹⁰⁶. The detailed protocol is presented in Annex 6.1.5.

Briefly, glass coverslips were cleaned to remove impurities in the surface before being coated with a cell repellent gel in three steps: first, a thin layer of silane was bounded covalently on the glass; then, an acrylamide layer was added by a chemical reaction; eventually, a PEG layer was chemically bounded over the acrylamide layer (Figure 2.2.A step 1). This coating is strongly repellent for cells for days or weeks.

These coating steps were followed by photolithography steps. A thin layer of positive photoresist was deposited on the PEG-coated glass surface (Figure 2.2.A step 2) by spin coating. The photoresist was then illuminated with UV light through a mask where the pattern is drawn (Figure 2.2.A step 3). The mask is either a chromium mask (ordered from the company Compugraphics or homemade) or a soft mask if the desired patterns are larger than 15 μm . Soft masks were printed by Nawel Cherkaoui or Kevin Phan from the IPGG platform team using a photoplotter. Photoresist was then developed so that the illuminated parts are dissolved (Figure 2.2.A step 4). The repellent gel layer that is not protected anymore by the photoresist layer was etched in air plasma (Figure 2.2.A step 5). The remaining layer of photoresist was then dissolved in acetone (Figure 2.2.A step 6). Optionally, glass coverslips can be coated with fibronectin which will adhere only on PEG free surface.

At the end of this protocol, the glass coverslip is covered with a PEG layer repellent to cells except on the designed patterns on which cell can adhere. If the pattern has a mesoscale size, it leads to cell confinement (Figure 2.2.B). If the pattern is composed of micro-lines with subcellular width, cells grow as a confluent monolayer, but these chemical cues lead to alignment and directed migration. We were able to successfully achieve a 3 μm resolution with this technique.

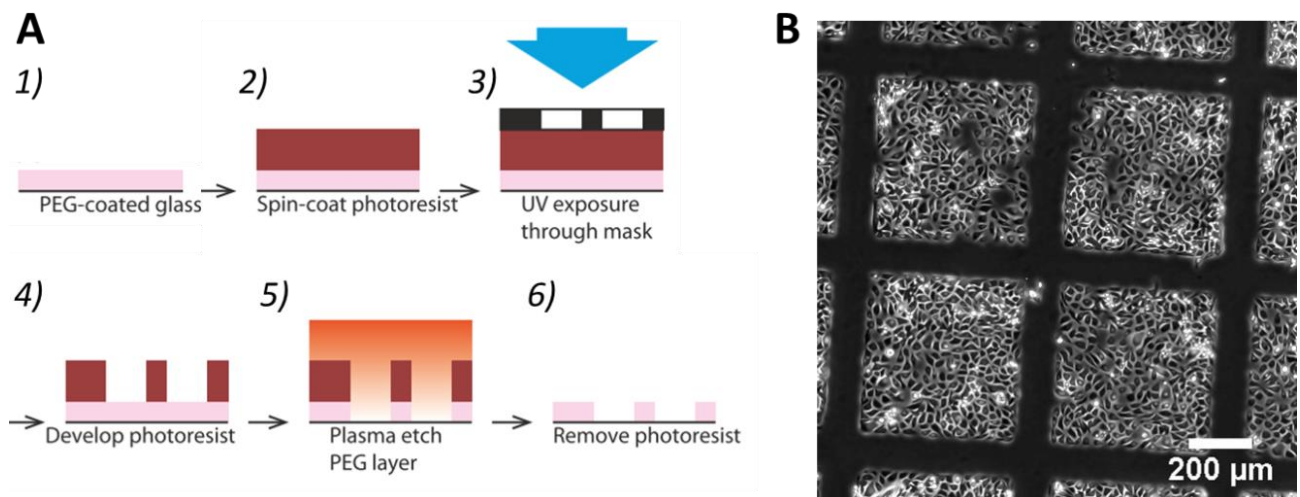


Figure 2.2: PEG-based substrate patterning.

A: Different steps for the PEG-based patterning protocol. Adapted from ¹⁰⁶.

B: HBECs confined in 500 μm wide fibronectin-coated squares fabricated with the PEG-based substrate patterning protocol.

2.2. Cell biology

This section presents cell lines and cell biology protocols implemented to investigate biological mechanisms of the observed cell collective behaviors. More details on the protocols can be found in Annex 6.1.6, 6.1.7 and 6.1.8.

2.2.1. Cell lines

During my PhD work, I investigated different collective behaviors inside confluent monolayers of cells. I selected several immortalized cell lines for their specific characteristics adapted to the different projects.

HBECs:

Most of the experiments on the laning behavior triggered by collective contact guidance presented in Chapter 3 have been performed with HBECs (Human Bronchial Epithelial Cells, gift from J. Minna's laboratory in Dallas, TX). They have originally been derived from healthy lung primary cells. At confluence, they have the specificity to be highly active and weakly cohesive⁵². At long time, cell-cell and cell-substrate adhesions mature and HBECs monolayers reach a jammed state¹⁶. They are typically 20 μm in diameter.

Other cell lines used in Chapter 3:

Other cell lines have been used occasionally for this work, as controls mainly:

- **MDCK:** Madin-Darby Canine Kidney cells are the typical example of immortalized epithelial cells. They are highly cohesive, less active and in a jammed state at high density.
- **HT1080:** HT1080 cells (gift from Dr Philippe Chavrier, Institut Curie) are human fibrosarcoma cells. At confluence, they have a highly chaotic behavior and do not jam⁵⁵.

C2C12:

The results on the formation of muscle like bilayered structures presented in Chapter 4 were obtained with C2C12 cells (gift from Clotilde Thery, Exosomes and Tumor Growth, Inserm U982, Institut Curie), an immortalized mouse myoblast cell line. These cells are committed muscle precursors. Under certain conditions, they differentiate into myocytes that fuse into myotubes which compose muscle fibers. For our experiments, we used C2C12 cells that have lost their ability to differentiate because of the large number of passages performed. C2C12 cells have a spindle-like shape when cultured on a substrate. They are typically 50 μm long and 10 μm wide. They have weak cell-cell adhesion and have been shown to secrete ECM and create 3D structures⁵³. In the present study, we used both normal C2C12 (C2C12 WT) and a stable cell line in which actin is labeled with mCherry (C2C12 β -actin m-cherry), to avoid imaging PDMS microgrooves in phase contrast and measure accurately cell orientation. This fluorescently marked cell line has been constructed by Aude Battistella and Fanny Cayrac from the BMBC platform using Crispr technique.

2.2.2. Cell culture conditions

HBECs were cultured in keratinocyte serum-free medium containing L-glutamine and supplemented with antibiotics and growth factors. HT1080, MDCK and C2C12 cells were cultured in classical high glucose Dulbecco's modified Eagle's medium supplemented with 10% FBS and 1% penicillin/ streptomycin antibiotics solution. Details about medium composition can be found in Annex 6.1.6.

Cells were maintained at 37°C under 5% CO₂ partial pressure and 95% relative humidity atmosphere. They were passaged every 2 to 4 days using Trypsin. As HBECs medium does not contain serum, the effect of trypsin was inhibited using defined trypsin inhibitor after each passage of HBECs.

2.2.3. Cell seeding for experiments

Experiments for Chapter 3 (unless otherwise stated):

HBECs and HT1080 cells were seeded at high density in wells of a glass bottom 12-well plate in which adequate PDMS substrates were previously deposited (225 000 cells/cm² i.e., 900 000 cells per well). MDCK and C2C12 were respectively seeded at a density of 500 000 and 600 000 cells per well. They were left to incubate for few hours until they were fully attached. Prior to imaging, cell monolayers were rinsed with PBS and 5 mL of fresh medium was added. For all experiments, the origin of time is taken at cell seeding time.

Experiments for Chapter 4:

C2C12 cells were typically seeded at a 100 000 cells/cm² density on PDMS substrate deposited in wells of a glass bottom 12-well plate. They were allowed to adhere and grow for approximately 1 day. Cell monolayers were then rinsed, and 5 mL of fresh medium was added. The origin of time is taken at cell seeding time. Alternatively, when data were averaged over repeats from different FOVs from independent wells and experiments, the origin of time was set at the onset of confluence in order to be able to compare wells in which the initial density was not the same due to inhomogeneity in cell seeding. Confluence is defined visually as the time at which no holes are observed in the entire FOV.

Wound healing assays:

In both chapters, for the wound healing assays, we used commercially available silicone-based Culture-Inserts 2 Well (Ibidi). Each well of the Ibidi insert covers a surface of 22 mm². Inserts were placed on glass, PDMS or soft gel and 30 000 to 60 000 cells were seeded in each well. They were left to incubate until they were fully attached and confluent. Then, culture inserts were removed, leaving free space at well edges. Cells were rinsed with PBS and fresh medium was added prior to imaging.

2.2.4. Drugs inhibition

When mentioned in Chapter 3, drugs were added prior to imaging, approximately 6h after cell seeding, in the fresh medium. To ensure that the drug was added homogeneously in the medium, we mixed gently the solution by pipetting up and down after drug addition. For perturbing the system, we used several drugs:

- **CK666** is an inhibitor of Arp2/3. The Arp2/3 complex is a nucleator of the branched actin network characteristic of cell protrusions such as lamellipodia. Thus, inhibiting Arp2/3 decreases lamellipodial protrusions and consequently reduces cell polarization. CK666 was used at concentrations ranging from 25 μM to 100 μM on HBECs.
- **Para-nitroblebbistatin** is an inhibitor of myosin II. It reduces cell contractility. We used this drug in concentrations ranging from 1 μM to 20 μM on HBECs. As we expose cell to light for several days, this non-phototoxic version was favored over the classical blebbistatin.
- **Mitomycin C** was used to block HBECs cell division. Approximately 5 h after cell seeding, cells were incubated with mitomycin C at 10 μg/mL during 1 h. Cells were then rinsed two times with PBS and two times with fresh medium, before replacing the medium with the drug by 5 mL of fresh medium. This procedure removes any trace of drug before imaging and avoids any toxicity effect.

2. Materials and methods

2.2.5. E-cadherin knock-down in HBECs

E-cadherin expression was efficiently reduced in HBECs using RNA interference process. E-cadherin gene was knocked down by selectively inactivating and ultimately degrading its corresponding mRNA using short hairpin RNAs (shRNAs). E-cadherin shRNA transcription was induced in cells by introducing in their nuclei corresponding DNA sequence by lentiviral transduction. The detailed protocol can be found in Annex 6.1.7. Briefly, HBECs were incubated overnight in their medium supplemented with polybrene in which E-cadherin shRNA (h) lentiviral particles were added. Lentiviruses infected the cells and their plasmids containing shRNA sequence and an antibiotic (puromycin) gene resistance entered cell nuclei. Cells expressing the shRNA were then grown before being selected and further cultured with puromycin. A western blot was performed by John Manzi, BMBC platform engineer, to check that E-cadherin (120kDa) expression had been knocked down in those cells whereas actin (42kDa) expression was unaffected (Figure 2.3). The ratio of band intensities between actin and E cadherin bands ($R = \frac{I_{E-cadherin}}{I_{actin}}$) were measured using ImageJ for both WT and E-cadherin knock down (KD) cells. Two western blot repeats confirmed the percentage of E-cadherin reduction in E-cadherin KD cells, defined as $\frac{R(WT) - R(Ecadherin\ KD)}{R(WT)}$, to be 75-80%.

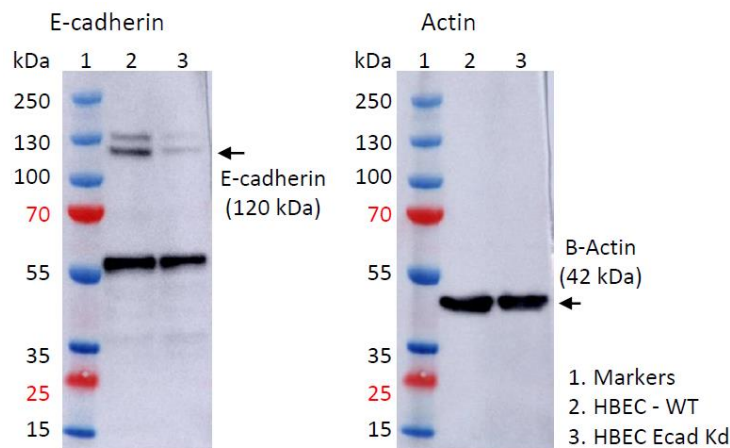


Figure 2.3 : The western blots for E-cadherin (left) and actin (right) in HBECs WT (track 2) and HBECs E-cadherin KD (track 3) show that the expression of E-cadherin was successfully reduced in E-cadherin KD cells while the actin expression was unaffected. Western blot performed by John Manzi.

2.2.6. Immunostaining

For observing the localization of specific proteins such as E-cadherin in our cells, we fixed them at specific time points and stained the proteins of interest with fluorescent dyes coupled to antibodies. More details on the protocol can be found in Annex 6.1.8. Briefly, HBECs were fixed with 4% paraformaldehyde, cell membranes were permeabilized with 0.1% Triton X-100 and antibody binding sites were saturated with a saturation solution of PBS + 2.5% Normal Goat Serum + 0.1% Bovine Serum Albumin. E-cadherin labeling was performed by incubating the cells sequentially with a rat anti-E-cadherin antibody solution (1:100) and a secondary fluorescent antibody (goat anti-rat alexa fluor 488) solution (1:1000). All these steps were separated by washing steps in PBS and performed at room temperature. Nuclei were stained with Hoechst 33342 prior to imaging.

2.3. Microscopy

Collective cell behaviors are observed and investigated using classical and confocal microscopy techniques presented in the following subsections. Characteristics of the microscopes used can be found in Annex 6.1.1.

2.3.1. Time-lapse microscopy

To monitor cell monolayer evolution, time-lapse multi-field experiments were performed on an automated inverted microscope (Olympus IX71 or Leica DM-IRB) equipped with thermal and CO₂ regulations. Experiments lasted typically several days. The displacements of the sample, the illumination sequences and the camera acquisitions were computer-controlled by Metamorph software (Universal Imaging).

Experiments presented in Chapter 3 were, for most of them, performed with a 4X objective in phase contrast. The field of view (FOV) size was 3.3 mm × 3.3 mm. The delay between two successive images of the same field was set to 5 minutes. In each well, to increase FOV size by stitching several FOVs, four vertical FOVs were chosen in the middle of the PDMS substrate with a 10% overlap. Complementary experiments such as wound healing assays were performed with a 10X objective.

Experiments presented in Chapter 4 were performed with a 10X objective in fluorescence microscopy to avoid imaging the grooves and ensure proper cell orientation detection. The FOV size was 1.3 mm × 1.3 mm. The delay between two successive images of the same FOV was set to 15 minutes. With this image acquisition setup, the obtained images encapsulate contribution from a wide focal plane and are biased towards acquiring the topmost layer. This is a concern for imaging systems with more than one cell layer and it can introduce errors in data interpretation.

2.3.2. Confocal microscopy

Classical microscopy techniques presented before do not offer a z resolution sufficient to localize proteins in 3D inside cell cytoskeleton or membrane. Moreover, the project presented in Chapter 4 deals with the formation of stacked layers of cells. To study this phenomenon, it is important to have a z resolution enabling to distinguish between cell layers. To get tridimensional images, we used confocal microscopy techniques that allow the imaging of thin focal planes. Final 3D images are obtained by stacking images from several focal planes.

We used two kinds of confocal microscopes available in the Cell and Tissue Imaging platform (PICT-IBISA) at Institut Curie:

- *A laser scanning microscope (LSM)*: with this equipment, the laser excites a small volume of the sample using a pinhole and the objective gets the corresponding emitted light, which provides high resolutions in the three directions. The final image is constructed by repeating this operation on different volumes of the sample in the three directions in a scanning process. Thus, getting one image is time consuming and the size of the FOVs is limited. Additionally, the

high light intensity needed can be phototoxic for cells. Thus, this technique is relevant for fixed or non-living samples. It can be combined with super resolution techniques to increase further spatial resolution. For super-resolution confocal imaging of the fibronectin coating on grooved PDMS substrate (Annex 6.5), an inverted LSM confocal microscope was used combined with super-resolution module Airyscan.

- *A spinning-disk microscope*: it allows exciting and gathering emitted light from several small volumes of the sample at the same time using a disk containing many pinholes. A whole focal plane can be imaged without scanning the sample only by rotating the disk, which increases the time resolution at the expense of spatial resolution. Slices of the sample are obtained by repeating the operation for different focal planes. This technique allows rapid acquisition of multidimensional images (xyz, time, different wavelengths) and is then well-suited for efficient 3D imaging of large FOVs of living samples with time lapse. Samples were imaged in fluorescence on an inverted spinning disk confocal microscope using a 20X oil objective and a sCMOS camera. The size of the z step was typically 1 μm . For long term imaging of living samples, the microscope is equipped with a thermostatic chamber to keep samples under physiological conditions.

2.4. Image analysis

Acquired images were analyzed using both ImageJ public domain software and Matlab (Mathworks). The pre-processing steps and data extraction from the images are presented in the following. In particular, local cell orientation and velocity field measurements are detailed.

2.4.1. Image pretreatment

Image pre-processing was performed using the ImageJ public domain software and automated by writing ImageJ macros. When necessary, images were first converted to 8 bits. Optionally, images were also binned to save computational time and memory, after checking that the loss of spatial resolution did not impact orientation and velocity measurements.

In Chapter 3, for each experimental well, four FOVs were binned and stitched using the pairwise stitching plugin¹⁰⁷. The images were then rotated to align the grooves with the x axis and cropped, the final stitched images being between 7 and 12.5 mm long and between 2 and 3 mm wide.

In Chapter 4, data analysis is performed on fluorescent images. The FOVs being large, the illumination is not homogeneous, and cells at the border of the FOVs appear less intense than the ones in the middle. To correct this effect, we computed the 2D illumination pattern for each experiment and used it to correct fluorescent images acquired. This step is crucial for using intensity disparities as an indicator of cell density inhomogeneity in a system. Briefly, first time point fluorescent images from all acquired FOVs were blurred using filters. Those blurred images were averaged altogether, and the

obtained image was divided by its maximal intensity value. This normalized image corresponds to the illumination pattern of the experiment and all fluorescent images acquired during this experiment were corrected by dividing them with the illumination pattern.

For the experiments presented in Chapter 4, the substrates were designed so that the left part and the right part of the grooved area were composed of grooves with different orientation. In the middle of the substrate called the interface, groove orientation changes discontinuously. The corrected fluorescent sequences were rotated to align this grooves' interface with the y axis and cropped. The position of the grooves' interface was recorded, and time of confluence was chosen as the first time at which no holes is detected inside the FOV. This time was used as the time origin and the interface position as the x axis origin when data were averaged over several independent FOVs.

For spinning disk 3D images, three FOVs were stitched and the focal planes corresponding to bottom and top cell layers were manually selected.

2.4.2. Local orientation measurement

Local orientation of cells was measured using the ImageJ OrientationJ plugin^{108,109} (<http://bigwww.epfl.ch/demo/orientation/>). This plugin measures the local intensity anisotropy by analyzing spatial intensity gradients. For each pixel of the original image, it computes the structure tensor J defined as:

$$J(x, y) = \begin{bmatrix} \int_{\text{ROI}} \nabla_x I(x, y) \cdot \nabla_x I(x, y) dx dy & \int_{\text{ROI}} \nabla_x I(x, y) \cdot \nabla_y I(x, y) dx dy \\ \int_{\text{ROI}} \nabla_x I(x, y) \cdot \nabla_y I(x, y) dx dy & \int_{\text{ROI}} \nabla_y I(x, y) \cdot \nabla_y I(x, y) dx dy \end{bmatrix}$$

where I is the intensity of the pixels. The ROI is a sliding Gaussian window of size σ corresponding to the typical size of an anisotropic feature in the original image. The dominant direction of anisotropy in the ROI is the direction of minimal gradient of intensity and is obtained by diagonalization of J . The result of the plugin is an image of same size in which each pixel codes for the local orientation in the range $[-90^\circ, 90^\circ]$ (Figure 2.4). To measure local orientation in C2C12 monolayers, the Gaussian window size was set to $\sigma=25 \mu\text{m}$. This corresponds to half a cell length.

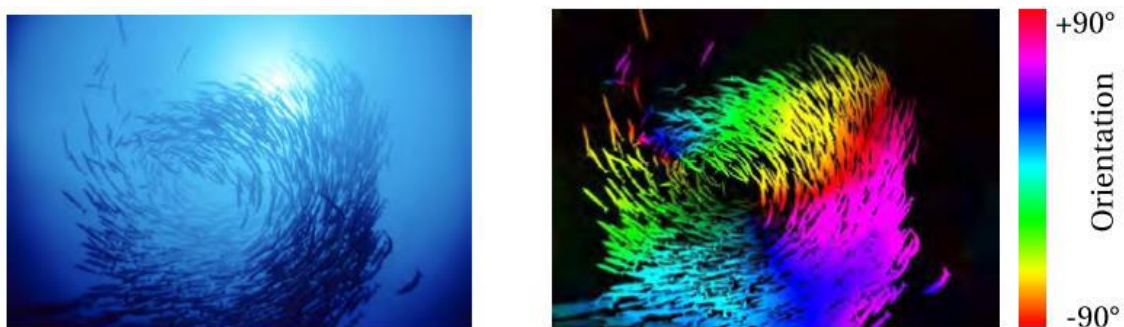


Figure 2.4: OrientationJ plugin for measuring the orientation field: example of OrientationJ used on a shoal of fish. Left: original image, right: color coded orientation field. Taken from G. Duclos thesis⁴⁵.

In Chapter 4, the substrate geometries studied were y invariant. Orientation fields were thus averaged in the y direction to get angle profiles along the x axis. As angles are circular data, angle averaging is not trivial. The method for angle averaging is graphically explained in Figure 2.5.A. Each

2. Materials and methods

angle θ_i defines a point x_i on the unit circle that can be described in complex numbers as $e^{i\theta_i}$. The circular mean $\bar{\theta}$ is the argument of the resultant vector $\bar{x} = \sum_i x_i$. As we are dealing here with orientation of apolar cells, -90° and 90° angles are equivalent. It leads to perfectly symmetrical angle distributions when cells are almost vertically oriented, the resultant vector being close to zero. For example, averaging $\theta_1 = 80^\circ$ and $\theta_2 = -85^\circ$ should give 87.5° and not $(80-85)/2 = -2.5^\circ$ (Figure 2.5.B.1). One needs to introduce a trick to correctly average the data: angles were doubled before performing the circular averaging presented before. The results were 2π -shifted if needed so that they lie in the range $[0^\circ, 360^\circ]$ (Figure 2.5.B.2). Angle averaged values were eventually obtained by dividing the results by 2 (Figure 2.5.B.3).

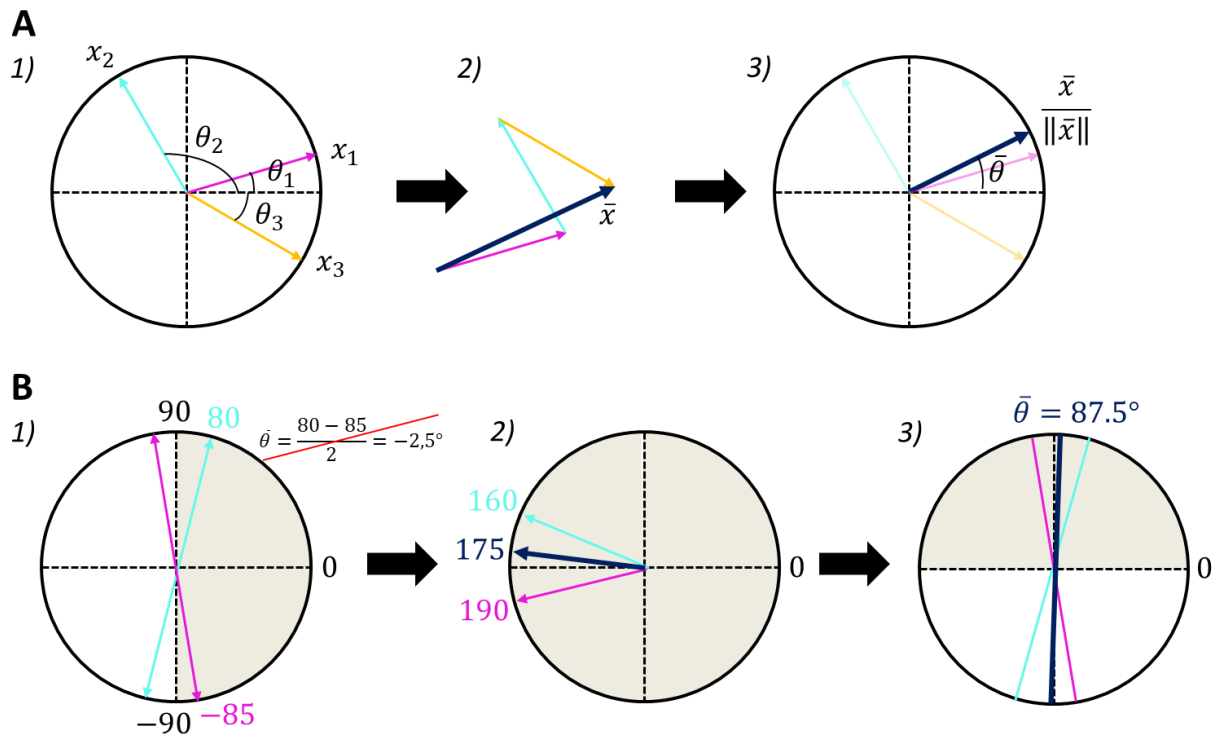


Figure 2.5: Algorithm for direction averaging.

A: Angle averaging. 1) Each angle corresponds to a vector on the unit circle. 2) The resultant vector \bar{x} is calculated. 3) The averaged angle $\bar{\theta}$ is the angle of the resultant vector \bar{x} .

B: Apolar direction averaging. 1) Direction angles are coded with angles between -90 and 90° . 2) Angles are doubled and averaged using the angle averaging algorithm in A. Obtained angles are shifted so that they lie in the range $[0^\circ, 360^\circ]$ rather than $[-180^\circ, 180^\circ]$. 3) Angle direction averaged is obtained by dividing the previously obtained angle by 2.

Inspired from Thibault Aryaksama thesis ¹¹⁰. The strategy used is based on notions developed in the book "Directional Statistics" ¹¹¹.

2.4.3. Particle Image Velocimetry (PIV)

To analyze collective behavior in confluent cell monolayers, cell displacements need to be extracted from the acquired image sequences. Typical FOVs in this study are larger than a millimeter in width and contain a very large number of cells. Thus, tracking each of them manually is not an option. A possible option would be to fluorescently tag each cell or nucleus and to automatize cell tracking. However, analyzed cell monolayers are at high cell density which leads to non-trivial detection issues: for example, it can be difficult to distinguish two neighboring cells. Also, the probability of getting

errors in single cell trajectories is high in the long-term experiments performed due for example to cell division. Thus, an alternative approach has been developed to map velocity fields by adopting the eulerian point of view: the velocity is calculated in fixed points of the image, confluent cell monolayers being treated as a continuum fluid. To do that, the Particle Image Velocimetry (PIV) technique is used routinely in our team^{24,112}. It allows extracting velocity field of confluent cell monolayers directly from phase contrast or fluorescent image sequences.

2.4.3.1. PIV principle

PIV principle is presented in Figure 2.6. First, the FOV is divided in a grid of sub windows. For each sub window, views at t and $t + \delta t$ are compared by calculating the cross correlation between these two successive images. The position of the correlation peak gives the most probable displacement, and thus the velocity vector, inside this sub window between the two successive time points. Iterating this process on all the FOV's sub windows and between each consecutive time points gives access to the velocity field $\vec{v}(x, y, t)$ for the whole image sequence.

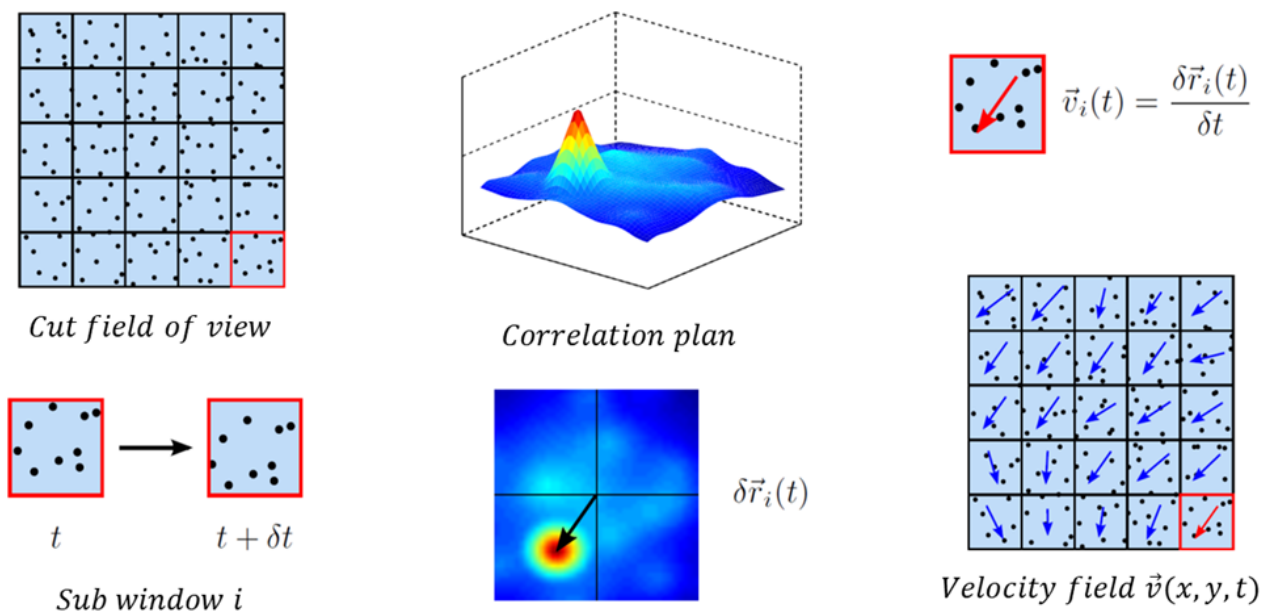


Figure 2.6: PIV principle. The image is first divided in sub windows. Cross correlation between a sub window at t and $t + \delta t$ is calculated, the position of the correlation peak gives the displacement and thus the velocity vector of the fluid in this sub window. Calculation of the velocity vectors for each sub window between each time step gives access to the velocity field $\vec{v}(x, y, t)$ for the whole image sequence. Adapted from Simon Garcia thesis¹¹³

2.4.3.2. Algorithm implementation

Velocity fields in confluent cell monolayers were extracted from stacks of images with a custom-made PIV algorithm based on the MatPIV software package¹¹⁴ for Matlab (MathWorks). To get an accurate velocity field, one must choose the adequate sampling frequency δt and PIV window size:

- dt must be:
 - small enough so that the cells do not deform, divide, or exchange places with their neighbors too much between two successive frames, the PIV being able to detect only translation and not rotation or deformation.
 - high enough to observe displacement between two frames distinguishable from noise.
- The PIV sub window size must be:
 - a power of 2 in pixels because the cross correlation is calculated using FFT (Fast Fourier Transform).
 - large enough so that details can be detected in the sub window. For Chapter 3, we performed PIV on phase contrast images in which the principal structures that we can distinguish are the cell borders. Thus, we chose sub window larger than a cell size to be sure that inside each sub window, we detect significant intensity gradient, mainly present in our images at cell borders. If the sub window was smaller, it could be totally contained inside a cell in which no typical visual features such as cell border could be detected and correlated in the next frame in our phase contrast images.
 - large enough so that the detected structures such as cell borders stay inside the same sub window between t and $t+dt$ (indeed, if the detected structures completely change sub window between t and $t+dt$, the correlation computed corresponds only to noise)
 - small enough so that the PIV window do not contain a group of cells in which the cells go in opposite direction during dt , so smaller than the correlation length of the velocity field.
- dt and the PIV sub window size must be adjusted in such a way that the displacement between t and $t+dt$ is less than 30% of half of the sub window size. Indeed, the correlation between successive sub windows is calculated until a shift of half a sub window in both directions. Yet, the border of the correlation plan is calculated with fewer pixels than the middle and thus is more sensitive to fluctuations. If there is not a well-defined correlation peak separated enough from the border of the correlation plan, the border fluctuations will be identified as the displacement inside the sub window, leading to an over representation of cell displacements corresponding exactly to half the sub window size between two frames.

Optionally, sub windows can overlap to get more vectors in the final PIV result. Note that in that case, the result is more resolved in space but contain the same quantity of information even though it is used several times.

A global filter is performed on the raw velocity field obtained by PIV to remove any aberrant vectors. Indeed, in case of successive sub-window hardly correlated, the noise might be comparable or higher than the signal and the results given by the PIV could be far from reality, often corresponding to a wrong detection of half the sub window size displacement as mentioned before. Practically, the global filter removes the vectors outside an acceptance interval which limits are defined by the velocity

distribution mean plus/minus a certain number of times its standard deviation. Here, this number g is set to 2.5. Deleted vectors are replaced by data interpolated from neighboring values. The proportion of interpolated vectors is checked to be less than 10%. Additionally, velocity fields have been smoothed with a sliding time average over a time window T . In Chapter 3, quantities extracted from these velocity fields have been averaged over 24 frames (i.e., 2 h) by a sliding time average.

The PIV parameters used for experiments analysis are given in the following table:

	Time between successive frames	Sub window size	Overlap	PIV pixel size	Sliding time average window
Chapter 3 experiments (HBECs or HT1080 cells)	5 min	52 μm	0.5	26 μm	30 min
Chapter 4 experiments (C2C12)	15 min	41 μm	0.5	20.5 μm	5 hours

The PIV sub window size of 52 μm for HBECs is smaller than the typical velocity correlation length¹⁶ but large enough to contain detectable structures such as cell borders. This PIV window size and time interval are perfect to measure displacements below 9 μm between two frames (1/3 of half the sub window size) i.e., velocities below 100 $\mu\text{m}/\text{h}$.

One needs to be extra careful regarding the results obtained by PIV. Indeed, PIV always gives results, but the controls of the validity are low. To check the validity of the result, the velocity field and the actual cell displacement on the movies were visually compared. Moreover, sub window size, global filter strength g and sliding time average window impacts on the obtained results were quantified. The conclusion of this analysis presented in Annex 6.2 is that, in the conditions of our study, PIV gives robust results for the large-scale features of the velocity fields.

2.4.4. Cell tracking

In Chapter 4, single cell displacements in the system have been investigated by mixing 1 to 10% of fluorescent cells in a population of WT cells. This trick allows to easily follow single fluorescent cell trajectories in confluent monolayers of non-fluorescent cells. Representative single cell tracks have been drawn on the images using the manual tracking Image J plugin.

2.5. Statistics

All the experiments presented in this manuscript were performed in at least two independent replicas, each condition being tested in at least two independent wells for each replica. The details of the data set contents are given in the legend of the corresponding figures. Error bars represent the standard deviations over all the FOVs analyzed, after pooling together results from all wells and independent experiments testing the same condition.

Chapter 3:

Experiments were performed in 12-well plates, each well testing a well-defined condition (groove depth, drugs, cell lines, etc.). For each experimental well, one final FOV was obtained by stitching four overlapping FOVs and is between 7 and 12.5 mm long and between 2 and 3 mm wide. For each figure, the size of the FOVs analyzed is given in the figure legend. Moreover, for each condition tested, the total number of wells analyzed (n) and the number of independent experiments they come from (N), are reported in the figure legends.

Chapter 4:

Experiments were performed in 12-well plates. Four substrate geometries were tested in each experiment (three independent wells per condition). In each well, five FOVs were acquired along the grooves interface, the FOVs being separated by at least one FOV size. Experiments were performed in two independent replicas. In the end, 30 FOVs from 6 independent wells from two independent experiments were analyzed for each condition.

Confocal imaging of the system was performed in glass bottom 35 mm² dish and in at least two independent replicas. Representative images are presented in the manuscript. Flows in the two cell layers (Figure 4.14) are averaged over five FOVs of the same dish.

3. Collective contact guidance drives polar laning of chaotic epithelial cells

3.1. Motivations: impact of contact guidance on collective cell dynamics	53
3.1.1. Collective contact guidance in confluent monolayers	53
3.1.2. Active nematic laning	53
3.1.3. Chaotic behavior of HBEC monolayers.....	55
3.1.4. Scientific question and experimental setup	57
3.2. Experimental results.....	59
3.2.1. Emergence of a stable laning pattern on micro-grooved substrates.....	59
3.2.1.1. <i>A laning pattern with alternating plug flows develops on grooved substrates</i>	<i>59</i>
3.2.1.2. <i>The transition from chaotic dynamics to laning is mediated by groove depth and is characterized by large x correlation length.....</i>	<i>61</i>
3.2.1.3. <i>Lanes' spatial positions are stable in time.....</i>	<i>65</i>
3.2.1.4. <i>The laning pattern is non-periodic and is characterized by an increase in y coordination</i>	<i>66</i>
3.2.1.5. <i>Summary of disorder-to-laning transition characteristics.....</i>	<i>68</i>
3.2.2. Laning is independent from cell division and cell-cell adhesion	69
3.2.3. Laning relies on cell protrusions rather than cell contractility.....	71
3.2.4. Other cell types do not experience large-scale laning on micro-grooved substrates...	74
3.3. Discussion	77
3.3.1. Length scales of HBECs laning are remarkably large.....	77
3.3.2. Cell-cell adhesion is not necessary for HBECs large-scale laning	77
3.3.3. Cell protrusions are critical for large-scale laning, but cell contractility is not	78
3.3.4. Non-periodic large-scale laning is not explained by an active nematic description	78
3.4. Continuum theory of an active polar fluid with anisotropic friction	80
3.4.1. Ingredients and assumptions of the model.....	80
3.4.2. Velocity fluctuations response to anisotropic friction	81
3.4.3. Disorder-to-laning transition in an active polar fluid with anisotropic friction	83
3.4.4. Summary of the active polar fluid theory contributions.....	84

3.5. Self-propelled particle-based simulations	85
3.5.1. Model for self-propelled particle-based simulations	85
3.5.2. Friction anisotropy orients particle displacements	85
3.5.3. Friction anisotropy results in the emergence of laning	86
3.5.4. The disorder-to-laning transition mediated by friction anisotropy is compatible with experiments.....	88
3.5.5. Friction anisotropy favors the laning transition controlled by polarization-velocity coupling and excluded volume interactions strength.....	89
3.6. Conclusion and perspectives	92

3.1. Motivations: impact of contact guidance on collective cell dynamics

Collective migration can be triggered both *in vivo* and *in vitro* in situations of wound healing or mesoscopic confinement (see 1.1.2). Cells *in vivo* and *in vitro* are also known to be guided by topographical cues such as nano-to-micro scale oriented collagen structures in their underlying ECM (see 1.3). As discussed in the introduction, contact guidance has been extensively studied for single cell migration but to a much lesser extent for the dynamics of cell assemblies. Indeed, collective contact guidance has been mainly studied in situations of wound healing in which cells collectively invade free space. In such a situation, anisotropic topography enhances collective motion in the direction of the topography and inhibits it in the perpendicular direction. However, collective migration can also occur in confluent cell populations without mesoscopic confinement or free space imposing a preferred direction for the collective motion. In such situations, cells can still be guided by anisotropic topographical cues. Yet, how such cues impact the cell collective behavior in confluent monolayers remains largely unknown.

3.1.1. Collective contact guidance in confluent monolayers

Locally correlated cell motion, known as “cell streaming”, has been shown to emerge within confluent monolayers, even in the absence of a global expansion motion. This streaming behavior originates from cell active self-propulsion and cell-cell interactions^{115–118}. Typically, the streams are highly mobile, and can appear and disappear at random places, in a swirl like turbulent motion.

The impact of the structure of the substrate has been studied only in a limited number of works. Londono and colleagues have observed such streaming behaviors in confluent monolayers of ARPE-19 epithelial cells and BJ fibroblast cells on both flat and grooved substrates⁹² (Figure 3.1.A). On grooved substrates, cells migrate in narrow streams ($\sim 50 \mu\text{m}$) oriented along the grooves. The percentage of cells migrating in streams wider than $40 \mu\text{m}$ as well as the average stream width increase on grooved substrate compared to flat substrate. Thus, topographical cues increase cell coordination in confluent cell monolayers. Perturbation experiments also suggest that cell coordination is independent from the strength of cell-cell junctions and from cell contractility but results from mechanical exclusion interactions.

Recently, Leclech and colleagues have reported that endothelial cells (HUVECs) on grooves (Figure 3.1.B.1) migrate along the grooves in antiparallel collective streams of width around $100 - 200 \mu\text{m}$ (Figure 3.1.B.2)¹¹⁹. The velocity pattern is periodic and the velocity profile along the direction perpendicular to the grooves is sinusoidal (Figure 3.1.B.3). The stream length increases and the stream width decreases as groove depth increases. Interestingly in that case, the streaming behavior relies on cadherin-based cell-cell junctions and disappears when these junctions are impaired.

3.1.2. Active nematic laning

The periodic velocity pattern observed in endothelial monolayers and consisting of alternating antiparallel streams (Figure 3.1.B.2) has been successfully understood in the framework of active nematic

3. Collective contact guidance drives polar laning of chaotic epithelial cells

systems. Leclech and colleagues adapted the active nematic 2D description presented in the introduction (see 1.2.4.1) by adding an aligning field in the free energy to account for the aligning effect of the grooves. In agreement with experimental results, the model predicts the emergence of a periodic laning pattern, the lane width decreasing as the strength of alignment is increased ¹¹⁹.

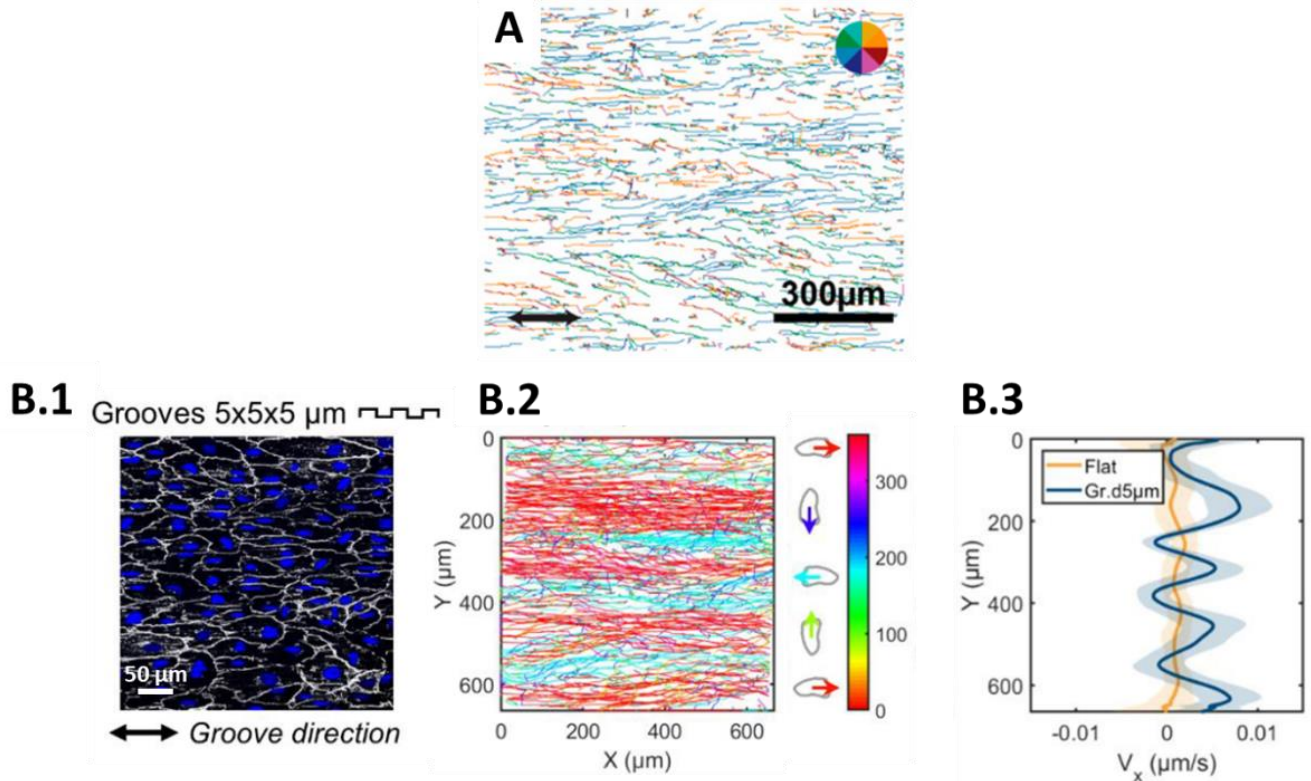


Figure 3.1 : Cell streaming in confluent cell monolayers on grooved substrates.

A: BJ fibroblast migration tracks colored by direction of motion allow identification of cellular streams oriented along the grooves. Groove orientation is highlighted by the double-headed arrow. Adapted from ⁹².

B: Emergence of periodic antiparallel cell streams in confluent monolayer of endothelial cells (HUVECs). B.1: Monolayer of endothelial cells on a grooved substrate, immunostained for VE-cadherin (cell-cell junction, white) and DAPI (nucleus, blue). Cells are elongated and align with the grooves. Double-headed arrow shows the groove direction. B.2: Accumulated cell trajectories after 24h of migration show antiparallel cell streams. The color codes for the direction of migration. B.3: Corresponding x velocity profile along y is sinusoidal. Adapted from ¹¹⁹.

Nematic laning has been experimentally observed in another active nematic system: the microtubule kinesin system ¹²⁰. Guillamat and colleagues introduced anisotropy in the microtubules' substrate using a magnetic field. The magnetic field modifies the substrate in such a way that microtubules flow preferentially along the axis perpendicular to the magnetic field. When introducing such anisotropy, the system experiences a transition from a chaotic behavior toward a nematic laning pattern (Figure 3.2.A.1). The microtubules organize into periodic alternating streams migrating in antiparallel direction, the velocity profile being sinusoidal (Figure 3.2.A.2). Inside flowing lanes, microtubules have a chevron like orientation (Figure 3.2.A). Lane width decreases when activity, mediated by ATP concentration, is increased. These experimental results are well reproduced by simulations of active nematic systems in which anisotropy is introduced in the friction to impose an "easy" direction of flow ¹²¹ (Figure 3.2.B). Note that in these simulations, substrate anisotropy was imposed with anisotropy in the friction whereas in the model describing endothelial streaming, substrate anisotropy was imposed with an aligning term in the free energy.

Nematic laning can be qualitatively understood as follows: anisotropy in the system favors the growth of a laning instability with a given period (corresponding to two lane widths). Flows are associated with chevron shape orientation gradients combined to active dipolar forces (see 1.2.4). Nematic laning thus relies on active contractility and orientation gradients but not on active polar traction forces.

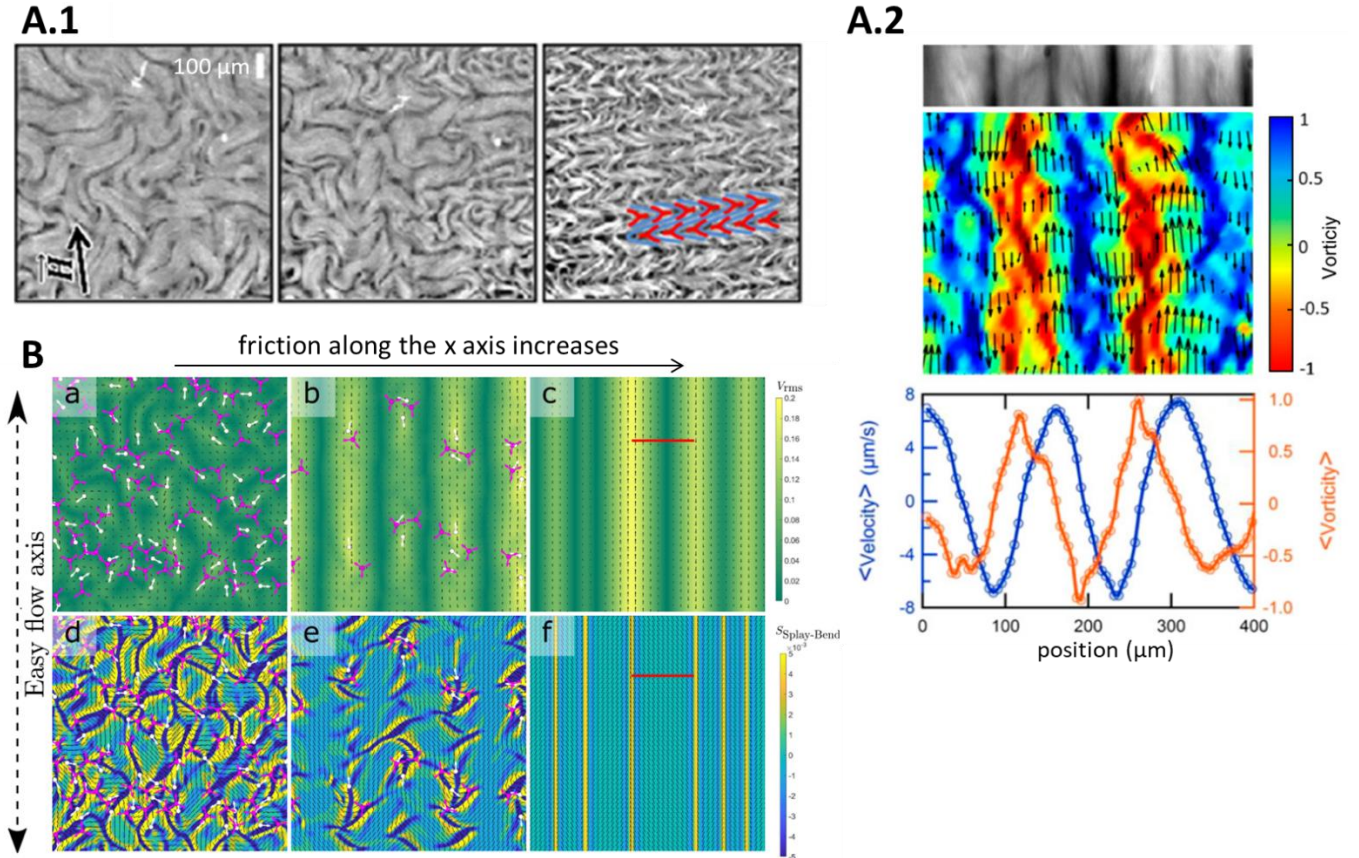


Figure 3.2 : Nematic laning on anisotropic substrates.

A: Nematic laning in a microtubule-kinesin system on an anisotropic substrate. A1: from left to right, microtubules experience a transition from a chaotic state to a nematic laning state in response to a magnetic field H that makes the substrate anisotropic. In the nematic laning phase (right), microtubules adopt a periodic chevron like orientation. A2: In the nematic laning phase, microtubules flow in periodic antiparallel lanes with a sinusoidal velocity profile. Top: transversal cut of the time-averaged fluorescence micrograph of an aligned active nematic film; Middle: corresponding local velocity (vector plot) and local normalized vorticity (color density plot); Bottom: downstream average of velocity and vorticity across the horizontal position. Adapted from ¹²⁰.

B: Simulations of active nematic systems with increasing friction anisotropy (from left to right) show a transition from a chaotic toward a nematic laning state with similar features than observed in the experimental microtubule-kinesin system. (a-c) show the velocity field colored by the velocity magnitude and (d-e) show the director field colored by the splay-bend order parameter (yellow and deep blue colors correspond to large deformation of the director field). Note the chevron like orientation pattern. Adapted from

¹²¹.

3.1.3. Chaotic behavior of HBEC monolayers

Human Bronchial Epithelial Cells (HBECs) seeded on glass have been reported to present a chaotic dynamics characteristic of highly active nematic systems on isotropic substrate ⁵². Indeed, velocity is correlated over a distance around $100 \mu\text{m}$ in HBEC monolayers ^{16,52} (Figure 3.3.a,b - Figure 3.4.A-C). Moreover, vortices of different sizes are observed in the vorticity field (Figure 3.3.b) and $+1/2$ and $-1/2$ nematic topological defects

3. Collective contact guidance drives polar laning of chaotic epithelial cells

are detected in the orientation field (Figure 3.3.c). These defects are continuously created and annihilated in the system as the rate of defects creation and annihilation have similar values varying from 1 to 0.5 h^{-1} with time. Note that the root mean square velocity also decreases with time (Figure 3.4.B). The typical size of the velocity correlated domains first increases over time by active jamming and eventually decreases at later stages as the system freezes (Figure 3.4.D)¹⁶. This behavior has been associated to both an increase in cell density and a maturation of cell-cell and cell-substrate adhesion.

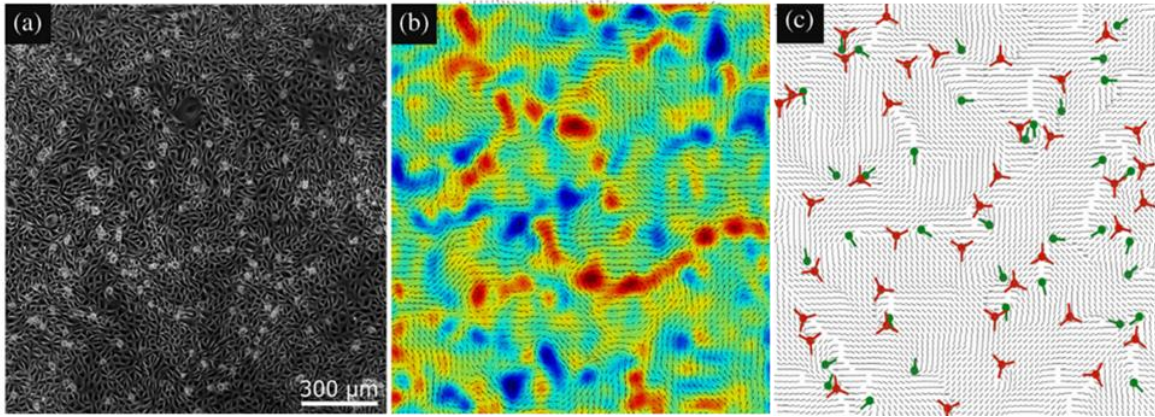


Figure 3.3: Turbulent dynamics of epithelial HBEC monolayers on glass substrates. Adapted from⁵².

(a) Phase contrast image. (b) Normalized vorticity map overlaid with the velocity field illustrates the collective chaotic behavior inside a confluent HBEC monolayer. (c) Cell orientation map reveals the presence of $+1/2$ (green dots) and $-1/2$ (red dots) defects.

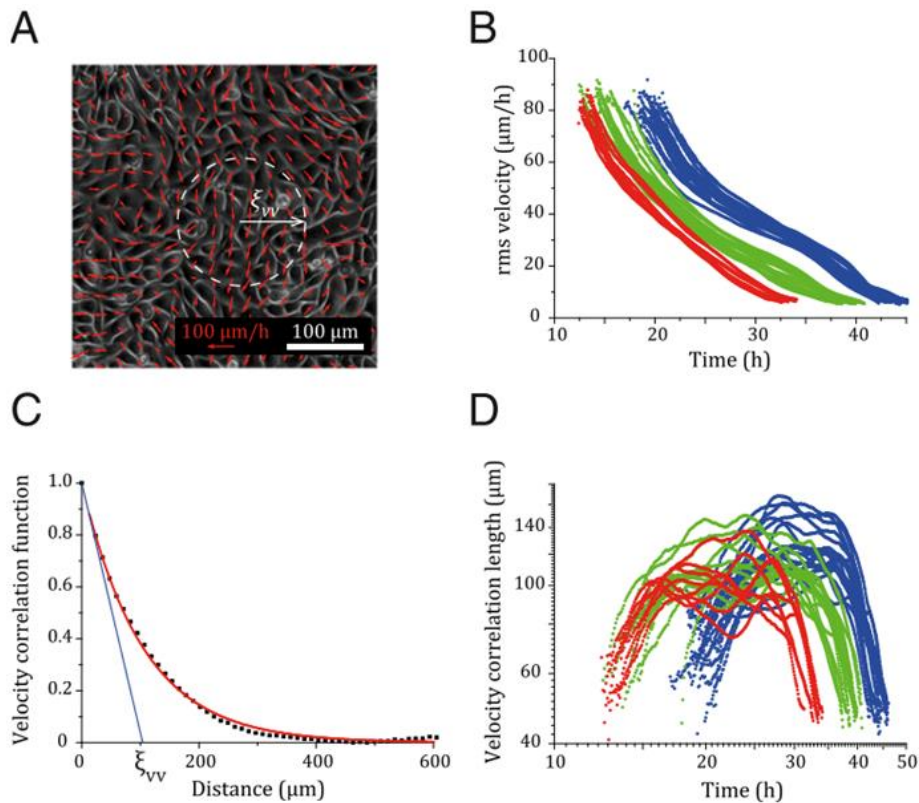


Figure 3.4: Active jamming in HBEC monolayer. Adapted from¹⁶.

A: Velocity field superimposed on the corresponding phase contrast image shows the collective behavior in a HBEC monolayer. B: The root mean square velocity decreases over time. Different colors correspond to different initial number of cells seeded in the experimental well.

C: Velocity radial correlation fitting with a decreasing exponential function gives the correlation length ξ_{vv} at a given time point.

D: The correlation length first increases and then decreases as the system freezes for all initial cell density.

3.1.4. Scientific question and experimental setup

HBECs are highly active cells that organize as an active nematic system at confluence. Their dynamics is chaotic, similarly to microtubule-kinesin systems on isotropic substrates. One can then ask the following question: “what is the collective response of such chaotic epithelial monolayers to anisotropic subcellular topographical cues?”

Investigating this question is of interest first from a biology point of view. Indeed, it will give insight on the impact of oriented ECM fibers on the dynamics of confluent active chaotic epithelial cell assemblies. This question is also relevant from a physics point of view in the field of active matter. Substrate anisotropy in chaotic active nematic systems leads to nematic laning in the microtubule/ kinesin system and in simulations. However, epithelial cells are complex units able to exert dipolar forces on their surroundings but also able to self-propel in the direction of their polarization. It is therefore interesting to check if the predictions for active nematic systems on anisotropic substrates remain valid for active epithelial cells, or if other effects should be considered to describe their collective behavior.

In this chapter, we investigate the collective dynamics of confluent HBEC monolayers on anisotropic topographical cues. To do that, HBECs are seeded at high density ($225\,000\text{ cells/cm}^2$) on flat and micro-grooved PDMS substrates. The grooves and ridges are $4\ \mu\text{m}$ wide and thus constitute subcellular orienting topographical cues. Their depth ranges from 0 to $2.5\ \mu\text{m}$ (Figure 3.5.B). Note that on a flat substrate, HBECs are typically $20\ \mu\text{m}$ in diameter, and thus extend over 2 to 3 ridges on a grooved substrate (Figure 3.5.B.2, C). The total grooved area is $13\ \times\ 13\ \text{mm}$ in size and is placed in the bottom of a well of diameter $22\ \text{mm}$ (Figure 3.5.A). We monitor the monolayer evolution by phase contrast microscopy and measure the velocity field using Particle Image Velocimetry (PIV) on FOVs that are between 7 and $12.5\ \text{mm}$ long and between 2 and $3.5\ \text{mm}$ wide (Figure 3.5.A) from 10 hours after cell seeding until the system completely freezes. In the following, the origin of time is the time of cell seeding. Confluence is typically reached between 10 to 15 hours after cell seeding.

3. Collective contact guidance drives polar laning of chaotic epithelial cells

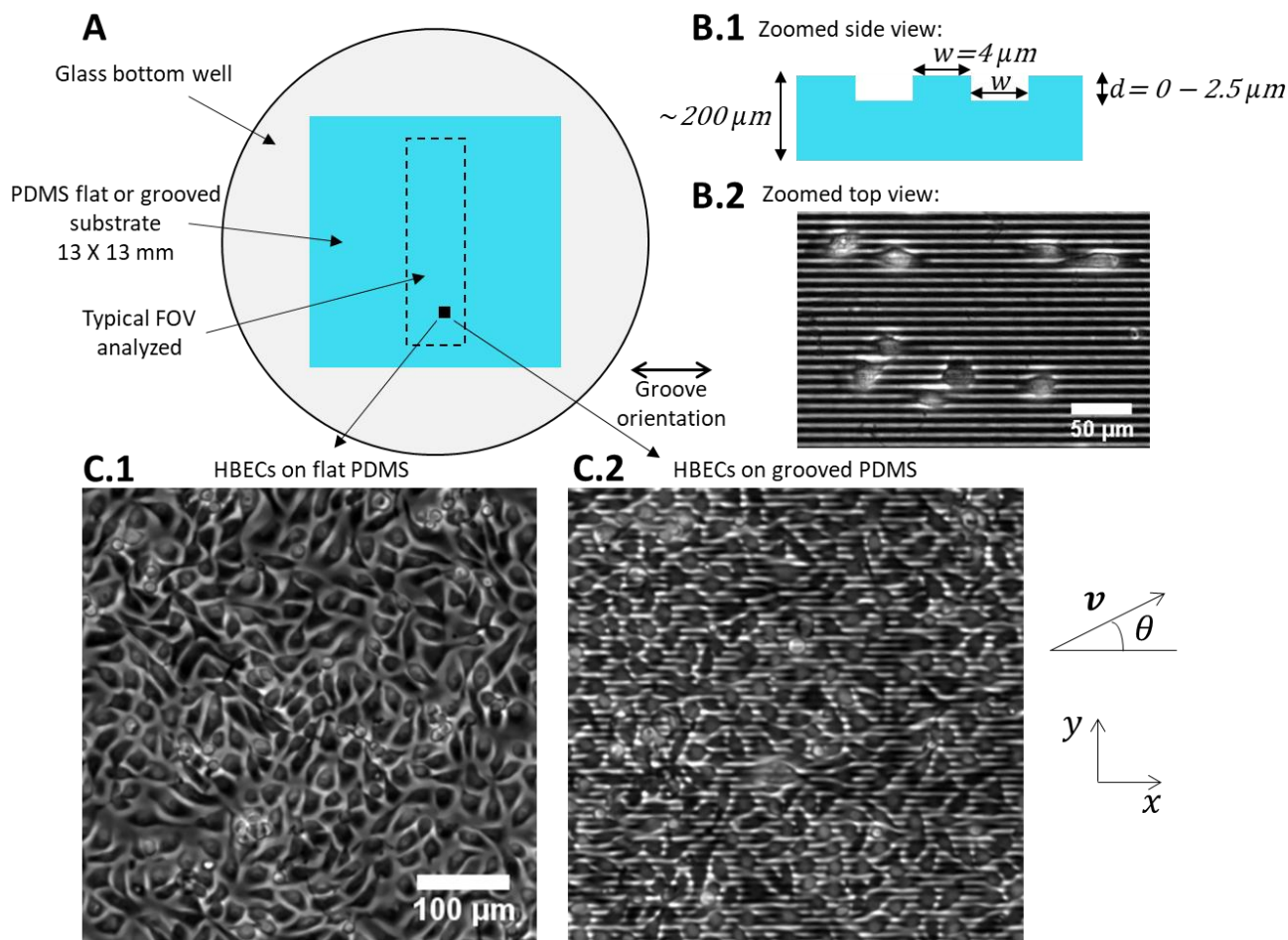


Figure 3.5 : Dimensions of the experimental system.

A: Schematic of one experimental well: PDMS substrates are deposited in the bottom of wells of a glass bottom 12 well plate and are 13 X 13 mm in size. One FOV is analyzed per experimental well and is obtained by stitching smaller FOVs. After rotation of the images to align grooves with the x direction, final FOVs are typically 7 to 12.5 mm long and 2 to 3.5 mm wide.

B.1: Schematic side view of the grooved substrate. Grooves are 4 μm wide and 0 to 2.5 μm deep. Ridges are 4 μm wide.

B.2: Phase contrast image of single HBECs on a grooved substrate. Cells typically span over 2 to 3 ridges.

C: Phase contrast image of confluent HBECs on flat (C.1) and grooved (C.2) PDMS substrates. The convention for the x and y axis, as well as for velocity angle measurements are presented at the right of the images.

3.2. Experimental results

3.2.1. Emergence of a stable laning pattern on micro-grooved substrates

3.2.1.1. A laning pattern with alternating plug flows develops on grooved substrates

We first investigate HBEC monolayer dynamics on grooved PDMS substrates with groove depth of $1.75\ \mu\text{m}$. 35 hours after cell seeding, the x velocity absolute values $|v_x|$ are larger than the y velocity absolute values $|v_y|$ (Figure 3.6.A, C). This shows that the cells are guided along the grooves. Strikingly, HBECs organize in alternating collective lanes oriented along the grooves and migrating in antiparallel directions (Figure 3.6.A). The v_x velocity profile along y is a non-periodic square signal alternating between $-v$ and $+v$ with $v \sim 50\ \mu\text{m}/\text{h}$ (Figure 3.6.B.1). The velocity profile in each lane is approximately flat, which is characteristic of a plug flow: in a lane, all the cells migrate at the same velocity regardless of their y position in the lane (Figure 3.6.B.2). Between two adjacent lanes, the velocity changes sign discontinuously, over less than $50\ \mu\text{m}$ (Figure 3.6.B.3-4). Thus, the shear is localized between two rows of cells. This velocity pattern is referred to as a “laning” state in the following.

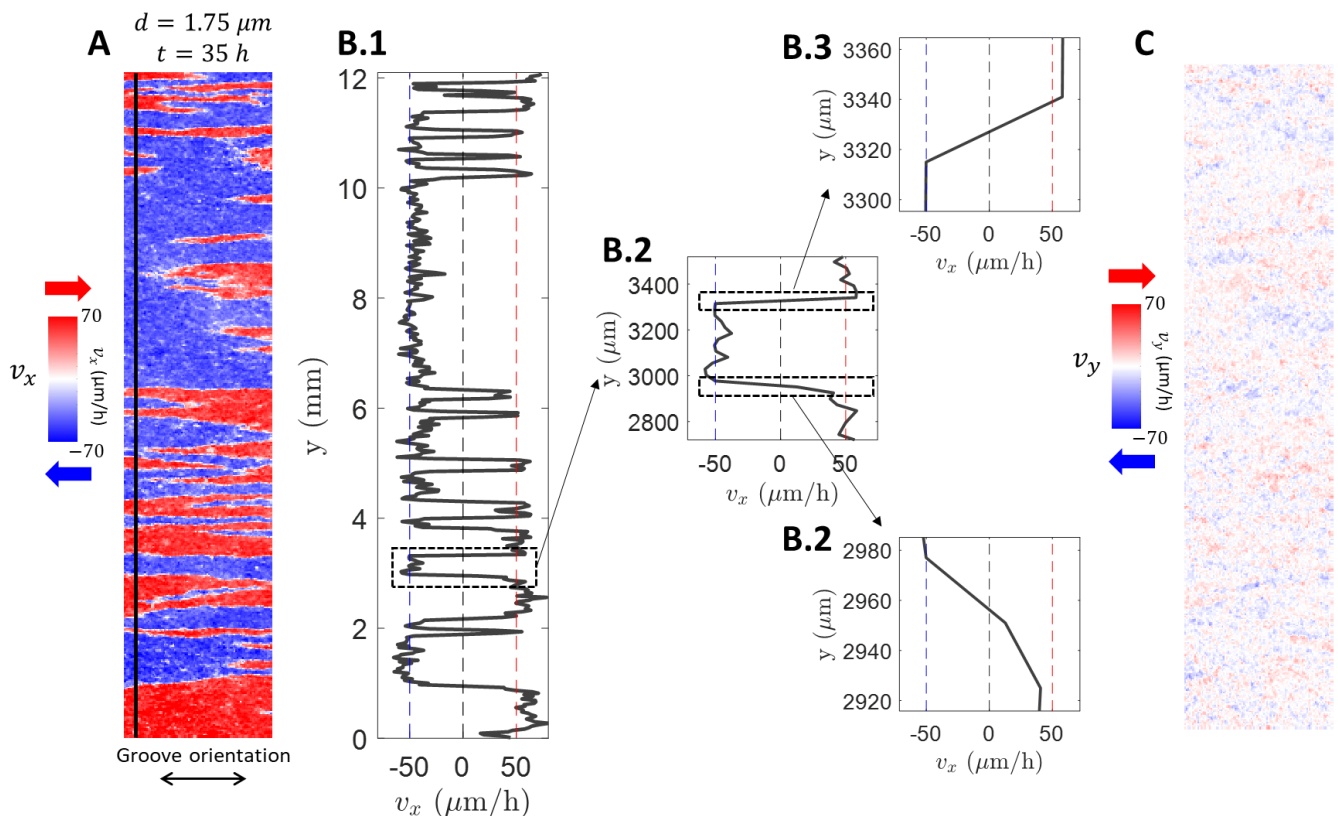


Figure 3.6 : A laning pattern is observed in HBEC monolayers on grooved substrates.

A: Representative v_x laning pattern 35 h after seeding cells on $1.75\ \mu\text{m}$ deep grooves. The FOV is $12\ \text{mm} \times 2.7\ \text{mm}$. Double-headed arrow shows the groove orientation.

B.1: x velocity profile along y corresponds to a non-periodic square signal. The profile shown is a representative profile along the black line in the FOV displayed in A. B.2: Zoom in the v_x profile, corresponding to the dashed box in B.1. In a lane, the velocity profile is flat which corresponds to a plug flow. B.3, B.4: Zooms in the v_x profile in regions between two lanes, corresponding to the dashed boxes in B.2. Between two lanes, velocity changes sign sharply in less than $50\ \mu\text{m}$ (two cell sizes).

C: Corresponding v_y 35 h after seeding cells on $1.75\ \mu\text{m}$ deep grooves shows restricted movements across the grooves.

3. Collective contact guidance drives polar laning of chaotic epithelial cells

If we analyze the system evolution with time, we find that HBECs are initially more disorganized compared to the laning state that we observe 35 hours after cell seeding. The lanes coarsen with time reaching lengths of several millimeters and widths of several hundred micrometers (Figure 3.7.A). To our knowledge, such scales have never been reported before in collective migration in confluent monolayers. Conversely, on flat PDMS substrates, HBECs experience a chaotic dynamics with a velocity correlation length of the order of $100\ \mu\text{m}$ ^{16,52} (Figure 3.7.B). On both substrates, the velocity decreases with time and monolayers completely freeze between 50 to 60 hours post cell seeding.

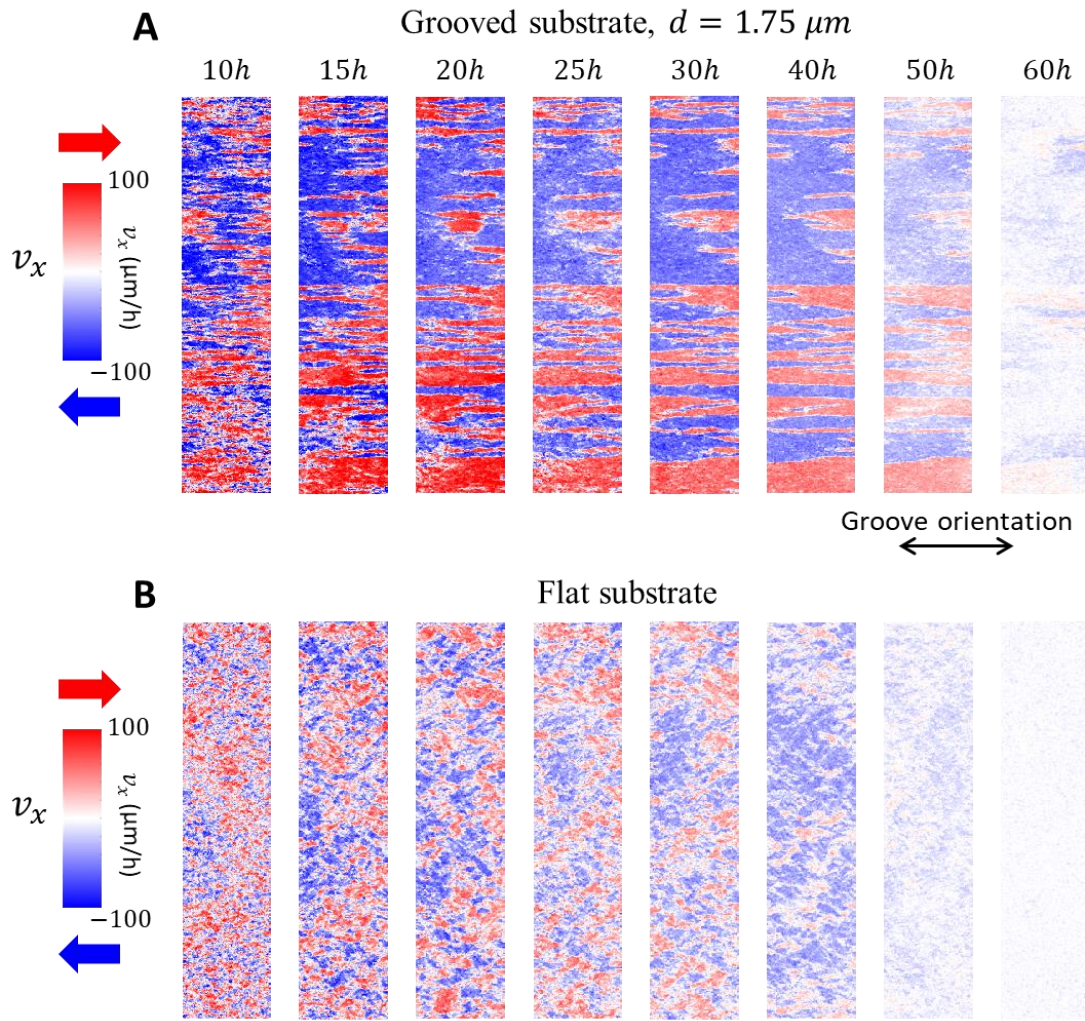


Figure 3.7 : HBEC monolayers develop a stable laning pattern on $1.75\ \mu\text{m}$ deep grooves while they experience chaotic dynamics on a flat substrate. Time evolution of v_x is displayed respectively for a HBEC monolayer on a grooved PDMS substrate (A) and on a flat PDMS substrate (B). The double-headed arrow indicates groove orientation in A. Grooves and ridges are $4\ \mu\text{m}$ wide and grooves are $1.75\ \mu\text{m}$ deep. Representative FOVs are $12\ \text{mm} \times 2.7\ \text{mm}$. Time is indicated in hours after cell seeding. Note that the systems jam after 60 hours post cell seeding: the root mean square velocity decreases over time and reaches, 60 hours after cell seeding, in average value around $10\ \mu\text{m}/\text{h}$.

Interestingly, by normalizing the x component of the velocity v_x by the root mean square velocity $v_{rms} = \sqrt{\langle v_x^2 + v_y^2 \rangle}$, we find that the laning pattern is initially not impaired by the velocity decay but is lost once the system completely freezes (Figure 3.8). In the following, analyses focus on monolayer evolution from 10 to 40 hours post cell seeding, when cells are still highly motile.

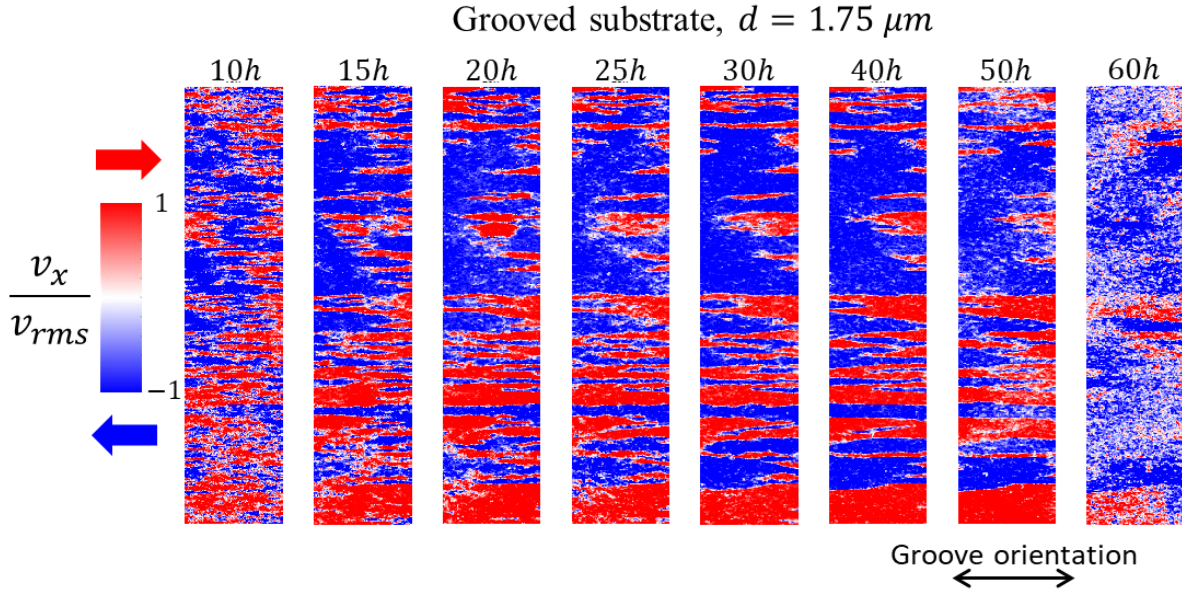


Figure 3.8 : Time evolution of v_x normalized by v_{rms} is displayed for a HBEC monolayer on a grooved PDMS substrate. The double-headed arrow indicates groove orientation. Grooves and ridges are $4 \mu\text{m}$ wide and grooves are $1.75 \mu\text{m}$ deep. Representative FOVs are $12 \text{ mm} \times 2.7 \text{ mm}$. Time is indicated in hours after cell seeding. The laning pattern is lost when the system freezes, after 60 hours post cell seeding.

3.2.1.2. The transition from chaotic dynamics to laning is mediated by groove depth and is characterized by large x correlation length

To investigate the laning transition, HBEC monolayer dynamics is analyzed for different groove depths between 0 and $2.5 \mu\text{m}$. For all depths, the root mean square velocity $v_{rms} = \sqrt{\langle v_x^2 + v_y^2 \rangle}$ decreases with time similarly (Figure 3.9.A). 35 hours after cell seeding, the velocity amplitude difference between flat and grooved substrates is less than $10 \mu\text{m}/\text{h}$ for all depths (Figure 3.9.B).

Grooves are subcellular cues that tend to guide cell migration. To quantify the degree of cell migration guidance by grooves, we define an apolar order parameter for the velocity orientation $S = \langle \cos(2\theta) \rangle_{FOV}$, where θ is the velocity angle with the x axis (i.e., with the groove orientation). $S = 0$ if velocity vectors are randomly oriented in the FOV whereas $S = 1$ (respectively $S = -1$) is reached when velocity vectors are aligned with the grooves (respectively perpendicular to the grooves). In our experiments on flat substrates, S takes values around zero. Conversely for grooved substrates with groove depth $1.75 \mu\text{m}$, S is larger than 0 and increases with time until it reaches a plateau around 0.9 (Figure 3.9.C). A similar behavior is also observed for grooves with depth between 0.45 and $2.5 \mu\text{m}$. S plateau value increases with groove depth until a value around 0.9 (Figure 3.9.D). Thus, cell migration orientation is randomly distributed on flat substrates and is increasingly biased along the grooves as groove depth increases. Moreover, this guidance effect is enhanced with time for grooves deeper than $0.45 \mu\text{m}$, suggesting that the guidance is enhanced by the development of collective behaviors for deep enough grooves.

3. Collective contact guidance drives polar laning of chaotic epithelial cells

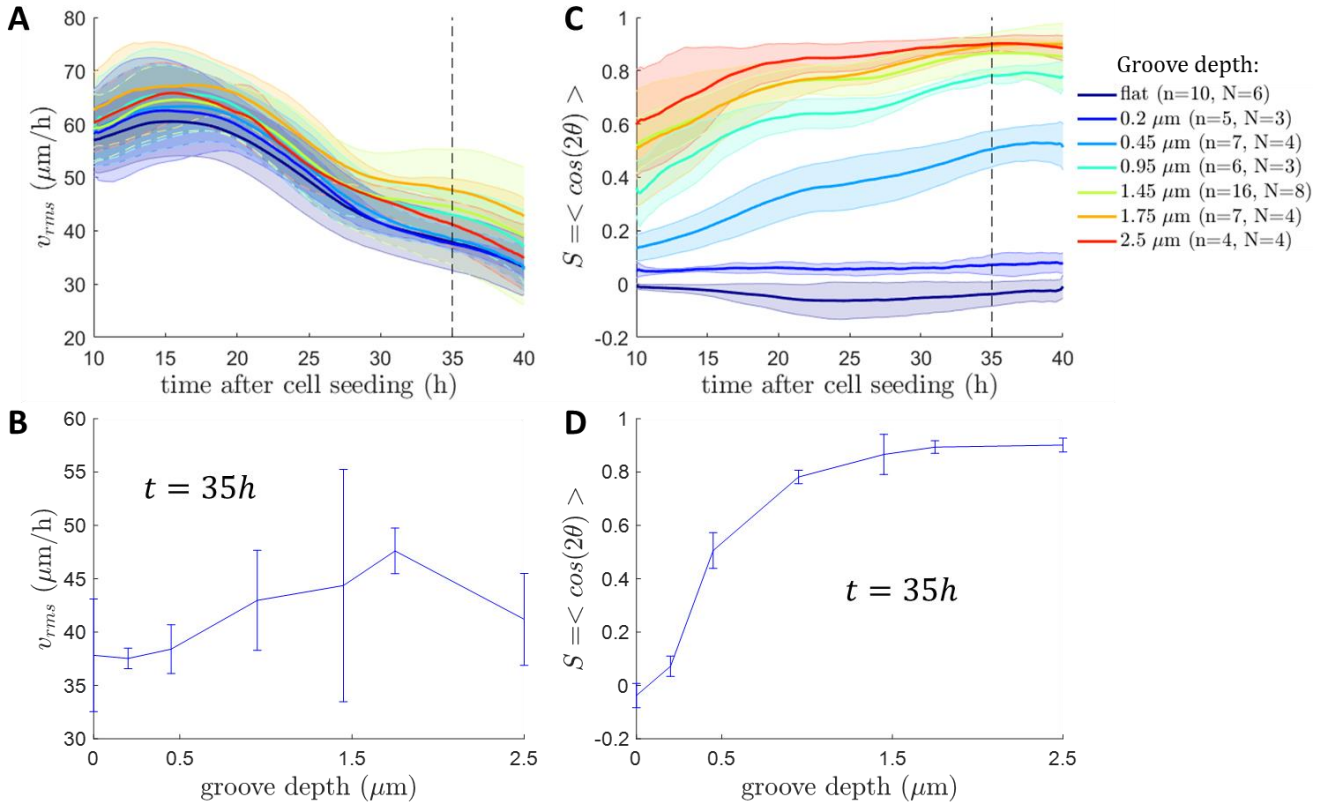


Figure 3.9: Increasing groove depth has low impact on cell velocity (A, B) but enhances cell guidance by the grooves (C, D).

A: v_{rms} evolution with time for different groove depths.

B: v_{rms} evolution with groove depth 35h after cell seeding (dashed line in A).

C: Apolar order parameter $S = \langle \cos(2\theta) \rangle$ evolution with time for different groove depths.

D: S evolution with groove depth 35h after cell seeding (dashed line in C).

A, C: The color codes for groove depth. For each groove depth, n is the number of FOVs analyzed (one FOV corresponds to one experimental well), and N is the number of independent experiments. Shaded areas correspond to the standard deviation to the mean. B, D: Error bars correspond to the standard deviation to the mean.

The effect of grooves on cell dynamics can be further investigated by analyzing the bivariate histograms of v_x and v_y in HBEC monolayers 35 hours after cell seeding for increasing groove depths. On flat substrate, the distribution of (v_x, v_y) is a ring and corresponds to the distribution of randomly oriented vectors of approximately constant norms. As groove depth increases, (v_x, v_y) adopts a bimodal distribution with two well-defined peaks at symmetrical values on the x axis (Figure 3.10.A). The average value of $\sqrt{v_x^2}$ increases with groove depth up to $1.75 \mu\text{m}$ (Figure 3.10.B). On the other hand, v_y fluctuations around zero $\sqrt{v_y^2}$ decrease as groove depth increases (Figure 3.10.A, C). Thus, the increased cell guidance on deeper grooves results from both a higher value of $\sqrt{v_x^2}$ and a lower value of $\sqrt{v_y^2}$.

The spatial structure of the velocity field shows a transition from a chaotic toward a laning state as groove depth increases (Figure 3.11). As mentioned before, v_x amplitude increases whereas v_y amplitude decreases with groove depth. More strikingly, the domains sharing the same velocity get longer until taking

the shape of well-defined straight lanes migrating in antiparallel direction. This laning pattern is characterized by large scale correlations of v_x in the x direction (larger than the width of the FOV).

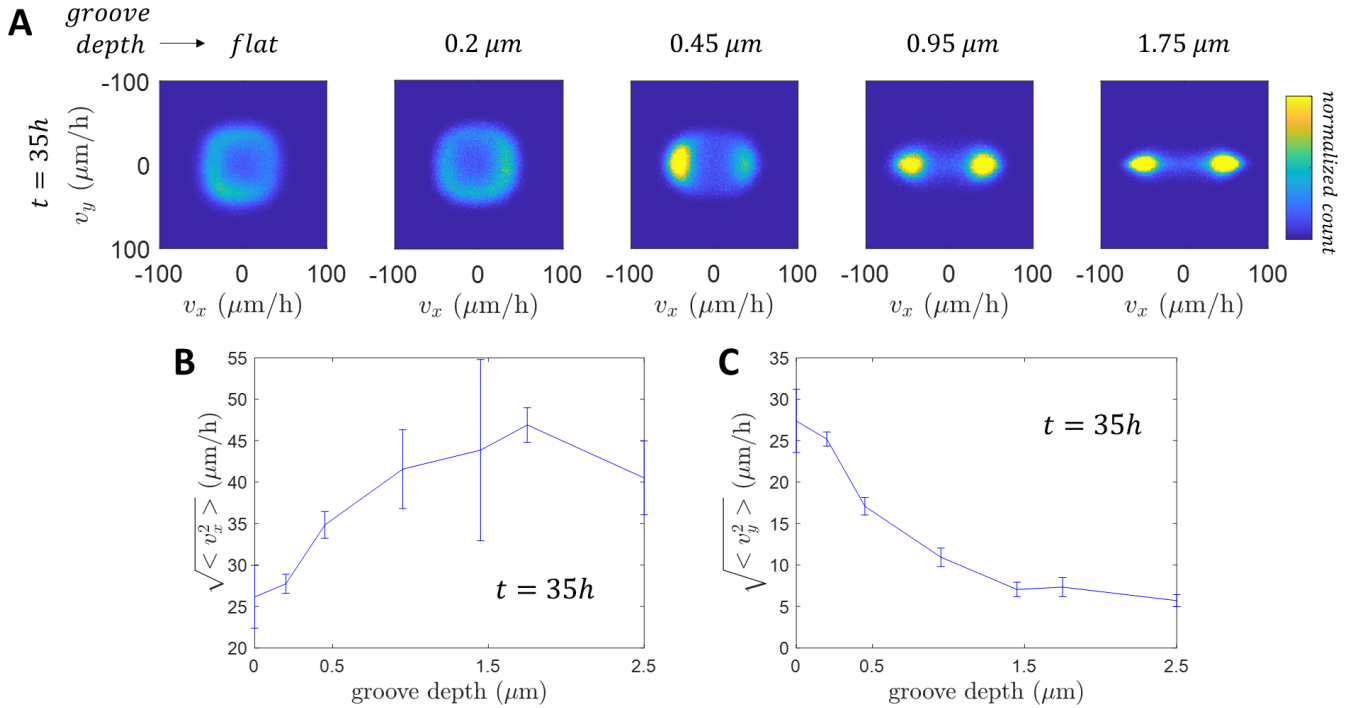


Figure 3.10 : Increasing groove depth leads to a bimodal distribution of v_x and reduces the fluctuations of v_y around zero.

A: bivariate histograms of (v_x, v_y) 35 hours after cell seeding for different groove depths. The data from all the analyzed FOVs are combined. Note that some histograms are not symmetrical. This is because in some FOVs, zones in which cells migrate in one direction are larger than zones migrating in the opposite direction. This might be due to initial cell seeding inhomogeneity in the experimental well, impossible to control. This asymmetry is not intrinsic to the system and is expected to disappear if the experiments were performed in a larger number of replicates.

B, C: $\sqrt{\langle v_x^2 \rangle}$ increases (B) while $\sqrt{\langle v_y^2 \rangle}$ decreases with groove depth (C) 35 hours after cell seeding. Error bars correspond to standard deviation to the mean over $n=10, 5, 7, 6, 16, 7, 4$ FOVs analyzed respectively for groove depth equal to 0, 0.2, 0.45, 0.95, 1.45, 1.75, 2.5 μm .

To quantify the emergence of laning with time and groove depth, we measure for each FOV the x velocity correlation function in the groove direction (x axis) defined by:

$$C_x(t, dx) = \frac{\langle v_x(t, \mathbf{r})v_x(t, \mathbf{r} + dx) \rangle_{\mathbf{r}}}{\langle v_x(t, \mathbf{r})^2 \rangle_{\mathbf{r}}} \quad (3.1)$$

At a given time point after cell seeding, C_x decreases with dx . This effect is observed for all groove depths but is stronger for shallower grooves (Figure 3.12.A). This correlation function is well fitted by a decreasing exponential $C_x(t, dx) \sim C_0 e^{-dx/L_x(t)} + offset$, where $L_x(t)$ corresponds to the x correlation length of v_x at time t . Note that on deep grooves, the lanes are typically longer than the FOV width (~ 3 mm) and thus have a length comparable to the system size (13 mm). With that in mind, $L_x(t)$ that quantifies the x correlation decay should have the same evolution than lane length but may be underestimated when the laning pattern is well established on deep grooves. Also note that the first points of the correlation function decay rapidly because of local v_x fluctuations and thus data corresponding to $dx \leq 52$ μm are excluded from the analysis.

3. Collective contact guidance drives polar laning of chaotic epithelial cells

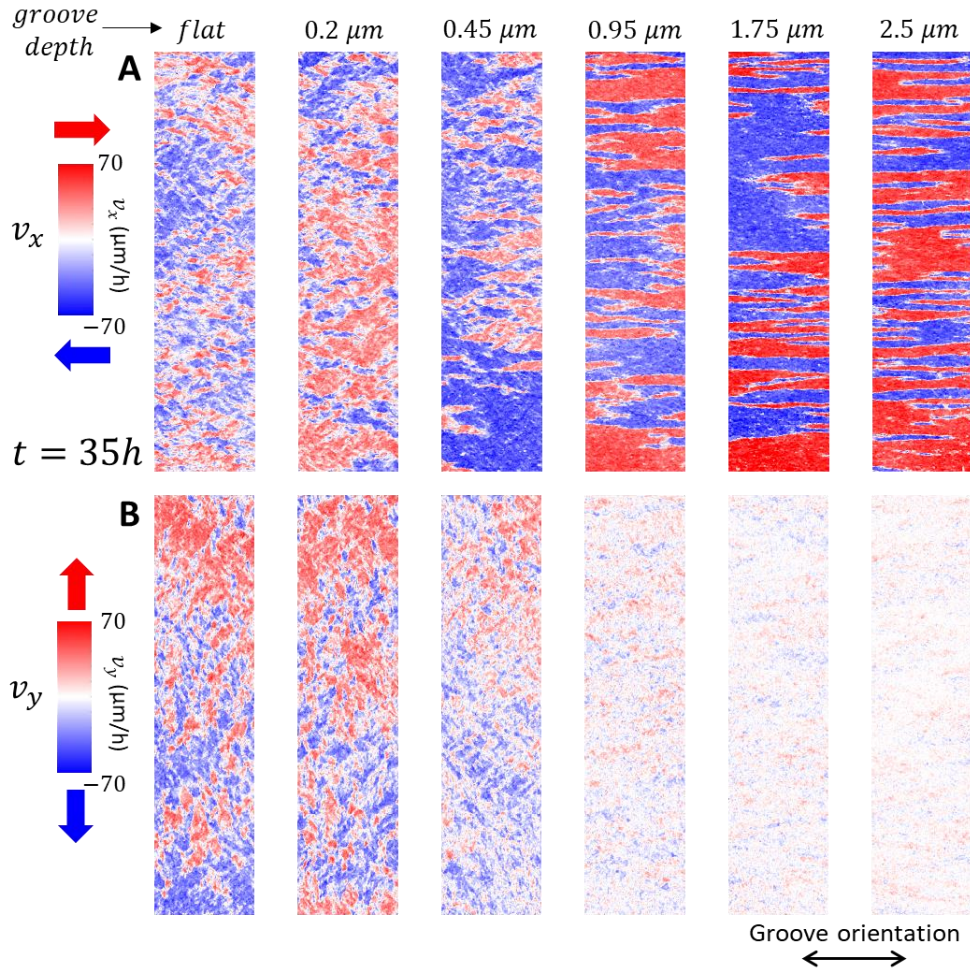


Figure 3.11 : The transition from turbulence to laning is mediated by groove depth. v_x (A) and v_y (B) are displayed for HBEC monolayers on PDMS grooved substrates 35 hours after cell seeding. From left to right, groove depth increases from 0 to 2.5 μm . The double-headed arrow indicates groove orientation. FOVs are 12 mm X 2.7 mm.

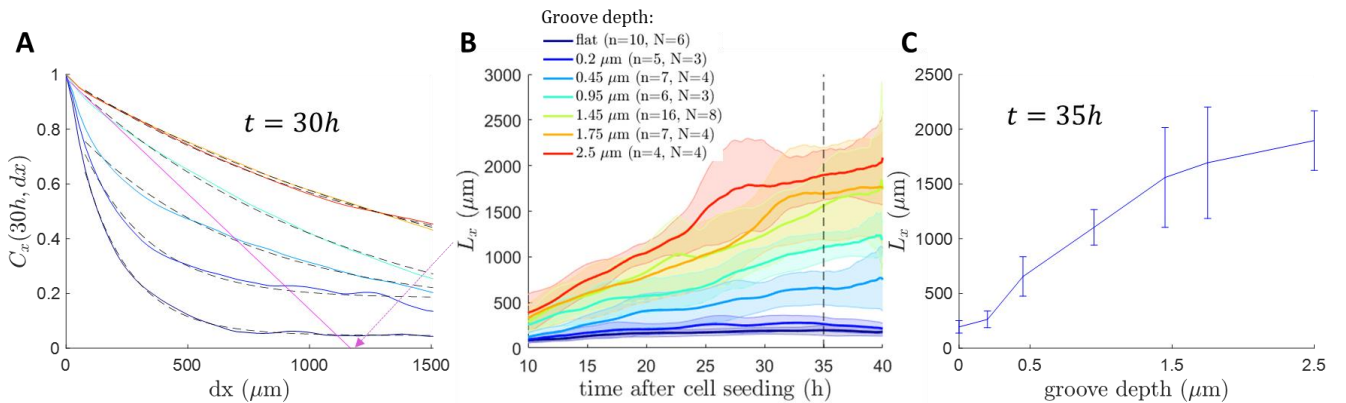


Figure 3.12 : Long-range correlation along x characterizing a laning pattern increases with groove depth.

A: v_x correlation functions along x for 6 different FOVs with different groove depths 30 hours after cell seeding are fitted by decreasing exponentials, which define the x correlation length L_x .

B: x correlation length evolution with time for different groove depths. The color codes for groove depth. For each groove depth, n is the number of FOVs analyzed (one FOV corresponds to one experimental well), and N is the number of independent experiments. Shaded areas correspond to the standard deviation to the mean.

C: x correlation length evolution with groove depth 35 hours after cell seeding (dashed line in B). Error bars correspond to standard deviation to the mean.

For grooves deeper than $0.45 \mu\text{m}$, the x correlation length $L_x(t)$ increases significantly with time (Figure 3.12.B) because the laning pattern organizes with time (Figure 3.7.A). Moreover, $L_x(t)$ increases continuously as groove depth increases (Figure 3.12.C). For deeper grooves, 35 hours after cell seeding, $L_x(t)$ reaches $1900 \pm 300 \mu\text{m}$ which corresponds to a 10-fold increase compared to the value on a flat substrate ($200 \pm 60 \mu\text{m}$). Thus, the transition from a chaotic toward a laning state is characterized by a progressive increase of the x correlation length and is mediated by groove depth. Therefore, in the following, we use the x correlation length as a descriptor of the laning transition: a x correlation length L_x that increases with time toward values significantly higher than $200 \mu\text{m}$ (value on flat substrates) indicates the emergence of a laning pattern.

3.2.1.3. Lanes' spatial positions are stable in time

It is also interesting to analyze the time correlation function defined as:

$$C_t(t, dt) = \frac{\langle v_x(\mathbf{r}, t)v_x(\mathbf{r}, t + dt) \rangle_{\mathbf{r}}}{\langle v_x(\mathbf{r}, t)^2 \rangle_{\mathbf{r}}} \quad (3.2)$$

For monolayers on $1.75 \mu\text{m}$ deep grooves, the time correlation increases with time. 10 hours after cell seeding, the time correlation decays sharply with dt and reaches value lower than 0.4 for $dt = 5h$. After 20 hours post cell seeding, the time correlation is higher than 0.4 up to $dt = 18h$ (Figure 3.13.A). It means that once established, lanes' positions are stable in time. Moreover, 20 hours after cell seeding, time correlation increases as groove depth increases (Figure 3.13.B). For deep enough grooves, the monolayer that is initially disorganized progressively organizes into a stable laning state, and the stability of the laning pattern with time increases as groove depth increases.

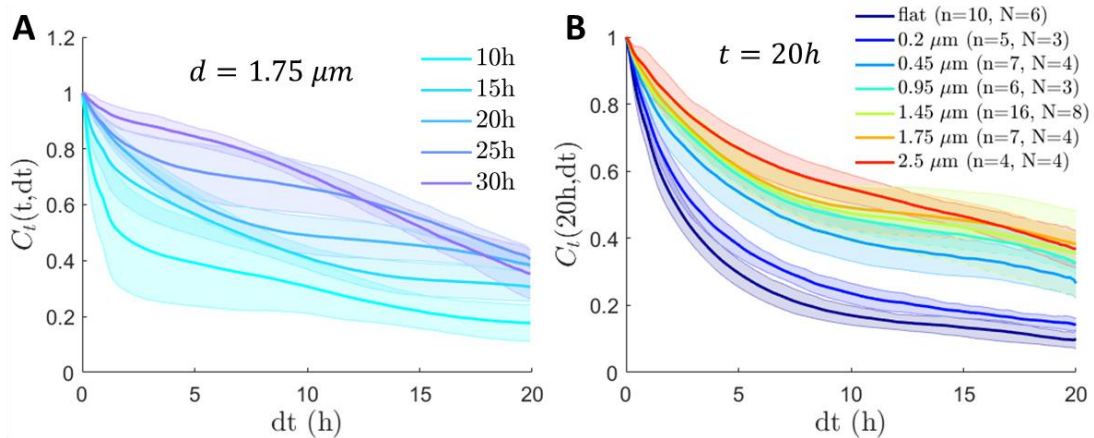


Figure 3.13 : Once established, lanes are stable in time, and this effect is stronger for deeper grooves.

A: Time correlation of HBEC monolayers on $1.75 \mu\text{m}$ deep grooves increases with time. The color codes for the time t in hours after cell seeding. Shaded areas correspond to the standard deviation to the mean over $n=7$ FOVs from $N=4$ independent experiments.

B: Time correlation of HBECs monolayers 20 hours after cell seeding increases with groove depth. The color codes for groove depth. For each groove depth, n is the number of analyzed FOVs (one FOV corresponds to one experimental well), and N is the number of independent experiments. Shaded areas correspond to the standard deviation to the mean.

3. Collective contact guidance drives polar laning of chaotic epithelial cells

3.2.1.4. The laning pattern is non-periodic and is characterized by an increase in y coordination

As mentioned before, the v_x velocity profile along y is a non-periodic rectangular signal alternating between $+v$ and $-v$ (Figure 3.14.B). Between two adjacent lanes, the velocity changes sign in a discontinuous manner. Strikingly, the laning pattern is non-periodic. When repeating several times the experiment in the same conditions, the obtained patterns are heterogeneous among the repeats (Figure 3.14.A). Nevertheless, we can measure an average lane width for each FOV by averaging lane widths obtained by extracting zero crossing positions from 11 velocity profiles in each FOV (Figure 3.14.B).

The average lane width increases with time and is significantly larger on grooves deeper than $0.45 \mu\text{m}$ compared to flat substrates (Figure 3.15). Thus, compared to a flat substrate, the laning pattern on deep enough grooves is characterized by a larger coordination in the y direction (Figure 3.15.B). However, no relationship is found between groove depth and the average lane width for $d > 0.45 \mu\text{m}$.

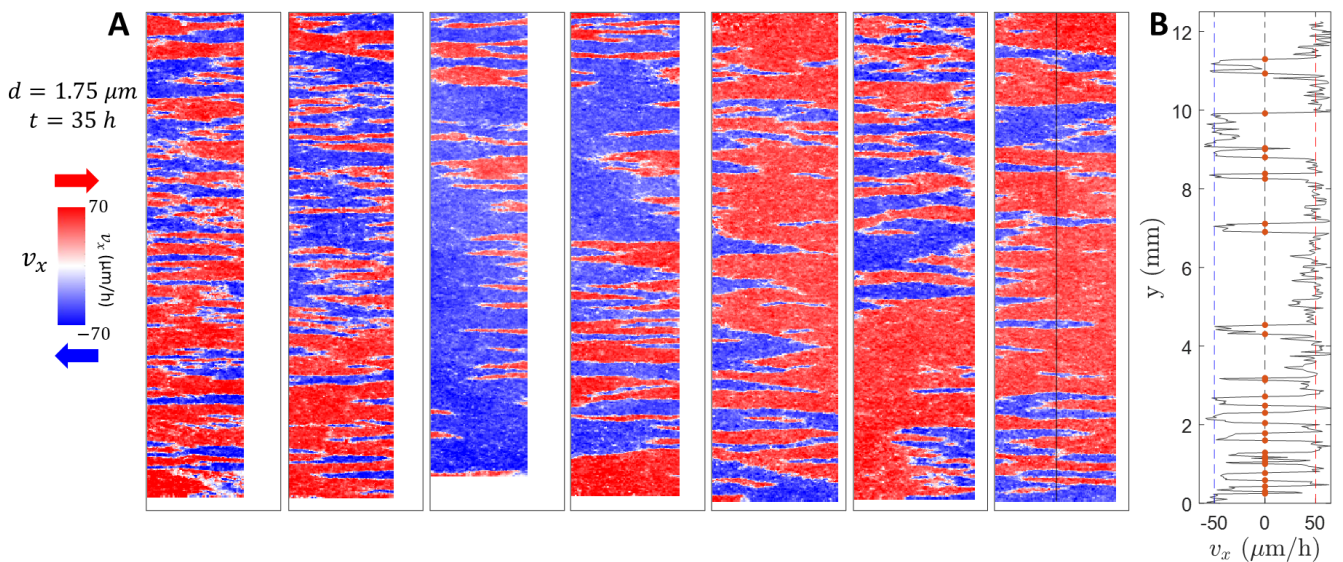


Figure 3.14 : The laning pattern is a non-periodic pattern made of alternating plug flows in opposite directions.

A: v_x laning patterns acquired for 7 different FOVs show the diversity of the laning patterns obtained in the same experimental conditions. v_x is displayed 35h after cell seeding on $1.75 \mu\text{m}$ deep grooves for $n=7$ different repeats of the experiment. Rectangles around the FOVs are $3.4 \times 12.5 \text{ mm}$.

B: x velocity profile along y corresponds to a non-periodic rectangular signal. The profile shown is a representative profile corresponding to the middle black line of the last FOV displayed in A. Orange dots show the zero crossing of v_x profile and are used to measure lane widths.

Lane widths distribution is heterogeneous among different FOVs but also in each FOV (Figure 3.14). For a given groove depth, we characterize lane width heterogeneity by analyzing the width distribution from 11 velocity profiles in each FOV (the number of velocity profiles analyzed is $11 \cdot n$ where n is the number of FOVs analyzed for a given groove depth). We define the probability for a lane to be larger than w by:

$$\tilde{p}(w) = \frac{\#\text{lanes larger than } w}{\#\text{lanes}}$$

$\tilde{p}(w)$ is a continuous function of w , normalized to 1. It is thus more practical than $p(w)$, the probability of a lane to have a width between $w - dw$ and $w + dw$, which is a discrete function whose values depend on the bin size dw chosen.

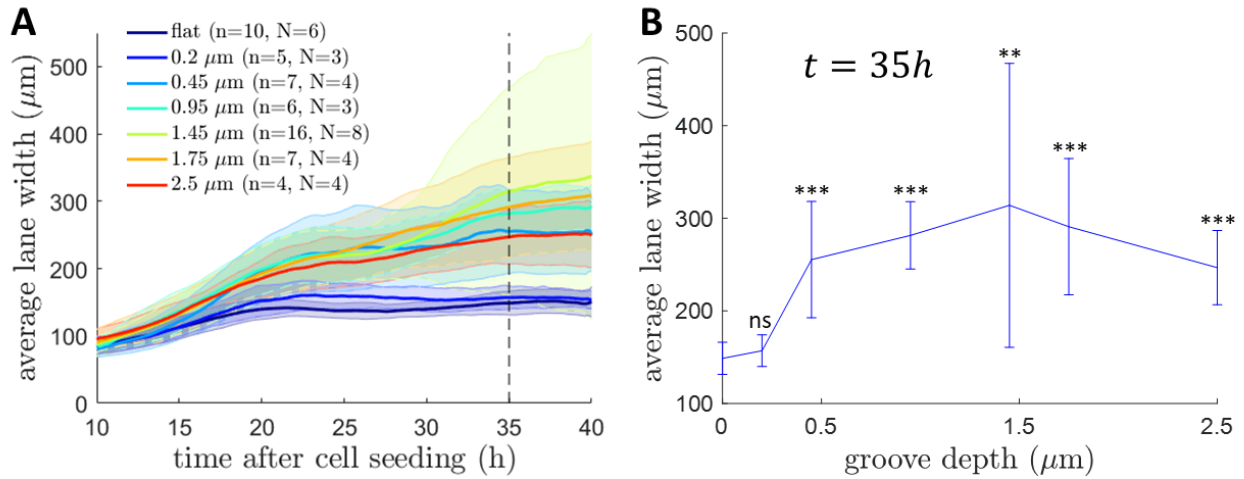


Figure 3.15 : Average lane width increases with time and is higher on deep enough grooves compared to flat substrates.

A: Average lane width evolution with time for different groove depths. The color codes for groove depth. For each groove depth, n is the number of FOVs analyzed (one FOV corresponds to one experimental well), and N is the number of independent experiments.

Shaded areas correspond to the standard deviation to the mean over the repeats.

B: Evolution of the average lane width with groove depth 35 hours after cell seeding (dashed line in A). Error bars correspond to standard deviation to the mean. The stars on top of the error bars indicate the p -value of the two-sample t -test against the hypothesis that the mean of average lane widths for flat substrates is less than the mean of average lane widths for the given groove depth. ns: $p > 0.05$; *: $p \leq 0.05$; **: $p \leq 0.01$; ***: $p \leq 0.001$.

First, we analyze the evolution with time of $\tilde{p}(w)$ for monolayers on 1.75 μm deep grooves. Figure 3.16.A displays $\tilde{p}(w)$ for different time points in semi log scale. For all width w , the probability for a lane to be larger than w , $\tilde{p}(w)$, increases with time. This indicates that the lanes coarsen with time. Initially, for $t \leq 20$ h after cell seeding, $\tilde{p}(w)$ is a straight line in semi log scale meaning that $\tilde{p}(w) \sim e^{-\frac{w}{\langle w \rangle}}$. Thus, lane widths are exponentially distributed. At later time points, from $t = 25$ to 40 hours after cell seeding, $\tilde{p}(w)$ presents a similar sharp exponential decay for $w \leq 1000 \mu\text{m}$. For w between 1000 and 3000 μm approximately, $\tilde{p}(w)$ also decreases exponentially, but with a larger length scale of decay that increases with time. This is in good agreement with the fact that $\langle w \rangle$ increases with time through coarsening (Figure 3.15.A). At later time points, for $t = 35$ to 40 hours after cell seeding, lanes larger than 4 mm appear, and $\tilde{p}(w)$ deviates from an exponential decay for $w > 3000 \mu\text{m}$.

Conversely on flat substrates, as time goes on, the distribution $\tilde{p}(w)$ stays exponential for all w ($\tilde{p}(w) \sim e^{-\frac{w}{\langle w \rangle}}$) with an increasing average lane width (Figure 3.16.B). This corresponds to the fact that the velocity correlated domain size increases with time by active jamming.

We now fix $t = 35$ h after cell seeding and analyze the effect of varying groove depth d on $\tilde{p}(w)$. First, we observe that $\tilde{p}(w)$ is similar for flat substrates and 200 nm deep grooves (Figure 3.16.C). For grooves deeper than 0.45 μm , $\tilde{p}(w)$ is larger for all values of w and the slope of $\tilde{p}(w)$ for $w > 1000 \mu\text{m}$ is higher compared to flat substrates. This means that large lanes were more present in proportion on deep enough grooved substrates, which indicates the laning transition for $d \geq 0.45 \mu\text{m}$ (Figure 3.16.C). The initial decay of $\tilde{p}(w)$ is similar for all groove depth meaning that thin lanes that could still coarsen are present at least 35 hours after cell seeding even when laning appears for $d \geq 0.45 \mu\text{m}$.

3. Collective contact guidance drives polar laning of chaotic epithelial cells

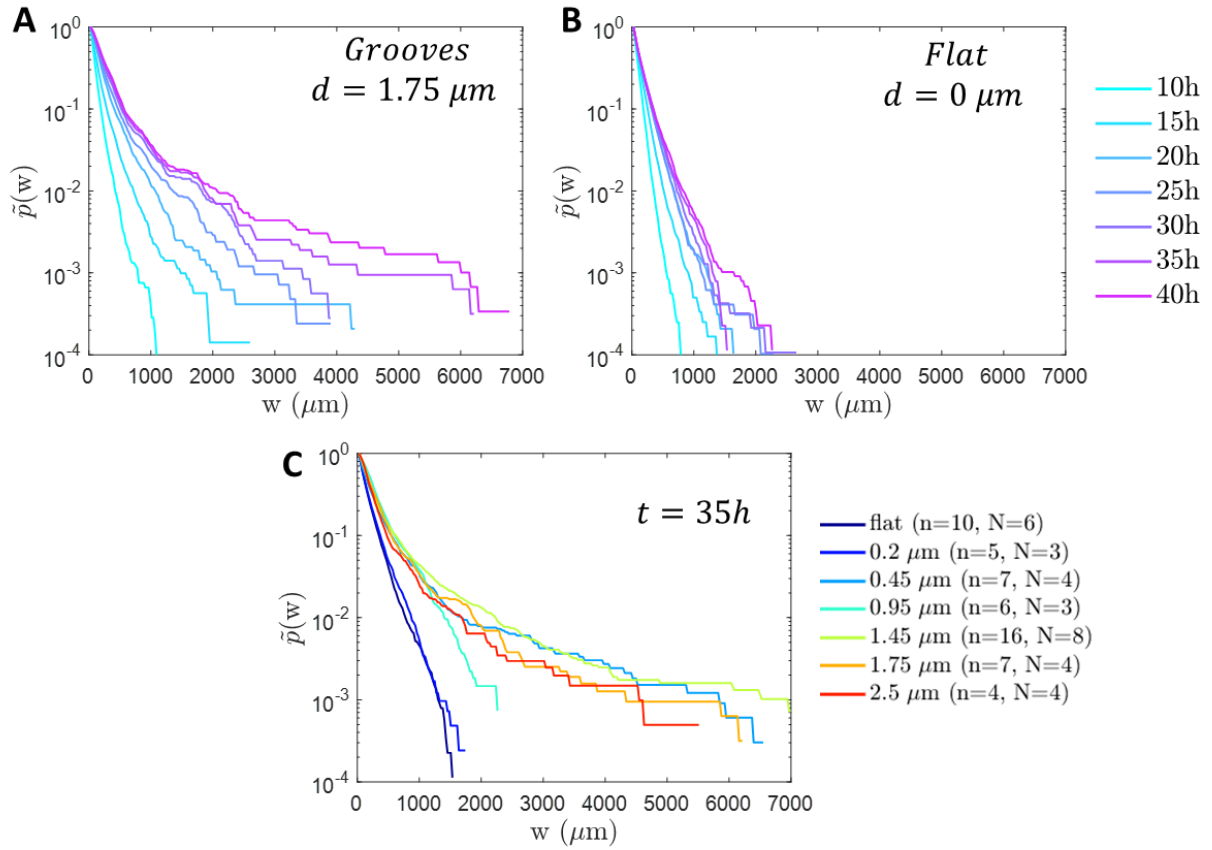


Figure 3.16 : Lane width distribution evolves with time and groove depth.

A: $\tilde{p}(w)$ in semi log scale for monolayers on $1.75 \mu\text{m}$ deep grooves for different time points.

B: $\tilde{p}(w)$ in semi log scale for monolayers on flat PDMS substrates for different time points.

A, B: For each time point, lane widths data set is composed of all widths extracted from 11 v_x profiles in each of the n different experimental wells, $n=7$ and 10 respectively for $1.75 \mu\text{m}$ deep grooves and flat substrates. Color codes for the time point, indicated in hours post cell seeding.

C: $\tilde{p}(w)$ in semi log scale 35 hours after cell seeding for HBEC monolayers on grooves for increasing groove depth. The color codes for groove depth. For each groove depth, lane widths data set is composed of all widths extracted from 11 v_x profiles in each of the n different experimental wells (N is the number of independent experiments).

3.2.1.5. Summary of disorder-to-laning transition characteristics

Cell migration is oriented by grooves, the guidance being more efficient on deeper grooves. The transition from chaotic dynamics towards a laning state is mediated by groove depth. The laning state is characterized by large-scale x and y correlation of the x velocity. The x correlation length L_x and average lane width increase with time. The final pattern is thus the result of a coarsening process of domains sharing the same velocity that merge to form longer and larger domains and ultimately lanes. Once established, lanes' positions are stable in time. Lanes are typically longer than the FOV size and lane widths are exponentially distributed with an over representation of millimeters large lanes. The laning pattern is not periodic and the system does not present an intrinsic length scale for lane width. Strikingly, in a lane, cells migrate at the same velocity in a plug flow and the shear between adjacent lanes is localized between two cell rows.

Increasing the depth of the grooves increases the x correlation length meaning that horizontal lanes of cells migrating in the same direction get longer and straighter for deeper grooves. The laning state is also characterized by a higher y coordination compared to flat substrates.

Note that this laning behavior is also observed for cells plated on a chemical pattern of alternating $4\mu\text{m}$ wide lines of PEG and fibronectin (3 independent experiments) (Figure 3.17). Thus, PDMS topography is not necessary in the laning transition, but a subcellular anisotropy is.

We conclude that substrate anisotropy triggers the transition of HBECs from chaos to laning. To understand the underlying mechanism of HBECs laning, we performed several perturbation experiments and investigated the collective dynamics of other cell types plated on grooves. The results are presented in the next subsections.

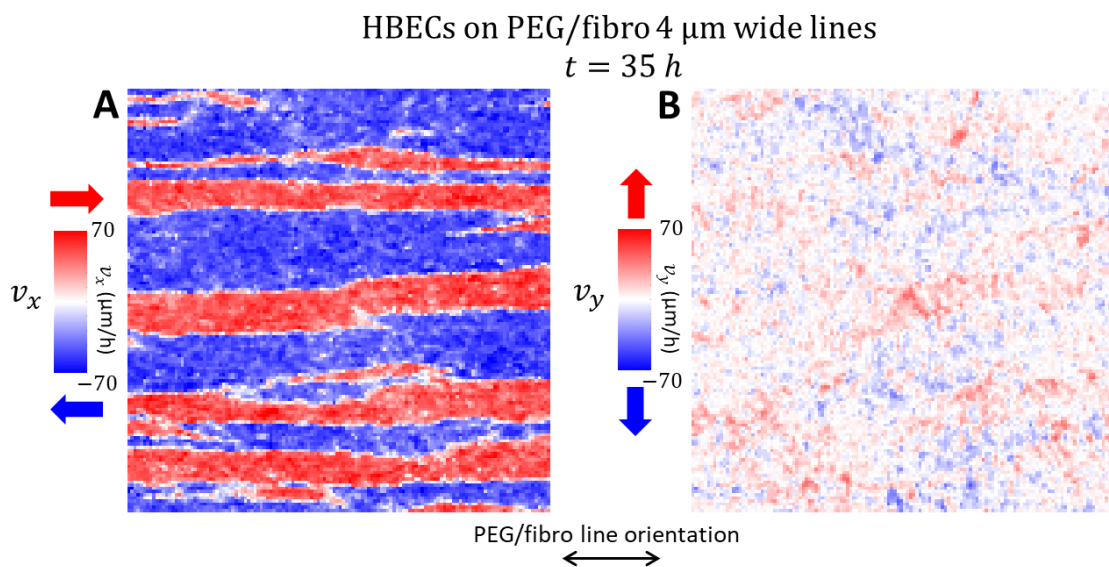


Figure 3.17 : A laning pattern appears in HBEC monolayers seeded on chemically micro-patterned substrates. v_x (A) and v_y (B) are displayed for a HBEC monolayer 35 hours after cell seeding. The FOV is $3.5 \times 3.5\text{ mm}$. The substrate is an alternating of $4\mu\text{m}$ PEG and fibronectin wide lines. The double-headed arrow shows the micro-patterned line orientation.

3.2.2. Laning is independent from cell division and cell-cell adhesion

First, we investigate the role of cell division and cell-cell adhesion in the laning behavior of HBECs on grooved substrates.

Cell division is inhibited using mitomycin C five hours after seeding the cells at high density on $1.45\mu\text{m}$ deep grooves. As the cell density increase is slower (Figure 3.18.A), the system freezes at later times compared to control experiments. However, the velocity decay with or without mitomycin C treatment is similar until 40 hours after cell seeding (Figure 3.18.B). As in control experiments, cells are guided by the grooves and a laning pattern is established. As cells organize in a laning pattern, the guidance (Figure 3.18.C) and the x-correlation length L_x (Figure 3.18.D) increases with time similarly for monolayers with cell division or monolayers treated with mitomycin C. These results show that the transition from a chaotic toward a laning state is not mediated by an increase in cell density.

3. Collective contact guidance drives polar laning of chaotic epithelial cells

However, in sparse population of cells on grooved substrates, cells are guided by the grooves, but cell direction is randomly distributed in the population with no laning pattern. Thus, direct cell-cell contact is important in the laning process that appears in confluent monolayers.

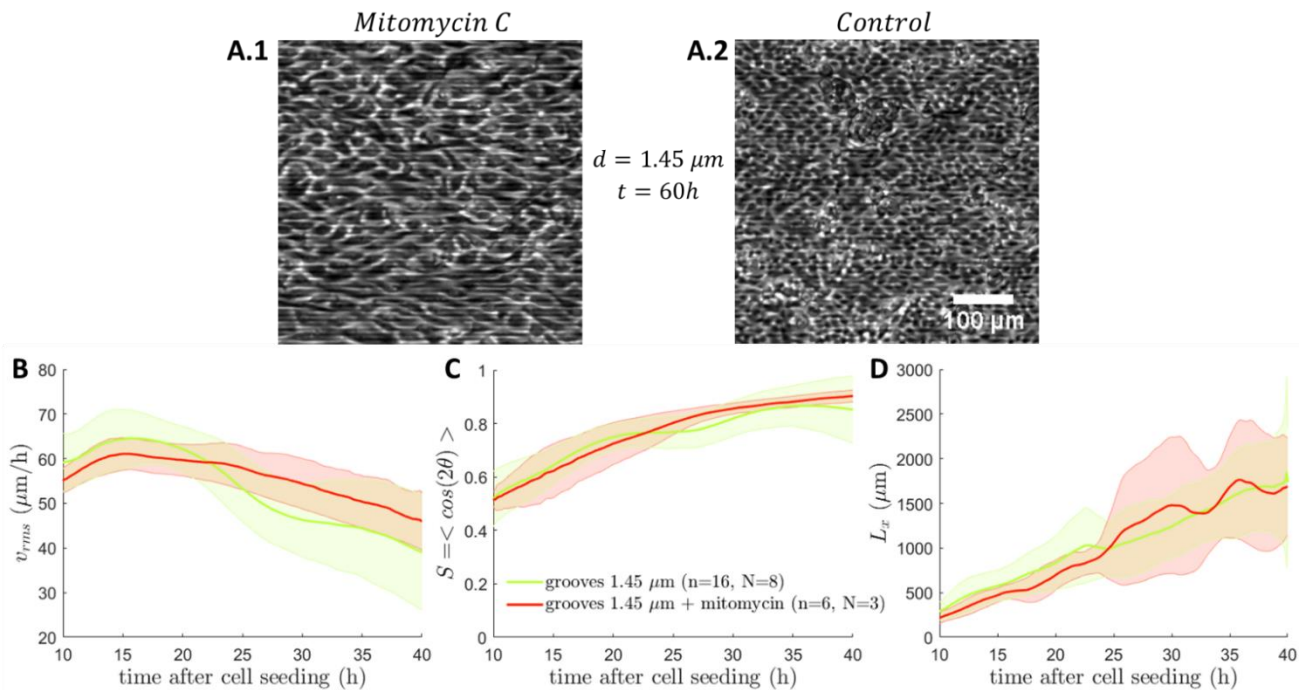


Figure 3.18 : Laning pattern emergence is independent from cell division.

A: Mitomycin C treatment successfully reduces cell division. Indeed, phase contrast images taken 60 hours after cell seeding show that cell density is much lower in mitomycin C treated cells (A.1) compared to control experiments (A.2). Note that A.1 and A.2 share the same scale bar.

B-D: v_{rms} (B), S (C), and the x correlation length L_x (D) have a similar time evolution in monolayers on $1.45 \mu\text{m}$ deep grooves with or without cell division. Cell division was inhibited using mitomycin C. The color codes for the experimental condition. For each condition, n is the number of FOVs analyzed (one FOV corresponds to one experimental well), and N is the number of independent experiments. Shaded areas correspond to the standard deviation to the mean.

We now investigate the role of cell-cell adhesion for laning emergence. Wound healing assays clearly show that HBECs dissociate at the front edge and are therefore not cohesive compared to other cell types such as MDCK (Figure 3.19.A). This suggests that HBECs do not rely on cell-cell adhesion to exhibit collective behavior.

To confirm this conclusion, cells on a micro-grooved substrate were fixed 30 hours after cell seeding and stained for E-cadherin. At that time, the laning pattern is already well established (Figure 3.7.A). However, E-cadherin is mainly localized in the cytoplasm and not at the cell-cell contacts (Figure 3.19.B.1). As a negative control, when the system is frozen three days after cell seeding, E-cadherin clearly localizes at cell-cell junctions (Figure 3.19.B.2).

Moreover, we made E-cadherin knock down (KD) cells in which the E-cadherin expression was reduced by more than 75% (see 2.2.5). These cells also exhibit laning when seeded on grooved substrates (Figure 3.19.C). v_{rms} , S and the x correlation length have a similar time evolution for WT and KD cells (Figure 3.19.D-F) even if v_{rms} remains larger and cell guidance along grooves S is initially lower for KD cells.

Altogether, these results show that the laning pattern emerges independently from E-cadherin cell-cell adhesion.

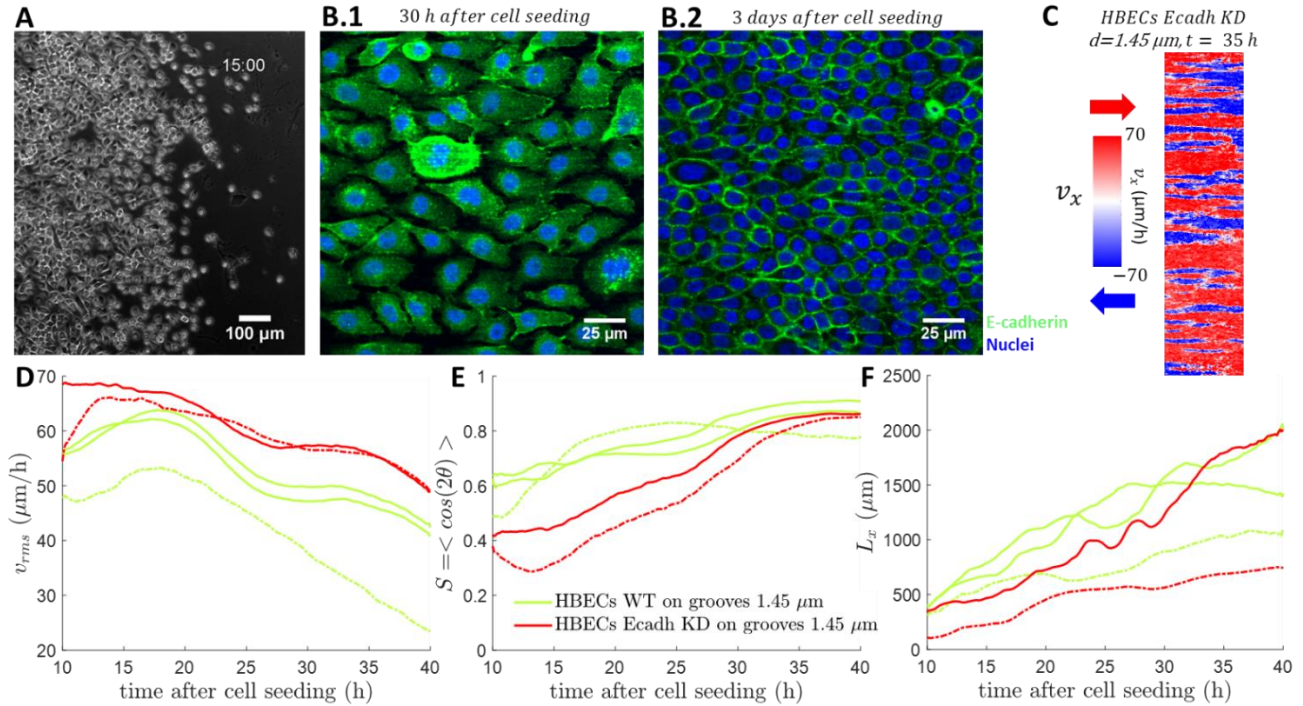


Figure 3.19 : Laning pattern emergence is independent from E-cadherin based cell-cell adhesion.

A: HBECs are not cohesive in the migrating front of a wound healing assay 15 h after removing the barrier.

B: E-cadherin immunostaining of HBEC confluent monolayers on a grooved substrate shows that E-cadherin is mainly cytoplasmic 30h after cell seeding during laning (B.1), whereas E-cadherin is localized at well-defined cell-cell junctions 3 days after cell seeding when the system is frozen (B.2). Also note the increase in cell density.

C: Representative v_x laning pattern 35h after seeding HBECs E-cadherin KD on 1.45 μm deep grooves. FOV is 12 X 2.7 mm.

D, E, F: v_{rms} (D), S (E), and the x correlation length L_x (F) have a similar time evolution in monolayers on 1.45 μm deep grooves with or without E-cadherin KD. The color codes for the experimental condition. The line style distinguishes the two independent experiments that were performed.

3.2.3. Laning relies on cell protrusions rather than cell contractility

To further investigate the mechanism underlying laning in HBEC monolayers on grooved substrates, we tested the role of cell contractility and cell protrusions. We first perturb the system with para-nitroblebbistatin, an inhibitor of myosin II. This drug is known to reduce cell contractility as myosin II is the molecular motor responsible for actin stress fiber contraction. Thus, increasing concentration of para-nitroblebbistatin reduces cell velocity (Figure 3.20.B). This effect of the drug is very clear at least from the beginning of the experiment 10 hours after cell seeding to 30 hours after cell seeding. However, increasing concentration of para-nitroblebbistatin does not impair dramatically neither cell guidance by the grooves (Figure 3.20.C) nor the emergence of collective laning (Figure 3.20.A, D). Indeed, the x correlation length L_x increases with time similarly from the beginning of the experiment and for all concentrations in the range 0 to 10 μM (Figure 3.20.D). We then conclude that contractility is not crucial for laning.

As cell contractility is not crucial for laning, we hypothesize that the ability of cells to form directed protrusions such as lamellipodia is. Indeed, to actively self-propel in the direction of their intrinsic polarity, cells must break symmetry to develop a migrating front characterized by protrusions such as lamellipodia. These structures are characterized by a branched actin network. The integration of newly formed actin

3. Collective contact guidance drives polar laning of chaotic epithelial cells

filaments in this actin network is mediated by the Arp2/3 complex. To decrease lamellipodial protrusions, we perturb the system with CK666, an inhibitor of Arp2/3, at concentrations ranging from 0 to 100 μM . The root mean square velocity decreases as CK666 concentration is increased (Figure 3.21.B, E). Cell guidance by the grooves is also reduced significantly by Arp 2/3 inhibition but cells are still strongly guided by the grooves as S remains larger than 0.5 for all CK666 concentrations (Figure 3.21.C, F). However, the ability of cells to exhibit laning is progressively lost as CK666 concentration increases (Figure 3.21.A). Indeed, the x correlation length decreases significantly when CK666 concentration increases until reaching values lower than 200 μm for concentrations larger than 75 μM (Figure 3.21.D, G). These results support the fact that the ability of cells to form protrusions such as lamellipodia in the direction of their intrinsic polarization is key for HBECs to exhibit collective behaviors and in particular laning on micro-grooved substrates.

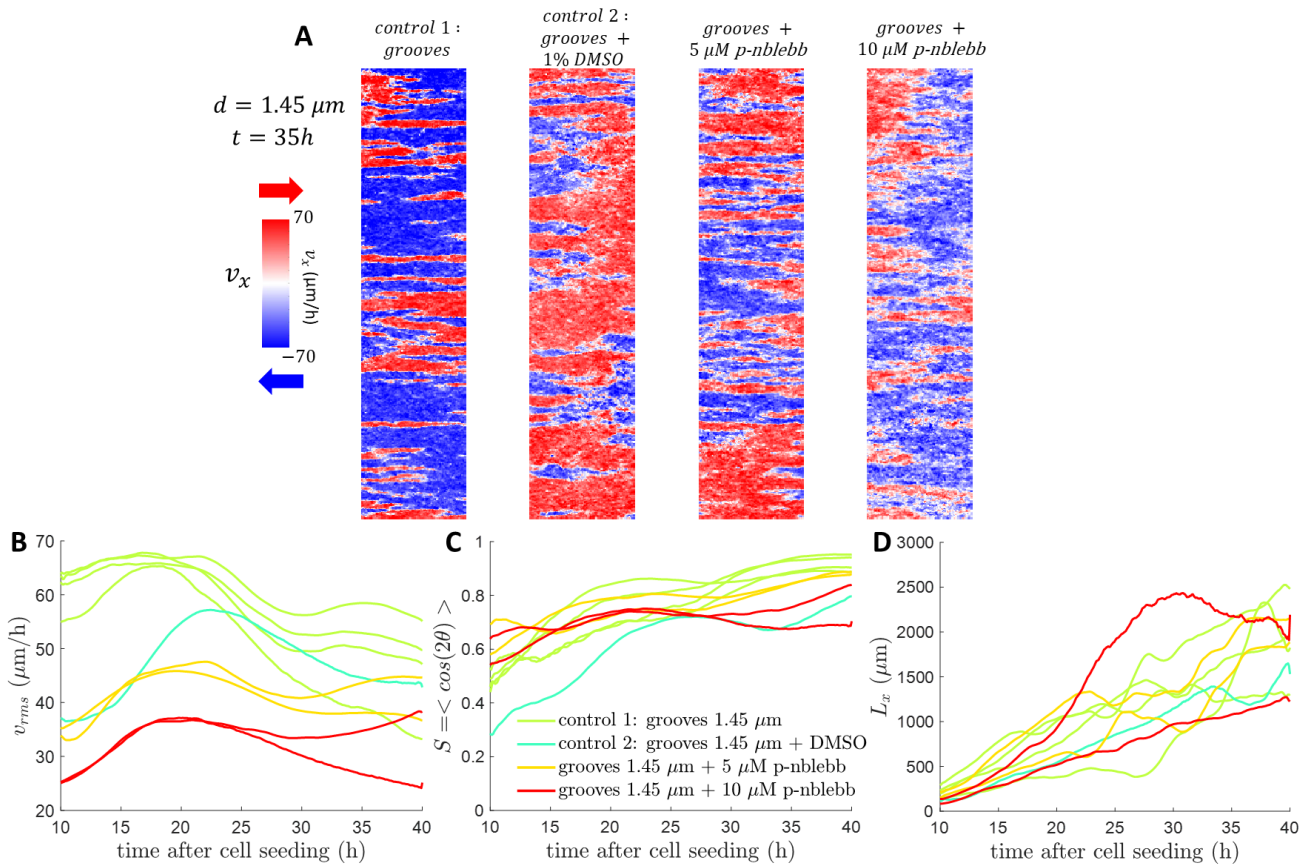


Figure 3.20 : Laning pattern emergence is independent from cell contractility.

A: A laning pattern in the x velocity component is observed 35 hours after cell seeding even when cell contractility is impaired by inhibiting myosin II with para-nitroblebbistatin. FOVs size is 11.6 mm X 2.7 mm. Myosin II inhibition leads to a decrease of v_{rms} (*B*) but does not prevent cell guidance by the grooves (*C*) and does not impair the emergence of a laning pattern, as the x correlation length (*D*) have a similar time evolution in monolayers on 1.45 μm deep grooves with or without para-nitroblebbistatin. The color codes for the experimental condition. The impact of 5 μM and 10 μM para-nitroblebbistatin has been tested in two independent experiments. Note that 1% DMSO (drug solvent amount used for the highest drug concentration case) reduces the velocity only in the first 10 hours of the experiment and does not prevent the emergence of a laning pattern.

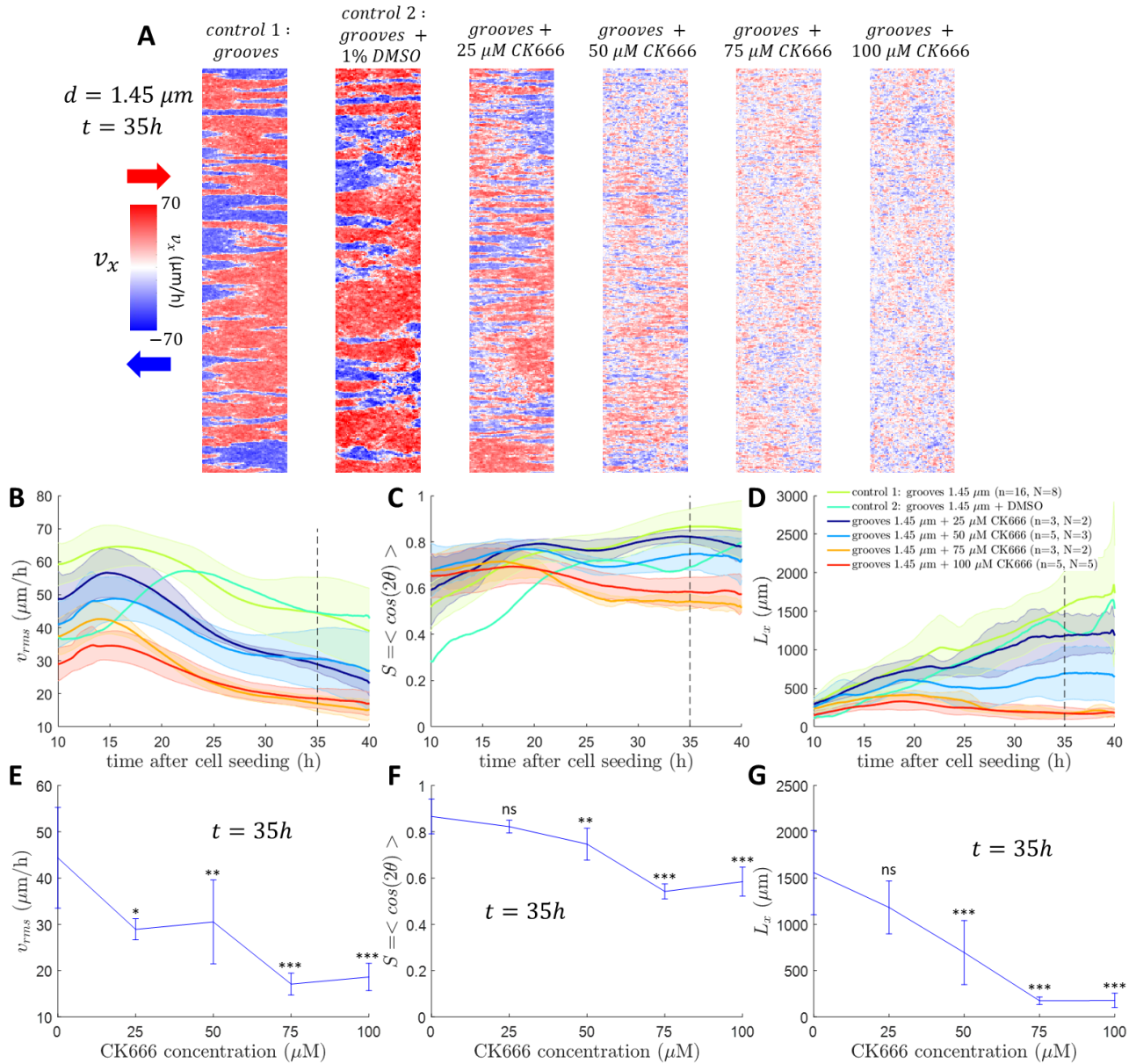


Figure 3.21 : Laning pattern emergence relies on lamellipodia-based migration.

A: The laning pattern observed 35 hours after cell seeding in the x velocity component of HBEC monolayers on 1.45 μm deep grooves is progressively altered as CK666 concentration increases. FOVs size is 10.9 mm X 2.3 mm. Arp2/3 inhibition with CK666 leads to a decrease of v_{rms} (**B**, **E**), decreases cell guidance along the grooves S (**C**, **F**), and dramatically decreases the x correlation length L_x (**D**, **G**) revealing that the emergence of laning is impaired.

B, **C**, **D:** v_{rms} , S and x correlation length evolution with time for different CK666 concentrations in HBEC monolayers on 1.45 μm deep grooves. The color codes for the experimental condition. For each condition, n is the number of FOVs analyzed (one FOV corresponds to one experimental well), and N is the number of independent experiments. Shaded areas correspond to the standard deviation to the mean. Note that 1% DMSO (drug solvent amount used for the highest drug concentration case) reduces the velocity only in the first 10 hours of the experiment and does not prevent the emergence of a laning pattern.

E, **F**, **G:** v_{rms} , S and x correlation length evolution with CK666 concentration 35 hours after cell seeding (dashed line in **B**, **C** and **D**). Error bars correspond to standard deviation to the mean. The stars on top of the error bars indicate the p -value of the two-sample t -test against the hypothesis that the mean of v_{rms} , S or L_x without CK666 is greater than the mean of v_{rms} , S or L_x for the given CK666 concentration. ns: $p > 0.05$; *: $p \leq 0.05$; **: $p \leq 0.01$; ***: $p \leq 0.001$.

3. Collective contact guidance drives polar laning of chaotic epithelial cells

3.2.4. Other cell types do not experience large-scale laning on micro-grooved substrates

We finally investigate the collective response to grooved topography of other cell types that differ from HBECs in terms of properties (activity, cell-cell interactions, propulsion mechanism). First, HT1080 fibrosarcoma cells exhibit chaotic flows in the bulk of a patterned stripe with presence of $+1/2$ and $-1/2$ topological defects⁵⁵. HT1080 are thus active turbulent nematic cells. Compared to HBECs, HT1080 fibrosarcoma cells are slower but stay motile at a constant velocity around $25 \mu\text{m}/\text{h}$ for a longer time (Figure 3.22.E) and don't jam. When seeded on grooved substrates, they are guided by the grooves as $S > 0$ but the guidance by the grooves is less efficient compared to HBECs (Figure 3.22.F). Moreover, HT1080 do not form large polar lanes when plated on grooved substrates (Figure 3.22). The x correlation length L_x is smaller for HT1080 on both flat and grooved substrates compared to HBECs even on flat substrates (Figure 3.22.G). To summarize:

- HT1080 cells are not able to develop lanes on grooved substrates
- HT1080 cells experience chaotic dynamics on both flat and grooved substrates with a velocity correlation length smaller than HBECs on flat substrates.

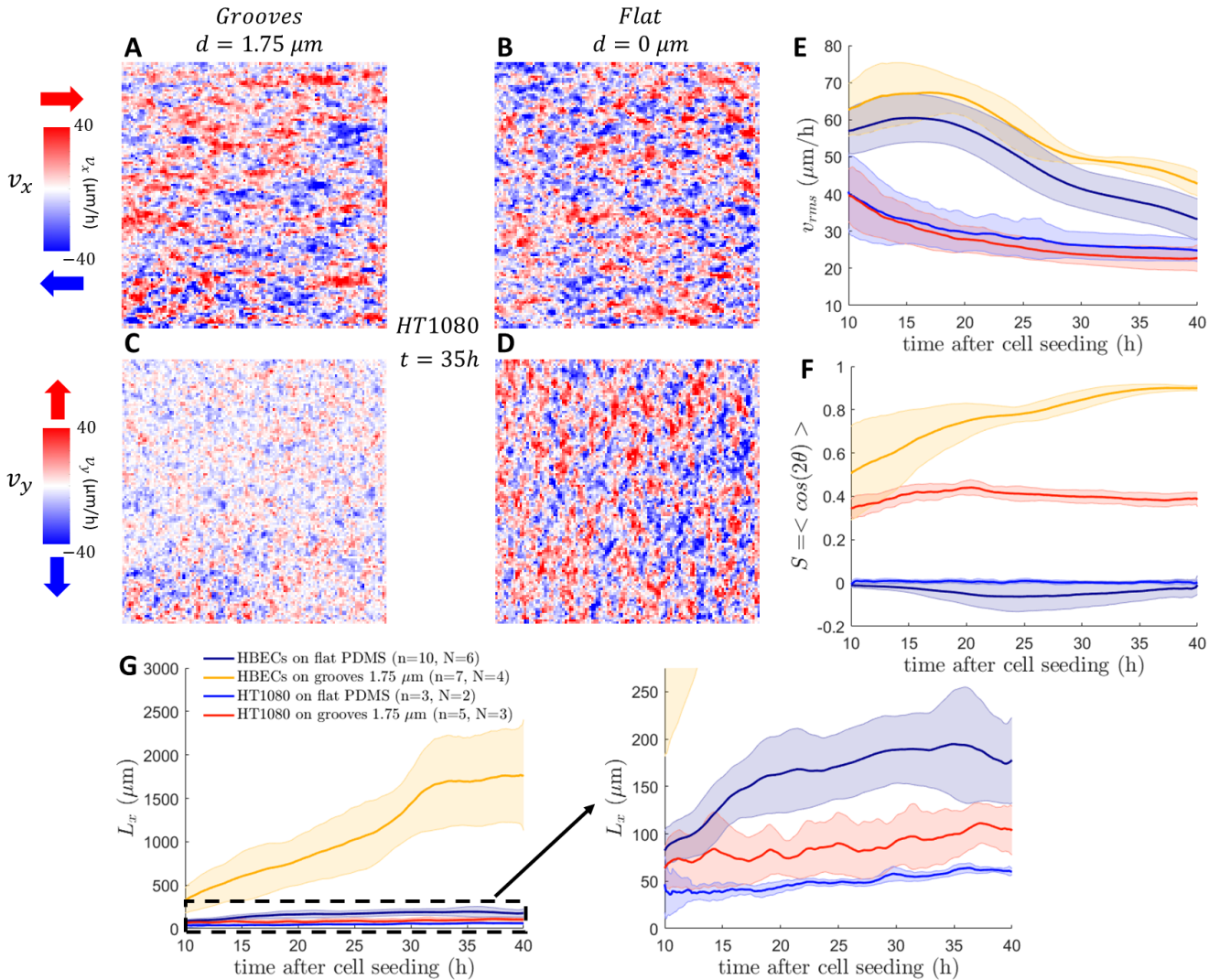


Figure 3.22 : HT1080 cells do not experience large-scale laning on grooved substrates.

A-D: v_x (A, B) and v_y (C, D) are displayed for HT1080 plated on $1.75 \mu\text{m}$ deep grooves (A, C) and flat substrates (B, D) 35 hours after cell seeding. FOVs displayed are $3 \times 3 \text{ mm}$.

E-G: v_{rms} (E), S (F) and x correlation length (G) evolution with time for HT1080 and HBECs on flat and grooved substrates. The color codes for the cell type and substrate. For each condition, n is the number of FOVs analyzed (one FOV corresponds to one experimental well), and N is the number of independent experiments. Shaded areas correspond to the standard deviation to the mean. G-right is a zoom corresponding to the dashed box in G-left.

We also investigated the collective behavior of C2C12 myoblasts on grooved substrates. These cells are elongated nematic cells that are less active than HBECs and HT1080. Their velocity is indeed lower than HBECs and HT1080 cells. They are known to be apolar and to rely on cell contractility to migrate. Moreover, when confined in stripes, they develop a shear flow localized at the border but no chaotic dynamics in the bulk of the stripe⁴⁹. C2C12 myoblasts plated at high density on micro grooves are guided by the grooves as v_y is lower than v_x (Figure 3.23.A-C). However, they don't experience large-scale laning on grooves (Figure 3.23).

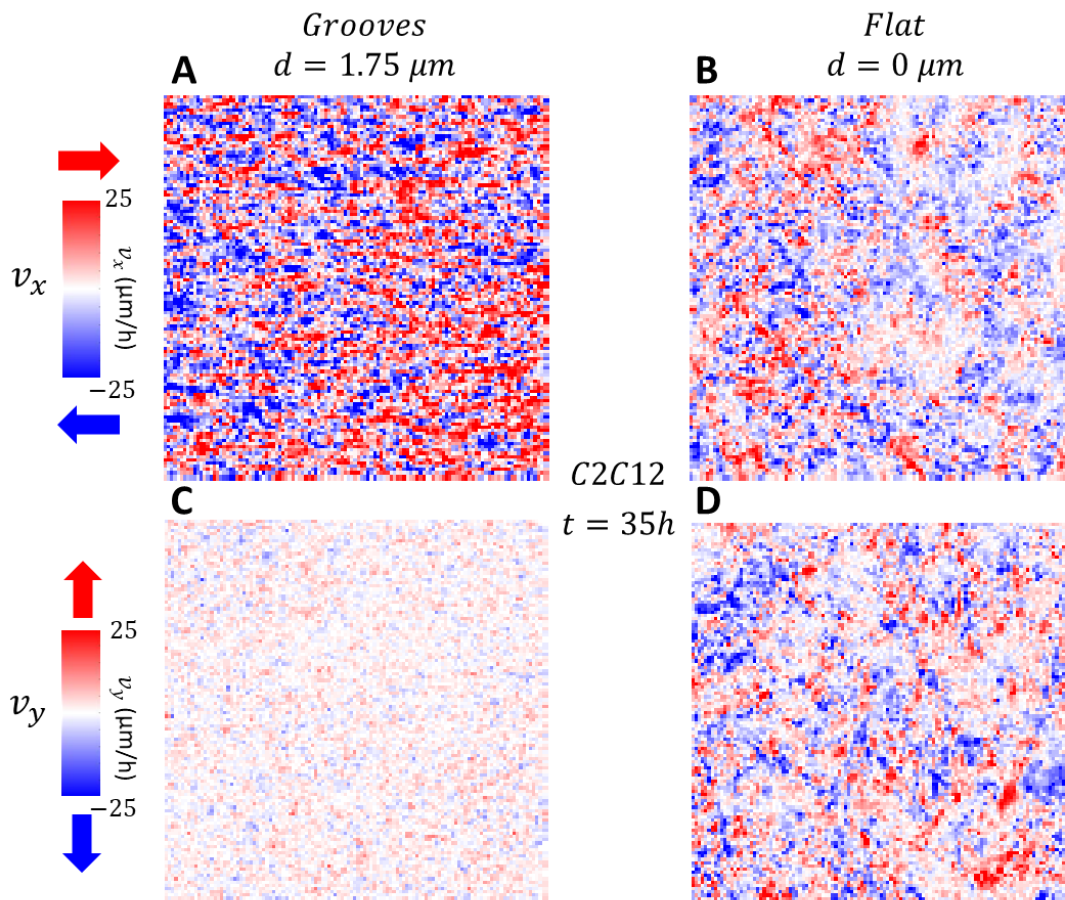


Figure 3.23 : C2C12 myoblasts do not experience large-scale laning on grooved substrates.

A-D: v_x (A, B) and v_y (C, D) are displayed for C2C12 plated on 1.75 μm deep grooves (A, C) and flat substrates (B, D) 35 hours after cell seeding. FOVs displayed are 3 X 3 mm.

Finally, MDCK epithelial cells have strong E-cadherin cell-cell junctions. When plated sparsely on a substrate, they grow in islands that eventually merge to form a cell sheet characterized by strong cell-cell adhesions. Their velocities are lower than HBECs, HT1080 and C2C12. After confluence, cells move around their positions with a small correlation length (lower than 50 μm ¹⁶) (Figure 3.24.B, D). On grooved substrates, the velocity in y is restricted by the grooves but no large-scale laning pattern is observed (Figure 3.24.A, C).

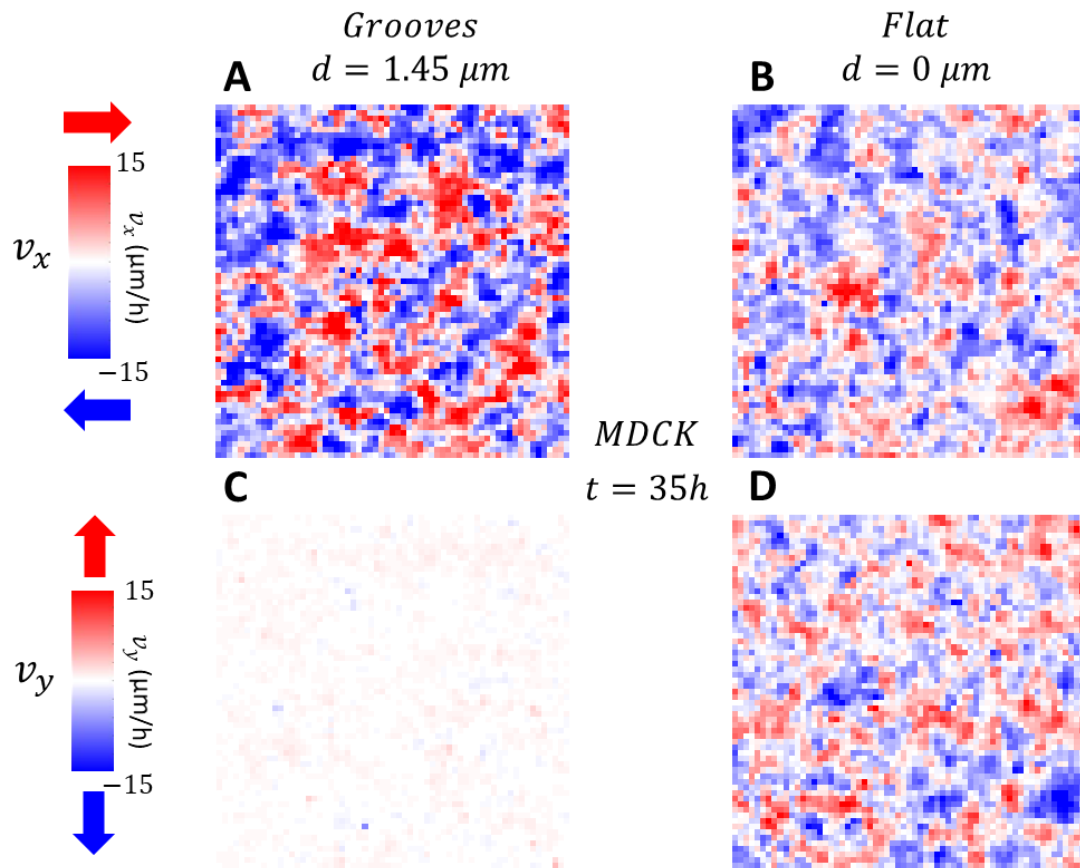


Figure 3.24 : MDCK do not experience large-scale laning on grooved substrates.

A-D: v_x (A, B) and v_y (C, D) are displayed for MDCK plated on $1.45 \mu\text{m}$ deep grooves (A, C) and flat substrates (B, D) 35 hours after cell seeding. FOVs displayed are $1.3 \times 1.3 \text{ mm}$.

3.3. Discussion

In this section, we discuss the results that we obtained, in view of former works in the field of collective cell migration and collective contact guidance.

3.3.1. Length scales of HBECs laning are remarkably large

We have observed the emergence of a laning pattern in confluent HBECs on grooved substrates at much larger scales than have previously reported studies of cell streaming on grooved substrates. Indeed, the lanes that we observed are millimeters long ($\geq 3 \text{ mm} \sim 150$ cell sizes) and hundreds of micrometers wide ($100 \mu\text{m}$ up to $7\text{mm} \sim 5$ up to 350 cell sizes). To our knowledge, such length scales have never been reported before in collective migration in confluent monolayers without confinement nor free space to invade. In comparison, in ARPE-19 epithelial cell and BJ fibroblast monolayers, cell streams have been reported to be around $50 \mu\text{m}$ wide and the associated correlation length is around $100\text{-}150 \mu\text{m}$ ⁹². Leclech and colleagues have reported larger stream width around $100 - 200 \mu\text{m}$ and stream length around $500 \mu\text{m}$ in confluent endothelial cells¹¹⁹, that are smaller length scales than the ones that emerge in the HBECs laning described here.

3.3.2. Cell-cell adhesion is not necessary for HBECs large-scale laning

Remarkably, well-developed E-cadherin cell-cell adhesions are not necessary for this large-scale laning establishment. The role of cell-cell adhesion in collective migration is debated in the literature and seems to be both cell type and geometry dependent.

For example, MDCK cells confined in circles can experience collective rotation that is altered by a down regulation of adherens junctions¹⁸. A similar observation has been made in HaCaT human keratinocytes that experience collective oscillations in square patterns: a down regulation of cell-cell junction also destabilizes the collective behavior and favors a disordered state²⁵. This suggests that in these confined situations, force transmission at junctions is crucial for the collective behavior to emerge. Similarly in confluent unconfined endothelial cell monolayers on grooved substrates, cell-cell adhesion has been shown to be critical in the formation of a periodic streaming pattern¹¹⁹.

In a ring pattern, the picture is more subtle: the establishment of 1D collective cell migration for MDCK depends on cell-cell junction, but once the collective rotation is established, cell-cell junctions are not required to maintain it³³.

Conversely, in confluent ARPE-19 epithelial cells, anti E-cadherin treatment does not significantly change the distance over which alignment to grooves propagate in a region of the monolayer without grooves⁹². In this study, authors demonstrate that the collective behavior emerges from mechanical exclusion interactions rather than force transmission through cell-cell junctions.

Altogether, it suggests that the mechanism governing our system is different from the ones at play in the periodic anti-parallel collective migration of endothelial cells on grooved substrates and in the collective migration of cells such as MDCK under confinement. We postulate that large-scale laning relies on mechanical

exclusion interactions rather than on force transmission at junctions. This hypothesis is further investigated in a next section using particle-based simulations.

In addition, we showed that no large-scale laning develops in confluent MDCK monolayers on grooves. This suggests that too strong adhesions prevent large-scale collective behavior in confluent monolayers. In such low activity, highly cohesive cell types, confinement in small enough pattern seems necessary to trigger collective migration. In contrast, HBECs that are highly active and have initially not well-defined junctions can experience large-scale laning without confinement nor free space to invade.

3.3.3. Cell protrusions are critical for large-scale laning, but cell contractility is not

We have shown that reducing cell contractility via myosin II inhibition with para-nitroblebbistatin reduces cell speed but does not prevent the emergence of large-scale laning in HBECs. This secondary role of contractility have also been reported for the collective behavior in confluent ARPE-19 epithelial cells⁹², the 1D collective rotation of MDCK in rings³³ and oscillations of HaCaT confined in squares²⁵. However, this feature is not common in other collective migration phenomena. For example, blebbistatin treatment impairs oscillatory waves of radial motion in MDCK confined in circles^{60,122}. Similarly, C2C12 myoblasts rely on cell contractility to develop collective migration. Indeed, C2C12 monolayer is an active nematic system and thus relies on gradients of orientation coupled to active contractile forces to develop collective behavior. For example, inhibiting contractility in C2C12 confined in stripes suppresses the shear flow that develops at the boundary. In the present study, we showed that C2C12 do not develop a large-scale laning pattern when seeded at confluence on grooves. Altogether, it shows that large-scale laning does not emerge from a contractility-based mechanism.

The complementary microscopic mechanism that supports cell motility is the directed formation of protrusions such as lamellipodia that are characterized by a branched actin network whose nucleator is Arp2/3. We showed that Arp2/3 inhibition with CK666 decreases cell speed similarly to blebbistatin treatment, but in addition, it impairs large-scale laning emergence. It is known that Arp2/3 inhibition decreases lamellipodial protrusions and that the persistence of lamellipodia is key for cell directionality^{123,124}. In situations reported above in which a loss of contractility is not critical for the collective behavior, the acquisition of a front rear cell polarity through lamellipodial protrusions has been shown to be crucial for the emergence and maintenance of collective motion. This is for example the case for the 1D collective rotation of MDCK in rings³³, for the global oscillations of HaCaT in square patterns²⁵ and for waves propagation in MDCK wound healing assay¹²⁵. We thus conclude that the directed protrusion formation is key for the emergence of collective migration in HBECs.

3.3.4. Non-periodic large-scale laning is not explained by an active nematic description

The transition from a nematic chaotic phase to nematic laning that has been reported in simulations and experiments for active nematic systems flowing along a preferred orientation is characterized by periodic alternating lanes in which the orientation adopts a chevron organization (Figure 3.2). This transition depends

critically on the interplay between active anisotropic stresses (contractility), flow gradient-polarity couplings and anisotropic friction (see 3.1.2). Recently, it has been proposed that endothelial cell monolayers on microgrooves form periodic laning patterns (Figure 3.1.B), which are described via a similar transition from an ordered nematic phase to a nematic laning phase¹¹⁹.

In contrast with nematic laning, HBECs laning on micro-grooved substrates is characterized by non-periodic alternating lanes that coarsen over time until the system freezes. HBECs laning is not characterized by an intrinsic length scale that imposes a well-defined lane width. Moreover, no chevron organization could be observed in cell orientation or polarization. Rather, all cells inside a lane migrate with the same velocity with very sharp discontinuities between lanes. Finally, cell contractility is not crucial for laning emergence as discussed above. Laning relies rather on lamellipodial protrusions. All these differences suggest that a different mechanism is at play to trigger large-scale laning in HBECs on grooved substrates and that a polar description should be better adapted than a nematic description.

We explore this idea in the next two sections where we present theoretical analyses performed in collaboration with two groups of theoreticians. Section 3.4 presents a continuum theory and section 3.5 particle-based simulations.

3.4. Continuum theory of an active polar fluid with anisotropic friction

To better understand the mechanism underlying the chaotic dynamics to laning transition in HBEC monolayers on anisotropic substrates, I worked in close collaboration with theoreticians from the team “Physical approach of biological problems” at Physico Chimie Curie. Carles Blanch-Mercader, Samuel Bell and Jacques Prost proposed a hydrodynamic description in which a HBEC monolayer on a micro-grooved substrate is modeled as an active polar fluid with anisotropic friction that favors a disorder-to-order transition. In this section, I present the main insights that their work provides for our experimental system. More details on the model and the calculations can be found in Annex 6.3. The theoretical panels shown in this section were made by Carles Blanch-Mercader.

3.4.1. Ingredients and assumptions of the model

To describe our experimental system, our collaborators used a coarse-grained hydrodynamic approach with two main degrees of freedom: the velocity field \mathbf{v} and the polarization field \mathbf{p} , which capture respectively the local cell velocity and cell polarization. The polarization field might reflect the orientation of active traction forces or the orientation of cellular migratory structures such as lamellipodia.

They followed the standard approaches of non-equilibrium thermodynamics to constraint the constitutive equations of our active polar fluid (see 1.2.4.1). For simplicity, our system is assumed to be incompressible. First, the time evolution of the polarization field reads:

$$\frac{Dp_\alpha}{Dt} \approx \frac{h_\alpha}{\gamma} + kv_\alpha \quad (3.3)$$

The first term captures the relaxation of the polarization field with γ being a rotational viscosity and $h_\alpha = -\frac{\delta\mathcal{F}}{\delta p_\alpha}$ the molecular field computed from the equilibrium free energy. We consider that the free energy associated with distortions of the polarization field reads:

$$\mathcal{F} = \int_{\mathcal{A}} \left\{ \frac{\chi}{2} p_\alpha^2 + \frac{\beta}{4} p_\alpha^4 + \frac{\mathcal{K}}{2} (\partial_\alpha p_\beta)^2 \right\} da \quad (3.4)$$

We choose the elastic parameters $\chi > 0$ and $\beta > 0$, meaning that the preferred bulk equilibrium state is disordered with $\mathbf{p} = 0$ and $\mathbf{v} = 0$ (see 1.2.5.3). The energy cost associated with gradients of polarization is accounted for by the final term, which is the Frank free-energy in the one-constant approximation with elastic modulus \mathcal{K} .

The second term in (3.3) is a velocity-polarization coupling term with strength k . It describes the re-orientation of the polarization field by the velocity field. Polarization alignment with the velocity is allowed by symmetries in the presence of a substrate and has already been observed experimentally in cell monolayers (see 1.2.5.3).

The force balance equation includes a shear viscosity η , an effective pressure field P that ensures incompressibility, active traction forces of cells in the direction of their polarization $T_0 \mathbf{p}$ and friction with the substrate. As active traction forces can develop only in active systems, T_0 is proportional to $\Delta\mu$, the energy gain per unit of energy source consumed. To describe the effect of the anisotropic structure of subcellular grooves on cells, we consider that the friction is anisotropic and described by the effective friction coefficients λ_{\parallel} and λ_{\perp} acting respectively when the local velocity is parallel and perpendicular to the orientation of the

grooves. As cells are guided by the grooves, we typically impose $\lambda_{\parallel} \leq \lambda_{\perp}$. How does increasing groove depth modify λ_{\parallel} and λ_{\perp} is not obvious and this point will be further discussed in the next subsection.

Note that, conversely to what is usually done in hydrodynamic descriptions of active ordered fluids, the active nematic anisotropic stresses $-\zeta\Delta\mu(p_{\alpha}p_{\beta} - \frac{v_{\alpha}^2\delta_{\alpha\beta}}{2})$ are ignored here. Rather, activity in the system is captured in the force balance as polar active traction forces exerted by the cells on their substrates. In our case, this is a reasonable assumption as we experimentally showed that inhibiting cell contractility does not prevent the emergence of a laning pattern but inhibiting the formation of lamellipodia, that are polar structures involved in cell migration, does. Moreover, flow gradient-polarity couplings are also ignored here. Indeed, we showed experimentally that flows are uniform in lanes, which suggests that, in our system, polarization alignment in shear flows are subdominant compared to polarization alignment in uniform flows. This description is thus fundamentally different than what has been proposed to describe nematic laning in microtubule-kinesin systems and endothelial cell monolayers (see 3.1.2).

3.4.2. Velocity fluctuations response to anisotropic friction

With this model, Carles Blanch-Mercader computed the velocity fluctuations in the disordered phase. In this subsection, the comparison between these expressions and the experimental observations is used to infer expressions of the friction coefficients λ_{\parallel} and λ_{\perp} depending on a friction anisotropy parameter h that has a similar effect than groove depth in experiments.

A steady state solution of the equations describing the system is the uniform disordered phase defined by the conditions $\mathbf{v} = \mathbf{p} = 0$ and $P = P_0$. Note here that the disordered state does not capture the local complexity of the nematic chaotic state observed in HBEC monolayers on flat substrate but has the same characteristics at large length scales. If fluctuations of amplitude D^v and D^p are introduced respectively in the force balance and in the dynamical equation of the polarization field, the solution deviates from the perfect disordered state. Close to the disordered state, one can set $\mathbf{v} = \epsilon\delta\mathbf{v}$, $\mathbf{p} = \epsilon\delta\mathbf{p}$ and $P = P_0 + \epsilon\delta P$, with $\epsilon \ll 1$ a small dimensionless parameter. After linearizing the equations and in the case of vanishing polarization fluctuations ($D^p = 0$):

$$\langle v_{x,y}(r, t)^2 \rangle = \frac{D^v}{4\pi\eta\tau(\lambda_{\parallel,\perp} + \sqrt{\lambda_{\perp}\lambda_{\parallel}})} \quad (3.5)$$

where τ is a cut-off for small time scales.

As presented in 3.2.1.2, we measured $\langle v_x(r, t)^2 \rangle$ and $\langle v_y(r, t)^2 \rangle$ for our experimental case of HBEC monolayers and varying groove depth. We observed that $\langle v_x^2 \rangle$ increases with groove depth and $\langle v_y^2 \rangle$ decreases with it, while $v_{rms} = \sqrt{\langle v_x(r, t)^2 + v_y(r, t)^2 \rangle}$ is approximately independent on the groove depth (blue points in Figure 3.25.A-C). This effect is also observed for HT1080 cells that stay disordered even on 1.75 μm deep grooves (red points in Figure 3.25.A-C).

To match the experimental data, one must find a single parameter increasing friction anisotropy and modifying λ_{\parallel} and λ_{\perp} in such a way that the root mean square velocity stays constant while $\langle v_x(r, t)^2 \rangle$ increases and $\langle v_y(r, t)^2 \rangle$ decreases. To impose that, we set $\lambda_{\perp}\lambda_{\parallel} = \lambda^2$ and $\lambda_{\perp} = h\lambda_{\parallel}$ with $h \geq 1$ being the friction anisotropy. With this definition and using the previous relations (3.5), one finds:

3. Collective contact guidance drives polar laning of chaotic epithelial cells

$$v_{rms}^2 = \langle v_x(r, t)^2 \rangle + \langle v_y(r, t)^2 \rangle = \frac{D^p}{4\pi\eta\tau\lambda} = cste \quad (3.6)$$

$$\frac{\langle v_x(r, t)^2 \rangle}{v_{rms}^2} = \frac{1}{\left(\frac{1}{\sqrt{h}} + 1\right)^{h \rightarrow \infty}} \rightarrow 1 \quad (3.7)$$

$$\frac{\langle v_y(r, t)^2 \rangle}{v_{rms}^2} = \frac{1}{\left(\sqrt{h} + 1\right)^{h \rightarrow \infty}} \rightarrow 0 \quad (3.8)$$

Figure 3.25.D-F shows the variation of v_{rms} , $\sqrt{\langle v_x(r, t)^2 \rangle} / v_{rms}$ and $\sqrt{\langle v_y(r, t)^2 \rangle} / v_{rms}$ with h . Increasing h in the model has the same effect as increasing groove depth in experiments. We checked that these dependences are also satisfied when D^p is non-vanishing (blue curves in Figure 3.25.D-F).

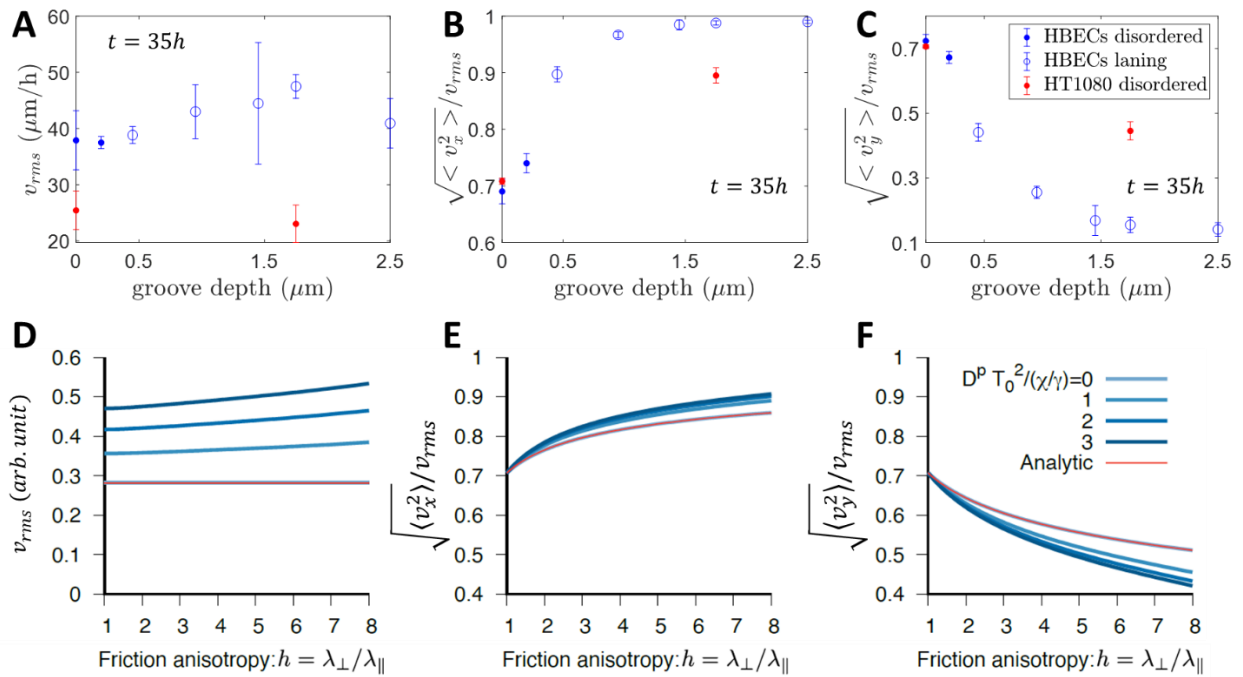


Figure 3.25 : The effects of increasing groove depth in experiments (A-C) are well-captured by increasing the friction anisotropy $h = \lambda_{\perp} / \lambda_{\parallel}$ while maintaining the friction scale $\lambda = \sqrt{\lambda_{\parallel} \lambda_{\perp}}$ constant in the hydrodynamic description (D-F).

A-C: In experiments, 35 hours after cell seeding, v_{rms} does not show a dependence with groove depth (A) while $\sqrt{\langle v_x(r, t)^2 \rangle} / v_{rms}$ increases (B) and $\sqrt{\langle v_y(r, t)^2 \rangle} / v_{rms}$ decreases (C) when groove depth increases for both HBEC and HT1080 monolayers. Error bars correspond to standard deviation to the mean (for HBECs $n=10, 5, 7, 6, 16, 7, 4$ FOVs for groove depth equal to 0, 0.2, 0.45, 0.95, 1.45, 1.75, 2.5 μm and for HT1080, $n=3, 5$ for groove depth equal to 0, 1.75 μm).

D-F: Similarly, the theoretical description of the disordered state predicts that v_{rms} does not vary dramatically (D), $\sqrt{\langle v_x(r, t)^2 \rangle} / v_{rms}$ increases (E) and $\sqrt{\langle v_y(r, t)^2 \rangle} / v_{rms}$ decreases (F) when friction anisotropy h increases. The values of $\frac{D^p T_0^2}{\chi/\gamma}$ for the blue curves in panels D-F change as indicated in the legend of panel F. The solid red curves correspond to the analytical expressions in the case $D^p = 0$ and are in perfect agreement with the numerical resolutions in the case $D^p = 0$ (lighter blue curves). The units were set as $D^p / \tau = \mathcal{K} / \chi = \eta = 1$ and the parameter value is set to $kT_0 = 0.3$.

One can note that the highest values of $\sqrt{\langle v_x^2 \rangle} / v_{rms}$ and lowest values of $\sqrt{\langle v_y^2 \rangle} / v_{rms}$ are obtained for grooves deep enough to be in the laning regime in HBEC monolayers compared to both disordered HT1080 and theoretical predictions. Let's remind here that the theoretical predictions presented in this subsection are

valid in the disordered state. The emergence of collective laning in HBECs reinforces cell guidance along grooves. This justifies that $\sqrt{\langle v_x^2 \rangle} / v_{rms}$ is higher and $\sqrt{\langle v_y^2 \rangle} / v_{rms}$ is lower for HBECs laning compared to HT1080 and theoretical predictions for large substrate anisotropy.

Therefore, this analysis suggests that the effect of increasing groove depth is well captured by changing the friction anisotropy $h = \frac{\lambda_{\perp}}{\lambda_{\parallel}}$ while maintaining the friction scale $\lambda = \sqrt{\lambda_{\parallel}\lambda_{\perp}}$ constant.

3.4.3. Disorder-to-laning transition in an active polar fluid with anisotropic friction

In this hydrodynamical model, our collaborators identified a disorder-to-polar laning transition presenting similar features than the HBECs laning. To do that, they investigated the stability of the disordered phase to linear perturbations, in the absence of fluctuations. In this subsection, I explain the physics behind this disorder-to-polar laning transition without entering in the details of the calculation that can be found in Annex 6.3.3.

The linear stability analysis reveals that the polar active fluid experiences a transition from a disordered to an ordered state which is controlled by the value of kT_0 . When $kT_0 = 0$, one finds that the disordered phase is always stable. As kT_0 increases, a critical threshold $(kT_0)_c$ can be identified above which perturbations of the disordered state get unstable, meaning that they grow exponentially. This result shows that the interplay between the velocity-polarization coupling k and the polar traction force T_0 can destabilize the disordered phase. The value of the critical threshold is:

$$(kT_0)_c = \frac{\chi\lambda}{\gamma\sqrt{h}} \quad (3.9)$$

When the disordered phase becomes unstable for $kT_0 > (kT_0)_c$ and in the case of anisotropic friction $h > 1$, the most unstable perturbations correspond to perturbations with infinite wavelength in the x direction, with spatial modulation in the y -direction, and with p_x and v_x exponentially growing with time while p_y and v_y decay to zero, and thus correspond to a laning pattern. Because the most unstable perturbation has an infinite wavelength also in the y direction, no characteristic finite wavelength is selected by the linear dynamics and the laning pattern is non-periodic. Linear dynamics simulations above threshold show that, starting from an initial random perturbation of the polarization field (Figure 3.26.B), a non-periodic laning pattern is indeed selected (Figure 3.26. C). Altogether, this shows that at the onset of the instability, the dynamics of small perturbations around the disordered phase selects a non-periodic laning pattern, similar to the laning pattern observed with HBECs (Figure 3.6).

Figure 3.26.A shows the phase diagram in the plane (h, kT_0) . Interestingly, the critical threshold decreases sub linearly with h : $(kT_0)_c \sim h^{-\frac{1}{2}}$ (blue curve in Figure 3.26.A). It means that for a given value of kT_0 below the critical threshold obtained for $h = 1$, the system can cross the polar laning threshold by increasing the friction anisotropy h (dashed orange horizontal line in Figure 3.26.A). For such a fixed value of kT_0 , which depends on the material properties of the cell monolayer, and for sufficiently small values of h , the disordered state is linearly stable (dot I in Figure 3.26.A). When h is increased enough, the critical threshold $(kT_0)_c$

eventually becomes smaller than kT_0 , the disordered state is not stable anymore and a laning pattern emerges (dot II in Figure 3.26.A). Similarly, in HBEC monolayers, laning is triggered by an increase in groove depth.

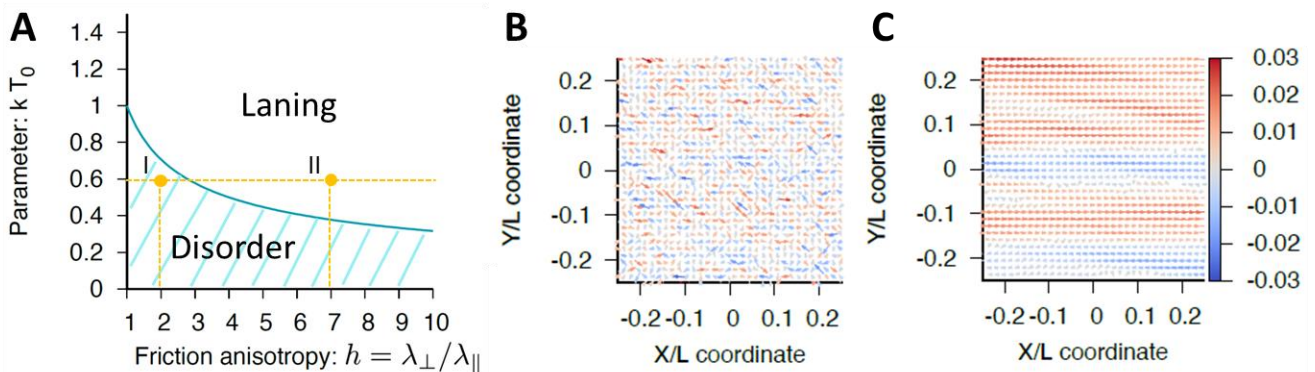


Figure 3.26 : Disorder-to-polar laning transition in active polar fluid with anisotropic friction.

A: Phase-diagram in the plane (h, kT_0) . The solid line corresponds to the critical threshold $(kT_0)_c$. The material parameters are set to $\chi = \lambda = \gamma = \mathcal{K} = 1$, $\eta = 10$. The horizontal orange dashed line corresponds to a fixed value of kT_0 , the orange dots (respectively I and II) highlight two possible states along this line (respectively disorder and laning) and the vertical orange dashed lines the corresponding values of h .

B, C: Linear dynamics above threshold. Snapshots at different time points (B: $t=0.4$, C: $t=2$) of the polarization field from an initial random perturbation. The scale of the arrow length is normalized at each snapshot for visualization purposes. The parameters are set to $\chi = \lambda = \gamma = \mathcal{K} = 1$, $\eta = 10$, $kT_0 = 2$ and $h = 4$. The position coordinates are normalized by the system size $L=800$. The color bar indicates the normalized value of p_x .

3.4.4. Summary of the active polar fluid theory contributions

We have shown that the laning transition in HBEC monolayers can be interpreted by a large wavelength instability of an active polar fluid in a disordered state mediated by the interplay between active traction forces and velocity-polarization coupling. Anisotropy in the system, which we introduced through anisotropic friction, favors the emergence of an ordered phase by lowering the threshold of the disorder-to-order transition. Moreover, when the friction is anisotropic, the most unstable perturbations above threshold correspond to a laning pattern with no finite wavelength selection. Thus, the polar active fluid model captures well the principal features of the laning transition observed experimentally:

- The transition can be triggered by an increase in groove depth modeled here by friction anisotropy that effectively facilitates the transition from disorder to order.
- In the ordered state, a laning pattern is selected with no characteristic finite wavelength.
- The transition is not dependent on anisotropic nematic active stresses (cell contractility) but is mediated by polar contributions (polar active traction and polarity-velocity coupling).

However, this linear instability analysis has some limits. First, this linear continuum approach is valid close to the disordered state and at the onset of the instability. Thus, it cannot describe the final state of the system when the instability is well developed. In HBECs laning, the velocity profiles have plug flow structures in the lanes and the shear flows are localized within one cell size between two lanes. This discontinuity in the velocity profile is not captured by this continuum description. Moreover, our hydrodynamical theory relies on phenomenological parameters and the dependence of these parameters with more microscopic parameters is not explicit. This limits our understanding of the instability mechanism and the dynamics of the polar laning pattern for varying cell-related parameters.

3.5. Self-propelled particle-based simulations

To investigate the microscopic mechanisms leading to laning, we collaborated with Bart Smeets from the “BIOSYST-MeBioS” group at KU Leuven. We performed and analyzed self-propelled particle-based simulations. In this section, I present the main ingredients of the numerical model proposed by Bart Smeets and compare the numerical results we obtained to the experimental ones. More details about the simulations can be found in Annex 6.4. The theoretical panels shown in this section were made by Bart Smeets.

3.5.1. Model for self-propelled particle-based simulations

We investigate the evolution of simulated systems composed of interacting particles at high density. Each particle i is characterized by a polarization \mathbf{p}_i and a normalized velocity $\hat{\mathbf{v}}_i = \frac{\mathbf{v}}{v_0}$, v_0 being the center of the root mean square velocity distribution of a single freely moving particle. Each particle is governed by a polarization evolution equation and a normalized overdamped force balance equation (see details in Annex 6.4).

The polarization evolution equation includes a velocity-polarization coupling term. k_s is an adimensional parametrization of the velocity-polarization coupling and is the dimensionless equivalent of the parameter k introduced in the continuum model. The force balance equation includes self-propulsion in the polarization direction, friction with the substrate and interactions with neighboring particles. The effect of the grooves is modeled by introducing anisotropy in the friction, described by the parameter $h_s \geq 1$. When $h_s = 1$, the friction is isotropic, whereas for higher h_s , the friction is anisotropic, and the particles flow preferentially in the x direction in which they experience lower friction. Note that h_s is the equivalent of h introduced in the continuum model. Interactions with neighbors are excluded volume interactions and are modeled through a repulsive soft potential, with k_c being the adimensional contact stiffness between particles. Note that the interactions are purely repulsive, and no adhesion has been included in the model. This is reasonable as we experimentally showed that cell-cell adhesion is not necessary for HBEC laning.

Therefore, the system dynamics is controlled by only three parameters: h_s the friction anisotropy, k_s the strength of the polarization-velocity coupling and k_c the contact stiffness between neighbor particles.

Periodic boundary conditions are imposed. Particles are disks initially homogeneously distributed in the system so that the density is 1.2 to ensure confluence (meaning that some overlaps are allowed). Their initial condition is $\mathbf{p}_i = 0$ and $\mathbf{v}_i = 0$. Simulations are run until the systems reach a steady state. To analyze simulation results, single particle velocities are coarse-grained to obtain the locally averaged normalized velocity field $\hat{\mathbf{v}}(\mathbf{r}, t)$.

3.5.2. Friction anisotropy orients particle displacements

We first fix the values for the strength of the polarization-velocity coupling and the contact stiffness ($k_s = 6$ and $k_c = 2.5$) and vary anisotropy in the friction h_s from 1 to 5. The values of k_s and k_c have been chosen so that the velocity distribution in the isotropic case $h_s = 1$ is a ring pattern, like for HBECs on flat substrates. Like increasing groove depth in experiments (Figure 3.9, Figure 3.10), increasing h_s leads to a

3. Collective contact guidance drives polar laning of chaotic epithelial cells

transition from a ring to a bimodal distribution of (\hat{v}_x, \hat{v}_y) (Figure 3.27.A). Thus, in the simulations, we also find that increasing h_s does not affect \hat{v}_{rms} (Figure 3.27.B) but increases $\sqrt{\langle \hat{v}_x^2 \rangle} / \hat{v}_{rms}$ and decreases $\sqrt{\langle \hat{v}_y^2 \rangle} / \hat{v}_{rms}$ (Figure 3.27.C). Consequently, the guidance along the axis of lower friction (x axis) characterized by the apolar order parameter S increases with h_s (Figure 3.27.D). As these results agree with the experimental observations when increasing groove depth (see Figure 3.9, Figure 3.10), we conclude that h_s in simulations mimics well the groove depth in the experiments.

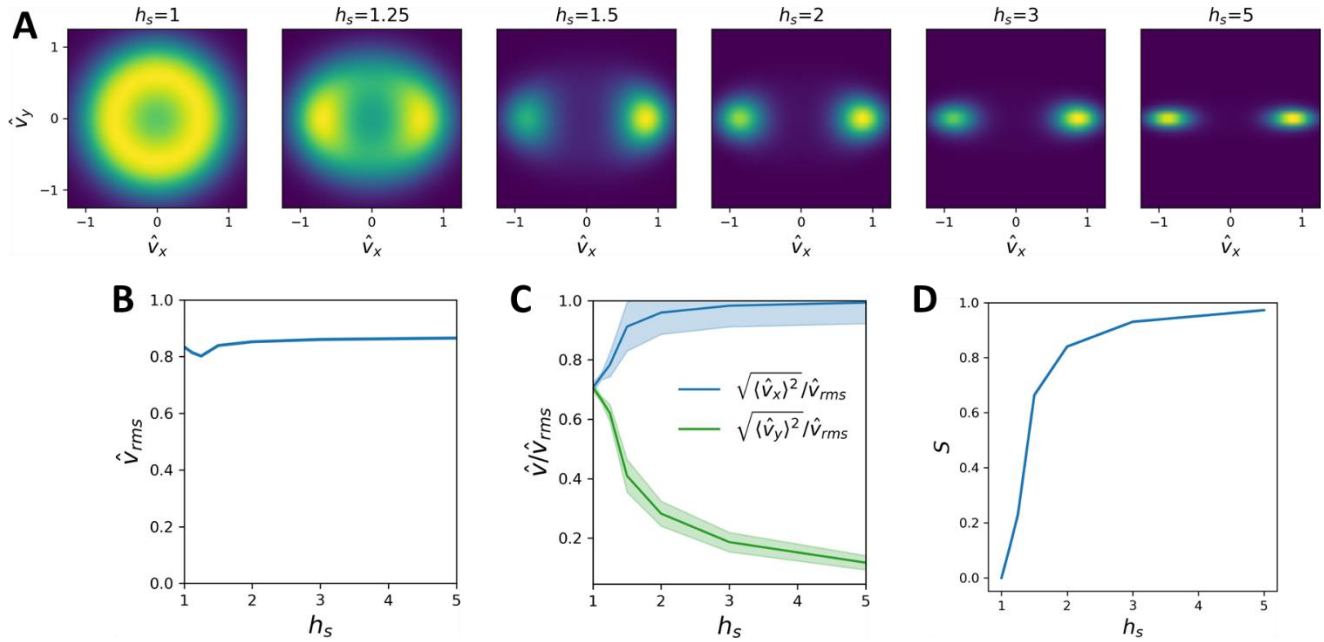


Figure 3.27 : In particle-based simulations, friction anisotropy guides the particles along the x axis.

A: Bivariate histograms of (\hat{v}_x, \hat{v}_y) for increasing h_s show a transition from a ring distribution to a bimodal distribution. Note that here, the normalization is different for each value of h_s to highlight the shape of the distribution. B: \hat{v}_{rms} does not vary with h_s . C:

$\sqrt{\langle \hat{v}_x^2 \rangle} / \hat{v}_{rms}$ increases and $\sqrt{\langle \hat{v}_y^2 \rangle} / \hat{v}_{rms}$ decreases with friction anisotropy h_s . Shaded areas correspond to the standard deviation. D:

The local guidance S increases with h_s .

A-D: k_s and k_c were respectively fixed to 6 and 2.5. For each value of h_s , the data presented are averaged over 5 repeats. One repeat consists in a simulation of a 2X10 mm frame containing particles of diameter 20 μm .

3.5.3. Friction anisotropy results in the emergence of laning

If we set $h_s = 3$, value for which the particles are guided along the x direction at a constant speed (Figure 3.27.A), the simulated system evolves toward a laning state (Figure 3.28.A) that presents features similar to the experimental HBEC laning (Figure 3.28.B):

- the lane length corresponds to the system size (Figure 3.28.A.1)
- the laning pattern is not periodic: the system does not present an intrinsic length scale that fixes the lane width (Figure 3.28.A.1, A.2)
- in each lane, particles migrate at a fixed velocity in a plug flow (Figure 3.28. A.1, A.2)
- between two lanes, the velocity changes sign sharply between two rows of particles. (Figure 3.28.A.3)

One can note that as we impose periodic boundary conditions, laning in simulations is “perfect” in the sense that the lanes cross the whole system and are extremely straight. On the other hand, in experiments,

several effects prevent a “perfect” laning pattern to establish. First, the density increases over time and the system freezes before a steady laning state is reached. Second, the analyzed FOVs correspond to a subset of the whole experimental wells (Figure 3.5). As the initial density can’t be precisely controlled, it is not perfectly homogeneous in the whole system which might lead to large-scale density effects outside the FOV that will affect the laning pattern in the experimental FOV.

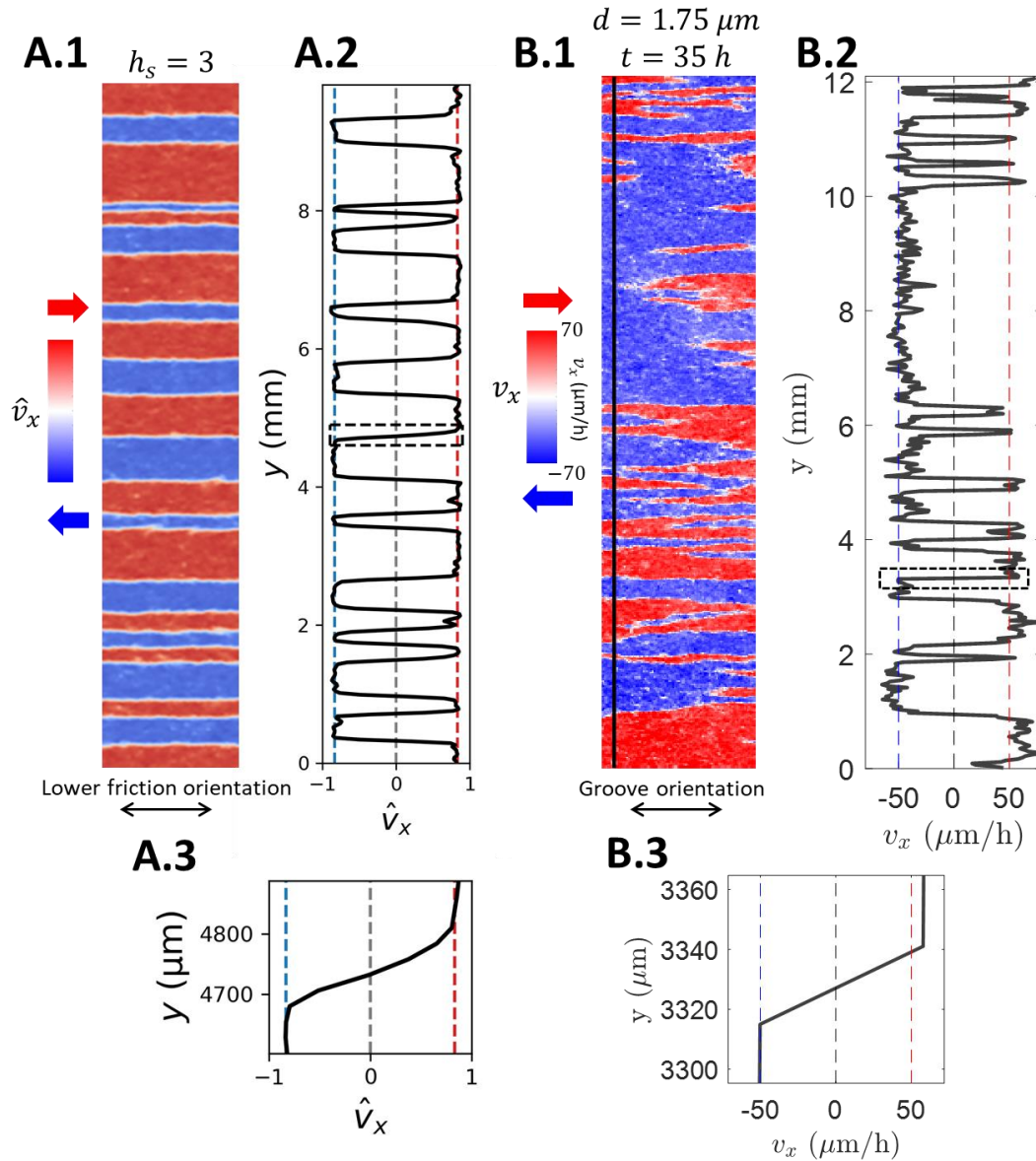


Figure 3.28: In particle-based simulations (A), anisotropic friction leads to laning with characteristics similar to HBECs laning (B). A: A1: \hat{v}_x for a system simulated until a steady state is reached for $k_s = 6, k_c = 2.5$ and $h_s = 3$. The double-headed arrow shows the axis of lower friction. A.2: Corresponding velocity profile along y , taken in the middle of the FOV. A.3: Zoom in the profile of A.2. The simulated system is composed of “20 μm ” diameter particles at high density in a frame “10 mm” long and “2 mm” wide. Note that these sizes are scaled to be close to experimental sizes but what matters for simulations is the ratio between system size and particle size.

B: B.1: Representative v_x laning pattern 35 h after seeding HBECs on 1.75 μm deep grooves. The FOV is 12 mm X 2.7 mm. B.2: x velocity profile along y corresponds to a non-periodic rectangular signal. The profile shown is a representative profile along the black line in the FOV displayed in B.1. B.3: zoom in the v_x profile, corresponding to the dashed box in B.2.

3.5.4. The disorder-to-laning transition mediated by friction anisotropy is compatible with experiments

We find that, for fixed values of k_s and k_c , increasing friction anisotropy h_s leads to a transition from a disordered to a laning state in simulations (Figure 3.29.A), similarly to increasing groove depth in experiments (Figure 3.11). Interestingly, we note that, at the transition (h_s around 1.5), the lanes are much wider than in experiments. If we further increase anisotropic friction, the average lane width decreases (Figure 3.29.A, B). This shows that large friction anisotropy stabilizes thinner lanes in simulations. Even if in experiments we do not clearly observe this decay at large groove depth (Figure 3.15), we observe for both experiments and simulations that the laning pattern is characterized by larger γ coordination compared to the turbulent pattern in isotropic conditions.

Then, we analyzed the distribution of lane widths via the cumulative function $\tilde{p}(w)$ in simulations with varying friction anisotropy (Figure 3.29.C). This probability is a decreasing exponential for all values of h_s . As we increase friction anisotropy, the slope of $\tilde{p}(w)$ in semilog scale increases first smoothly before a sharp increase at the laning transition between $h_s = 1.25$ and $h_s = 1.5$. If we increase friction anisotropy further, this slope decreases. This agrees with the observation that average lane width increases sharply at the transition and then decreases if we increase friction anisotropy further (Figure 3.29.B).

The maximal lane width observed in simulations is 3 mm. Much larger lanes have been observed experimentally (Figure 3.16.C). This might be due to large-scale density effects in the experimental well larger than the FOVs' size as discussed before. If we remove lanes larger than 3 mm from the analysis of the experiments, the results obtained are in good semi quantitative agreement with the simulation ones (Figure 3.29.C, D). Indeed, for $w > 500 \mu m$, $\tilde{p}(w)$ decays exponentially and the slope of $\tilde{p}(w)$ in semilog scale increases sharply at the laning transition also in experiments. However, we do not clearly observe in experiments the decay of the slope for the largest groove depth tested. After the laning transition, for $h_s \geq 1.5$ or grooves deeper than $0.45 \mu m$, the initial decay is different between simulations and experiments. When laning is established in simulations, lanes smaller than $300 \mu m$ have completely disappeared. This is not the same in experiments for which $\tilde{p}(w)$ presents a sharp exponential decay for small width. The reason is that we never reach a perfect laning pattern in experiments and thus thin lanes are not coarsened 35 hours after cell seeding, leading to a larger presence of small lanes in experiments.

Note also that the "lane width" on isotropic substrate is larger in experiments than in simulations. In simulations, all the particles are disks with diameter sharply peaked around $20 \mu m$ whereas real cells have more variety of shapes and sizes. Moreover, compared to simulated particles, HBECs are deformable and have a nematic organization on flat substrate that is not described by the numerical model. Also, in experiments, the density increases with time and the adhesion between cells mature progressively. This leads to an increase in the correlated domain size by "active jamming"¹⁶. As these effects are not included in the model, simulations with isotropic friction exhibits smaller correlated regions compared to the chaotic behavior in HBEC monolayers on flat substrates.

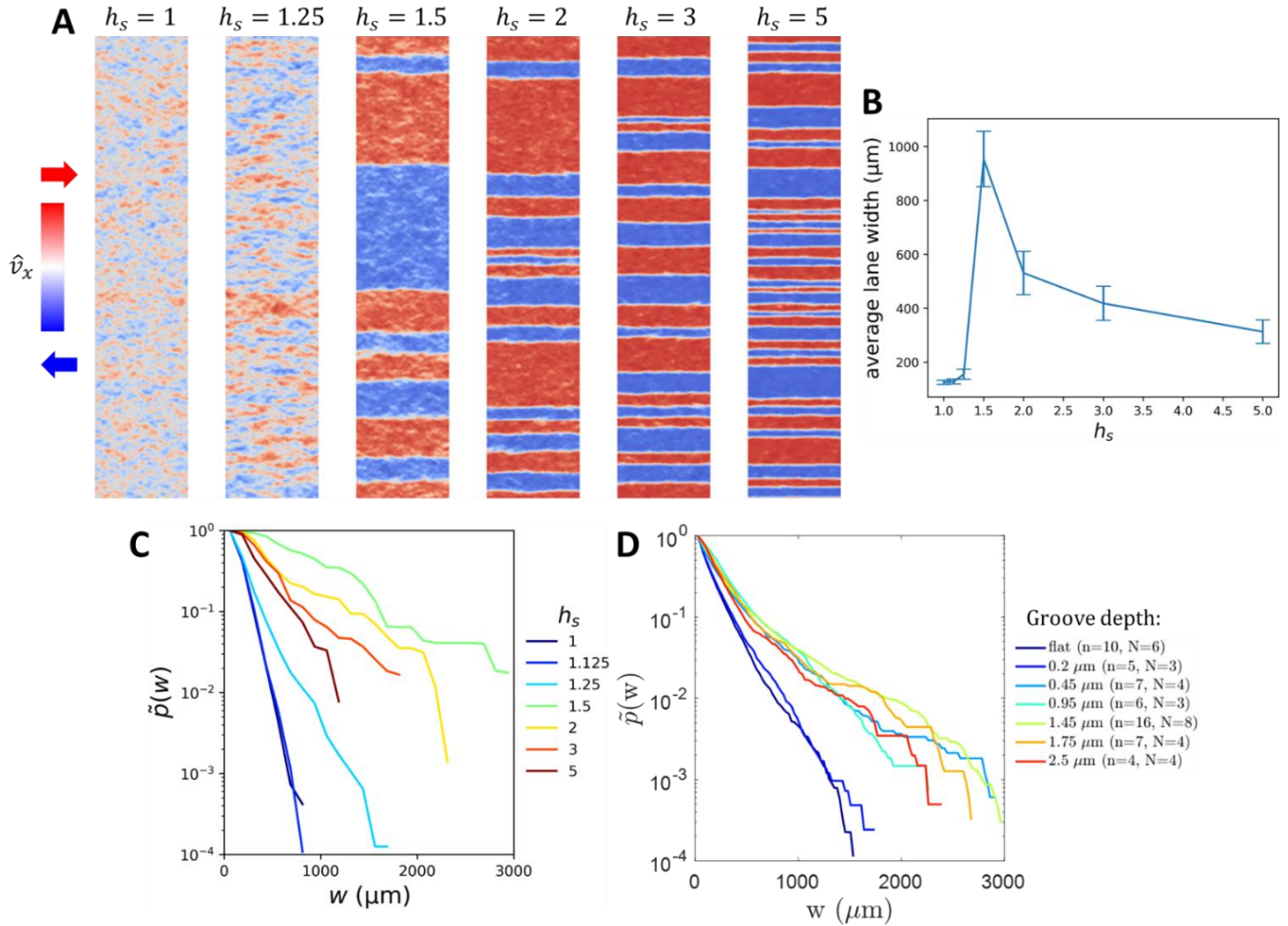


Figure 3.29: In self-propelled particle-based simulations for fixed $k_c = 2.5$ and $k_s = 6$, the transition from disorder to laning is mediated by an increase in friction anisotropy h_s .

A: A transition from disorder to laning is observed between $h_s = 1.25$ and $h_s = 1.5$. From left to right, \hat{v}_x is displayed for systems simulated until a steady state is reached for $k_s = 6$, $k_c = 2.5$ and $h_s = 1 - 5$.

B: The average lane width increases at the transition and then decreases when h_s is further increased. Error bars represent standard deviation to the means over 5 repeats.

C, D: Lane width distribution in simulations and comparison with experimental data. Lane width cumulative probability $\tilde{p}(w)$ for simulated systems (C) and experimental systems (D). C: Simulated systems correspond to fixed $k_c = 2.5$ and $k_s = 6$ and for increasing friction anisotropy h_s . For each h_s , the distribution is obtained for 5 repeats of the simulation. Each lane width in the distribution is measured as the distance between two points at which the velocity crosses zero in the profile along the middle line of the frame (see Figure 3.28.A). D: Curves were obtained as presented in 3.2.1.4 but here lanes larger than $3000 \mu\text{m}$ have been excluded from the analysis. Color codes for groove depth.

3.5.5. Friction anisotropy favors the laning transition controlled by polarization-velocity coupling and excluded volume interactions strength

We now investigate the final state in simulations when varying both the polarization-velocity coupling k_s and the friction anisotropy h_s . Like the measure performed for HBEC laning (Figure 3.12), we define a characteristic length of the x-correlation decay $L_{x,s}$ to characterize the transition from disorder to laning. More details on the definition of $L_{x,s}$ can be found in Annex 6.4.3. The results are summarized in the phase diagram Figure 3.30 which corresponds to a heat map of the characteristic length $L_{x,s}$ in the phase space (h_s, k_s). Bluish

3. Collective contact guidance drives polar laning of chaotic epithelial cells

colors correspond to small $L_{x,s}$ characterizing a disordered state whereas reddish colors correspond to large $L_{x,s}$ characterizing an ordered state.

When $h_s = 1$, we observe a flocking transition when the polarization-velocity coupling strength k_s is increased. For low k_s , the system is disordered (Figure 3.30.B.I) whereas for k_s higher than a critical value around 9, the system is in a polar flocking phase in which particles migrate all in the same direction in large groups (Figure 3.30.B.II). When $h_s \geq 1$, the ordered phase (reddish colors in the phase diagram) corresponds to a laning state (Figure 3.30.B.III). The k_s critical threshold for the disorder-to-order transition is lowered by friction anisotropy, consistently with the prediction from the continuum theory. In HBEC experiments, we vary substrate anisotropy by varying groove depth and observe a transition from disorder to laning. This corresponds to a line in the simulations phase diagram (Figure 3.30.A) for an intermediate value of k_s . To sum up, there is a flocking transition at $h_s = 1$ that is not only oriented by anisotropic friction but also facilitated by it.

Furthermore, the scaling between the critical value of k_s and the friction anisotropy h_s predicted by the continuum theory ($(k_s)_c \sim 1/\sqrt{h_s}$) (Figure 3.26.A) is in good agreement with the simulation results (dashed line in Figure 3.30.A). The variation of $(k_s)_c$ with h_s follows a power $-1/2$, thus $(k_s)_c$ decay with h_s is slow. For $k_s \leq 3$, the disordered state is stable for all the values of h_s tested. This corresponds to what we observe for HT1080 cells, that have a chaotic behavior on flat substrate and on 1.75 μm deep grooves (on which HBECs experience laning).

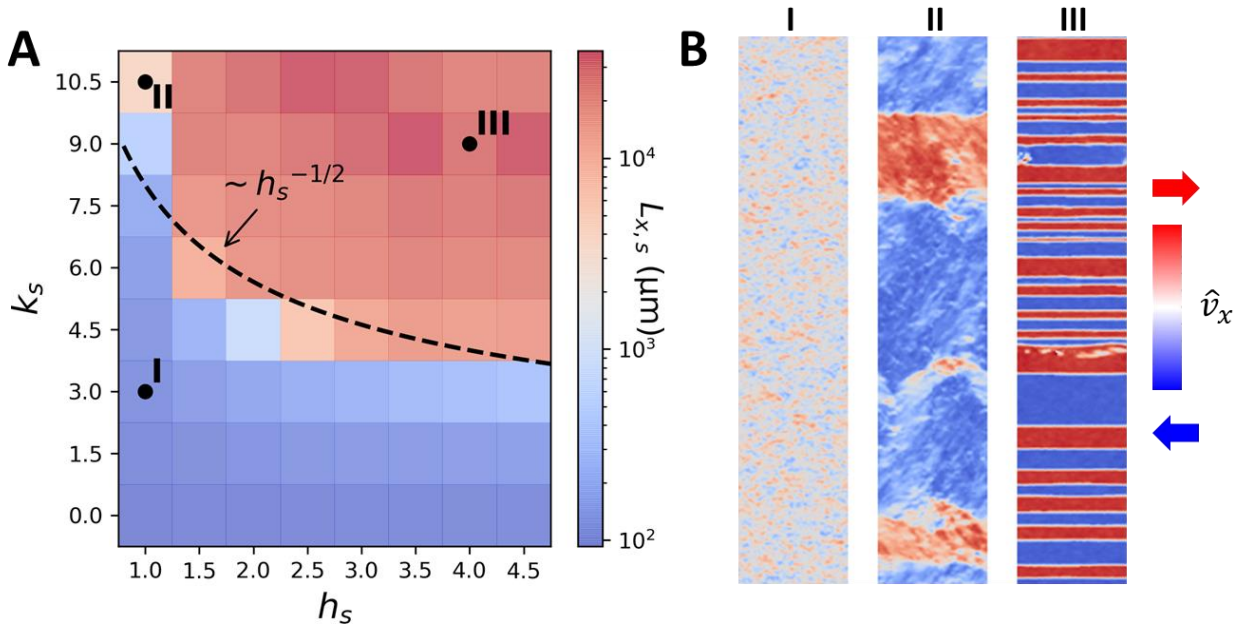


Figure 3.30: Friction anisotropy favors laning by decreasing the critical threshold value of k_s .

A: Phase diagram of $L_{x,s}$ values in the phase space (h_s, k_s) . Snapshots of \hat{v}_x corresponding to the numbered dots are shown in B. The dashed curve in A shows the scaling $\frac{1}{\sqrt{h_s}}$ that is the predicted scaling for the critical velocity-polarization coupling in the continuum theory. This plot is obtained for $k_c = 2.5$. For each point in the phase diagram, $L_{x,s}$ is averaged over 5 repeats of the simulation. The simulated systems are composed of “20 μm ” diameter particles at high density in a frame “10 mm” long and “2 mm” wide.

B: B.I shows \hat{v}_x for a typical disordered state, B.II for a flocking state, and B.III for a laning state.

Similar results can be obtained by varying k_c and h_s at fixed k_s . It means that both sufficiently large velocity-polarization coupling and repulsion between neighboring particles are required for collective behavior emergence in simulated systems. Altogether, we conclude that friction anisotropy in simulations both favors the disorder-to-order transition and stabilizes a laning pattern in systems in which the polarization-velocity coupling and the strength of excluded volume interactions are high enough. HT1080 cells that have a similar chaotic behavior on flat substrates than HBECs do not perform laning on grooves with depth 1.75 μm . Simulations suggest that this inability of these fibrosarcoma cells to experience large-scale collective behavior might be the results of lower strength of excluded volume interactions or lower strength of velocity-polarization coupling.

Here, anisotropy was introduced in the friction term. Note that we also simulated systems in which anisotropy was introduced in other terms of the governing equations such as in the polarization-velocity coupling or in the noise and observed a similar laning transition. It shows that any kind of anisotropy in the system that orients the migration along a given axis favors the emergence of an ordered laning state.

3.5.6. Conclusion

In self-propelled particle-based simulations, both polarization-velocity coupling and excluded volume interactions contribute to a disorder-to-flocking transition with isotropic friction. Friction anisotropy lowers the disorder-to-order transition threshold and stabilizes the ordered phase in a laning pattern that has the same characteristics than the observed laning pattern in HBEC monolayers on micro-grooved substrates (plug flow, localized shear flow, non-periodicity, lane width distribution). Moreover, the exponential lane width distribution evolution when increasing friction anisotropy is in good agreement with experimental data. Simulations give the additional information that very large anisotropy should stabilize thin lanes.

Thus, we can conclude that microscopically, collective migration in HBECs relies on the ability of cells to self-propel and realign their polarization in the direction of their velocity and on soft repulsion between neighboring cells. The anisotropy introduced by the grooves favors the emergence of large-scale collective migration and stabilizes a laning pattern. The laning transition can be observed in cell populations in which the strength of the velocity-polarization coupling and the strength of repulsion between contacting cells are high enough. As no adhesion between particles was included in the model, we further validated that cell-cell adhesion is not necessary in the emergence of laning.

3.6. Conclusion and perspectives

We experimentally observed a transition from a nematic chaotic state to polar laning in HBEC confluent monolayers mediated by collective contact guidance. The laning pattern is not periodic and lane width ranges from 100 μm to a few mm while lane length is larger than 3 mm. In each lane, the cells migrate in a plug flow and the shear between two lanes is localized between two rows of cells. We quantified the laning state that is characterized by large correlation in the y direction and increasing correlation length in the x direction when increasing groove depth. The transition is independent from cell division and cell-cell adhesion. The facts that in each lane the cells select a preferred velocity, that the pattern is not periodic, and that cell contractility is secondary in the laning emergence compared to the ability of cells to protrude in a directed manner, show that the laning state observed is a phenomenon fundamentally different from the nematic laning previously observed in endothelial cells or microtubule-kinesin systems.

Thus, we proposed a hydrodynamic description of active polar fluids that captures well our results. We show that our system undergoes a disorder-to-order transition controlled by active polar traction forces and polarization-velocity coupling. The effect of the grooves is well-described by introducing anisotropy in the friction that both favors the transition and selects a laning pattern in the ordered state. Self-propelled particle-based simulations confirm these results and reproduce semi-quantitatively the laning pattern observed experimentally, including the plug flows, the localized shear, and the distribution of lane width. Additionally, as the simulations rely on excluded volume interactions and do not encapsulate adhesion, we further validate that cell-cell adhesion is not necessary for such large-scale collective migration, but strong enough excluded volume interactions are.

In this project, we also tested other cell types and found that they respond differently to the contact guidance cues presumably because they explore different regimes. The next step of this project would be to better link the theoretical parameters to the cell machinery to predict if a given cell type will experience large-scale polar laning. Impairing the formation of the branched actin network is thought to decrease the ability of cells to exert polar traction forces and indeed inhibits laning in HBECs. However, what is the biological mechanism of excluded volume interactions or polarization-velocity coupling is an open question. To answer that, one would need to identify the biological definition of polarization at the microscopic level.

For example, HT1080 fibrosarcoma cells that also have a chaotic behavior do not experience large-scale collective migration. It would be of interest to identify which microscopic ingredients among polar traction forces, polarization-velocity coupling and excluded volume interaction strength is too low compared to HBECs to support polar laning. HT1080 could be more deformable and invasive, or not able to align velocity and polarization, or exert too low polar traction forces on the substrate. A strategy to decipher the microscopic differences in term of cell-substrates interactions would be to perform traction force microscopy in confluent HBEC and HT1080 monolayers and to compare the value of the traction forces and the alignment between traction forces and velocity for these two cell types.

An interesting point raised by this work is also the fact that HBECs experience a transition from a chaotic dynamic with characteristics of active nematic systems to a laning state with characteristics of active polar systems. This aspect is not encapsulated in the theoretical descriptions proposed as we considered the

initial state to be fully disordered. Extension in the theoretical description could be proposed to fully capture the transition from nematic chaos to polar laning by considering both a nematic and a polarization field. For the simulations, better describing the nematic chaotic state would require adding anisotropy in the particle shape and nematic aligning interactions. We hypothesize that in both cases, the polar terms will get dominant in the ordered phase and that laning will be conserved. Indeed, it has been suggested theoretically that fluctuations of the polar traction forces exerted by the cells on their substrate can lead to an effective active nematic stress after coarse graining the polar orientation field^{126,127}. The grooves in our experiments reduce the fluctuations which could explain that the nematic signatures disappear to the advantage of polar signatures.

Although we did not identify *in vivo* situations in which the laning phenomenon is at play, such large-scale collective behaviors triggered by substrate anisotropy may be involved for example in development or tissue regeneration. Finding a role for laning *in vivo* would be a major achievement. In particular, HBECs are bronchial cells and dysfunctions such as asthma have been linked to delayed jamming of the monolayers¹²⁸. To start with, we could investigate the impact of asthma or oncogene mutations on the laning emergence in HBEC monolayers.

Finally, we think that our results are general in polar active matter on 2D substrates in which particle displacements are biased along a given orientation without imposing a preferred direction. By biasing trajectories orientation, laning should be observed in colloidal rollers populations or crowds of robots for example.

4. Crisscross bilayering of myoblasts controlled by collective contact guidance

4.1. Motivations: between 2D and 3D, multilayering in cell populations.....	97
4.1.1. Multilayered tissues <i>in vivo</i>	97
4.1.2. Engineering multilayered tissues.....	99
4.1.3. Spontaneous multilayering <i>in vitro</i>	100
4.1.4. Spontaneous 2D to 3D transitions at topological defects	102
4.1.5. Scientific question and experimental set-up	105
4.2. Orthogonal bilayering at a perpendicular interface.....	107
4.2.1. The perpendicular interface triggers large-scale bilayering.....	107
4.2.2. The interface induces a steep orientation gradient	107
4.2.3. A bilayering front spontaneously forms at the interface and propagates	110
4.2.4. Cells in the progressing top layer are oriented perpendicularly to bottom cells.....	112
4.2.5. Flows involved in orthogonal bilayering progression.....	114
4.2.6. The cell reservoir is not needed for crisscross bilayering initiation and progression	117
4.2.7. Summary: description of bilayering at a perpendicular interface.....	119
4.3. Impact of the orientation mismatch at the interface.....	120
4.4. Discussion	123
4.4.1. Formation of orthogonal bilayers at large scales	123
4.4.2. In the top layer, cells migrate perpendicularly to their long axis.....	124
4.4.3. ECM orientation guides cell migration in the top layer.....	125
4.4.4. C2C12 flows: contractile vs extensile?	126
4.5. Active nematic fluid description	128
4.5.1. Expected flows and forces in an active nematic layer at an interface	128
4.5.1.1. <i>Active nematic orientation imposed by the substrate</i>	128
4.5.1.2. <i>Constitutive and conservation equations</i>	130
4.5.1.3. <i>Analytical profiles and comparison with experiments</i>	131
4.5.1.4. <i>Estimation of the screening length</i>	133
4.5.2. Flows prediction in chevron geometries	134
4.5.3. Toward a two layers model	138

4.6. Conclusion and perspectives.....	139
4.6.1. Conclusion	139
4.6.2. Role of cell division, cell contractility, cell-cell, and cell-substrate adhesion.....	139
4.6.3. ECM-mediated interactions between the two layers	140
4.6.4. Impact of cell chirality	140
4.6.5. Building more complex flows and structures through micropatterning	140

4.1. Motivations: between 2D and 3D, multilayering in cell populations

The previous chapter focused on the early dynamics of epithelial cells that maintain a 2D monolayer structure. In contrast to epithelia, other tissues organize usually with a 3D architecture. To study their formation, behavior, and response to perturbations, 2D *in vitro* models are insufficient and 3D *in vitro* models such as organoids have been developed. However, the organization of tissues can be more complex than purely 2D cell sheets or 3D spheroids. This chapter is dedicated to the formation of intermediate structures of stacked layers of cells.

4.1.1. Multilayered tissues *in vivo*

Stratified epithelia such as the skin epidermis are examples of multilayered tissues. Properties of each layer, such as the shape and type of cells, the 2D organization, the amount of keratin and cell division, vary from the basal to the apical part of the tissue. Here, we focus on multilayered tissues resulting from the stacking of similar and well-formed 2D cell sheets.

This kind of organization is common *in vivo* and can be found for instance in the media of elastic arteries, that is composed of stacked layers of smooth muscle cells and elastic lamina. These intermediate layers wrap around the vessel, but each layer has a tilted orientation that alternates across the different layers (Figure 4.1.B). This complex “herringbone” structure is thought to provide mechanical strength to the artery wall^{129,130}.

Similar stacked structures are also found in animals that lack a rigid skeleton and rely on a hydrostatic skeleton to support their shape, deformations and motions¹³¹. Typically, these structures have a cylindrical shape and are filled with water-based (incompressible) medium, so that their volume is fixed. These cylindrical cavities are surrounded by muscle layers with a well-defined orientation of fibers, which fixes the direction of contraction. Common muscle fiber orientations found in hydrostatic skeletons are presented in Figure 4.1.A. The contraction of circular, radial, or transverse muscle fibers, is responsible for a decrease in diameter and results in the elongation of the structure. Conversely, the contraction of longitudinal fibers allows for retraction of the length and expansion of the diameter. Coordinated contraction of these layers allows for complex deformations such as bending or motion.

The same organization is also found in the intestine. It is composed of an epithelium surrounded by discrete layers of smooth muscle cells: an inner layer of circumferentially aligned muscles, that is orthogonal to an outer longitudinally aligned layer¹³² (Figure 4.1.C). This organization allows for peristalsis: a wave of coordinated contraction and relaxation of the tube diameter, propelling digested contents through the gastrointestinal track (Figure 4.2.B). Invertebrate earthworms also rely on a hydrostatic skeleton and use the same kind of mechanism to drive their motion (Figure 4.2.A). Polyps such as Hydra are other organisms that rely on a hydrostatic skeleton to deform. The Hydra has a simple uniaxial body plan, with a head on one end and a foot on the other. Its body is mainly tubular, filled with water and made of a bilayer of epithelial cells. The supra cellular actin fibers at the interface between the two cell layers are orthogonally oriented: in the

4. Crisscross bilayering of myoblasts controlled by collective contact guidance

outer layer (the ectoderm), they align along the body axis, whereas in the inner layer (the endoderm), they orient perpendicular to the body axis¹³³ (Figure 4.1.D).

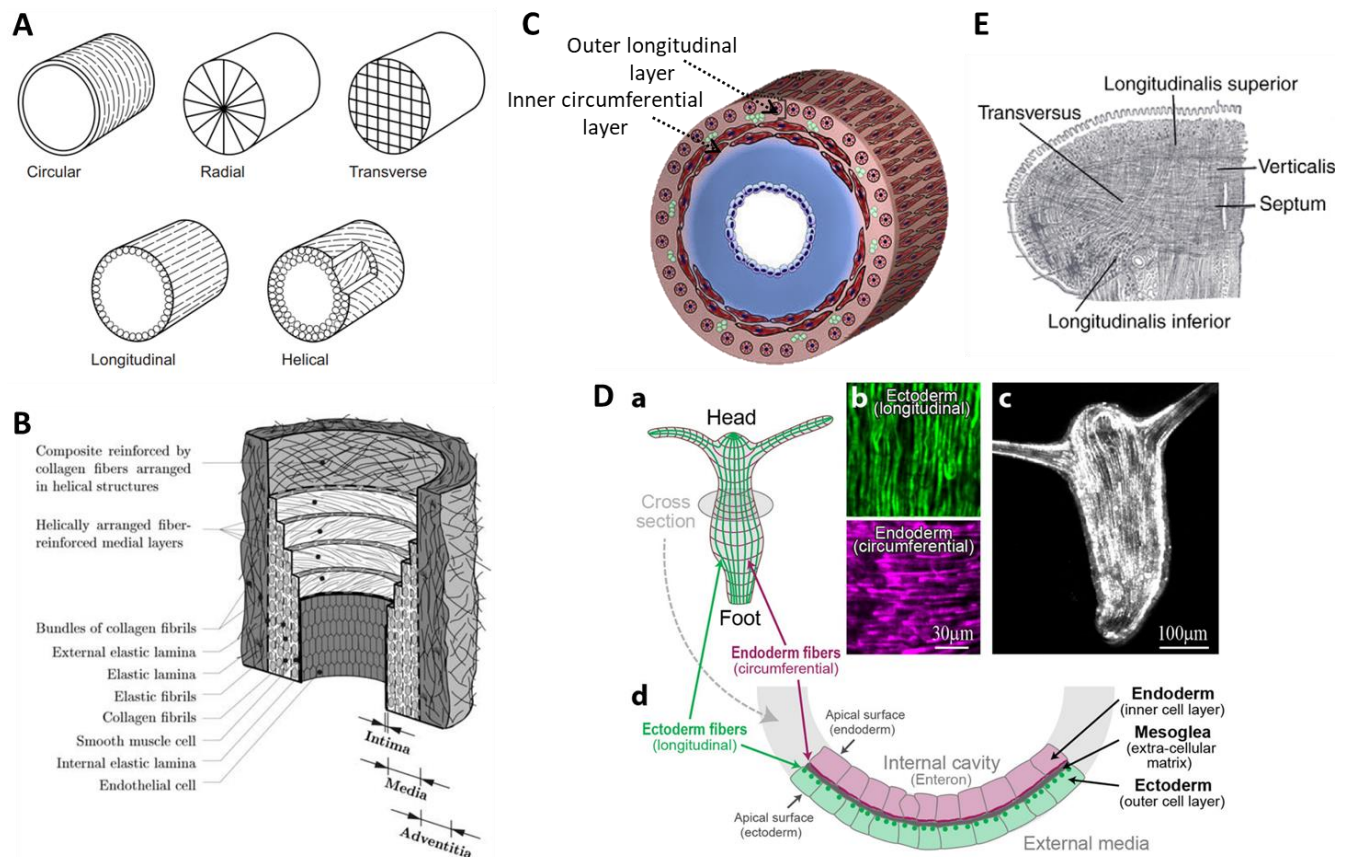


Figure 4.1 : Hydrostatic skeletons and muscular hydrostats in vivo.

A: Schematic diagram illustrating common muscle fiber orientations found in hydrostatic skeletons¹³¹.

B: Schematic model presenting the organization of a healthy elastic artery¹³⁰. The “herringbone” structure of the media gives mechanical strength to the artery wall.

C: Orthogonal organization of smooth muscle layers around the gastrointestinal track, adapted from¹³².

D: Structure of a mature Hydra¹³³. a: Schematic illustration showing that supracellular actin fibers orient along the body axis in the outer layer (green) and perpendicular to the body axis in the inner layer (purple). b: Corresponding fluorescent images of the supracellular actin fibers. c: Image showing the supracellular ectodermal actin fiber organization in a small mature Hydra. d: Schematic illustration of a perpendicular cross-section of the tubular Hydra body showing that the perpendicularly oriented actin fibers are located at the interface between the two cell layers.

E. Tongue anatomy: intrinsic muscles in a coronal cross-section of the mammalian tongue¹³⁴. Muscle fibers form a complex 3D array supporting tongue’s movements and deformations.

Conversely to hydrostatic skeletons, muscular hydrostats are not filled with liquid. They are muscle structures consisting of densely packed, three-dimensional arrays of muscle cells that use their intrinsic incompressibility to transmit forces through internal pressure. Their complex structure and constant volume allow for highly controlled movements and deformations. Arms and tentacles of cephalopods, tongues of many vertebrates and elephants’ trunks are muscular hydrostats¹³¹. The elephant trunk has the particularity to contain muscle fibers oriented helically around the organ’s long axis, allowing for torsion or twist in either direction. The mammalian tongue is a muscular hydrostat composed of intricate muscle fibers arrays orthogonally aligned with each other in all directions¹³⁴ (Figure 4.1.E). This complex structure allows the tongue to perform an almost limitless number of possible deformations¹³⁴.

Thus, structures of stacked well-organized layers of smooth muscle cells are central in the functioning of a wide range of animals and organs.

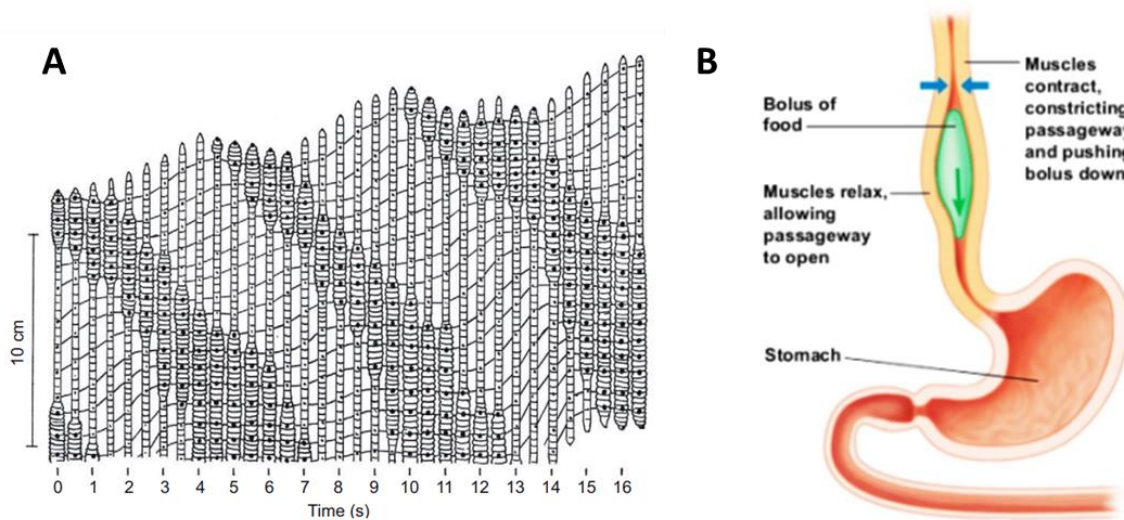


Figure 4.2 : Peristaltic movements in animals' motion and digestion.

A: Diagram showing peristaltic-based locomotory cycle of an earthworm. Regions undergoing longitudinal muscle contraction are stationary (indicated by large dots) and are drawn twice as wide as regions undergoing circular muscle contraction. Time tracks of individual points are indicated by the lines connecting each drawing (Gray and Lissman, 1938)¹³¹

B: Peristaltic movements in the human gastrointestinal track lead to proper digestion, schematic taken from <https://www.embibe.com/exams/peristalsis/>.

4.1.2. Engineering multilayered tissues

In vitro strategies to build multilayered structures have been developed in the context of tissue engineering. Tissue engineering aims at finding techniques and strategies to reconstruct a part or an entire functional organ to either repair damaged tissues or use it as an *in vitro* model for drug discovery. Research in this field addresses most of the tissues found in the human body, including cardiac¹³⁵ and muscle tissues¹³⁶.

The simplest idea to repair a damaged tissue is to deliver directly at the location of the wound products or dissociated cells to stimulate regeneration *in situ*. However, cell survival or anchoring at the right location is not always satisfactory. Another idea is then to engineer *in vitro* a tissue that resembles the native tissue using biocompatible “scaffolds” and to transplant it with its supporting structure. The scaffold is designed to provide a 3D environment that mimics the morphology and composition of the host to promote cell adhesion and proper functional tissue self-organization. Most of the scaffolds are designed to be degraded gradually as the tissue regenerates. This method has some drawbacks including the risk of immune rejection of the scaffold before degradation. To overcome these issues, scaffold-free methods have been developed such as decellularized tissues used as support, 3D bioprinting and self-assembly techniques using only patients' cells stimulated to produce their own scaffold¹³⁷. However, these techniques, because of the large final proportion of ECM and because of the low control on cell spatial organization, are not adapted to produce cell-dense tissues with complex 3D structures.

To produce cell-dense tissues with a physiological architecture, “cell sheet engineering” is a promising technology^{138,139}. It consists in fabricating functional 3D tissues by stacking confluent cell monolayers. To do that, cells are seeded on a culture dish coated with thermo-responsive polymers, such as poly(N-isopropylacrylamide). At 37°C, cells adhere to the surface and grow as a monolayer, whereas, at lower temperature, the cell monolayer detaches from the surface while preserving strong cell-cell adhesions and its underlying ECM. This cell sheet can be manipulated and stacked onto another cell sheet (Figure 4.3.A). Repeating this procedure allows for multilayer fabrication. As the cells-secreted ECM is preserved, the resulting tissue adheres easily to a damaged host organ without the need of sutures or scaffolds, improving regeneration in various animal models. Clinical trials using cell sheet technology are ongoing for several tissues (heart, esophagus, cornea, etc.)¹³⁸.

In the context of arteries or muscles, the alignment and orientation of cells within layers is crucial for proper mechanical and biological properties (see 4.1.1). To align cells within the monolayer before harvesting it, several microfabrication techniques can be used, such as grafting thermo-responsive polymers on grooved substrates or directly chemically patterning thermo-responsive surfaces. These anisotropic surfaces have both the ability to orient cells and to allow detachment of the aligned cell monolayer. Thus, the sheets can be stacked with controlled and varying orientations through layers (Figure 4.3.B). For example, stacking aligned cell sheets into a herringbone configuration characteristic of the native medial layer of elastic arteries has been successfully performed (Figure 4.3.C). It gives hope to produce tissue engineered vascular patches that mimic the complex structure and function of the native artery, to cure congenital heart defects requiring vascular reconstruction¹⁴⁰. Similarly, C2C12 myoblasts (muscle precursor cells) have been successfully stacked perpendicularly¹⁴¹. This bilayered tissue robustly maintains for at least 3 days both individual layer orientation and the specific 90° angle mismatch characteristic of the intestine muscle layers¹⁴¹ (Figure 4.3.D).

Thus, by stacking well-formed layers of cells, *in vitro* complex tissues such as muscles can be reconstructed. With this technique, the whole structure is engineered layer by layer and the result in terms of biological and mechanical functions might be different than the *in vivo* native structures that self-organize during development. However, how such multilayered tissues can spontaneously develop and self-organize has not been extensively investigated. In the following, we report situations in which well-organized multilayered systems spontaneously form *in vitro*.

4.1.3. Spontaneous multilayering *in vitro*

In vitro, the spontaneous formation of well-organized cell multilayers has first been observed more than 50 years ago by T. Elsdale and colleagues in cultures of embryonic human lung (EHL) fibroblasts. Those cells are elongated and tend to align with each other. They first form a monolayer that is composed of domains of well-defined orientation that are disorganized at large scales. When culturing them further, cells spontaneously organize into a thick superimposition of cell layers, cells in successive layers being perpendicularly oriented¹⁴² (Figure 4.4.A). This “crisscross” multilayering is highly dependent on cell-secreted ECM. Thus, T. Elsdale and colleagues hypothesized that fibroblasts secrete a rich collagen ECM, allowing cells to migrate on top of the first cell layer, creating this way a crisscrossed second layer.

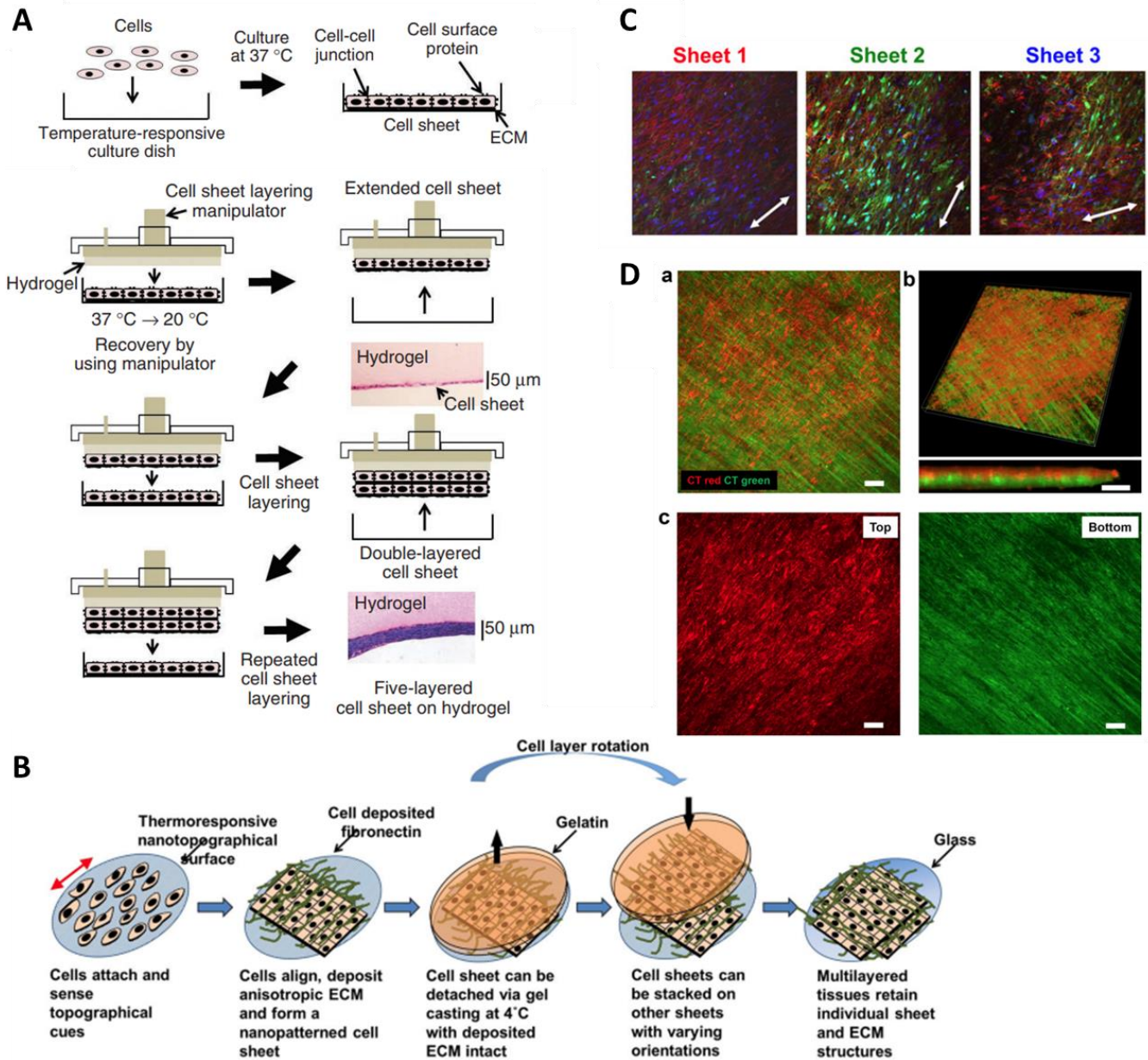


Figure 4.3: Fabrication of multilayered tissue with controlled layers' orientation by cell sheet engineering

A : Fabrication of 3D cell-dense tissues is performed by stacking cell sheets cultured on temperature-responsive dishes and harvested using a hydrogel-coated manipulator, adapted from ¹³⁹.

B : Thermo-responsive nanofabricated substrata can be used to stack anisotropic cell sheets with varying cell and ECM orientation between layers ¹⁴³. The double-headed red arrow indicates nanostructures' orientation.

C : Three anisotropic sheets of primary human mesenchymal stem cells from bone marrow stacked at different angles in a "herringbone" like structure ¹⁴⁰. Sheets 1 and 3 are labeled with Rhodamine-Phalloidin (red); sheet 2 is labeled with Cell Tracker Green. The double-headed white arrows indicate the cell orientation in the 3 cell sheets.

D : Two layers of C2C12 mouse myoblasts have conserved orthogonal orientation 3 days after being orthogonally stacked. (a) Max projection confocal image of a z-stack. Top (Bottom) layer is stained with red (green) membrane dye. Scale bar: 100 μm. (b) 3D tissue rendering utilizing confocal z-stack images. Scale bar: 40 μm. (c) Confocal image of top and bottom sheets. Scale bar: 100 μm.¹⁴¹

4. Crisscross bilayering of myoblasts controlled by collective contact guidance

Multilayer organization of spindle-shaped cells depends on the tissue the cells are extracted from. For examples, fibroblast-like cells from chick embryos form aligned domains with parallel bilayering for skin cells and orthogonal bilayering for heart cells¹⁴⁴. In a more recent study, authors produced a tissue with a self-assembly method by seeding cells on microstructures and letting the tissue self-organize into a bilayer structure, the bottom layer being aligned with the microstructure. For corneal fibroblasts and smooth muscle cells, cells in the top layer display a well-defined angle mismatch with cells in the bottom layer, which is reminiscent of herringbone like structures (Figure 4.4.B.1, B.2), while they are randomly oriented for dermal fibroblasts (Figure 4.4.B.3, B.4), similar to the native tissue arrangements¹⁴⁵.

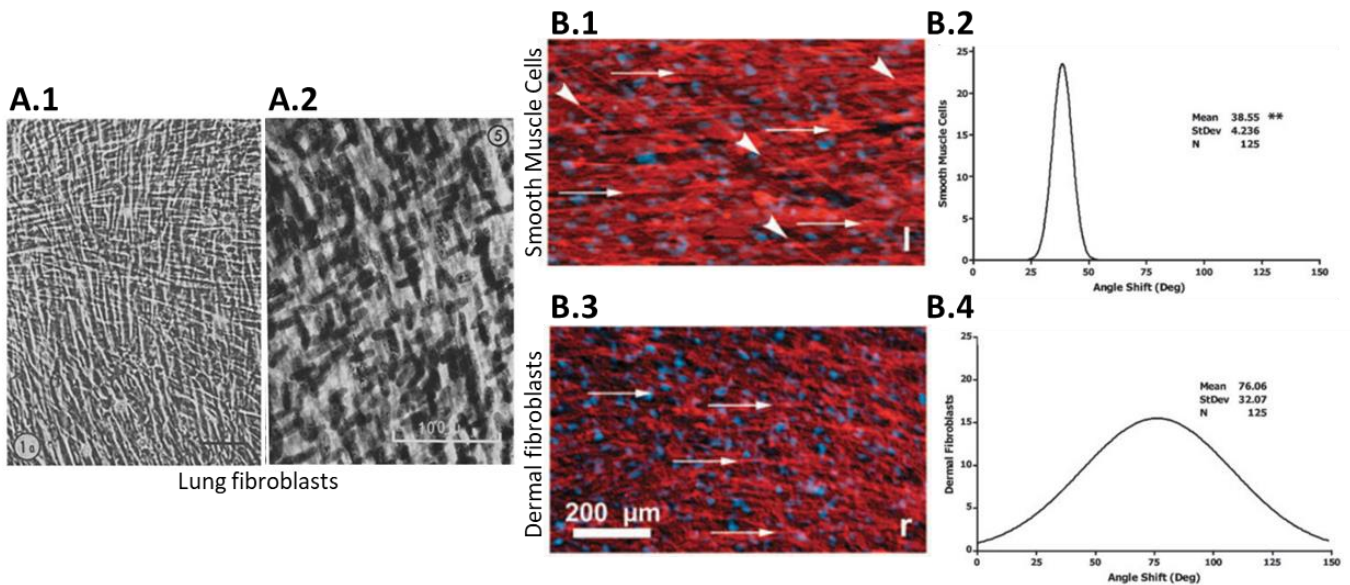


Figure 4.4 : Spontaneous formation of well-organized multilayered systems in vitro

A: Orthogonal multilayers in a dense culture of EHL fibroblasts, scale bars: 100 μm ^{142,146}.

B: Microstructures trigger the self-formation of cell bilayers with a well-defined angle mismatch for smooth muscle cells (B.1, B.2) but the top layer is randomly organized for dermal fibroblasts (B.3, B.4).

B.1, B.3: Actin filaments (red) and nuclei (blue) are shown for cell populations cultured on grooved substrates at day 13. Gratings have a 4 μm period and a 1 μm linewidth. Normal white arrows represent gratings (and bottom cells) orientation. Head arrows indicate the top cell orientation that we can guess from the wide field fluorescent image in B.1.

B.2, B.4: Normal distribution of angle mismatch between layers measured for each cell type. The second layer of smooth muscle cells displays a 39 ± 4 degree shift from the first cell layer (B.2), whereas the dermal fibroblasts' angle shift was 76 ± 32 degrees (B.4), suggesting that this cell type does not organize in a well-controlled 3D structure.

The mechanism of formation of these well-oriented multilayered structures is not known. Recent studies have tried to identify at which location is initiated the transition from a 2D cell monolayer to a 3D multilayered system. Notably, based on the theoretical framework of active matter, this transition has been related to local discontinuities in the orientation field, namely to topological defects.

4.1.4. Spontaneous 2D to 3D transitions at topological defects

T. Elsdale observed that the formation of crisscross bilayers originates at non-motile frontiers between well-aligned cellular domains that meet with non-parallel confrontations with a large enough angle^{142,147} (Figure 4.5.A). In the framework of active matter and liquid crystals, we now understand that these structures

appear notably at topological defects in the orientation field. Recent studies in active biological matter have reported transitions from 2D monolayers to 3D structures at topological defects.

In murine neural progenitor cell monolayers, cell depletion is observed at $-1/2$ defects whereas cell accumulation arises at $+1/2$ defects in a form of 3D cellular mounds¹⁴⁸ (Figure 4.5.B). The same phenomenon has been observed in colonies of rod-shaped bacteria. In this system, cell accumulation at $+1/2$ defects leads to the formation of multilayers¹⁴⁹ (Figure 4.5.C). Both systems can be described as active extensile nematics. As explained in the introduction (see 1.2.4.3), the interplay between orientational gradients and active stresses leads to a net flow at $+1/2$ defect cores. The flows predicted by the active nematic theory at defects are in agreement with experimental flow measurements, cell accumulation at $+1/2$, and depletion at $-1/2$.

In MDCK monolayers, extrusion events have also been shown to localize preferentially at $+1/2$ defects¹⁵⁰. In this study, authors went one step further by inferring stresses inside the monolayer using Bayesian inversion stress microscopy. The stress maps around topological defects have the same patterns than the one predicted by the continuum theory of active nematics: topological defects are areas of high stress because of large distortions in cell orientation and active anisotropic stresses. They conclude that high compression at the head of $+1/2$ defects triggers cell extrusion and cell death.

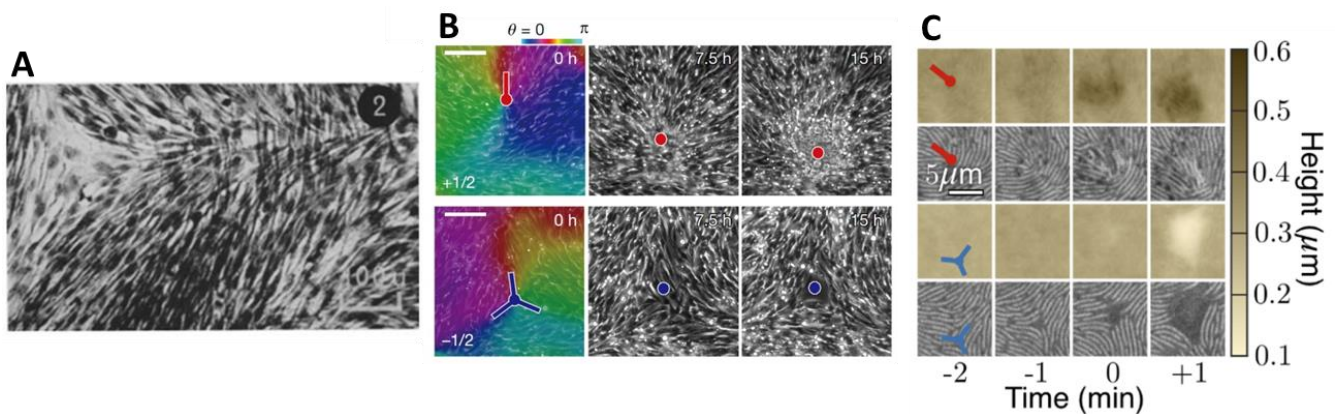


Figure 4.5 : Transition from 2D to 3D at topological defects in active biological matter.

A: Confluent EHL fibroblasts culture. Portions of three groups of parallel-arranged cells are shown. Orthogonal overlapping above the frontier between two of the groups is just commencing. Scale bar: $100 \mu\text{m}$ ¹⁴².

B: Time lapse of topological defects observed at a fixed position on glass in neural progenitor cell culture. The red and blue spots correspond to $+1/2$ and $-1/2$ topological defects, respectively. Color codes for cell orientation. Cell accumulation in a cell mound is shown at a $+1/2$ defect. Respectively, cell depletion is shown at a $-1/2$ defect. Scale bar: $100 \mu\text{m}$ ¹⁴⁸.

C: Snapshots of the height and reflectance fields of a bacterial population for a layer-formation event at a $+1/2$ defect (top), and a hole-opening event at a $-1/2$ defect (bottom)¹⁴⁹.

As presented in introduction, C2C12 myoblast monolayers are composed of domains in which cells orient in the same direction. Half-integer topological defects position between these domains. At later stages, C2C12 cells organize into crisscross multilayers⁵³ (Figure 4.6.A). Trinish Sarkar, a former PhD student in the team, analyzed the early dynamics of this active monolayer^{53,151} and in particular the evolution of the density of defects, that decays over time until reaching a finite non-zero value (Figure 4.6.B). In addition to classical self-propelled $+1/2$ defects (Figure 4.6.C.1) that annihilate with $-1/2$ defects, he identified stationary $+1/2$ defects around which the flows are reduced (Figure 4.6.C.2). Cells accumulate at the core of these immotile defects (Figure 4.6.D) and eventually migrate collectively on the apical side of the cells forming the tail of the

4. Crisscross bilayering of myoblasts controlled by collective contact guidance

defect (Figure 4.6.F). Cells in the top layer remain perpendicular to the cells in the bottom layer, which leads to the formation of perpendicular bilayers. This phenomenon is possible because C2C12 cells secrete ECM, on which other cells can adhere (Figure 4.6.E). We hypothesize that the final structure of the tissue results from the sum of this local orthogonal bilayering events and could be at stake in the development of such structures *in vivo*.

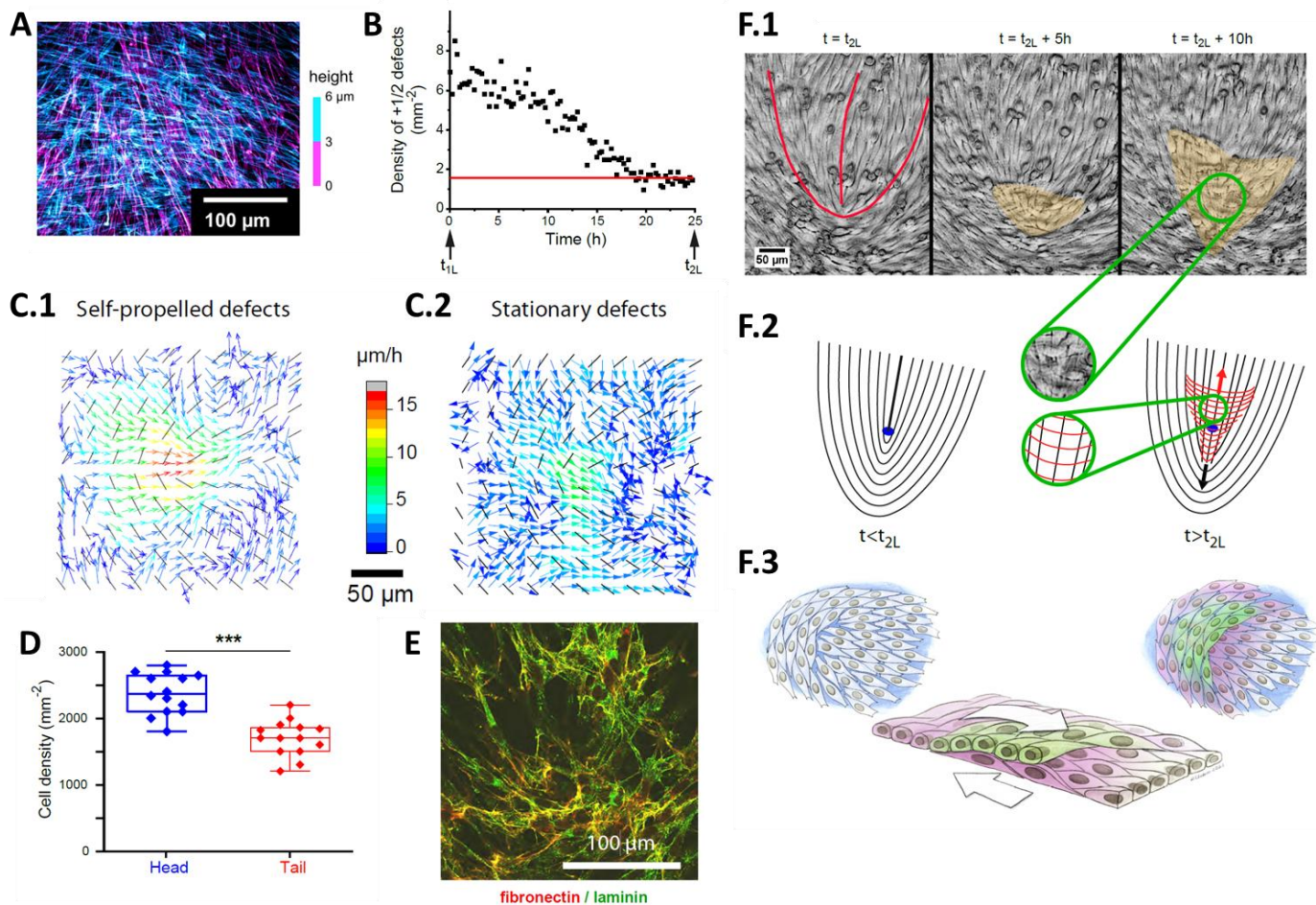


Figure 4.6 : Crisscross bilayering of C2C12 cell sheets initiates at +1/2 topological defects (adapted from ⁵³)

- A. Confocal image of a C2C12 culture showing the two layers that have orthogonal orientations. Fixed cells, actin labeling. The color codes for the height.
- B: The density of +1/2 defects decreases with time but plateaus at typically 2 defects/mm² several hours before the onset of bilayering (t_{2L}).
- C: Velocity fields of self-propelled (C.1) and stationary (C.2) +1/2 defects. Velocities are visualized with colored arrows. The color codes for the magnitude of the velocity. Orientations of the cells are given by the black lines.
- D: As cells at the head of the stationary defects flow toward their stationary core, the cell density increases at the head (measurements within 1h before bilayering).
- E: Fibrillar ECM is found between layers on a fixed multilayered sample. The confocal slice is between layer 1 and layer 2.
- F.1: Sequence of snapshots (phase contrast) illustrating the progression of the bilayering. The orange area highlights the crisscross bilayer. The outline of the defect at $t=t_{2L}$ is shown as a red line. F.2: Schematic of the bilayering process. The red lines correspond to the orientation field lines of layer 2 while the black lines refer to layer 1. The blue dot shows the initial position of the core. Note the crisscross organization of the two layers when $t>t_{2L}$ (insets). F.3: Artist view of the bilayering process. Purple (respectively green) is used to represent bottom (respectively top) layer.

These previous studies therefore showed a clear correlation between +1/2 defects and extrusion or multilayering events. For C2C12 cells that secrete ECM, local multilayering events at stationary +1/2 defects add up and contribute to the formation of crisscross stacked layers. However, the mechanism explaining these observations is not clear.

One of the difficulties in the study of multilayering is that crisscross bilayers form at +1/2 defects that are randomly positioned in the monolayer. Thus, it is difficult to precisely monitor and perturb these bilayering events to fully investigate the underlying mechanism. In particular, orientation gradients in cell monolayers are spontaneously generated and are not controlled. Consequently, the role of orientation gradient steepness and spatial organization in multilayering can't be tested.

From a tissue engineering point of view, the simultaneous crisscross bilayering initiation at random locations in the monolayer prevents from controlling the final structure of the bilayer at large scales. The self-formation of macroscopic tissues made of stacked muscle layers with well-defined orientation would be a significant progress for tissue repair and drug discovery.

4.1.5. Scientific question and experimental set-up

Inspired by the formation of crisscross bilayers at +1/2 defects, we hypothesized that we could generalize this observation and control large-scale (\sim cm) crisscross bilayers by imposing the cell orientation on a "stretched" +1/2 defect (Figure 4.7.A, B). To impose cell orientation in such a spatial configuration (Figure 4.7.B), we use the strategy of contact guidance. We thus designed a micro-grooved substrate composed of vertical grooves on the left part and horizontal grooves on the right part (Figure 4.7.C) (see chapter 2 for experimental details). In the following, I refer to this geometry as the "perpendicular interface".

This geometry creates a strong orientation gradient at a fixed interface that can induce flows and ultimately bilayering at a larger scale and in a well-controlled geometry (Figure 4.7.C). This setting could facilitate the investigations on the formation mechanism for self-organized bilayering. In particular, the geometry can be tuned to challenge the bilayering mechanism. For instance, varying the angle of the grooves in the right part of the interface allows investigating the role of the orientation gradient in bilayering events. Based on experimental results obtained with this set up, that we complemented by a theoretical continuum description of active nematics, we aim at answering the following fundamental questions:

- Is it possible to successfully trigger the self-formation of well-organized bilayered cell structures on centimeter scales by engineering the cell substrate?
- What is the mechanism underlying bilayer formation in C2C12 myoblast monolayers?

To investigate these questions, we seed cells on micro-grooved PDMS substrates fabricated with the perpendicular interface geometry (Figure 4.7.C) at a density of 100 000 cells/cm². Cells are allowed to adhere and grow for approximately 1 day before imaging. The origin of time is taken either at cell seeding or at the time when confluence is reached. The second option is chosen when data are averaged over repeats from different FOVs from independent wells and experiments. Confluence is defined visually for each FOV as the time at which no holes are observed anymore in the entire FOV and is usually reached around 30 hours after cell seeding. Difference in time of confluence is due to inhomogeneity in the initial cell seeding density. The

4. Crisscross bilayering of myoblasts controlled by collective contact guidance

conventions used to describe experimental results are presented Figure 4.7.C. We will use the cardinal points to describe the direction of cell displacement and the cell orientation. The origin of the x axis is set at the interface position.

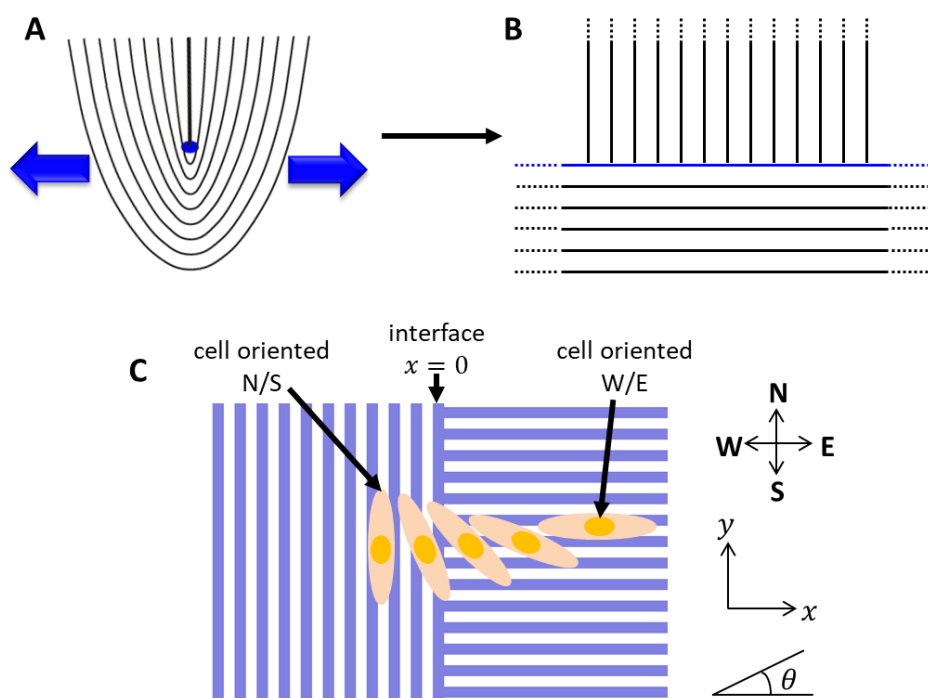


Figure 4.7 : Principle and description of the experimental set-up

A, B: We aim at generalizing and scaling up the observations of crisscross bilayering at spontaneous $+1/2$ defects (A) by imposing the cell orientation in a “stretched” defect configuration (B). In the normal $+1/2$ defect geometry, the orientation mismatch is localized at the core (blue point in A) while in the “stretched” $+1/2$ defect geometry, the orientation mismatch is localized along an infinite line (blue line in B). The black lines highlight cell orientation around a $+1/2$ defect in A and cell orientation that we want to impose using contact guidance in B.

C: Schematic diagram of the designed micro-grooved substrate (“perpendicular interface”) and expected cellular orientation. Groove and ridge width is $4\ \mu\text{m}$, groove depth is typically $1.5\ \mu\text{m}$ (between $1.3\ \mu\text{m} - 1.6\ \mu\text{m}$). C2C12 myoblasts are more elongated in shape than HBECs, their length and width are typically 50 and $10\ \mu\text{m}$. The conventions used in the manuscript are presented at the top and the right of the schematic. In particular, the angles are measured with respect to the x axis, and we use the cardinal points to describe cell orientation and cell displacement direction. The origin of the x axis is set to the interface position. Note that similarly to the experimental set-up in Chapter 3, the total grooved area is deposited in a well of a 12 well glass-bottom plate and is $13 \times 13\ \text{mm}$ in size. The interface is in the middle of the grooved area and its total length is thus $13\ \text{mm}$.

The first step in this project was to optimize the substrate treatment. Several surface treatments were tested and lead to different C2C12 monolayer evolution at a perpendicular interface. These results are presented in Annex 6.5. The best results were obtained when the PDMS substrates were plasma treated, allowed to rest for approximately 8 hours and coated with fibronectin. In the following, the substrates were treated using this procedure. The next section presents the monolayer evolution on a perpendicular interface.

4.2. Orthogonal bilayering at a perpendicular interface

4.2.1. The perpendicular interface triggers large-scale bilayering

First, we seed C2C12 myoblasts on a perpendicular interface micro-grooved substrate and monitor the evolution of the monolayer using fluorescence microscopy. Cells successfully spread and form a confluent monolayer in which cells orient along the grooves in both sides of the interface, the orientation sharply changing from N/S to W/E at the interface (Figure 4.8. top left image, Figure 4.9.A). I first qualitatively describe a representative fluorescent movie whose snapshots at different time points can be found in Figure 4.8. Note that all images were acquired and are displayed in the same conditions so that an increase in brightness can be directly related to an increase in cell density.

Over time, the images get increasingly brighter. Thus, we conclude that density increases in both sides of the interface leading eventually to a multilayered structure. We observe a collective migration from the interface eastward. It corresponds to the formation of a new layer on top of the bottom layer formed by cells that are extruded at the interface and collectively migrate eastward. This can explain why the cell density in the west zone near the interface is lower than in other locations 25 hours after confluence and later. The top layer formed by eastward migration is delimited by the interface (blue dotted line) and by a front of maximal intensity (magenta dashed line). In the following, we refer to this front as the “bilayering front”. The bilayering front that propagates from west to east becomes increasingly brighter, suggesting an increase over time of cell density at this location. 70 hours after confluence, the bilayering front has propagated through the whole FOV.

We thus succeed to form bilayers over more than a cm long interface and over a few hundred micrometers in width, without stacking layers but only relying on a spontaneous bilayering mechanism at a perpendicular interface. We now quantify this phenomenon and investigate the structure of the bilayers formed this way. The first step toward bilayering is to induce a gradient of orientation. Next, we quantify the orientation gradient imposed at the interface.

4.2.2. The interface induces a steep orientation gradient

At confluence, C2C12 cells form a monolayer that aligns with the grooves (Figure 4.8. top left image, Figure 4.9.A). At the discontinuous interface between perpendicular orientations, cells change their orientation sharply (Figure 4.9.A). However, they can do so by changing their orientations with positive angles (90° to 0° from west to east) or with negative angles (-90° to 0° from west to east) (Figure 4.9.B). For this reason, alternating $+1/2$ and $-1/2$ defects are found along the interface (Figure 4.9.C).

To quantify the orientation evolution in the monolayer across the interface, it is common to average the measured quantities along the y direction to work with 1D averaged profiles. A similar strategy is used below to quantify cell flows. However, the topological defects at the interface prevent us from considering the system as quasi 1D. Indeed, cell reorientation with positive or negative angles would lead to angles averaged

4. Crisscross bilayering of myoblasts controlled by collective contact guidance

to zero at the interface. I thus decided to introduce a 10° angle in the east part of the grooves, breaking the symmetry of the perpendicular setting and hoping that this small angle wouldn't impact significantly the bilayering progression. In this configuration, topological defects at the interface disappear (Figure 4.10.A), allowing to average quantities over y . Unless otherwise stated, the grooves at the east of the interface have this 10° tilt in the following, to get rid of complications introduced by topological defects. I refer to this geometry as the "10° interface".

Figure 4.10.B shows the cell orientation profile across the interface. Cell orientation is precisely fixed by the grooves' orientation far from the interface and changes sharply at the interface from 90° to 10° on a $200\ \mu\text{m}$ distance which corresponds to 4 cell lengths approximately. This steep gradient is a necessary ingredient to trigger bilayering at the interface. In the following, I describe in more details the dynamics of cell sheets on 10° interfaces.

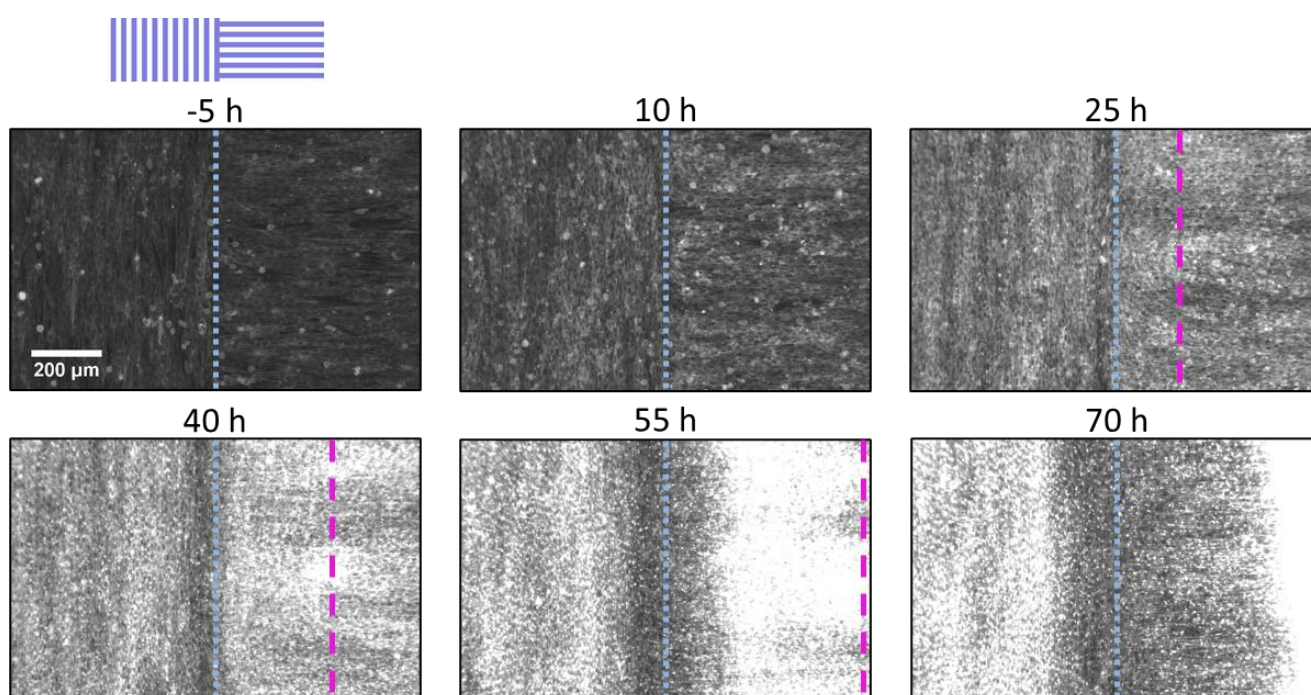


Figure 4.8 : Evolution of a C2C12 monolayer on a perpendicular interface micro-grooved substrate. Fluorescent images are displayed for different times, indicated in hours after confluence (reached 30 h after cell seeding). Schematic of the underlying substrate is shown at the top left. Blue dotted lines indicate interface position. Magenta dashed lines highlight the bilayering front. The bilayering front corresponds to the zone delimitating the migrating top layer at the east of the interface. Here, the bilayering front position is qualitatively estimated as the zone of higher intensity. Note that a second layer appears at the east of the interface between 10 to 25 hours after confluence and propagates eastward. 70 hours after confluence, the bilayering front is outside the FOV. Note also that all images share the same intensity normalization so that an increase in brightness can be directly linked to an increase in cell density.

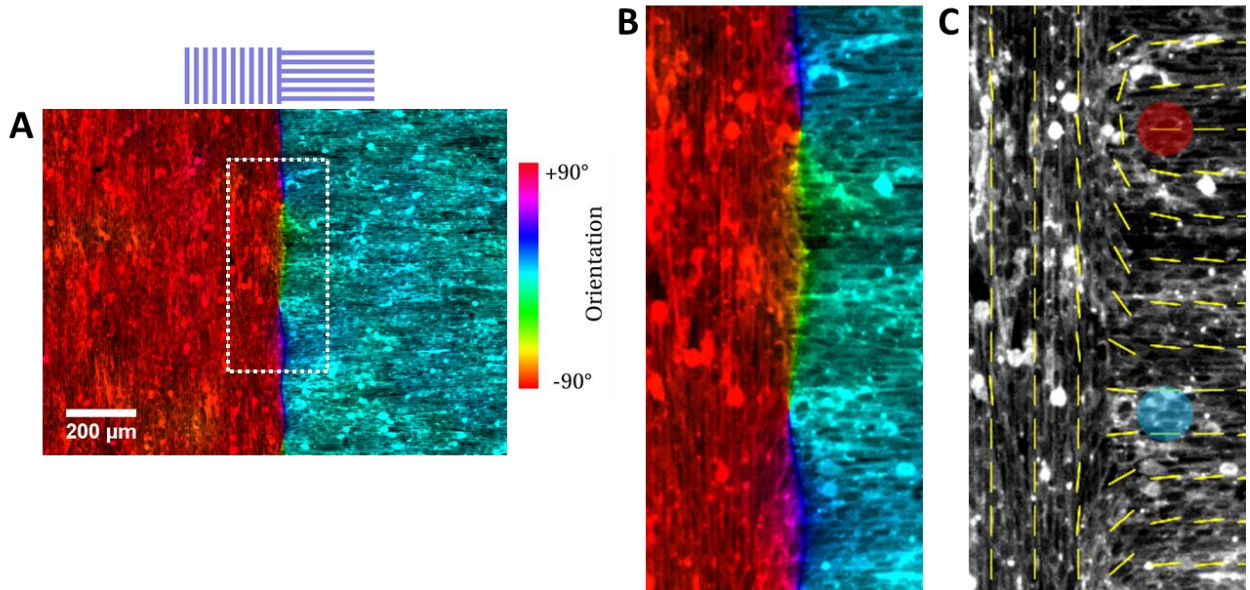


Figure 4.9 : C2C12 cells' orientation on a perpendicular interface at confluence.

A: Fluorescent image showing cellular actin tagged with mCherry overlaid with the color-coded orientation.

B: The zoom in the color-coded image (dashed box in A) highlights that the cells can reorient with positive angles (bluish colors) or negative angles (yellowish colors).

C: The orientation field representation of cellular orientation helps us identify alternating $+1/2$ and $-1/2$ topological defects highlighted respectively with red and blue transparent dots.

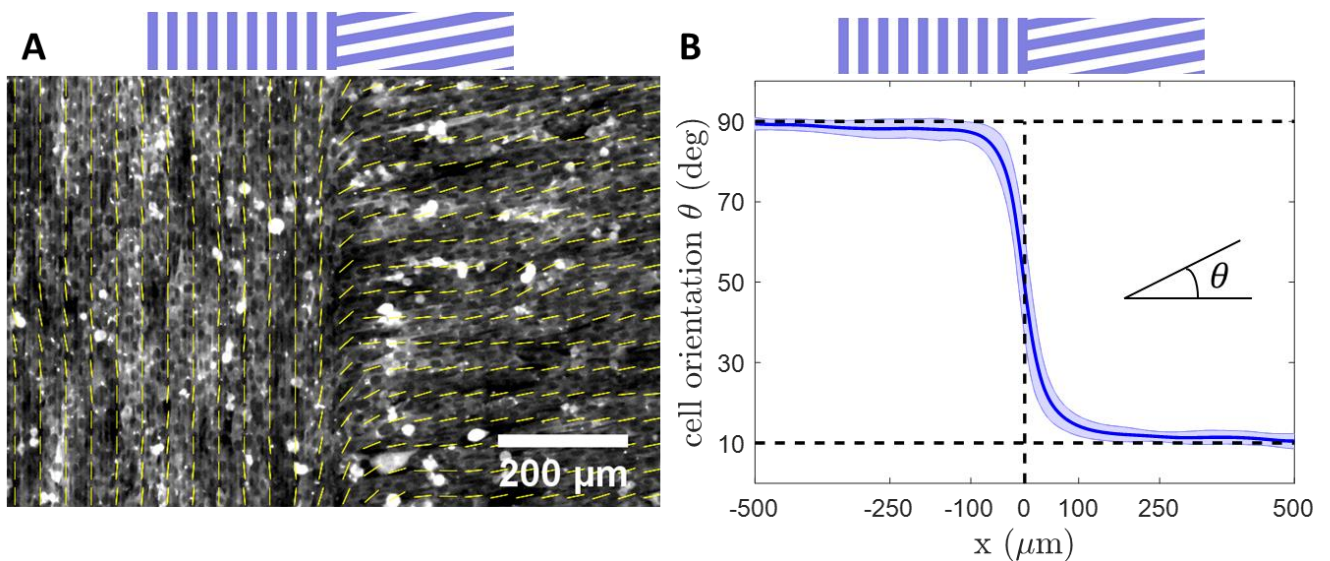


Figure 4.10 : Cell orientation on a 10° interface.

A: Fluorescent image of a C2C12 monolayer at confluence on a 10° interface overlaid with the cellular orientation field. No defect is found at the interface. The geometry of the substrate is shown in the top schematic.

B: Cell orientation across the interface at confluence. Data are averaged along the interface and over 30 FOVs from 6 different wells from 2 independent experiments (5 separated $1.3 \text{ mm} \times 1.3 \text{ mm}$ FOVs were analyzed per well). Shaded area corresponds to the standard deviation to the mean over the different FOVs. The vertical dashed line highlights the position of the interface at $x = 0$ and horizontal dashed lines indicate $\theta = 10$ and 90° .

4.2.3. A bilayering front spontaneously forms at the interface and propagates

With the 10° interface geometry that suppresses the presence of topological defects at the interface, we still observe the formation of a bilayer from the interface and progressing eastward (Figure 4.11.A), similarly to what we observe on the perpendicular interface (Figure 4.8). To investigate the dynamics of the bilayer progression, we can analyze the cell density variation in space and time. Because the intensity of fluorescence is related to cell density, we analyze the intensity profiles.

Figure 4.11.B.1 shows the intensity profile across the interface 30 h after confluence, normalized by the intensity profile 5 hours before confluence. Far from the interface, the normalized intensity is flat and larger than 1 meaning that the cell density increases homogeneously in these regions. Because we do not observe collective motion in these areas, the increase of cell density is not due to a net flow of cells but to cell division in the system (green arrows in Figure 4.11.A and green dashed boxes in Figure 4.11.B). At the east of the interface, a peak of maximal intensity can be detected in the intensity profile. This peak corresponds to a quantitative definition of the “bilayering front” (dashed magenta lines in Figure 4.11.A, B). We also observe displacements at the east of the interface corresponding to the progression of the top layer (orange arrows in Figure 4.11.A and orange dashed boxes in Figure 4.11.B). 55 h after confluence, the bilayering front is farther from the interface and the zone with a progressing top layer is larger (Figure 4.11.B). At both time points, the intensity at the west side near the interface remains very close to the initial intensity and is much smaller than the cell density far from the interface. This zone thus seems to play the role of a “cell reservoir” feeding the progressing top layer (blue arrows in Figure 4.11.A and blue dashed boxes in Figure 4.11.B).

Now that we have described the different zones in the system for two given time points, we describe the time evolution of the intensity profiles. Figure 4.11.C shows the intensity profiles every 5 hours after confluence, normalized by the intensity profile 5 hours before confluence. The density profile is initially flat which corresponds to homogeneous cell density across the interface. Far from the interface, cell density increases continuously without migration (green arrows in Figure 4.11.A and green dashed boxes in Figure 4.11.B)

At the east of the interface, the “bilayering front” is detected from 15 h after confluence and propagates eastward as time goes on (magenta diamond curve in Figure 4.11.C). The evolution of the bilayering front position with time allows to estimate the bilayering front speed which we find to be $14.5 \pm 1.1 \mu\text{m/h}$ (95% confidence bounds) (Figure 4.11.D). At later time points, the cell density is larger at the bilayering front than at the west far from the interface. This suggests that both a local increase in cell density due to division and the migration of cells cooperate to increase cell density at the bilayering front.

After a slight initial increase, the cell density in the previously identified “cell reservoir” decreases to a value close to the density at confluence. At late time points, the density at this location is approximately constant and much smaller than the cell density far from the interface. Altogether, these observations suggest that the formation and progression of a second layer is sustained by cells coming from the interface and migrating eastward. The low-density region at the west side of the interface behaves as a “cell reservoir” for the top layer.

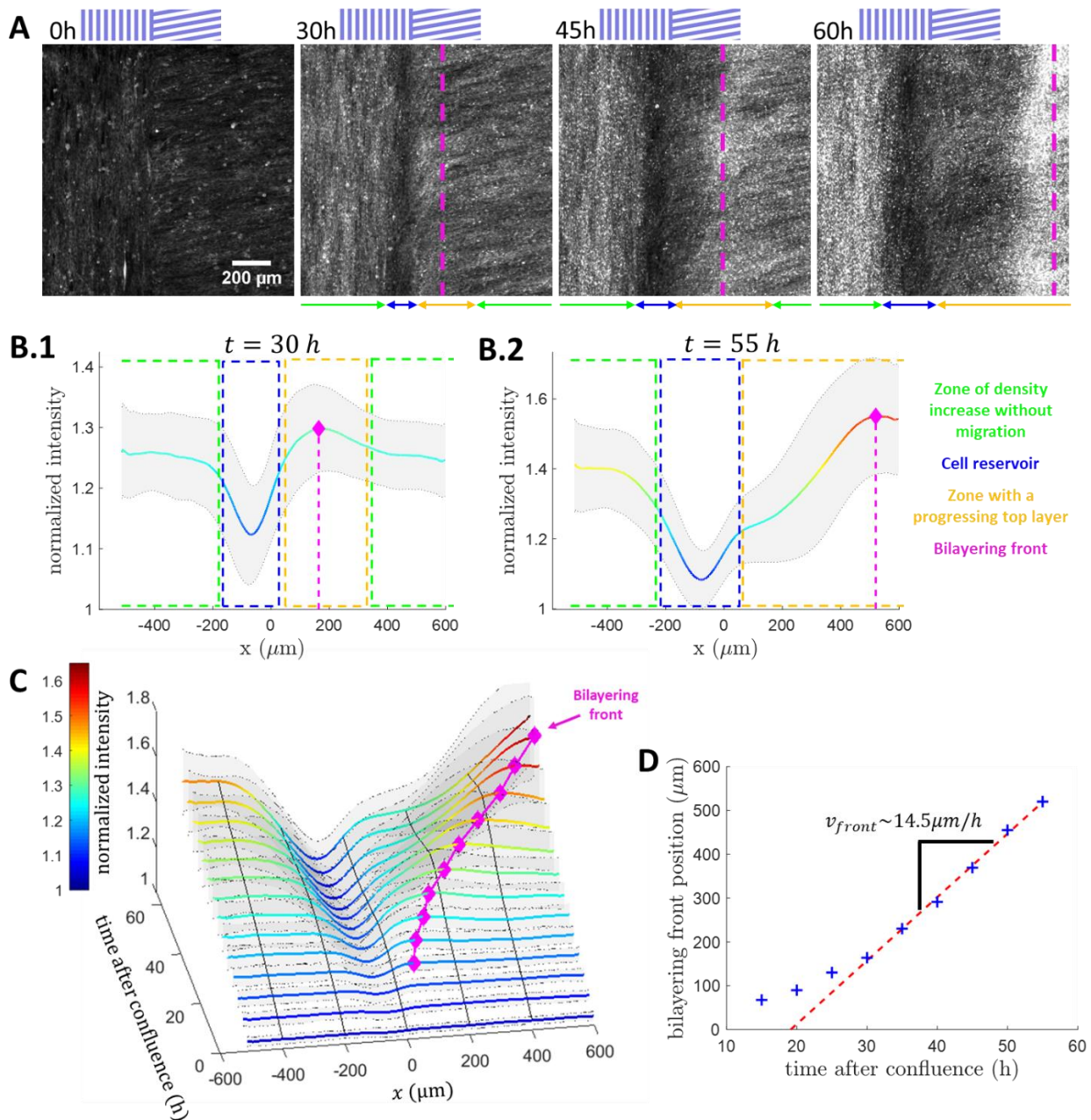


Figure 4.11 : Bilayering front progression on a 10° interface.

A: Fluorescent images of a C2C12 sheet at different time points show that a bilayering front is formed at the interface and propagates eastward. Time indicates the number of hours after confluence. The schematics show the location and design of the interface. Dashed lines highlight the location of the bilayering front. Colored arrows at the bottom indicate the different zones in the system.

B: Intensity profiles across the interface 30 h (B.1) and 55 h (B.2) after confluence. Colored dashed boxes indicate the different zones in the system.

C: Intensity profiles across the interface for different time points after confluence. Front curves correspond to earlier time points, and the time between two successive curves is 5 h. The black lines link intensity values for different times at a fixed distance from the interface. For example, the middle black line corresponds to the evolution of the intensity with time at the position of the interface $x = 0$.

B, C: Data are averaged along y , normalized by the intensity profile 5 hours before confluence, and averaged over 30 FOVs taken from 6 separated experimental wells from two independent experiments. Gray shaded areas show the standard deviation to the mean over the FOVs. The color codes for the normalized intensity value. Magenta diamonds highlight the intensity peak position which quantitatively defines the bilayering front position.

D: Time evolution of the bilayering front distance from the interface allows estimating the bilayering front velocity.

4. Crisscross bilayering of myoblasts controlled by collective contact guidance

Thus, the quantitative analysis of intensity variations in space and time suggests:

- the formation of bilayers without migration far from the interface
- the formation of a second layer triggered by cell depletion at the cell “reservoir” and cell migration on top of bottom cells eastward.

We now investigate in detail the organization of cells in this bilayer system.

4.2.4. Cells in the progressing top layer are oriented perpendicularly to bottom cells

To investigate the structure of the bilayer system, cells were seeded on a perpendicular interface and the system was imaged with confocal microscopy during bilayer progression. Four days after cell seeding, a second layer is present everywhere except at the location of the previously identified “cell reservoir” (Figure 4.12.A). East of the interface but close to it, top layer cells are oriented N/S, forming a well-defined 90° angle mismatch with respect to the cells in the bottom layer (Figure 4.12.A). We therefore successfully triggered the self-formation of an orthogonal bilayer with bottom W/E-oriented cells and top N/S-oriented cells (Figure 4.12.A). If we compare different FOVs along the interface, we find that cells in the top layer at the bilayering front can reorient from N/S to W/E from west to east either with positive angles (Figure 4.12.A right) or with negative angles (Figure 4.12.A left). Monitoring the system evolution with only 10% of fluorescent cells allows to observe the displacement of the bilayering front (magenta dashed line) toward the east with time (Figure 4.12.B, C). Moreover, we identify an array of alternating topological defects in the top layer along this bilayering front, that is at this location, on top of W/E-oriented cells (Figure 4.12.B, C).

At distance from the interface, both east and west of the device, the top and bottom layers are aligned (Figure 4.12.A). In the previous subsection, the continuous increase of cell density far from the interface was mentioned. However, no net flows are observed at these locations. The parallel bilayers are formed by local extrusion of cells resulting from the density increases due to cell division. In the following, I will refer to this mechanism as “parallel bilayering”. This phenomenon won’t be discussed in detail in this manuscript.

The schematic presented Figure 4.12.D summarizes the main findings regarding the spontaneously formed orthogonal bilayers several days after cell seeding at a perpendicular interface:

- Far from the interface, cells in the two layers are well-aligned and the layers are parallel
- In the cell reservoir, there is no top layer but only a monolayer
- East of the interface, the two layers are orthogonally oriented
- The bilayering front corresponds to a zone in the top layer where the orientation changes from N/S to W/E. It is paved by an array of topological defects of alternating charges. This zone moves away from the interface with time.

Thus, not only we succeeded to trigger the spontaneous self-formation of bilayers over more than a cm long interface and over a few hundred micrometers in width, but also, the bilayers were well-organized with an orthogonal mismatch between the bottom and the top layer. We now investigate in more details the formation mechanism of such well-organized crisscross bilayers.

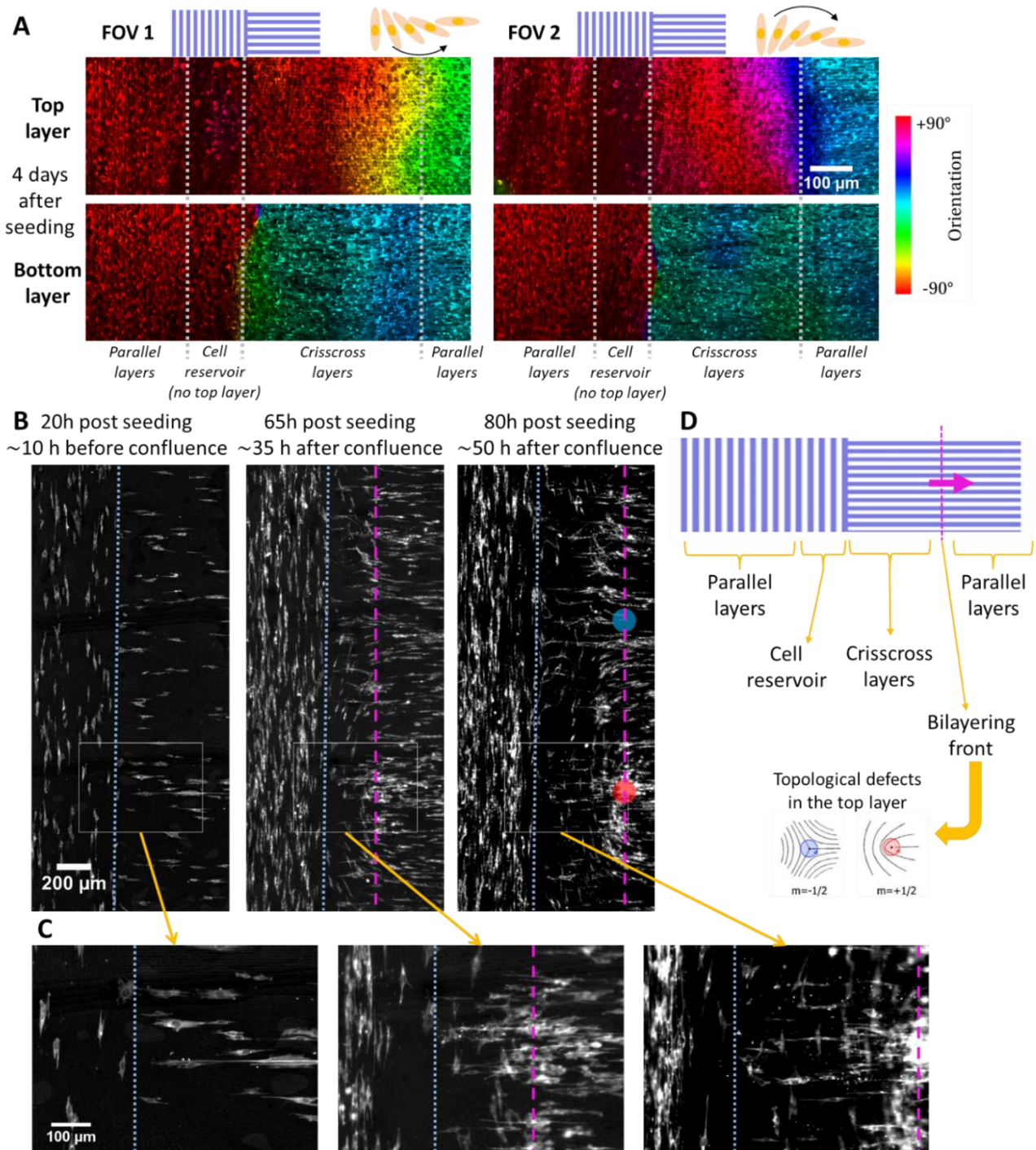


Figure 4.12 : Cell orientation in the two layers on a perpendicular interface.

A: Fluorescent confocal images of the top and bottom layers 4 days after cell seeding color coded by cell orientation. The schematics show the location and design of the interface. The z distance between bottom and top images is 8 μm . Left and right images correspond to two separated FOVs along the same interface with cell reorientation in the top layer from N/S to W/E with negative (left) and positive (right) angles. The cell reorientation in the top layer is sketched on top of the images. Legends in the bottom highlight the different zones in the bilayered system.

B: Fluorescent images with 10% of fluorescent cells 20 h, 65 h and 80 h after cell seeding taken with a classic microscope, meaning that we observe contributions from all the layers. The blue dotted lines are positioned at the interface location and the magenta dashed lines highlight qualitatively the bilayering front position. Colored dots highlight topological defects (red: $+1/2$; blue: $-1/2$) in the top layer.

C: Zoomed images corresponding to the white boxes in B.

D: Schematic of the bilayer system structure several days after cell seeding.

4.2.5. Flows involved in orthogonal bilayering progression

To better understand the mechanism of orthogonal bilayer initiation and progression, cell flows were measured in the system using PIV. The profiles across the interface of the x and y component of the velocity field (v_x and v_y) for increasing time points after confluence can be found in Figure 4.13.A, B. v_x positive (respectively negative) corresponds to an eastward (respectively westward) flow and v_y positive (respectively negative) corresponds to a northward (respectively southward) flow in the system. Flow directions measured at confluence and during bilayer progression are summarized in Figure 4.13.C.

Just after confluence and before the initiation of bilayering, PIV results reflect the flows in the confluent monolayer. At confluence, a southward flow and an eastward flow are measured near the interface (front curves in Figure 4.13.A, B; Figure 4.13.C left). Far from the interface, cells migrate along the grooves in both directions and the flows average to zero.

After bilayering initiation, we assume that PIV measurements reflect the flows in the topmost layer. This hypothesis is validated in the following using confocal experiments. In the top layer, an eastward flow in the x direction is measured from around 200 μm west of the interface to the east limit of the FOV (rear curves in Figure 4.13.A). v_x is maximal just before the bilayering front previously defined as the position of the fluorescence intensity peak (magenta diamonds in Figure 4.11.B, C and Figure 4.13.A). The maximal x velocity value is of the order 10 $\mu\text{m}/\text{h}$ and the bilayering front was measured to move at 14.5 $\mu\text{m}/\text{h}$ (Figure 4.11.C). At the east of the bilayering front, where the two layers are formed by parallel bilayering, the x velocity decreases. This suggests the presence of a “traffic jam” in the top layer after the bilayering front. We also found that the y velocity in the progressing top layer is positive which corresponds to northward flows (rear curves in Figure 4.13.B). The cell displacement in the top layer is then in the direction of the cell orientation of the bottom layer (i.e., in the direction imposed by the underlying microstructure) (Figure 4.13.C).

However, because fluorescent images do not distinguish between cells of different layers, one cannot measure the velocity field in the bottom layer at times when the system is bilayered. To circumvent this problem, we performed spinning disk live imaging 60 hours after cell seeding (~ 30 h after confluence so shortly after bilayering initiation), allowing us to distinguish cells from different layers (Figure 4.14.A, B). By analyzing these images, we found that even after bilayering initiation, the bottom layer keeps the same flow organization, with a southward flow in the y direction and an eastward flow in the x direction near the interface (Figure 4.14.B, C, D, red curves). We also confirmed that the top layer at the east of the interface migrates eastward and that the x velocity is maximal just before the orientation change corresponding to the bilayering front. At the right of the bilayering front, the x velocity in the top layer decays continuously (Figure 4.14.A, C, blue curves).

Thus, this analysis validates the results obtained on the top layer by PIV on wide field fluorescent images and gives the additional information that the bottom layer does not change its behavior after the system gets bilayered. We conclude that the bottom layer behavior is dictated by the substrate even after bilayering initiation.

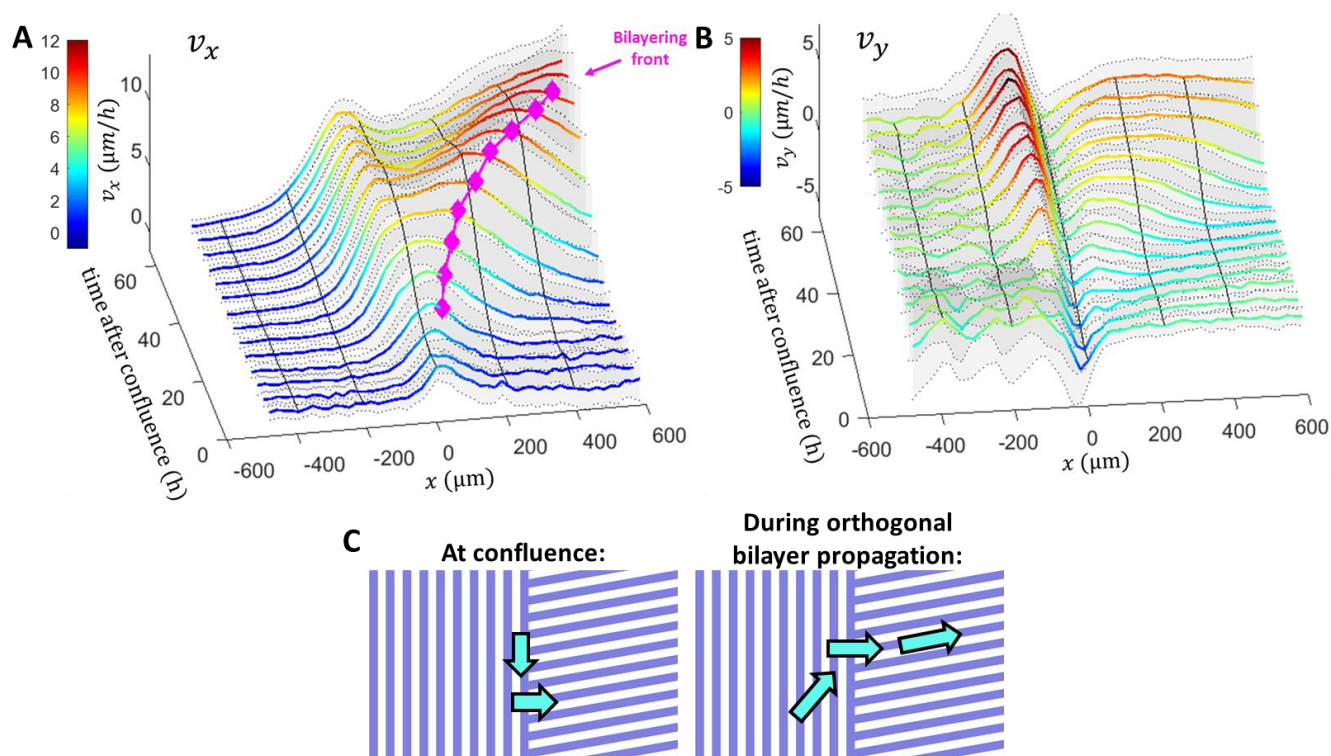


Figure 4.13: Flows in the system on a 10° interface measured using PIV.

A, B: Respectively x and y component of the velocity profiles across the interface at different times after confluence. Data are averaged along y and averaged over 30 FOVs taken from 6 separated experimental wells from two independent experiments. Gray shaded areas show the standard deviation to the mean over the FOVs. Front curves correspond to earlier time points, and the time between two successive curves is 5 h. The color codes for the velocity values. Note that the color codes are different in A and B. The black lines link values for different times at a fixed distance from the interface. For example, the middle black lines correspond to the evolution of the velocities with time at the interface ($x = 0$). Magenta diamonds in A highlight the bilayering front position defined using the intensity profiles (Figure 4.11.B, C).

C: Schematics of the flows' direction identified by PIV at confluence (left) and during orthogonal bilayer propagation (right)

Unfortunately, because of practical problems, spinning disk velocity measurements were only performed at the beginning of orthogonal bilayer progression, 60 hours after seeding the cells i.e., approximately 30 hours after confluence. Thus, we couldn't successfully monitor independently the two layers' evolution at longer times, when the orthogonal top layer is more advanced.

At this point, we can put in perspective three pieces of information:

- we observe the formation of a bilayer
- there is no top layer at the cell reservoir location
- the top layer to the east of the interface migrates eastward

These observations suggest that cells in the propagating orthogonal top layer to the east of the interface originate from the bottom layer cell reservoir. However, cell density and v_x , and consequently cell eastward fluxes, are lower in the cell reservoir than in the progressing top layer. Moreover, the velocity of the bilayering front, defined as the location of highest cell density, is larger than the cell velocity in the top layer. Altogether, these observations suggest that cells in the progressing orthogonal top layer not only come from the reservoir but also from other locations. We thus ask the question: where do the cells come from in this invading top layer?

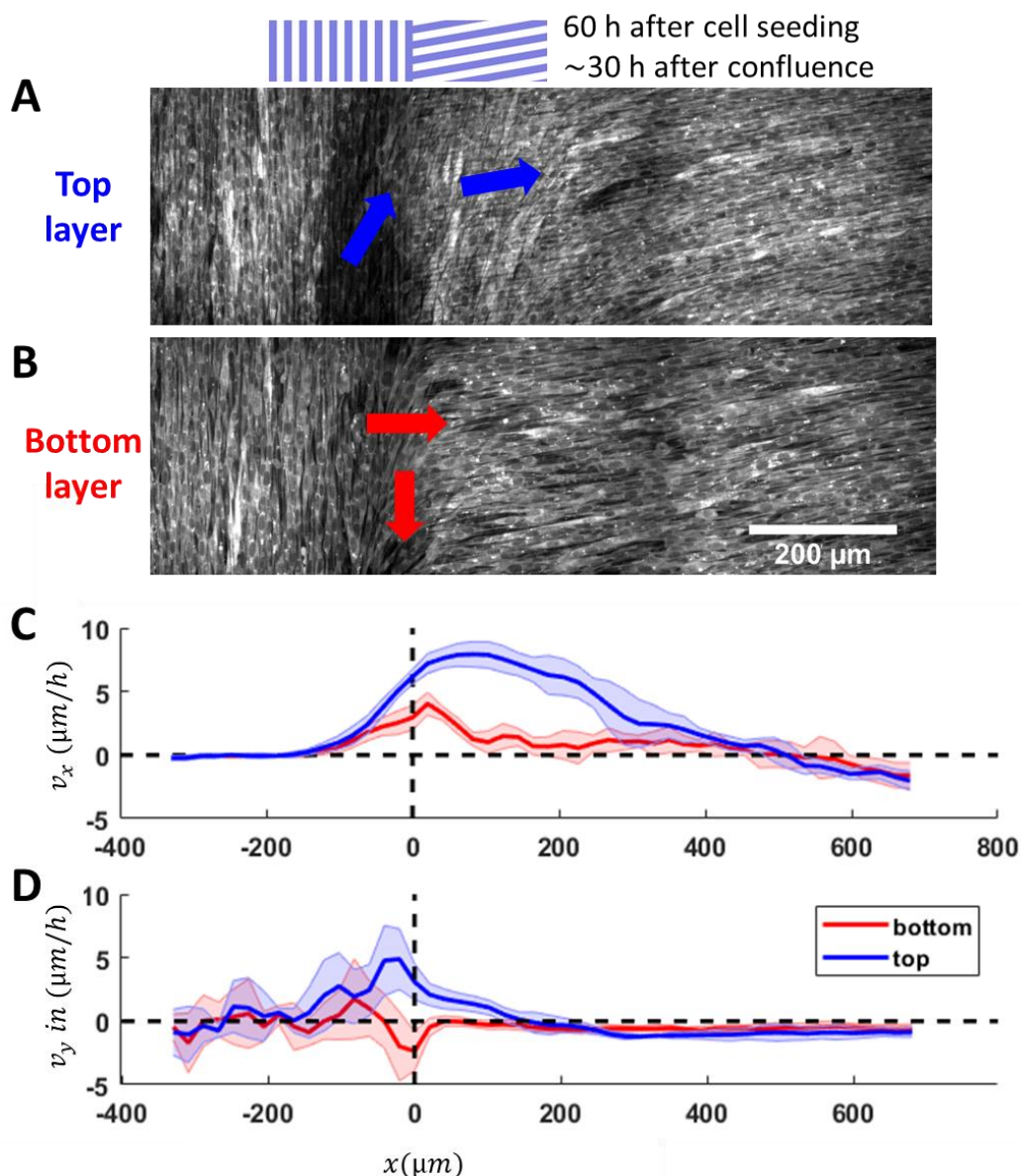


Figure 4.14 : Flows in the two layers 60 hours after cell seeding.

A, B: Confocal images of the top and the bottom layer taken approximately 60 hours after cell seeding. Arrows highlight the flows' direction. The schematic shows the location and design of the interface. The z distance between the two images is 11 μm .

C, D: Respectively x and y velocity profiles in the top and bottom layer measured with PIV. Data are obtained by averaging over y and over 5 FOVs. Shaded areas represent the standard deviation to the mean over the 5 FOVs. Vertical dashed lines highlight the position of the interface $x = 0$ and horizontal dashed lines correspond to $v_{x,y} = 0$.

To answer this question, we analyzed the behavior of individual cells by introducing a small percentage of fluorescent cells in a WT population seeded on a perpendicular interface. We identify two behaviors that can participate in the propagation of the orthogonal top layer.

First, some cells in the cell reservoir to the west of the interface, that are oriented N/S, are extruded from the bottom layer, cross the interface, and migrate on top of the bottom layer (Figure 4.15.A). The constant depletion of cells from the cell reservoir explains the absence of a top layer at this location. The eastward direction of cell flows at the west of the interface in the bottom layer suggests that the reservoir is fed by cells coming from the west of the device. However, two other mechanisms are also at play:

- i) Some cells to the east of the interface migrate towards the interface, rotate while crossing the interface and flow in the y direction. Then, similarly to what has been described above, they are extruded and integrate the invading top layer (Figure 4.15.B). The reservoir is thus fed by cells migrating from its west side and by cells migrating and reorienting from its east side. The invading top layer close to the interface is thus formed both of west cells from the cell reservoir and of east cells that reorient and extrude when crossing the interface.
- ii) The second mechanism appears at distance, eastward of the orthogonal bilayering front. At this location, cells are individually extruded from the bottom layer by parallel bilayering, rotate and integrate to the bilayer front that moves eastward (Figure 4.15.C). We refer to this mechanism as “reorientation after parallel bilayering”. This could explain why, once the bilayering phenomenon has been initiated, the bilayering front is faster than individual cells in the progressing top layer and why the bilayering front gets denser.

Note that in the top layer eastward of the interface, cells migrate perpendicularly to their long axis (see individual tracks in Figure 4.15 and cell orientation and flows in the top layer in Figure 4.14). This observation is noteworthy because C2C12 cells usually migrate in the direction of their long axis when sparse or even in a monolayer.

4.2.6. The cell reservoir is not needed for crisscross bilayering initiation and progression

We described above that cells forming the propagating top layer come from the west of the interface (cell reservoir) or are bottom east cells that reoriented at the interface. Based on these observations, we now hypothesize that the cell reservoir is not needed and that cell reorientation at the interface in the bottom layer is sufficient to trigger crisscross bilayering initiation and progression. To test this hypothesis, we designed and tested new substrate geometries altering the influence of a cell reservoir in the system.

We first designed what we refer to as the “double perpendicular interface escape geometry” (Figure 4.16.A), in which two semi-infinite zones of W/E grooves are separated by a 200 μm wide zone of N/S grooves. In that case, we observe orthogonal bilayering initiation and progression away from the interfaces in both sides (Figure 4.16.A), supporting the fact that even a small 200 μm wide cell reservoir is sufficient for bilayering initiation and maintenance.

To confirm the secondary role of the cell reservoir, we also designed a substrate composed of a cell-repellent (PEG-treated) half space and a half space with chemically patterned subcellular PEG and fibronectin lines that align cells W/E (Figure 4.16.B). This geometry entirely suppresses the cell reservoir. In this case, we observe a steep cell orientation gradient at the boundary, the cells being N/S oriented at the boundary and W/E oriented in the rest of the monolayer. In this geometry without cell reservoir, a top layer also forms and progresses away from the interface (Figure 4.16.B).

From these two experiments, we conclude that a cell reservoir is not needed and that bottom layer cells reorientation and extrusion at the interface is sufficient to initiate and maintain crisscross bilayering progression. In this situation, orthogonal bilayering progression from the interface corresponds exclusively to the bottom layer reorienting and folding on itself.

4. Crisscross bilayering of myoblasts controlled by collective contact guidance

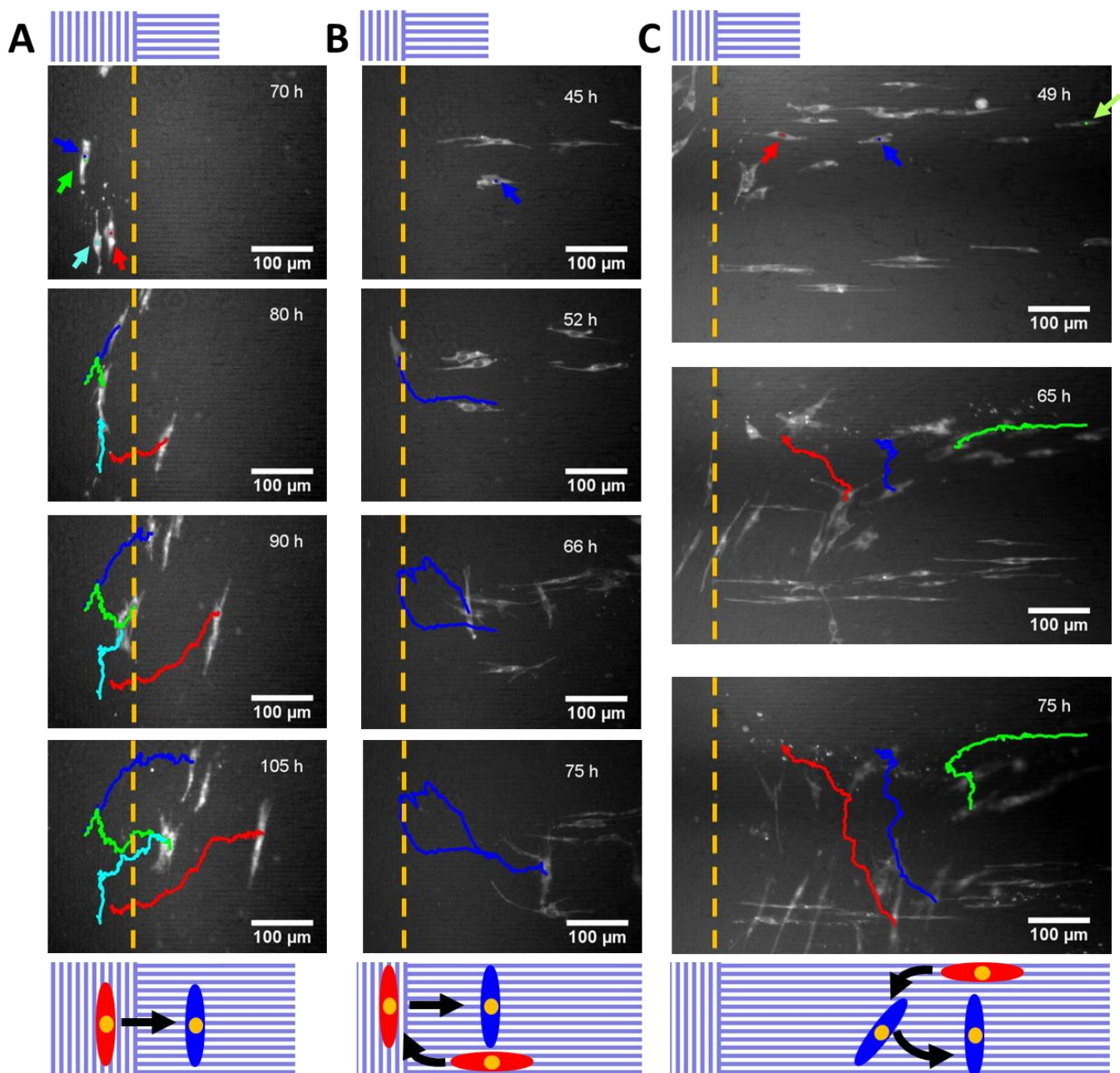


Figure 4.15: Different individual behaviors are responsible for the orthogonal bilayer progression.

A: Vertical cells in the “cell reservoir” extrude, cross the interface, and migrate perpendicularly to their long axis in the top layer.

B: An east cell migrates toward the interface, reorients, integrates the orthogonal top layer, and migrates eastward perpendicularly to its long axis.

C: Reorientation after parallel bilayering: cells at the east of the bilayering front integrate the top layer by parallel bilayering and progressively reorient from W/E to N/S.

A, B, C: Snapshots with initially 1% of fluorescent cells at different time points overlaid with individual cell tracks. Indicating time is the number of hours after cell seeding. The schematics on top show the location and design of the interface. Orange dashed lines highlight the position of the substrate interface. Arrows show the initial position of the tracked cells. Bottom schematics present idealistic single cell trajectories for the three identified mechanisms. Cells are colored in red when they are part of the bottom layer and in blue when they are part of the top layer.

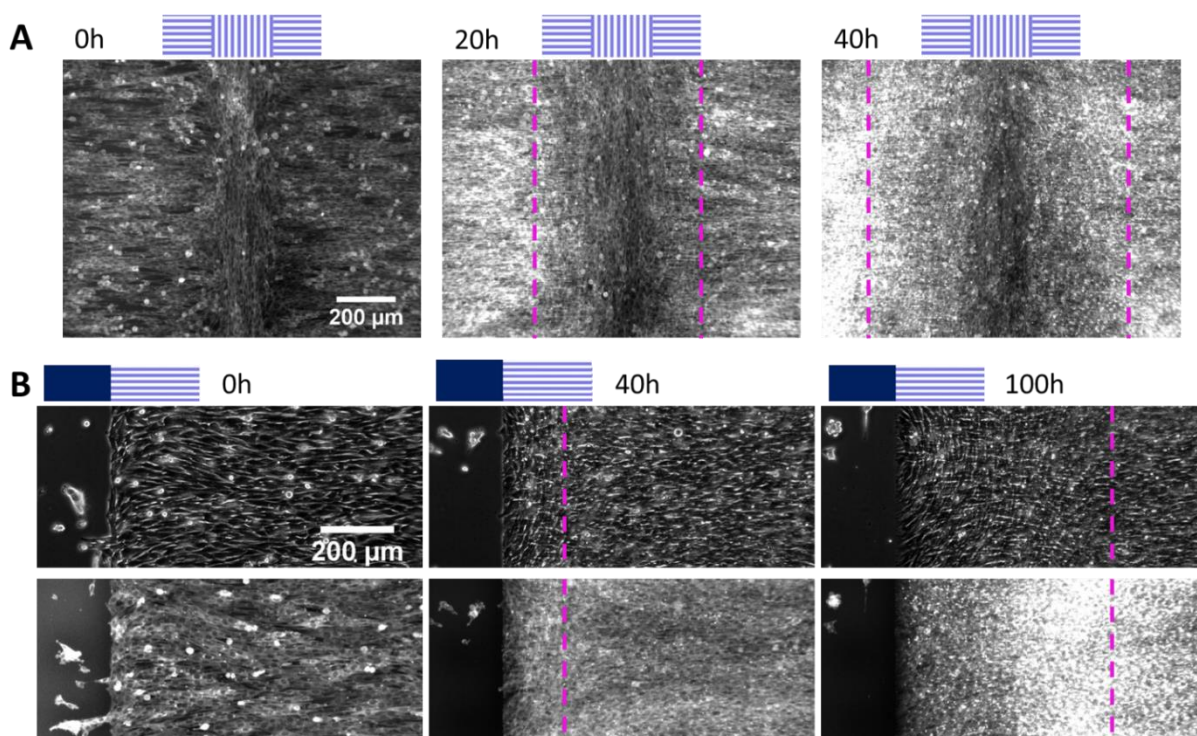


Figure 4.16 : Orthogonal bilayering progression without cell reservoir.

A: Fluorescent images at different time points showing simultaneous bilayering progression away from a double perpendicular interface.

B: Phase contrast and fluorescent images at different time points showing bilayering progression away from a cell repellent barrier.

A, B: Indicating time is the number of hours after confluence. The schematics on top show the location and design of the interface(s).

Magenta dashed lines highlight the orthogonal bilayering front.

4.2.7. Summary: description of bilayering at a perpendicular interface

Our current understanding of the orthogonal bilayering initiation and progression is summarized here. Initially, for a confluent monolayer on a perpendicular or a 10° tilted interface, the cells orient with the underlying grooves, forming a well-defined steep orientation gradient near the interface that leads to complex flows. As cell density increases with time, a second layer of cells parallel to the bottom layer forms on both sides far from the interface by parallel bilayering. At the interface, N/S-oriented cells at the west of the interface but close to it are extruded, integrate the top layer and migrate eastward on top of the bottom layer composed of W/E-oriented cells. In this process, top cells keep their initial N/S orientation, and therefore migrate perpendicularly to their long axis. The cells composing the migrating top layer are originally:

- N/S-oriented cells in the cell reservoir that translated toward the interface
- W/E-oriented cells at the east that migrated toward the interface and that reoriented while crossing the interface. This mechanism is sufficient to trigger and sustain the bilayering progression, even in the absence of a cell reservoir.

The bilayering front is also fed by cells to the east of the orthogonal bilayering front that initially integrate the top layer by parallel bilayering and that reorient when the bilayer front reaches their position.

The orthogonal bilayering that we observe is the consequence of a steep gradient of orientation at a fixed interface. In the next part, we experimentally investigate the role of this gradient of orientation in the bilayering process.

4.3. Impact of the orientation mismatch at the interface

To investigate the role of orientation gradient in the process of orthogonal bilayering, we vary the orientation mismatch across the interface. This is possible by designing and fabricating different micro-grooved PDMS substrate geometries. We keep the west part of the substrates composed of N/S-oriented grooves while we vary grooves' orientation in the east part from 10° to 80° with respect with the x axis. A 10° interface corresponds almost to a perpendicular interface and the results for this geometry are the ones presented in the previous section. An 80° interface corresponds to a very small angle mismatch of 10° between the west and the east of the substrate (Figure 4.17.A). As we go from a 10° to an 80° interface, we reduce the orientation mismatch at the interface and therefore the gradient of orientation. We then expect the flows to decrease. In the following, we name α the angle between the x axis and the grooves east of the interface.

At confluence, west cell orientation is 90° (N/S orientation) and east cell orientation is α . Thus, cells are precisely guided by the grooves (Figure 4.17.A, B). Note that the gradient of orientation at the interface increases when α decreases. As described in the previous section for a 10° interface, we measure for all values of α a southward flow in the y direction and an eastward flow in the x direction (Figure 4.17.C, D). As expected, the amplitude of the observed flows decreases as α increases until the flows get almost undetectable for the 80° interface (Figure 4.17.C, D).

After bilayering initiation, the eastward flow in the x direction decreases when α increases from 10° to 80° (Figure 4.18.A). Consequently, 50 hours after confluence, the bilayer front is further from the interface for a 10° angle than for a 55° angle (Figure 4.18.E). Note that here the bilayer front position is qualitatively estimated as the location in the top layer of higher density where the cells reorient from almost N/S to aligned with the bottom cells. For $\alpha = 80^\circ$, a bilayer front away from the interface is barely observed (Figure 4.18.E bottom). Thus, efficient bilayer progression requires a large enough orientation mismatch at the interface.

One can interestingly note that, 50 hours after confluence, flows in the top layer eastward of the interface are northward (Figure 4.18.B). If we measure the velocity angle when the vertical top layer has progressed 50 hours after confluence, we observe that the top layer cells follow approximately the grooves' direction (Figure 4.18.C, D). Note that this measure was not performed in the case of the 80° interface because in that case we did not observe a bilayer progression from the interface eastward.

To conclude, decreasing the orientation mismatch at the interface decreases the flows at the interface. We observe a bilayer progression from the interface to the east for $\alpha = 10, 35$ and 55° , but the x velocity towards the east in the top layer decreases when α increases. Moreover, a bilayer progression was not observed on an 80° interface. We thus conclude that the efficiency of bilayer progression decreases with α and is maximal in the case of the perpendicular interface ($\alpha = 0$). In the next section, we discuss the results presented above and their implications.

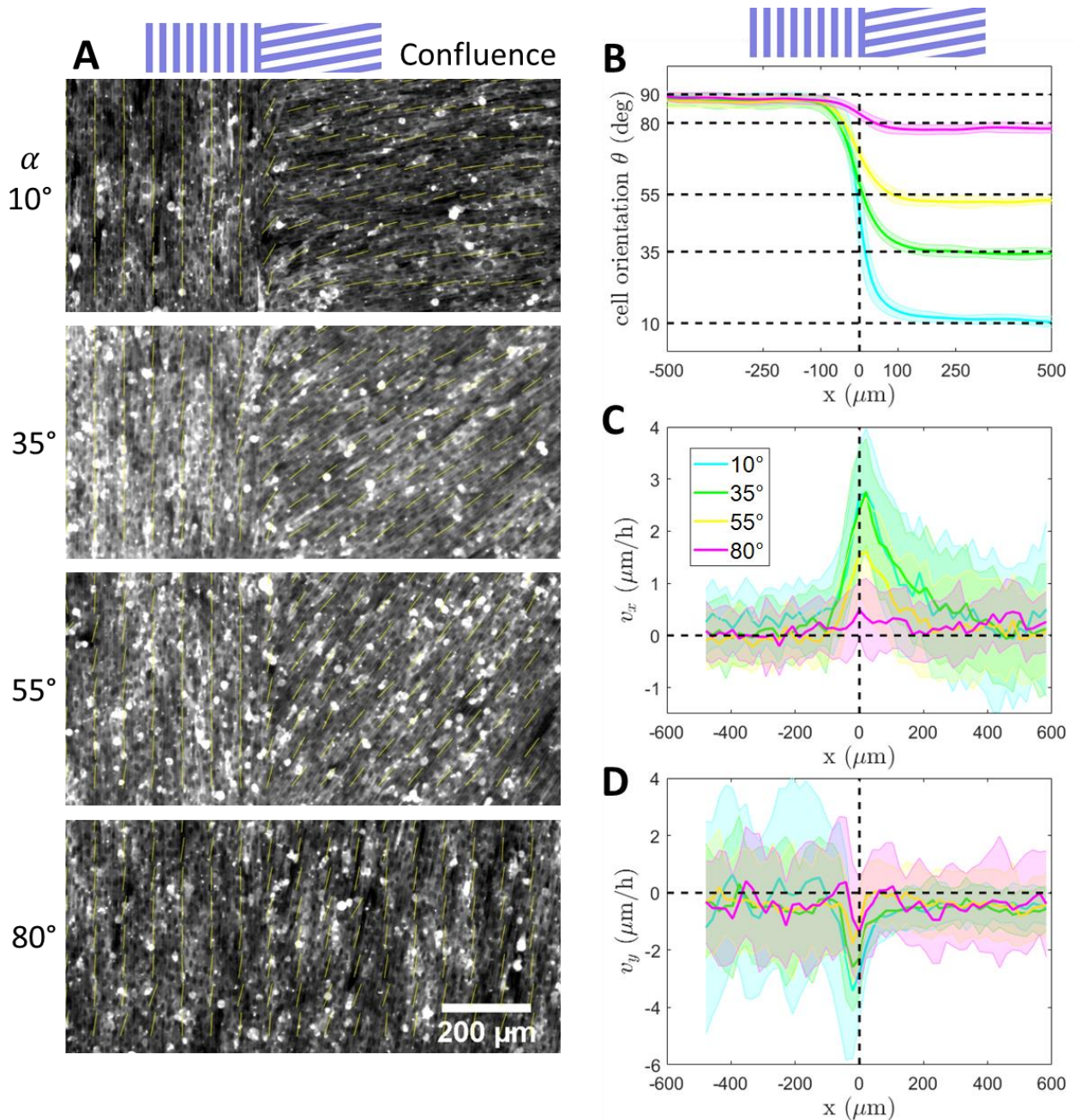


Figure 4.17: C2C12 confluent monolayer flows are influenced by the orientation mismatch at the interface.

A: Fluorescent images of a C2C12 monolayer at confluence for different values of α , the angle between the x axis and the east grooves. The images are overlaid with the orientation field (yellow lines that indicate cell orientation).

B, C, D: Cell orientation (B), x component of the velocity (C) and y component of the velocity (D) profiles across the interface at confluence. Color codes for α . The schematic and the black vertical dashed lines show the location of the interface. Data are averaged along y and averaged over 30 FOVs taken from 6 separated experimental wells from two independent experiments. Shaded areas show the standard deviation to the mean over the FOVs. B: Horizontal dashed lines highlight the orientation corresponding to 90° and $\alpha = 10, 35, 55, 80^\circ$. C, D: Horizontal dashed lines correspond to $v_{x,y} = 0$.

4. Crisscross bilayering of myoblasts controlled by collective contact guidance

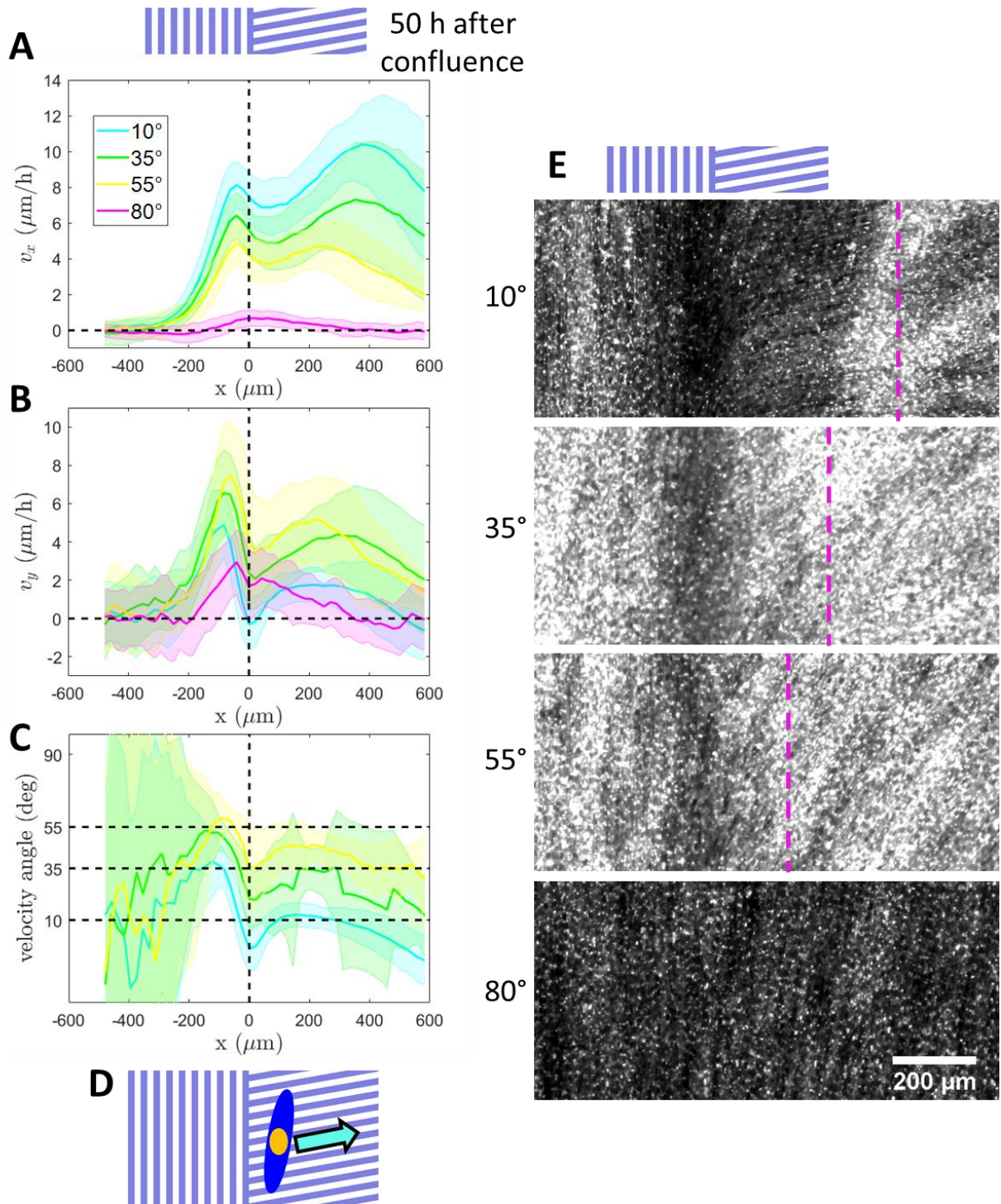


Figure 4.18 : Efficient eastward progression of a top layer from the interface requires sufficient orientation mismatch at the interface. A, B, C: x component of the velocity (A), y component of the velocity (B) and velocity angle (C) profiles across the interface 50 hours after confluence. Color codes for α . The schematic and the black vertical dashed lines show the location of the interface. A, B: Horizontal dashed lines correspond to $v_{x,y} = 0$. C: Horizontal dashed lines highlight angles corresponding to $\alpha = 10, 35, 55^\circ$. Data are averaged along y and averaged over 30 FOVs taken from 6 separated experimental wells from two independent experiments.

Shaded areas show the standard deviation to the mean over the FOVs.

D: Schematic showing that cells in the progressing top layer migrate eastward along the grooves, i.e., are guided by bottom cells.

E: Fluorescent images of the system 50 hours after confluence for different values of α . Magenta dashed lines estimate the position of the bilayering front. Note also that all images share the same intensity normalization so that higher brightness can be directly linked to higher cell density.

4.4. Discussion

4.4.1. Formation of orthogonal bilayers at large scales

In the present work, we succeed to form orthogonal bilayers over more than a cm long interface and over at least 500 μm in width by juxtaposing two domains of conflicting orientations. This final structure is obtained by a spontaneous bilayering mechanism at a steep angle on a micro-structured substrate. With the presented strategy, we successfully scale up and control in space the monolayer-to-crisscross bilayers transition that has been previously described in Sarkar et al.⁵³ at spontaneous $+1/2$ topological defects.

The flow patterns that we found at angle interfaces in our systems have some similarities with those found in confluent C2C12 cell monolayers near the boundary of a mesoscale stripe⁴⁹. Indeed, at our interfaces where the cells have a tilt SW-NE, the cells migrate southward and eastward (Figure 4.17), similarly to cells at the border of a stripe in which the cells spontaneously orient SW-NE (Figure 1.12.B). This suggests that the cell reservoir with N/S-oriented cells acts as an effective boundary. This might be due to anisotropic friction caused by the groove orientation that prevent cells in the east half space with W/E grooves to enter the west half-space with N/S grooves. A similar effect has already been reported by Londono et al. for ARPE-19 epithelial cells⁹².

Orthogonal bilayering is also observed in the absence of cell reservoir in the case where half of the space is inaccessible for cells and the other half is textured so that cells orient perpendicularly to the frontier. In that case, cells at the border orient along the boundary, extrude and form a top orthogonal layer by migrating away from the boundary (Figure 4.16). This observation is reminiscent of early works from Elsdale and colleagues in the 1960's: they created a frontier perpendicular to cell orientation in a monolayer by cutting the substrate of a fibroblast culture and observed both an alignment of the cells along the scratched frontier (Figure 4.19 left) and a top layer formation away from the scratch (Figure 4.19 right)¹⁴².

Altogether, we conclude that an effective fixed boundary that imposes a steep gradient of orientation triggers the spontaneous formation of a top layer migrating away from the boundary at large scales.

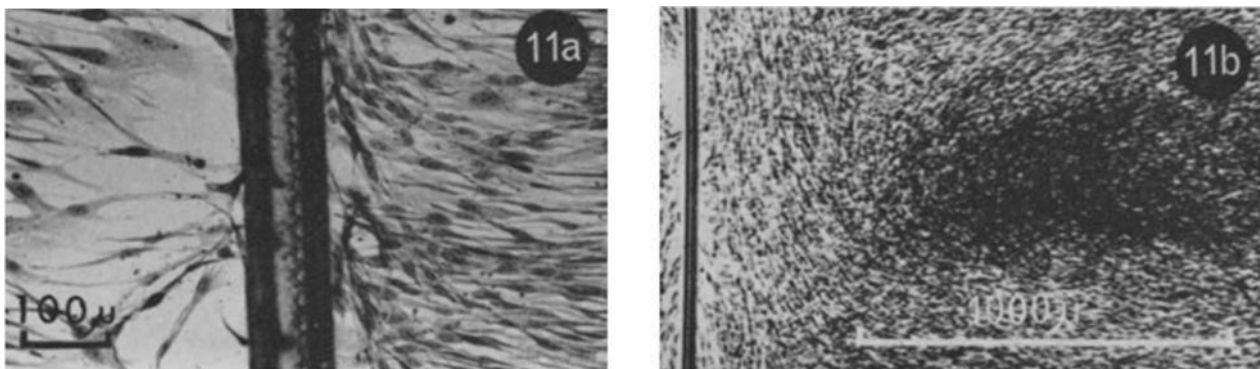


Figure 4.19 : Elsdale observed orthogonal bilayering in cutting experiments in 1969¹⁴². A stationary culture of EHL fibroblasts was cut leaving a single scratch on the dish and leading to a retraction of the cell sheet. The cells migrated toward the cut and oriented along the cut (11a). After a few days, we can distinguish an orthogonal bilayering front away from the cut (11b).

11a: Cells migrating toward a scratch. The cells on the right side are slightly in advance on those of the left and the first arrived cells are starting to turn parallel to the scratch. Scale bar: 100 μm .

11b: A few days later, Elsdale identified an "aggregation" beside a scratch that we identify now as large-scale orthogonal bilayering initiated at an orientation gradient induced by the scratch. Scale bar: 1000 μm .

4. Crisscross bilayering of myoblasts controlled by collective contact guidance

4.4.2. In the top layer, cells migrate perpendicularly to their long axis

For the perpendicular interface substrate, cells in the migrating top layer orient perpendicularly to the bottom cells. The question that one can ask is the following: why cells in the progressing top layer have a mismatch of orientation with the bottom layer? One hypothesis is that the ECM secreted by the cells in the bottom layer tends to orient cells in the top layer with a mismatch of orientation. To test this hypothesis, we seeded C2C12 fluorescent cells at very low density on top of a confluent C2C12 monolayer aligned on a grooved substrate (Figure 4.20.A). Fluorescent cells seeded this way align with bottom cells (Figure 4.20.B). Thus, a single cell seeded on top of an anisotropic monolayer with a well-defined orientation tends to align in the same direction. As mentioned previously, the top layer sufficiently far from the interface forms by parallel bilayering and thus at these locations, top cells produced by cell proliferation remain aligned with bottom cells. From these observations, we conclude that cells on top of a well-aligned cell monolayer are oriented by bottom cells. The mismatch of cell orientations that we observed between the two layers at the level of the progressing orthogonal bilayer must then be the result of the specific dynamics of the bilayer formation and progression from the interface eastward.

C2C12 cells usually migrate in the direction of their long axis when sparse or even in a monolayer. They are apolar and rely on their actin cytoskeleton contractility to propel along their main elongation axis orientation. Here, I would like to highlight the striking observation that, in the top layer to the east of the interface, cells that are N/S-oriented migrate perpendicularly to their long axis (see individual tracks in Figure 4.15 and cell orientation and flows in the top layer in Figure 4.14). Moreover, not only top cells remain N/S-oriented while migrating eastward, but also cells stay densely packed during the process. This collective cell migration in the direction perpendicular to the cell long axis is not common. However, it has previously been observed at the border of an expanding epithelial tissue. Indeed, in both an expanding zebrafish myocardial monolayer¹⁵² and a growing epithelial tissue composed of keratocytes¹⁵³, leader cells at the border of the tissue are elongated and orient perpendicularly to the direction of expansion and thus to their direction of migration. Similarly, fibroblasts in a circular wound closure experiment stay parallel to the wound edge while advancing towards the center of the wound, thus moving perpendicularly to their long axis¹⁵⁴.

To check whether the orientation of cells in the migrating top layer was because top cells collectively invade free space on top of the bottom layer, we performed a wound healing assay with C2C12 cells on a soft gel (12 kPa: stiffness comparable to the stiffness of a cell monolayer). Cells are initially aligned along the boundary, but 20 hours after removing the barrier, they dissociate at the front and tend to reorient before migrating (Figure 4.21). This experiment further suggests that the collective migration towards the east of N/S-oriented cells observed in the top layer in our system is not caused only by the presence of free space on top of the bottom layer but rather is linked to the specific dynamics of top layer initiation and progression from the interface.

Altogether, these observations suggest that cells in the progressing top layer stay almost N/S-oriented while migrating towards the right because of the specific collective dynamics of our system. Hydrodynamical theoretical arguments are proposed in 4.5.3 to explain the orientation of cells in the progressing top layer.

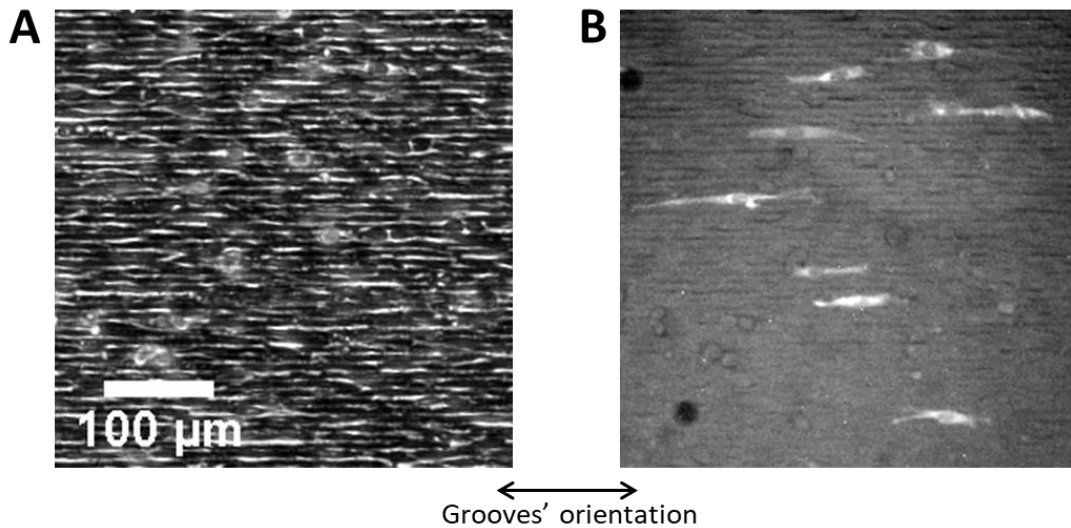


Figure 4.20 : Cells seeded on top of a confluent monolayer of cells aligned with grooves also align with the grooves' orientation.

A: Phase contrast image of the cell monolayer. WT cells were seeded at 100 000 cells/cm² and grown to confluence for 40h.

B: Fluorescent image of single cells seeded on top of the aligned monolayer at a density 12 500 cells/cm². Cells were allowed to attach for 3 hours before imaging.

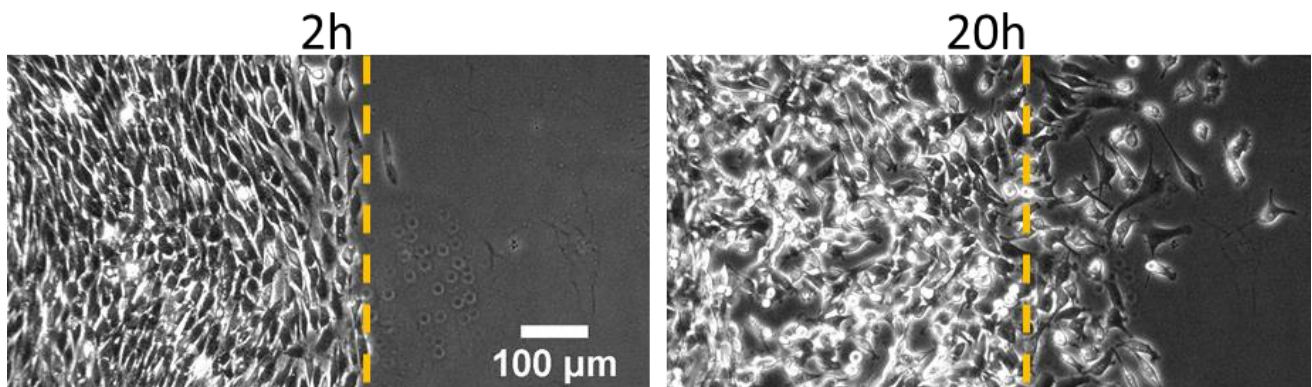


Figure 4.21 : Wound healing experiment with C2C12 on a soft gel. Phase contrast images at two time points after removing a barrier. Indicating time is the number of hours after barrier removal. Orange dashed lines highlight the barrier original position. Note that 2 h after removing the barrier, cells are N/S-oriented, while 20 h after, they are dissociated and randomly oriented at the invasion front.

4.4.3. ECM orientation guides cell migration in the top layer

An interesting observation that we have made is that cells in the migrating top layer do not migrate strictly eastward. They follow the direction of the cells' orientation in the bottom layer, which is itself fixed by the grooves beneath (Figure 4.18.C, D). This suggests that even if the cells' orientation in the bottom layer does not directly influence the top layer cell orientation close to the interface, it directs cell migration in the top layer. C2C12 myoblasts secrete fibrillar ECM oriented along the cell main axis orientation^{53,155} (Figure 4.6.E). Our present results suggest that these ECM fibers in the apical part of the bottom layer act as tracks that guide cell migration of the top layer.

4.4.4. C2C12 flows: contractile vs extensile?

C2C12 myoblasts are elongated cells that form nematic monolayers characterized by $+1/2$ and $-1/2$ topological defects. $+1/2$ topological defects self-propel tail first as it is expected for a contractile nematic system (see 1.2.4.3). However, the spontaneous shear flow that arises when those cells are confined in mesoscale stripes is compatible with an extensile nematic system (see 1.2.4.4). Similarly, the spiral rotation of C2C12 cells in a small circular confinement was found to be compatible with an extensile nematic system¹⁵⁶. In each of these experimental situations, cells adopt a specific orientation pattern. These seemingly contradictory observations suggest that the orientation pattern could impact the contractile or extensile nature of the system.

We can qualitatively try to predict the flows expected for a contractile or an extensile nematic system at our angle interfaces using a graphical method. Let us consider that each cell in the monolayer generates active force dipoles. When cells are aligned in the same direction, no collective net force can arise due to the local cancelation of these force dipoles (Figure 4.22.A). However, at the interface, the gradient of orientation generates a gradient of force dipoles that on average leads to a net force at the interface. This net force results from the interplay between gradients of orientation and active processes; they ultimately lead to flows. Our cartoon Figure 4.22.B, C shows that for a geometry where the east half-space has tilted grooves the expected flow in the system is:

- A north-eastward flow in a contractile nematic system (Figure 4.22.B)
- A south-westward flow in an extensile nematic system (Figure 4.22.C).

In our system, we find in the bottom layer at the interface a southward flow compatible with the extensile case and an eastward flow compatible with the contractile case of the active nematic theories proposed up to now. This means that our observations seem contradictory in the current framework of active nematic system description.

The main questions at this point are:

- Can we explain the flow pattern at the interface in the monolayer before bilayer formation in the framework of active nematics and clarify the apparent contradiction that C2C12 myoblasts can behave as an extensile or contractile nematic system depending on the experimental geometry?
- How does the interface initiate a bilayering process?
- Why do cells, once extruded at the interface, flow asymmetrically? (i.e., always toward the right on top of horizontal cells?)
- How do cells in the top layer migrate perpendicular to their long axis?

To gain a physical understanding of the orthogonal bilayering initiation and progression, we collaborated with Carles Blanch-Mercader, Samuel Bell and Jacques Prost, theoreticians from the group “Physical approach of biological problems” in the Physico Chimie Curie lab. The next section presents theoretical arguments to better understand the observed phenomenon. Predictions of the theoretical description are further validated with experiments on substrates designed with a new geometry.

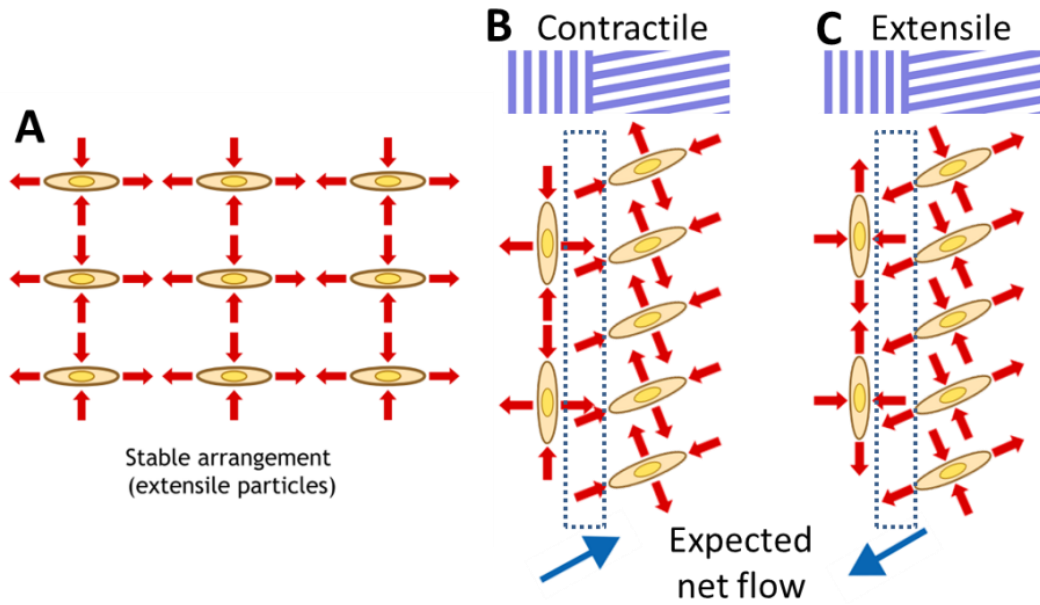


Figure 4.22 : Qualitative predictions of the flows at an angle interface in a pure contractile vs pure extensile nematic system.

A: No flows are expected when the cells are all aligned, schematic from ⁵⁰.

B, C: Schematic of the expected behavior of a purely contractile (B) vs extensile (C) nematic system at our discontinuous interface between orientations. The blue arrows show the expected flow direction at the interface, the direction is obtained by averaging the forces in the dotted box around the interface. We considered that the east half-space is composed of grooves with intermediate tilt.

This graphical method is a good way to qualitatively understand the emergence of flows in nematic systems, but an accurate prediction of the flows relies on solving the equations of the system.

4.5. Active nematic fluid description

As mentioned previously, some aspects of C2C12 monolayer collective dynamics have been well captured by a continuum description of active nematic fluids⁴⁹. The theoretical description that was developed in the context of this experimental work fits in the theoretical framework of active nematic fluids but proposes a novel approach to clarify the seeming contradiction that C2C12 myoblasts behavior has characteristics of extensile or contractile nematic systems depending on the context. In this section, I present the main ingredients and main insights of this theoretical description. This collaboration is still a work in progress. The theoretical curves shown in the following were provided by Carles Blanch-Mercader.

4.5.1. Expected flows and forces in an active nematic layer at an interface

First, we focus on the confluent monolayer stage and aim at better understanding the flows and forces that develop at the interface. The system is modeled as an incompressible 2D active nematic fluid and described by the nematic orientation field \mathbf{n} and the velocity field \mathbf{v} . Note that the geometry of our system is invariant in the y direction, and thus we are looking for solutions invariant in y. We first compute the equilibrium orientation field, assuming that the orientation of the cells is fixed by the grooves and not influenced by activity in the system. We then include activity in the description to predict the forces and flows that develop at the interface. Parameters are estimated by comparison with our experimental data. We eventually predict flows in other substrate geometries and test these predictions experimentally.

4.5.1.1. Active nematic orientation imposed by the substrate

We describe the effect of the grooves as an aligning nematic field in the free energy that is controlled by the elastic parameter H . The free energy in our system reads:

$$\mathcal{F} = \int_{\mathcal{A}} \left\{ \frac{\mathcal{K}}{2} (\partial_x \theta)^2 - H (\cos(\theta - \theta_s))^2 \right\} da \quad (4.1)$$

where θ is the angle of the orientation field \mathbf{n} and θ_s is the angle of the grooves with respect to the x direction. To describe the geometry of the substrate, we write $\theta_s = \theta_W + (\theta_E - \theta_W)\mathcal{H}(x)$, θ_W (respectively θ_E) being the orientation of the grooves at $x < 0$ (west) (respectively $x > 0$ (east)) and $\mathcal{H}(x)$ the Heaviside function. Practically for $10^\circ \leq \alpha \leq 80^\circ$, $\theta_W = 90^\circ$ and $\theta_E = \alpha$. The energy cost associated with gradients of orientation is accounted for by the first term, which is the Frank free-energy in the one-constant approximation with elastic modulus \mathcal{K} . The one constant approximation has been experimentally shown to be valid for C2C12¹⁵⁷. The second term favors alignment of the cells along the grooves and depends on the elastic constant H . At equilibrium, the orientation field is obtained by minimizing the free energy and is given by the following equation:

$$\theta = \left(\theta_W + 2 \operatorname{arccot} \left(\cot \left(\frac{\theta_E - \theta_W}{4} \right) e^{-x \sqrt{\frac{2H}{\mathcal{K}}}} \right) \right) \mathcal{H}(-x) + \left(\theta_E + 2 \operatorname{arccot} \left(\cot \left(\frac{\theta_W - \theta_E}{4} \right) e^{x \sqrt{\frac{2H}{\mathcal{K}}}} \right) \right) \mathcal{H}(x) \quad (4.2)$$

Far from the interface, cells orient along the grooves. At the interface, the orientation change is smooth and controlled by a single length scale $l_{nem} = \sqrt{\mathcal{K}/2H}$ (Figure 4.23.A). More precisely, we can define a length scale $dx_{\frac{1}{2}}$ corresponding to the distance over which the angle varies from half the total angle variation

$d\theta = \theta_W - \theta_E$ (Figure 4.23.B). In theoretical curves, we find $dx_{\frac{1}{2}} = 1.6l_{nem}$. We measure in experimental curves $dx_{\frac{1}{2}}$ and thus estimate the value of l_{nem} for different values of α (Table 4.1). We find $l_{nem} = 38 \pm 7 \mu\text{m}$. The theoretical model with $l_{nem} = 38 \mu\text{m}$ is in excellent agreement with experimental data (Figure 4.23.C).

α (deg)	θ_W (deg)	θ_E (deg)	$dx_{\frac{1}{2}}$ (μm)	l_{nem} (μm)
10	88	11	43	27
35	88	35	68	43
55	88	53	65	41
80	88	78	63	39

Table 4.1 : Measures made on experimental cell orientation profiles for different values of α (Figure 4.17.B). The definition of θ_W , θ_E , $dx_{\frac{1}{2}}$ can be found in Figure 4.23.B. From these four measures of l_{nem} , we compute the mean and the standard deviation and we conclude that $l_{nem} = 38 \pm 7 \mu\text{m}$.

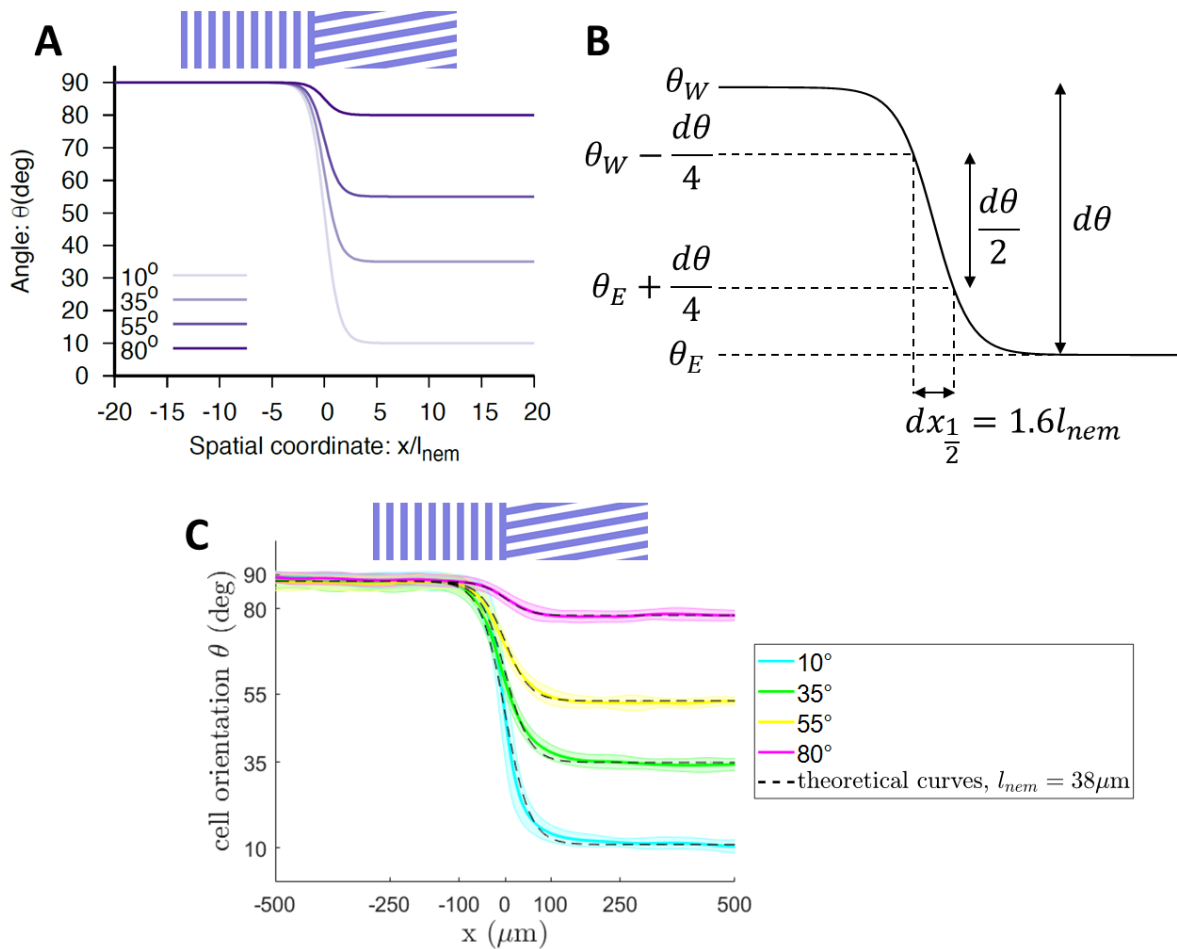


Figure 4.23 : Theoretical prediction and experimental measure of the cell orientation profile across an interface.

A: Equilibrium angle profiles (given by eq. (4.2)) obtained by minimizing the free energy. The color codes for α . We set units as

$$l_{nem} = \sqrt{\mathcal{K}/2H} = 1.$$

B: Graphical definition of θ_W , θ_E , $d\theta$ and $dx_{\frac{1}{2}}$. On theoretical curves, we find $dx_{\frac{1}{2}} = 1.6l_{nem}$ and use this relation to estimate l_{nem} in experimental curves (Table 4.1).

C: Cell orientation profiles across the interface at confluence. Color codes for α . The schematic shows the location and design of the interface. Data are averaged along y and averaged over 30 FOVs taken from 6 separated experimental wells from two independent experiments. Shaded areas show the standard deviation to the mean. Black dashed lines correspond to the theoretical curves for $l_{nem} = 38 \mu\text{m}$ and θ_W and θ_E values measured in Table 4.1.

4.5.1.2. *Constitutive and conservation equations*

In the following, we assume that the orientation pattern in the monolayer is imposed by the grooves and thus obeys the previously described equilibrium solution valid in the passive case. Consequently, we neglect cell reorientation in the initial monolayer due to flows. We thus assume that cell orientation is given by the passive model and that activity has an effect mainly on stresses and flows.

The constitutive equation for the total stress is derived following the standard approach of non-equilibrium physics (see 1.2.4.1) in the case of a 2D active incompressible fluid with nematic symmetry. It includes a shear viscosity η , an Ericksen stress with a pressure term that ensures incompressibility ($\partial_\gamma(v_\gamma) = 0$) and an active anisotropic stress term:

$$\sigma_{\alpha\beta}^{active} \approx -\zeta\Delta\mu \left(n_\alpha n_\beta - \frac{1}{2} n_\gamma n_\gamma \delta_{\alpha\beta} \right) \quad (4.3)$$

The constitutive equation for the total stress is supplemented with a force balance equation:

$$\partial_\beta \sigma_{\alpha\beta}^{tot} = \mu v_\beta + \lambda_s n_\alpha \partial_\beta n_\beta + \lambda_b n_\beta \partial_\beta n_\alpha \quad (4.4)$$

The first term in the right end side of this equation corresponds to a viscous friction with the substrate. We neglect anisotropic friction possibly due to the grooves. Thus, conversely to what we proposed in Chapter 3, we consider for simplicity that the friction μ is isotropic. As C2C12 myoblasts are more elongated than HBECS, we hypothesize that the main effects here come from the orientation profile and thus that this simplification only influences the precise shape of the flow profiles but not their sign.

The last two terms correspond to active nematic traction forces. We consider here the leading active and nematic contributions to the traction forces, and we disregard polar traction forces. These traction forces with the substrate are active terms and thus λ_s and λ_b are proportional to the chemical potential difference $\Delta\mu$. The term in λ_s is dominant in splay configurations and the term in λ_b is dominant in bend configurations. In the case of a pure splay or a pure bend configuration, one can show that these traction forces modify the amplitude of the active anisotropic nematic stresses $\zeta\Delta\mu$. Indeed, for a pure splay (resp. bend), the term $\lambda_b n_\beta \partial_\beta n_\alpha = 0$ (resp. $\lambda_s n_\alpha \partial_\beta n_\beta = 0$), and we can rewrite (4.4) as $\partial_\beta \sigma_{\alpha\beta}^{tot} = \mu v_\beta$ if we take the amplitude of the active stress to be $\zeta\Delta\mu + \lambda_s$ (resp. $\zeta\Delta\mu + \lambda_b$). By tuning λ_s , λ_b and ζ , one can for example impose extensile behavior in splay configurations and contractile in bend configurations. For a more complex orientational pattern that mixes splay and bend distortions, like in our geometries, one needs to solve the full equations.

The novelty of this description lies in studying the effects associated with these active nematic traction forces with different amplitudes λ_s and λ_b , that lead to different behaviors in splay- or bend-dominated orientation fields. Thus, they can help us clarify the apparent contradiction that C2C12 system can be described as an extensile or a contractile active nematic system.

As we study y-invariant geometries, the incompressibility condition leads to $v_x = 0$. One can show that the steady state force balance reduces to:

$$\partial_x \left(-P - \frac{\mathcal{K}}{2} (\partial_x \theta)^2 \right) + f_x^a = 0 \quad (4.5)$$

$$\eta \partial_{xx} v_y - \mu v_y + f_y^a = 0 \quad (4.6)$$

where f_x^a and f_y^a are active forces densities respectively in the x and y direction defined by:

$$f_x^a = -\partial_x \left(P_1 \frac{\cos(2\theta)}{2} \right) \quad (4.7)$$

$$f_y^a = -\partial_x \left(P_1 \frac{\sin(2\theta)}{2} + P_2 \theta \right) \quad (4.8)$$

θ is set to the equilibrium solution (4.2) obtained by minimizing the free energy (4.1). The active forces in the force balance depends on two parameters $P_1 = \zeta \Delta\mu + (\lambda_s + \lambda_b)/2$ and $P_2 = (\lambda_b - \lambda_s)/2$. Solving these equations ((4.5) and (4.6)) allows to compute the y velocity component that depends both on l_{nem} and on the screening length $l_\eta = \sqrt{\frac{\eta}{\mu}}$.

4.5.1.3. Analytical profiles and comparison with experiments

If $P_2 = 0$, then our theoretical description reduces to an active nematic system with rescaled amplitude of the active stresses P_1 . In this case, nematic active tractions have the same amplitude in splay and bend. The y component of the velocity in this case is displayed in Figure 4.24. When $P_1 < 0$, for a 10° interface, a shear is expected, whereas if we increase α , a northward flow is predicted (Figure 4.24.A). When $P_1 > 0$, for a 10° interface, a shear in the opposite direction is expected, whereas if we increase α , a southward flow is predicted (Figure 4.24.B). The absence of a shear flow in experiments for $\alpha = 10^\circ$ (Figure 4.17.D) suggests that, in the framework of this model, $P_2 \neq 0$ i.e., $\lambda_b \neq \lambda_s$.

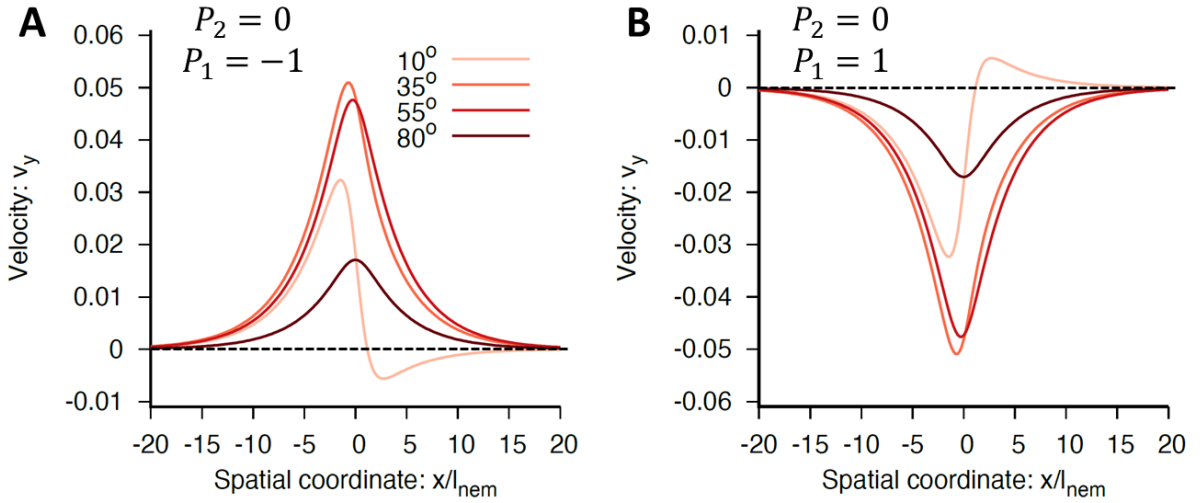


Figure 4.24 : Analytical steady-state y velocity profile in the 10 to 80° interface for $P_2 = 0$ i.e., $\lambda_s = \lambda_b$. In A, we set $P_1 = -1$ and in B, we set $P_1 = +1$. The rest of the parameters are $l_\eta = \sqrt{\eta/\mu} = 4$; $l_{nem} = \sqrt{\mathcal{K}/2H} = 1$; $\mathcal{K} = 1$; $\mu = 1$. The color codes for α . The dashed lines correspond to $v_y = 0$.

We then set $P_2 \neq 0$. The parameters P_1 and P_2 were varied. Here we set $P_1 = -1$ and $P_2 = -1.2$, because these values give the best description of our data. The flows that develop in this case are presented Figure 4.25.A. As observed in the experiments (Figure 4.25.B), a southward flow is predicted at the interface (Figure 4.25.A). We also theoretically predict that reducing the orientation mismatch, i.e., increasing α , decreases the flows at the interface (Figure 4.25.A). This effect was observed experimentally for the flows when varying α from 10 to 80° (Figure 4.25.B). However, even though we capture well the direction of the flows and the decrease in flow amplitude when increasing α , some aspects of the experimental flow profiles

4. Crisscross bilayering of myoblasts controlled by collective contact guidance

are not accurately predicted by this theoretical description. Indeed, the predicted flows are perfectly symmetrical around a maximum positioned east of the interface. This is not the case in experiments in which the flows are maximal west of the interface. We hypothesize that in this geometry for small α , the flows at the west of the interface are dampened by the grooves. Indeed, cell displacements are favored along the grooves and blocked across the grooves. To capture this effect, one should include in this theoretical description anisotropy in the friction. Further work will focus on that.

In the model, we assume incompressibility that prevents any flow in the x direction ($v_x = 0$). However, the x component of the active force at the interface is positive (Figure 4.25.C). In experiments, cell division and cell deformation can render the system compressible. If we relax the incompressibility hypothesis, this active force leads to flows at the interface toward the east. This is indeed what we observed experimentally (Figure 4.25.D). In agreement with experiments, the force, and thus the flows, decrease when α increases. Further work will also focus on relaxing the incompressibility condition in the model to accurately describe flows in the x direction.

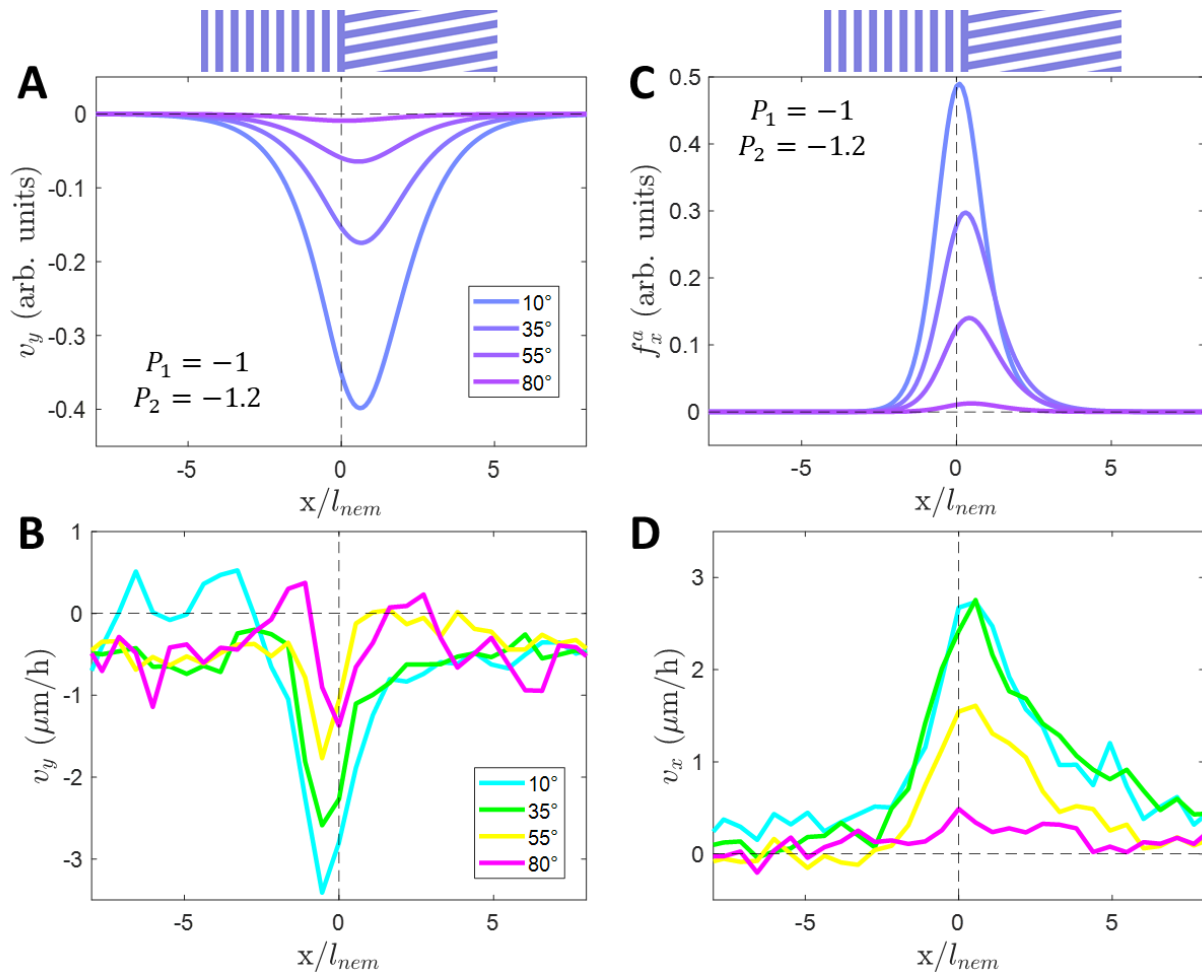


Figure 4.25 : Comparison between flows predicted by the active nematic theory and experimental flows at an interface.

A, C: analytical steady-state y velocity (A) and active force density x component (C) profiles in the 10 to 80° interface for $P_1 = -1$ and $P_2 = -1.2$. We set $l_\eta = \sqrt{\eta/\mu} = 1$; $l_{nem} = \sqrt{\mathcal{K}/2H} = 1$; $\mathcal{K} = 1$; $\mu = 1$. The color codes for α .

B, D: y component (B) and x component (D) velocity profiles across the interface at confluence. l_{nem} is set to 38 μm . Color codes for α . Data are averaged along y and averaged over 30 FOVs taken from 6 separated experimental wells from two independent experiments. Error bars have been omitted for clarity, see Figure 4.17.C, D.

A-D: The schematic and black vertical dashed lines show the location of the interface. Horizontal dashed lines correspond to $v_{x,y} = 0$.

Thus, this theoretical description captures well the flow direction at the monolayer stage before bilayering as well as the effect of varying α . It also gives an argument to understand why the cells that are extruded at the interface during bilayering always migrate eastward. Indeed, this theoretical description explains that there is a force pointing eastward that develops at the interface in the bottom layer (Figure 4.25.C). One of the consequences associated with this net force is that if an object (e.g., an extruded cell) is placed on top of the monolayer at the interface, and is in mechanical contact with the monolayer, this object will be pushed in the direction of the force (i.e., asymmetrically, and here eastward). Thus, we understand that once cells are extruded at the interface, they are pushed eastward by the active force developed in the bottom layer. The net force amplitude decreases when α increases from 10 to 80°. This explains why cells extruded at the interface migrate eastward increasingly slower when α increases from 10 to 80° (Figure 4.18.A).

To conclude, at an interface between orientations, active nematic tractions in the system result in complex flows and a monopole force density at the interface. The complex flows that develop in the monolayer can only be explained if we allow for active nematic traction forces with different amplitudes in bend and splay configurations. These new terms allow to reconcile contractile/ extensile characteristics observed for C2C12 in different geometries.

4.5.1.4. Estimation of the screening length

We now use the comparison between experimental (Figure 4.25.B) and theoretical curves (Figure 4.25.A) to estimate the value of the screening length l_η . The theoretical velocity profiles depend both on x/l_{nem} and on $r = l_\eta/l_{nem}$, with $l_{nem} = \sqrt{\frac{\kappa}{2H}}$ and $l_\eta = \sqrt{\frac{\eta}{\mu}}$. We observe that increasing r decreases the amplitude of the flows and increases the length over which the flows decay (Figure 4.26.A). As mentioned before, experimental flows are dampened at the east of the interface, possibly due to higher friction in the y direction (across the grooves). Thus, to estimate r by comparison between theoretical curves and experimental curves, we define the length dx_W at the west of the interface (Figure 4.26.B). With this trick, we can compare the length scale of y velocity decay at the west of the interface. We find that in theoretical curves for $\alpha = 10^\circ$ and $l_{nem} = 38 \mu m$, this length dx_W increases from 24 to 44 μm when r increases from 0.6 to 1.4. In experiments for $\alpha = 10^\circ$, we measure dx_W to be in this range and thus we roughly estimate $r \approx 1$, i.e., $l_\eta \approx l_{nem}$. This estimation of l_η around 40 μm is compatible with the estimation made from the velocity profiles of C2C12 monolayers confined in mesoscale stripes⁴⁹. With $l_\eta = l_{nem} = 38 \mu m$ and $\alpha = 10^\circ$, we find that the theoretical curve describes well the experimental flows at the west of the interface but not at the east of the interface as previously mentioned.

4. Crisscross bilayering of myoblasts controlled by collective contact guidance

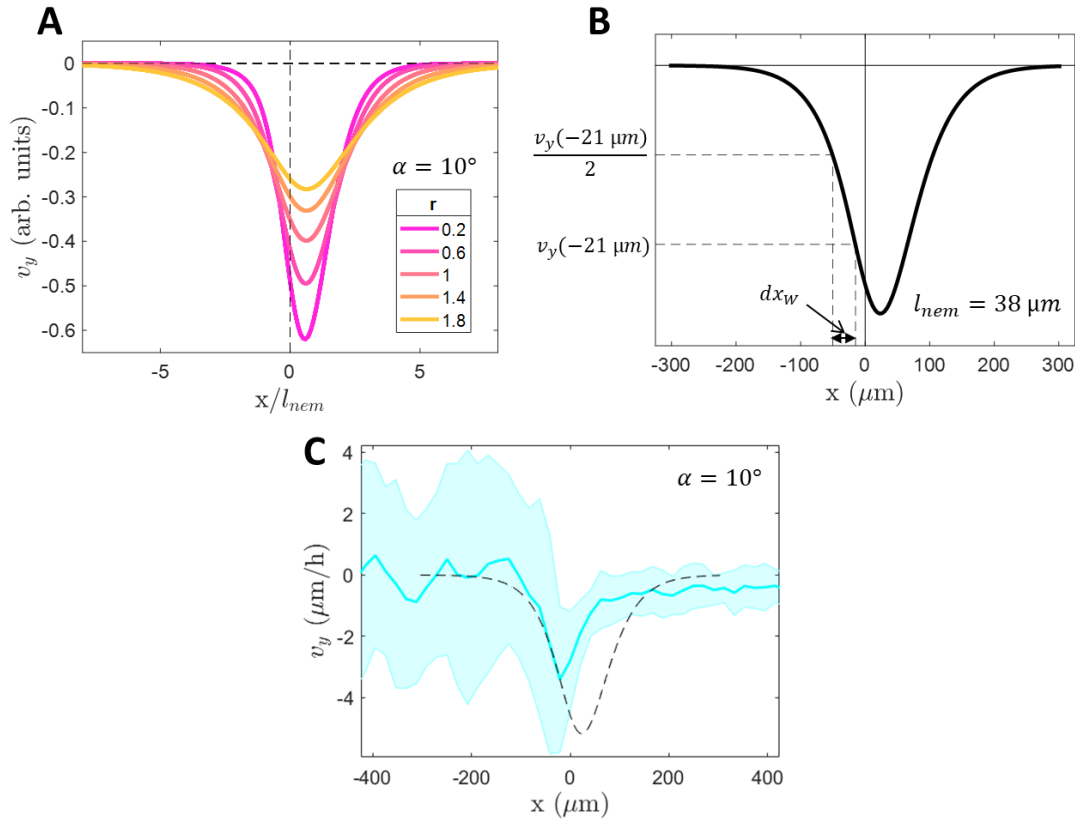


Figure 4.26 : Estimation of the screening length l_η by comparison between theoretical and experimental flows.

A: Analytical steady-state y velocity profiles in the 10° interface for different values of $r = l_\eta/l_{nem}$. We set $P_1 = -1$, $P_2 = -1.2$, $\mathcal{K} = 1$, $\mu = 1$ and $l_{nem} = \sqrt{\mathcal{K}/2H} = 1$. The color codes for r . The vertical dashed line shows the location of the interface, and the horizontal dashed line corresponds to $v_y = 0$.

B: Graphical definition of dx_w , that increases when r increases in theoretical curves. The curve is plotted for $l_{nem} = 38 \mu\text{m}$ and $r = 1$. $21 \mu\text{m}$ is the pixel size of PIV data. The horizontal black line corresponds to $v_y = 0$ and the vertical black line to the position of the interface $x = 0$.

C: y component velocity profile across the 10° interface at confluence. Data are averaged along y and averaged over 30 FOVs taken from 6 separated experimental wells from two independent experiments. Shaded areas show the standard deviation to the mean. The dashed black curve is the theoretical velocity profile for $r = 1$, i.e., $l_\eta = l_{nem} = 38 \mu\text{m}$ and normalized so that the values of v_y at $x = -21 \mu\text{m}$ match between the theoretical and the experimental curves. Other parameters are set as in A.

4.5.2. Flows prediction in chevron geometries

The theoretical description presented in the previous subsection predicts the flows' direction in cell monolayers that are seeded on 10 to 80° interface grooved substrates. However, the same theory can predict the cell flows in other y invariant geometries. For instance, we can theoretically predict flows in another geometry in which the grooves have a chevron shape. This geometry is defined by the angle Φ which ranges from 10° to 80° in our experiments (Figure 4.27.A.1). Grooves in the east part are mirror-symmetrical to grooves in the west part with respect to the y axis (Figure 4.27.A.1). Experimentally, the cells rotate counterclockwise when we travel across the interface for $\Phi = 10^\circ$ (Figure 4.27.A.2, B, C). This corresponds to a splay-dominated organization. Conversely, the cells rotate clockwise across interfaces for $\Phi = 55, 80^\circ$ (Figure 4.27.A.3, B, C), which corresponds to bend-dominated organizations. For $\Phi = 35^\circ$, it was not clear if the rotation of cells was purely clockwise or purely counterclockwise. It rather seems that cell rotation at the

interface is not well defined along the interface and is a complex combination of clockwise and counterclockwise rotations, which prevents an accurate measure of cell orientation by averaging along y . That is why the corresponding experimental curve is not plotted in Figure 4.27.C. Theoretically, we thus impose θ_W and θ_E according to Table 4.2. For $\Phi = 35^\circ$, we choose to investigate the clockwise rotation or bend dominated configuration, as it gave the best agreement with experimental data. The theoretical orientation profiles, for these values of θ_W and θ_E and for $l_{nem} = 38 \mu\text{m}$ measured in the previous geometry, are shown Figure 4.27.C with no adjustable parameter and are in good agreement with the experimental measurement for $\Phi = 10, 55, 80^\circ$.

Φ	θ_W West cell orientation	θ_E East cell orientation	Cell rotation across the interface
10°	260°	280°	Counterclockwise
35°	235°	125°	Clockwise
55°	215°	145°	Clockwise
80°	190°	170°	Clockwise

Table 4.2 : Values of θ_W and θ_E in the different chevron geometries characterized by the angle Φ and corresponding cell rotation.

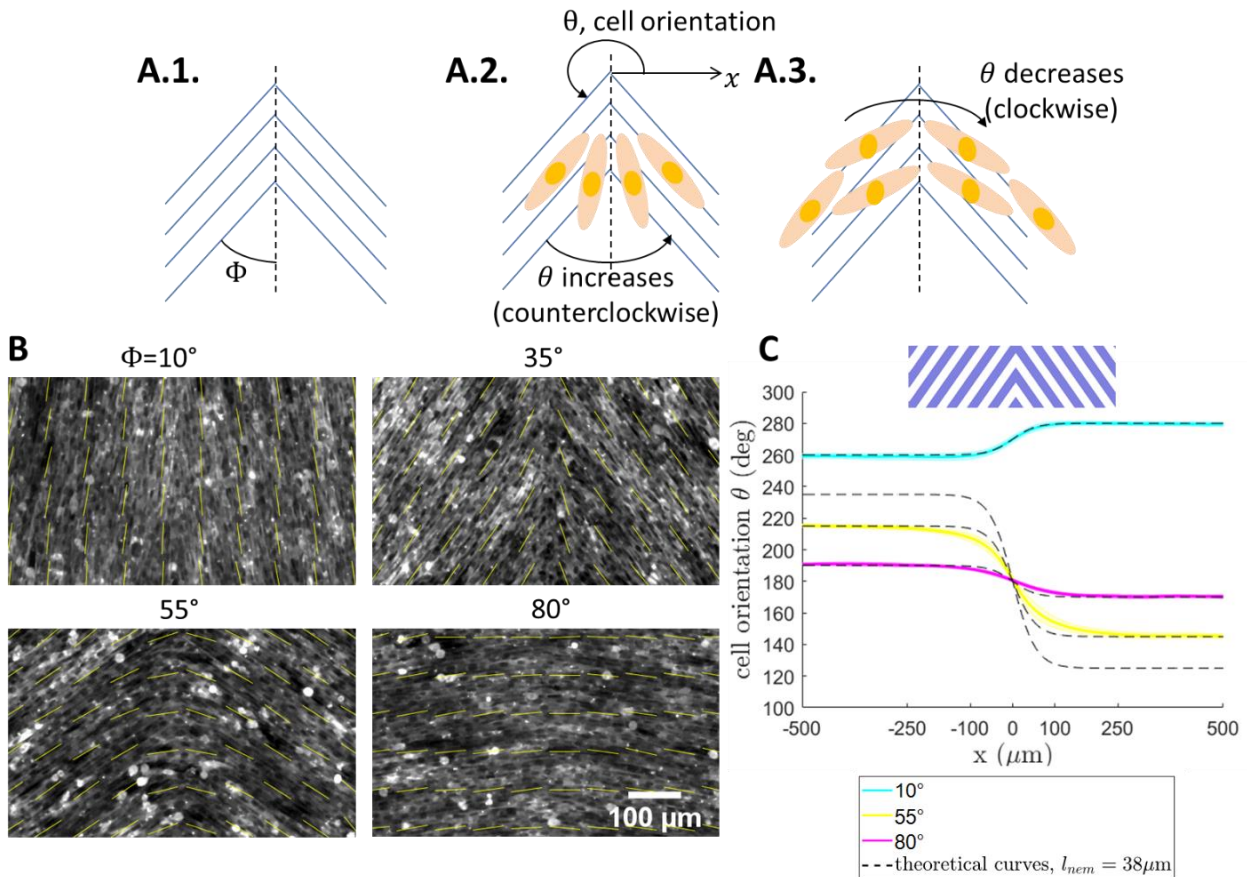


Figure 4.27 : Cell orientation in chevron shape geometries.

A.1: Schematic of the chevron geometry which is defined by the angle Φ . Blue lines indicate grooves' orientation.

A.2, 3: Cell orientation is defined by the angle θ that can either increase (A.2) or decrease (A.3) across the interface.

B: Fluorescent images of the system at confluence for different chevron geometries. Yellow lines indicate cell orientation.

C: Cell orientation profile across the interface at confluence. Color codes for Φ . The schematic shows the location and design of the interface. Data are averaged along y and averaged over 30 FOVs taken from 6 separated experimental wells from two independent experiments. Shaded areas show the standard deviation to the mean. Dashed black curves correspond to equilibrium angle profiles obtained by minimizing the free energy and given by equation (4.2) in which θ_W and θ_E are set to the values in Table 4.2. We set

$$l_{nem} = 38 \mu\text{m} \text{ as measured in 4.5.1.1.}$$

From these equilibrium orientation profiles, we can predict flows and active forces at the interface keeping the same parameter values (i.e., $P_1 = -1$, $P_2 = -1.2$, $l_\eta = l_{nem} = 38 \mu m$) as those estimated in the previous geometries presenting an orientation mismatch at the interface (see 4.5.1.3). The expected flows in the y direction are presented Figure 4.28.B. For $\Phi = 35, 55, 80^\circ$, a southward flow is expected, the amplitude of the flow decreasing when Φ increases. The y flow is reversed for $\Phi = 10^\circ$. In this case, a small northward flow is expected at the interface.

To check these predictions, we monitored the cell monolayer evolution on such chevron geometries (Figure 4.28.A). At confluence on $\Phi = 35, 55, 80^\circ$ chevron interfaces, we observed as predicted a southward flow, with a smaller amplitude for $\Phi = 80^\circ$. The behavior switches for $\Phi = 10^\circ$, and we observe at the interface a northward flow of very small amplitude (Figure 4.28.C). The theoretical curves are therefore in good agreement with experimental data (Figure 4.28.C). Indeed, in this case, having neglected possible anisotropy in the friction is not a problem as the geometry is symmetric with respect to the y axis. However, the amplitude of the flows for $\Phi = 35^\circ$ is expected to be larger compared to $\Phi = 55^\circ$. This difference might be because, as mentioned before, the cell orientation evolution at the interface in experiments for $\Phi = 35^\circ$ is more complex than what we propose in the theoretical description. 30 hours after confluence, a downward flow is observed for all angles (Figure 4.28.D), and we recover the larger amplitude of flows for $\Phi = 35^\circ$. At that time point a second layer might have developed, and the flows that are measured might be dominated by cell movements in the top layer.

Another interesting feature that we can theoretically predict is the active force in the x direction. As previously explained, by relaxing the incompressibility conditions in our description, this active force generates flows in the same direction. Moreover, we found that cell monolayers can evolve in the third dimension and the x component of the active force can direct migration of cells extruded at the interface. The x component of the active force is plotted in Figure 4.28.E. The sign of this force around the interface is the same as the expected flows that develop in the x direction either on a potential top layer or theoretically when the incompressibility hypothesis is relaxed. A convergent flow toward the interface with decreasing amplitude is predicted for Φ varying from 35 to 80° whereas an outward flow is expected for $\Phi=10^\circ$. This agrees with the flows in the x direction that we experimentally measure 30 hours after confluence for varying Φ (Figure 4.28.F).

To conclude, we successfully used the developed theoretical description to predict experimental flows in a new substrate design. With the same approach, one could use the model to predict flows in more complex geometries imposing angle gradients in the monolayer and predict how will cells flow and organize.

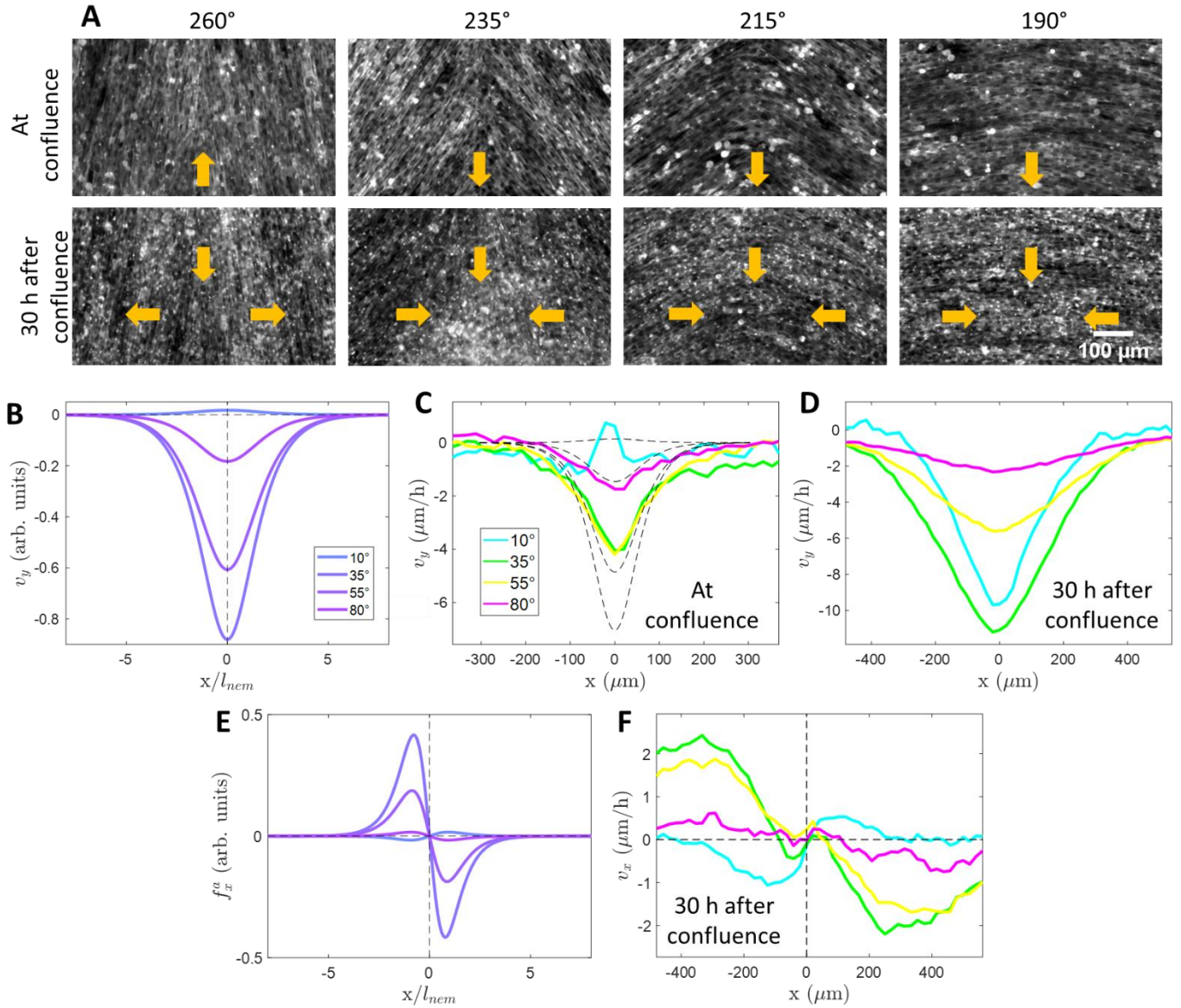


Figure 4.28 : Flows in chevron shape geometries.

A: Fluorescent images of the system at confluence and 30 hours after confluence for different chevron geometries. Arrows highlight flows direction.

B: Analytical steady-state y velocity profile for the different chevron shape geometries.

C, D: Experimental x component of the velocity profiles across the interface at confluence (C) and 30 hours after confluence (D). In C, the black dashed curves correspond to theoretical curves for $P_1 = -1$, $P_2 = -1.2$, $l_\eta = l_{nem} = 38 \mu\text{m}$, $\mathcal{K} = 1$, $\mu = 1$. All the curves share the same X8 normalization.

E: Analytical steady-state active force x component profile for the different chevron shape geometries.

F: Experimental y component of the velocity profiles across the interface 30 h after confluence.

B, E: $P_1 = -1$ and $P_2 = -1.2$. We set $l_\eta = l_{nem}$; $l_{nem} = \sqrt{\mathcal{K}/2H} = 1$; $\mathcal{K} = 1$; $\mu = 1$. The color codes for Φ .

C, D, F: Color codes for Φ . Data are averaged along y and averaged over 30 FOVs taken from 6 separated experimental wells from two independent experiments. Error bars have been omitted for clarity.

B, E, F: The black dashed vertical lines highlight the position of the interface $x = 0$ and the black dashed horizontal lines correspond to $v_{y,x} = 0$.

4.5.3. Toward a two layers model

In the previous subsections, we focused on a 2D theoretical description to better understand the flows and forces in the monolayer at an orientation interface. However, we observe at later stage a transition from a monolayer toward a bilayer system. To go further in the description and aim at better understanding the two layers dynamics on perpendicular interfaces, we propose to extend the previous approach. Here, I present the main ingredients and insights of this theoretical description.

We describe our system as two stacked interacting active nematic layers. Briefly, the two layers are described by the equations proposed above supplemented with interaction forces between the two layers, such as viscous friction or active nematic traction forces between the two layers. The bottom layer is still subjected to the aligning effects of the grooves, and we assume that its orientation field is imposed by the grooves. We also introduce aligning interactions between the top and the bottom layer. The mass conservation equations in both layers are adapted to allow for mass fluxes between layers. Those exchanges of mass are mediated by mechanics. For instance, cell extrusions correspond to large compressive stresses.

One can solve the steady state solutions of this two-interacting layered system and study the impact of the parameters on the flows in the two layers. A complete and systematic parameter study needs to be performed but the main physical mechanism underlying the bilayer progression from the interface is well captured by this description. Here I describe qualitatively the behavior of these two active nematic interacting layers. Because of higher stress at the interface, a mass flux develops from the bottom to the top layer at this location. The top layer at the interface made of extruded cells is subjected to the monopole force developed in the bottom layer. Thus, the extruded cells are pushed eastward and a flow in the top layer is observed from the interface toward the east, whereas a flow on the bottom layer is observed from the east to the interface. The continuous extrusion and displacement of cells at the interface lead to the collective top layer progression.

In this analysis, we neglect the couplings between flows and orientation. We considered that cellular orientations are fixed in the two layers and constrained by the aligning field of the grooves. However, in the experiments, cells extruded at the interface that migrate eastward remain perpendicular to bottom cells. This effect is not captured by the theoretical description. We propose the following mechanism to understand the orientation mismatch between layers: because the x velocity decays eastward of the bilayering front, cells in the progressing orthogonal layer are subjected to compressive shear flows caused by the gradient of x velocity decreasing from the bilayering front. In liquid crystals, rod-like particles subjected to a compressive shear flow tend to reorient perpendicular to the direction of compressive flows. The reorientation of the cells on the top layer can be similarly dominated by flow couplings near the interface, which would induce a N/S alignment and prevent the cells from aligning with bottom cells in the progressing top layer. Far from the interface, there is no net flow and thus the parallel alignment between layers is respected.

To conclude, cell orientation in the top layer is explained by two cues. Far from the interface, the flows are negligible and the parallel alignment between layers dominates. Close to the interface, flows develop and modify the cell orientation: compressive flows in the progressing orthogonal layer explain the N/S orientation of the cells. Up to now, this effect was neglected for simplicity but might dominate for the top progressing layer orientation. This is one of the main limitations of the model and further work should focus on studying the effect of flows on the orientation field of the top layer.

4.6. Conclusion and perspectives

4.6.1. Conclusion

In this project, we designed and optimized substrates with juxtaposed orthogonal orientation along an interface, to allow the controlled spontaneous formation of large-scale orthogonal bilayers. We showed that orthogonal bilayer initiation and eastward progression is explained by orientation gradient-induced complex flows and extrusion at the interface of cells coming from the cell reservoir or coming from the east of the interface after they rotated. With our experimental set-up, we could investigate the effect of gradient of orientation and conclude that decreasing the orientation mismatch at the interface progressively reduces the efficiency of bilayer formation and progression.

The flows that appear at the confluent monolayer stage are well predicted by an active nematic fluid theoretical description in which the nematic active traction forces have different amplitude in bend and splay configurations. This model also successfully predicts the flows in the chevron geometries.

We have shown that a two interacting layer theoretical description gives arguments to understand some experimental features of the bilayer stage: extrusion appears preferentially at the interface because of higher stresses and extruded cells are pushed away from the interface by the monopole force that develops in the bottom layer. The model does not predict the cell orientation in the migrating top layer as well as density inhomogeneity in the system. We explain the orientation in the progressing top layer by a hydrodynamical argument: the velocity pattern in the top layer imposes compressive forces in the top layer and prevents cells from reorienting with the bottom layer that thus remain N/S-oriented while migrating eastward.

With this simplified and well-controlled geometry, we were able to investigate in more details the bilayering process, both experimentally and theoretically, and thus to better understand the bilayering at spontaneous $+1/2$ defects.

Even though we shined some light on the physics underlying the bilayering phenomenon, some questions are still open. In the next paragraphs, I discuss some of these questions and propose perspectives for this work.

4.6.2. Role of cell division, cell contractility, cell-cell, and cell-substrate adhesion

Even though the model gives arguments to understand experimental observations, it assumes incompressibility in the system and neglects cell division which might add a contribution to cell reservoir feeding and orthogonal bilayer progression. Further work should focus on analyzing the effect of cell division by inhibiting it with mitomycin C. Localizing cell division in the system might also be useful as lower cell density at the interface might induce more cell division there and thus a cell restocking in the cell reservoir. To do that, one could use BrdU to detect cells that are dividing and ultimately have a spatial repartition of division in the system. With this information, we should be able to refine the model by including cell division.

The physical mechanism relies on cell contractility. We expect that perturbing the system with blebbistatin that reduces cell contractility, would reduce the flows, and impair orthogonal bilayering. Another interesting aspect would be to modify the strength of cell-cell junctions and cell-substrate adhesions and

observe if there is an inhibiting effect on the bilayering progression. As it has been shown not to impair topological defects bilayering⁵³, we expect the effect of cell-cell junction inhibition to be minor. However, the differences observed for different substrate treatments suggest that the strength of adhesion between bottom cells and substrate is crucial for bilayering initiation and progression (Annex 6.5). How the nature of the substrate (coating with different ECM proteins, stiffness, ...) impacts bilayering is thus an interesting question for future works.

4.6.3. ECM-mediated interactions between the two layers

We explain the cell displacement and orientation in the top layer with hydrodynamical arguments. We know that cells in the top layer are in contact with the bottom layer and that the cell-secreted ECM is crucial for proper bilayering. Our present results suggest that ECM fibers of the bottom layer act as tracks that guide cell migration of the top layer. Moreover, we showed that cells in the progressing top layer migrate perpendicular to their long axis whereas they migrate along their long axis on flat substrates. However, the biological support of this type of migration is not known at this point. Further studies should focus on the biomechanical interactions between the two layers. The first challenge is to successfully monitor flows in both layers with live imaging confocal experiments at higher resolution and for longer periods of time. The advantage of the experimental system developed in this thesis is that the location where orthogonal bilayering initiates is fully controlled. The other challenge would be to live image adhesion proteins and ECM proteins between cells in the same layer and between layers to decipher the biological support of the perpendicular migration of top cells along the long axis of bottom cells.

4.6.4. Impact of cell chirality

C2C12 cells have been previously shown to be chiral. Indeed, when plated in adhesive mesoscale stripes, they present a tilt angle with a clear signature of chirality: in more than 90% of the repeats, cells orient in a clockwise direction⁴⁹. In the interface experiment, we showed that decreasing the orientation mismatch at the interface decreases the speed at which cells in the top layer migrate eastward. To go further, we compared positive and negative α (see Figure 4.29). Preliminary results suggest that the x velocity of the top layer is lower on interface patterns with $\alpha < 0$ (Figure 4.29 right) compared to the case $\alpha > 0$ presented before (Figure 4.29 left). It means that the bilayering phenomenon is more efficient when the natural cell chirality (SW-NE) is respected. Further study should focus on the origin and impact of this intrinsic cell chirality.

4.6.5. Building more complex flows and structures through micropatterning

One of the conclusions of this study is that orientation mismatch leads to complex flows in the system and bilayering events. One opportunity offered by micropatterning the substrates is to guide flows in the system and ultimately the 3D structure of the final system. For example, we designed a pattern with two facing interfaces as in Figure 4.30. Two orthogonal bilayers are formed at the interfaces and migrate toward each other ultimately forming a complex structure called a cell cord. By designing more complex geometries in the substrate, we can imagine building fine-tuned final multilayered structures. With the same approach, one

could use the theoretical description to predict flows in other geometries imposing orientation gradients in the monolayer and ultimately predicts how cells will flow and organize.

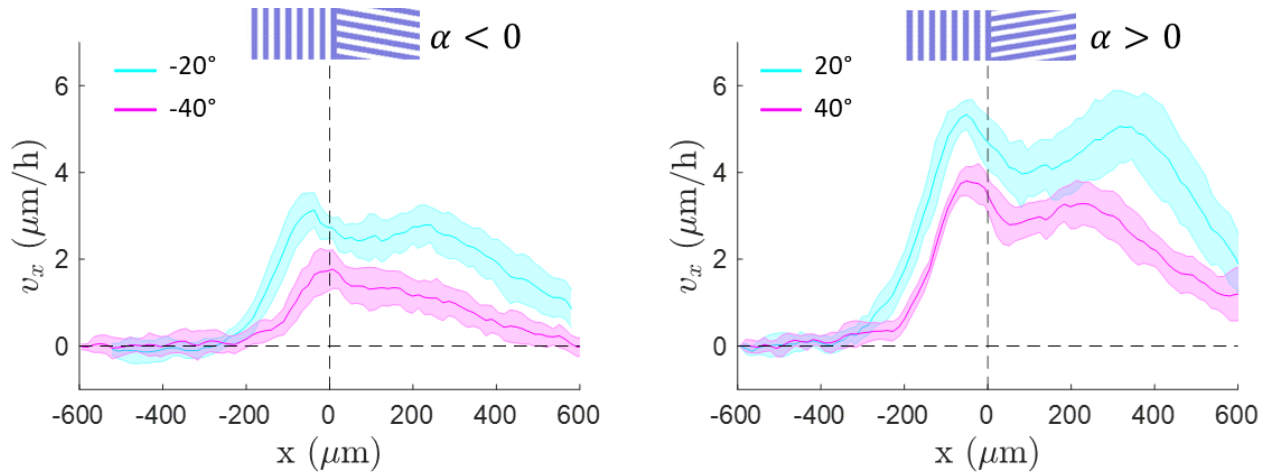


Figure 4.29 : Bilayering progression is more efficient on patterns which impose an orientation gradient in agreement with the cell's natural chirality (SW-NE). x component velocity profiles across the interface 70 h after confluence on interface patterns with $\alpha < 0$ (left) and $\alpha > 0$ (right). Color codes for α . The schematic and the black vertical dashed lines show the design and location of the interface. Horizontal dashed lines correspond to $v_x = 0$. Data are averaged along y and averaged over 10 FOVs along one interface. Shaded areas show the standard deviation to the mean over the FOVs.

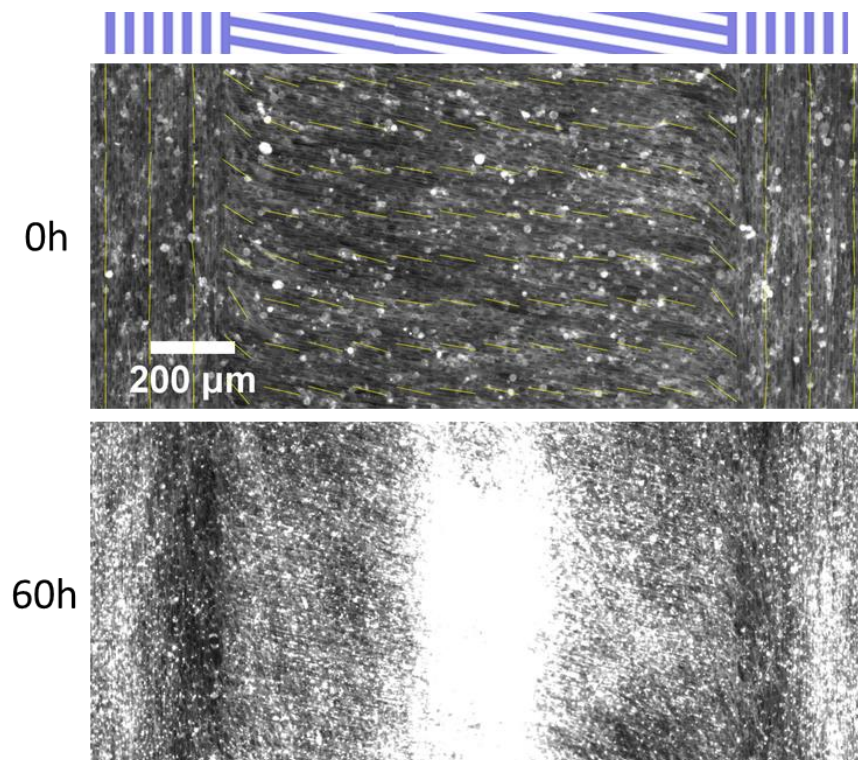


Figure 4.30: Cell cord formation on a two facing interfaces substrate. Fluorescent images taken at confluence (top) and 60 hours post confluence (bottom). The schematics on top show the location and design of the interfaces. Yellow lines indicate cell orientation at confluence.

5. Conclusion

In this manuscript, we focused on two different experimental situations in which we used contact guidance to trigger or control large-scale collective cell behaviors. The experiments performed involve microfabrication, cell and molecular biology and long-term live imaging microscopy techniques. The results were analyzed using image analysis techniques such as PIV and further interpreted using tools and concepts from active matter physics.

First, we showed that collective contact guidance regularizes chaotic flows in a HBEC monolayer. Indeed, when plated on deep enough microgrooves, HBECs organize in a laning pattern that we characterized in Chapter 3. The laning pattern consists in alternating, non-periodic, large-scale (millimeters long and 100 μm to millimeters wide) lanes migrating in antiparallel directions. The emergence of laning relies on the ability of cells to protrude in a directed manner rather than on their contractility or cell-cell adhesion. Our results are well captured by a hydrodynamic description of an active polar fluid that undergoes a disorder-to-order transition mediated by polar traction forces and a coupling between velocity and polarization. The effect of the grooves is described by anisotropy in the friction that both favors the transition and stabilizes the ordered state in a laning pattern. Self-propelled particle-based simulations experience the same laning transition and further validate that cell-cell adhesion is not needed for laning emergence but excluded volume interactions are. Further work should focus on linking theoretical parameters to the biological machinery to be able to tune in a predicted manner the response of our cells to anisotropic substrates.

Then, we engineered a PDMS micro-grooved substrate to control the spontaneous self-formation of C2C12 myoblast orthogonal bilayers. We successfully formed *in vitro* well-organized orthogonal bilayer structures 13 mm long and hundreds of micrometers large. We quantified the flows in our system and showed that a sufficient mismatch of orientation at a fixed interface is needed for the formation of such structures. To better understand the flows imposed by a mismatch of orientation, we proposed a refined theoretical description of active nematic fluids. The theoretical model was validated by experiments for a different “chevron-like” substrate geometry. The theory was then further extended to propose a two interacting layers description: a mismatch of orientation combined to cell active nematic traction forces leads to higher stress at the interface and thus cell extrusion. Extruded cells are pushed eastward from the interface by the monopole force that develops in the bottom layer. In further work, the role of cell division in this process, as well as the biomechanical microscopic interactions between the layers, need to be investigated. This project is a first step toward controlling cell flows and 3D structures in more complex geometries.

In both projects, we used the contact guidance strategy to regularize, trigger and control collective cell flows in confluent monolayers. Acting as a guiding field on the cells, it has proven to be a powerful tool and we think that more studies are needed to decipher the importance of collective contact guidance both *in vitro* and *in vivo*. The motivations of the work presented in this manuscript have roots in active matter physics and tissue engineering and we hope that some of our results will inspire further works in these fascinating fields.

6. Annexes

6.1. Materials and detailed protocols	147
6.1.1. Equipment's characteristics.....	147
6.1.1.1. <i>Microscopes' characteristics</i>	147
6.1.1.2. <i>References of other pieces of equipment</i>	147
6.1.2. Chromium mask preparation.....	148
6.1.3. Micro-structured wafer preparation	149
6.1.4. PDMS substrate preparation	151
6.1.5. Chemically micro or meso-patterned substrates preparation	152
6.1.6. Cell culture medium and cell biology products	154
6.1.7. E-cadherin knock down protocol.....	155
6.1.8. Immunostaining protocol	156
6.2. Robustness of PIV measurements to parameters change	157
6.2.1. Introduction.....	157
6.2.2. Impact of global filter and sliding time average	157
6.2.3. Impact of sub window size	159
6.3. Continuum theory of an active polar fluid with anisotropic friction	161
6.3.1. Conservation and constitutive equations.....	161
6.3.2. Velocity fluctuations response to anisotropic friction	163
6.3.3. Linear stability of the disordered state	165
6.3.4. Summary of the active polar fluid theory contributions	167
6.4. Equations for self-propelled particle-based simulations.....	169
6.4.1. Equations describing single particle trajectory	169
6.4.2. Equations including interactions between neighboring particles	169
6.4.3. Quantifying the laning transition in simulations	170
6.5. Impact of surface chemistry on bilayering	172
6.5.1. Cells dewet and form aggregates on non-treated PDMS substrates	172
6.5.2. PDMS activation and coating contribute to stable bilayering at a perpendicular interface ...	172
6.5.3. PDMS plasma activation decreases fibronectin absorption.....	174

6.1. Materials and detailed protocols

6.1.1. Equipment's characteristics

6.1.1.1. Microscopes' characteristics

Microscope	Type	Software	Objectives	Camera	Size of FOV (pixels)	Pixel size (μm)
<i>Olympus IX71</i>	Inverted microscope	metamorph	4X, 10X air	Retiga 4000R, CCD	2048 x 2048	10X: 0.747
				Prime BSI sCMOS (Teledyne Photometrics)	2048 x 2048	10X: 0.65 4X: 1.625
<i>Leica DM-IRB</i>	Inverted microscope	metamorph	10X air	Retiga 6000 (QImaging)	1379X1104 (bin 2)	0.918 (bin 2)
<i>Nikon Eclipse Ti</i>	Inverted spinning disk confocal microscope	metamorph	20X oil	Flash4 Hamamatsu sCMOS	1392X 1040	0.322 (in XY)
<i>Zeiss LSM880NLO</i>	Inverted laser scanning confocal microscope with airyscan module	zen	63X oil	NA	to be adjusted	0.035

6.1.1.2. References of other pieces of equipment

- Direct laser writing on wafer or chromium mask coated with photoresist was performed using a micro-Pattern Generator 101 (μPG 101; Heidelberg instruments) available at the IPGG technological platform.
- UV illumination of wafer or glass coverslips coated with photoresist through a mask was performed using a mask aligner (MJB3 Mask aligner; Karl Suss) available in the clean room of the lab Physico Chimie Curie.
- Measurements of resin layer height on wafers were performed with a mechanical profilometer (Ambios technology) available in the clean room of the lab Physico Chimie Curie.

6.1.2. Chromium mask preparation

Chromium masks were prepared using equipment and chemicals at the IPGG technological platform. Chromium mask blanks coated with AZ 1518 ready to expose were bought from MBW & A (reference: SL / 4x4x0,06 (Master) LRC D3 / AZ std).

The protocol needs to be performed under inactiv light until the end of step 2.b (photoresist development).

Step	Instructions	Time	Comments
1.	<i>Expose a chromium mask</i> (already coated with photoresist) with the desired pattern using direct laser writing (μ PG 101 pattern generator). The exposure pattern is designed with the Clewin software.		<ul style="list-style-type: none"> - Illumination parameters (exposure energy in mW and % filter) need to be calibrated to avoid over or under photoresist exposure and obtain a satisfying resolution. Typical values used were 10%-15% of 5 mW. - Make sure the filter is on. - Exposure lasted typically overnight
2.	<i>Develop the mask</i>		
a.	Prepare a solution of AZ351B developer in distilled water (1:3)		
b.	Develop the mask in AZ351B developer (1:3) Rinse with distilled water and air dry	2 min	
c.	Etch the mask in chrome etch solution Rinse with distilled water and air dry	1 min	Only chrome that is not protected by photoresist is etched. Etching duration can depend on the final pattern size and needs to be optimized.
d.	Strip the remaining resin in acetone under sonication Rinse with distilled water and air dry	few minutes	
3.	<i>Check the chrome pattern on the mask with a microscope</i>		

6.1.3. Micro-structured wafer preparation

We aim at preparing micro-structured wafers with 4 μm wide grooves and ridges, groove height ranging from 200 nm to 4.5 μm . We used silicon wafer of 3 or 4 inches in diameter (Silicon Materials).

The protocol needs to be performed under inactic light until the end of step 3 (photoresist development). Spin coating recipes to obtain specific groove depth are given in the table at the end of the protocol.

List of specific chemicals and providers:

- Omnicoat; MicroChem
- SU-8 2000 Permanent epoxy negative photoresist, SU-8 2002 or SU-8 2005; MicroChem
- SU-8 2000 thinner; MicroChem
- Silane: (Tridecafluoro-1,1,2,2-tetrahydrooctyl) trichlorosilane, 97%; abcr GmbH (reference: AB111444)
- PGMEA (Propylene glycol methyl ether acetate) or SU-8 developer

Step	Instructions	Time	Comments
<i>1. Coat the wafer</i>			
a.	Spin coat Omnicoat at 3000 rpm	30 s	Omnicoat ensures long term adhesion of the photoresist on the wafer.
b.	Bake at 200°	1 min	Let the wafer cool down after each baking step.
c.	Spin coat SU-8 2002 or SU-8 2005 (optionally diluted with thinner)	30 s	Spin coating recipe needs to be adjusted depending on the desired final photoresist height
d.	Soft bake at 95°	1 min	1 min 30 for 2.5 μm height 2 min for 4.5 μm height
<i>2. Expose the wafer</i>			
Option 1	Expose photoresist with UV light through a clean chromium mask (superimposed with a lp360 filter on top of the mask) using a mask aligner.	15 s (To adjust)	The mask should be in close contact with the wafer, chromium part facing the photoresist.
Option 2	Expose photoresist with direct laser writing using μPG 101 pattern generator. The exposure pattern is designed with the Clewin software.		- Illumination parameters (exposure energy in mW and % filter) need to be calibrated to avoid over or under photoresist exposure and obtain a satisfying resolution. Typical values used were 15%-25% of 30 mW. (Adjusting the % impacts principally groove and ridge width but also groove depth although marginally). - Make sure filter is off. - Exposure lasted overnight typically

3. Develop the wafer			
a.	Post-exposure bake at 95°	2 min	
b.	Develop in PGMEA or SU-8 developer	1 min	Non-exposed photoresist is dissolved.
c.	On top of a waste Becher, rinse with development solution and then with isopropanol		
d.	Air dry		
4. Check wafer's characteristics and silanize			
a.	Image the wafer using a reflective light microscope		Check groove and ridge width. Adjust illumination parameters if needed to correct under or over exposure.
b.	Check resin height using a mechanical profilometer		Adjust photoresist height by either changing the spin coating parameters or the dilution of photoresist in thinner (see table below). Be careful to the expiration date because time tends to deteriorate photoresist viscosity.
c.	Pour few drops of silane in a weighting boat in the bottom of a vacuum bell, add the wafer, make vacuum.	2 hours	Silane coating favors PDMS detachment from the wafer.

Table for spin coating recipes and corresponding measured photoresist height:

Photoresist	Thinner	Spin coating speed (rpm)	Spin coating duration (s)	Height of photoresist layer (μm)
SU-8 2002 (100%)	0%	3000	30	1.75
SU-8 2002 (75%)	25%	3000	30	0.95
SU-8 2002 (50%)	50%	3000	30	0.45
SU-8 2002 (33%)	67%	3000	30	0.2
SU-8 2002 (25%)	75%	3000	30	0.15
SU-8 2002 (100%)	0%	1000	30	2.5
SU-8 2002 (100%)	0%	4000	30	4.5

6.1.4. PDMS substrate preparation

In most of the experiments performed, cells were seeded on micro-grooved substrates made of Polydimethylsiloxane (PDMS, Sylgard 184). Fabricated micro-structured wafers have been used as mold to prepare such micro-grooved PDMS substrates using the following protocol:

Step	Instructions	Time	Comments
<i>1. Deposit PDMS on wafer</i>			
a.	Prepare and mix energetically a PDMS solution (ratio 10:1: 5 g of monomer and 0.5 g of crosslinking agent)		
b.	Degas PDMS solution in a vacuum chamber		Wait until complete degassing
c.	Pour PDMS solution on the wafer		
d.	Spin coat at 500 rpm	60 s	
e.	Reticulate at 65°	overnight	
<i>2. Detach PDMS from wafer and prepare the experimental plate</i>			
a.	Cut the grooved area with a scalpel		
b.	Detach grooved area with a tweezer and deposit it on clean glass coverslips, grooves facing up.		Ideally, detach the PDMS in the groove direction to avoid damaging the wafer
c.	Plasma clean the PDMS pieces	30 s	(Unless otherwise stated)
d.	Put the PDMS pieces in the bottom of wells of a glass bottom 12- well plate or in glass bottom 35 mm ² dishes.		Align grooves in the same direction in all wells to facilitate image analysis
<i>3. Fibronectin coating</i>			
a.	Coat the wells with fibronectin at 10 µg/mL at 37°C	1 h	(Unless otherwise stated) Note that the time between plasma treatment and fibronectin coating has an impact on fibronectin absorption by PDMS (see subsection 6.5.3). For Chapter 3, fibronectin coating was performed just after plasma cleaning, whereas for Chapter 4, PDMS was allowed to rest for 8 hours approximately before fibronectin coating.

6.1.5. Chemically micro or meso-patterned substrates preparation

The PEG-based patterning protocol allows for fabricating glass substrate coated with a well-defined pattern of PEG (cell repellent) and fibronectin regions. It has been used in the team for several years¹⁰⁶ and further optimized. Incubation steps are performed in a glass petri dish in which the coverslips are deposited without overlapping. The protocol needs to be performed under inactic light from step 3.b to step 4.d.

List of chemicals' abbreviations:

- allylchlorosilane 95%: ATC-silane
- acrylamide: Aam
- N,N'-methylenebis(acrylamide): BIS
- poly(ethylene glycol): PEG
- S1813 positive photoresist (Shipley): S1813
- Polydimethylsiloxane (Sylgard 184): PDMS
- Microposit™ 351 developer: 351 developer

Step	Instructions	Time	Comments
<i>1. Clean the glass coverslips</i>			
a.	Rinse the coverslips in ethanol under sonication Rinse with distilled water and air dry		
b.	Incubate the coverslips in a piranha solution: 30 mL of sulfuric acid + 10 mL of hydrogen peroxide Rinse with distilled water and air dry	5 min	Use reinforced gloves and a protective visor during this step. Be careful, the reaction is exothermic. Make sure no metal touches the solution.
c.	Further clean glass coverslips in air plasma	5 min	
<i>2. Deposit a covalent layer</i>			
a.	Incubate the coverslips in 15.5 mL of Toluene + 200 µL of ATC-silane Rinse with Toluene, distilled water, and air dry	5 min	Make sure no water touches the solution (that will react with silane). After incubation, the coverslips should be highly hydrophobic.
b.	Bake the silanized coverslips at 90°C	1 h	
<i>3. Deposit the gel layers</i>			
a.	Prepare the gel solutions: - A: 3 g Aam, 0.03 g BIS, 1.09 g benzophenone in 20 mL acetone - B: 0.6 g PEG, 0.9 g BIS, 1.09 g benzophenone in 20 mL methanol		Mix them well with the help of the sonicator.
b.	Incubate the coverslips in A	5 min	Use inactic light
c.	Illuminate them with UV light transilluminator (light from the bottom)	3 min	A thin white layer appears at the end of the illumination step.
d.	Rinse with acetone, distilled water, and air dry		The coated side corresponds to the bottom side that has been illuminated, and is now

			hydrophilic, meaning that no condensation is able to form on this side.
e.	Incubate the coverslips in solution B	5 min	Make sure that the coated side is the bottom side.
f.	Illuminate them with UV light transilluminator (light from the bottom)	3 min	Small white crystals float in the solution at the end of the process.
g.	Rinse with methanol, acetone, distilled water, and air dry		Turn the coverslips so that the coated side is on top at the end of the rinsing process. The coated side is still hydrophilic.
<hr/>			
4. Pattern the PEG layer with photolithography			
<hr/>			
a.	Spincoat S1813 positive photoresist on the PEG coated side of the coverslips at 4000 rpm	30 s	Use inactinic light
b.	Bake the coverlips at 115°C	1min	
c.	Illuminate the coverslips with UV light through a clean mask (chromium or soft mask attached to a mask's blank) using a mask aligner	8 s	The photoresist should be in contact with either the chrome part of a chromium mask or the ink of a soft mask.
d.	Develop the coverslips in a solution of 40mL distilled water + 10mL of 351 developer	10s	
e.	Put the coverslips in air plasma to remove the cell repellent layer in parts not protected anymore by photoresist.	4X 5 min	Avoid overheating coverslips by waiting between plasma treatments.
f.	Remove the photoresist with acetone Rinse with water and air dry		
<hr/>			
5. Prepare the final plate			
<hr/>			
a.	Drill holes in the bottom of a plastic bottom 6 or 12 well plate		
b.	Prepare 10:1 PDMS solution: 0.1 g crosslinking agent + 1 g of monomer. Mix well. Glue coverslips with PDMS at the bottom of the wells.		
c.	Bake at 65° C	at least 1h	
d.	Coat the wells with fibronectin		Optional
<hr/>			

6.1.6. Cell culture medium and cell biology products

HBECs were cultured in keratinocyte serum-free medium with L-glutamine (Keratinocyte-SFM with L-glutamine; Gibco) supplemented with:

- 1% antibiotics solution [penicillin (10, 000 units/mL) + streptomycin (10 mg/mL); Gibco]
- 20 mM Hepes buffer solution (Gibco)
- 30 µg/mL Geneticin Selective Antibiotic (G418 Sulfate) (Gibco)
- 250 ng/mL puromycin dihydrochloride (Gibco)
- 5 ng/mL prequalified human recombinant epidermal growth factor 1-53 (EGF 1-53; Gibco)
- 50 µg/mL bovine pituitary extract (BPE; Gibco).

HT1080, MDCK and C2C12 cells were cultured in Dulbecco's modified Eagle's medium (High glucose + GlutaMAX, Gibco) supplemented with 10% Fetal Bovine Serum (FBS, Sigma) and 1% antibiotics solution [penicillin (10, 000 units/mL) + streptomycin (10 mg/mL); Gibco].

Other cell biology products:

- Trypsin: TrypLE Express (Gibco)
- Defined trypsin inhibitor (Gibco)
- Fibronectin:
 - o Bovine plasma fibronectin (1 mg) (Gibco). Fibronectin solution was reconstructed by adding 1 mL of distilled water and stored at -20° C in small aliquots.
 - o Fluorescent fibronectin: Fibronectine Bovine TRITC (cytoskeleton inc)
- Drugs:
 - o CK-666 (Sigma-aldrich, SML0006-5mg)
 - o Para-nitroblebbistatin (Cayman Chemical)
 - o Mitomycin C (GmbH)

6.1.7. E-cadherin knock down protocol

E-cadherin was knocked down in HBECs through E-cadherin shRNA (h) lentiviral particles transduction (Santa Cruz Biotechnology, sc-35242-V). This product is a pool of concentrated, transduction-ready viral particles containing 2 target-specific constructs that encode 19-25 nt (plus hairpin) shRNA designed to knock down E-cadherin gene expression.

Here is the detailed protocol:

Day 1: plate HBECs WT cells in a 12 well plate (150 000 cells per well).

Day 2: cells are 50% confluent. Change the medium with 1 mL of medium + 5 µg/mL of polybrene (cationic polymer that can greatly enhance the efficiency of lentiviral infection; Santa Cruz Biotechnology). Thaw lentiviral particles aliquots on ice. Add 20 µL of E-cadh shRNA lentiviral particles (1.0×10^5 infectious units of virus). Mix gently and incubate overnight.

Day 3: replace medium by normal medium.

Day 4: passage cells in a 6 well plate

Day 5: add puromycin at 10 µg/mL to select cells expressing the shRNA. Make a control well to check that this puromycin concentration kills WT cells.

Day 8: passage in a 75 cm² flask in medium + 10 µg/mL puromycin.

Day 9 and +: continue culture them in medium + 10 µg/mL puromycin.

When starting an experiment, detach and seed cells in the experimental plate and keep a cell pellet for a western blot to check E-cadherin knock down efficiency.

6. Annexes

6.1.8. Immunostaining protocol

List of products and abbreviations:

- Paraformaldehyde: PFA
- Phosphate Buffered Saline: PBS
- Triton X-100
- Bovine Serum Albumine: BSA
- Normal Goat Serum: NGS
- Antibody I (Ab I): rat anti E-cadherin clone ECCD-2 (Invitrogen)
- Antibody II (Ab II): goat anti-rat alexa fluor 488 (Invitrogen)
- Hoechst 33342 (NucBlue Live ReadyProbes Reagent; Molecular Probes)

Step	Instructions	Time	Comments
<i>1. Fix the cells</i>			
a.	Aspirate the medium and rinse with PBS	3X	This removes all floating impurities.
b.	Fix with 4% (wt/vol) PFA in PBS	12 min	Stop all reactions and preserve the tissue
	Rinse with PBS+	3X 5 min	PBS+ = PBS + 1 mM CaCl ₂ + 1 mM MgCl ₂ After fixation, the sample can be conserved in the fridge in PBS before performing further steps
<i>2. Permeabilize</i>			
	Permeabilize in PBS+ with 0.1% Triton X-100	4 min	To make the cell membrane porous
	Rinse with PBS+	3X 5 min	
<i>3. Saturate</i>			
	Prepare saturation solution (SS): 0.1% BSA in PBS (ex. 0.1 mg BSA in 10 mL PBS). Saturate the sample with SS + 2.5% serum	1 h	Serum should be from the species of antibody II (ex. NGS) This ensures all binding sites are saturated, ensuring a better staining contrast
<i>4. Stain</i>			
	Aspirate SS		
	Incubate with SS + antibody I	2 h	room temperature rat anti E-cadherin: dilution 1:100 Ab I will fix on the target protein.
	Rinse with PBS+	3X 5 min	
	Incubate with SS + antibody II	30 min	Goat anti rat alexa fluor 488 1:1000 Ab II will fix on Ab I. Be careful, light can photobleach fluorophores of Ab II → protect the sample from light
	Rinse with PBS	3X 5 min	
	Conserve in PBS		
	Prior to imaging, add 1 drop of NucBlue® Live reagent (Hoechst® 33342 dye) per mL of PBS		To mark the nuclei

6.2. Robustness of PIV measurements to parameters change

6.2.1. Introduction

PIV measurements are filtered with a global filter and time averaged over a sliding time window. The impact of the filter strength and the sliding average time window is checked here. Moreover, PIV analysis has been performed with fixed sampling frequency and sub window size (chosen differently for different cell types). The sub window size impact on the obtained results is also quantified to assess the robustness of the method.

To do that, PIV analysis is run with different parameters on a 3.3 mm X 3.3 mm sequence of a HBEC monolayer in which images are separated by 5 min. The obtained results are then compared. The analyzed FOV is shown Figure 6.1.A.

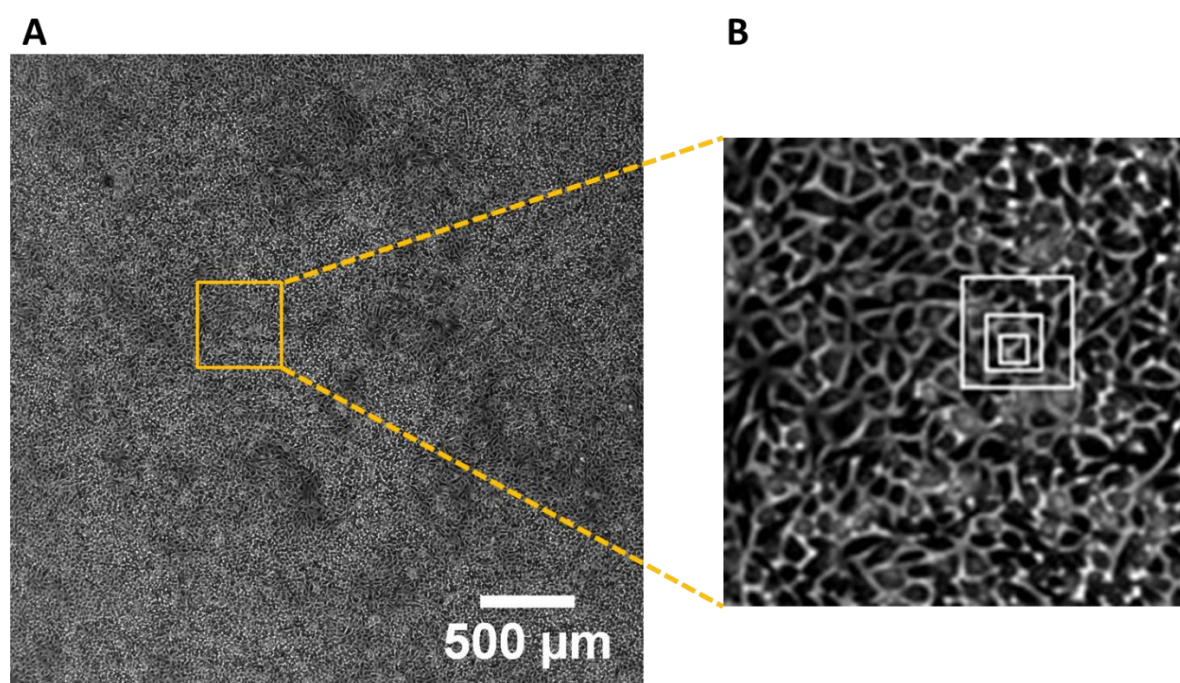


Figure 6.1: HBEC confluent monolayer 16 hours after seeding them at high density.

A: Phase contrast image, the FOV is 3.3 mm X 3.3 mm.

B: Zoomed view. White squares are respectively 104, 52 and 26 μm wide.

6.2.2. Impact of global filter and sliding time average

As explained in the main text (see 2.4.3), PIV results were filtered with a global filter. Practically, the global filter removes the vectors outside an acceptance interval which limits are defined by the velocity distribution mean plus/minus a certain number of times its standard deviation. Here, we refer to this number as “g”. Figure 6.2 shows the effect of the global filter on the PIV raw results. The x component of the velocity v_x is displayed along with their corresponding histograms (Figure 6.2.A, B), after v_x was filtered using a global filter with different values of g. The value $g=2.5$ has been chosen, as it successfully removes outliers but do not cut the main distribution (Figure 6.2.B). For $g=2.5$, the percentage of NaN values after the global filter is less than 5% (Figure 6.2.C).

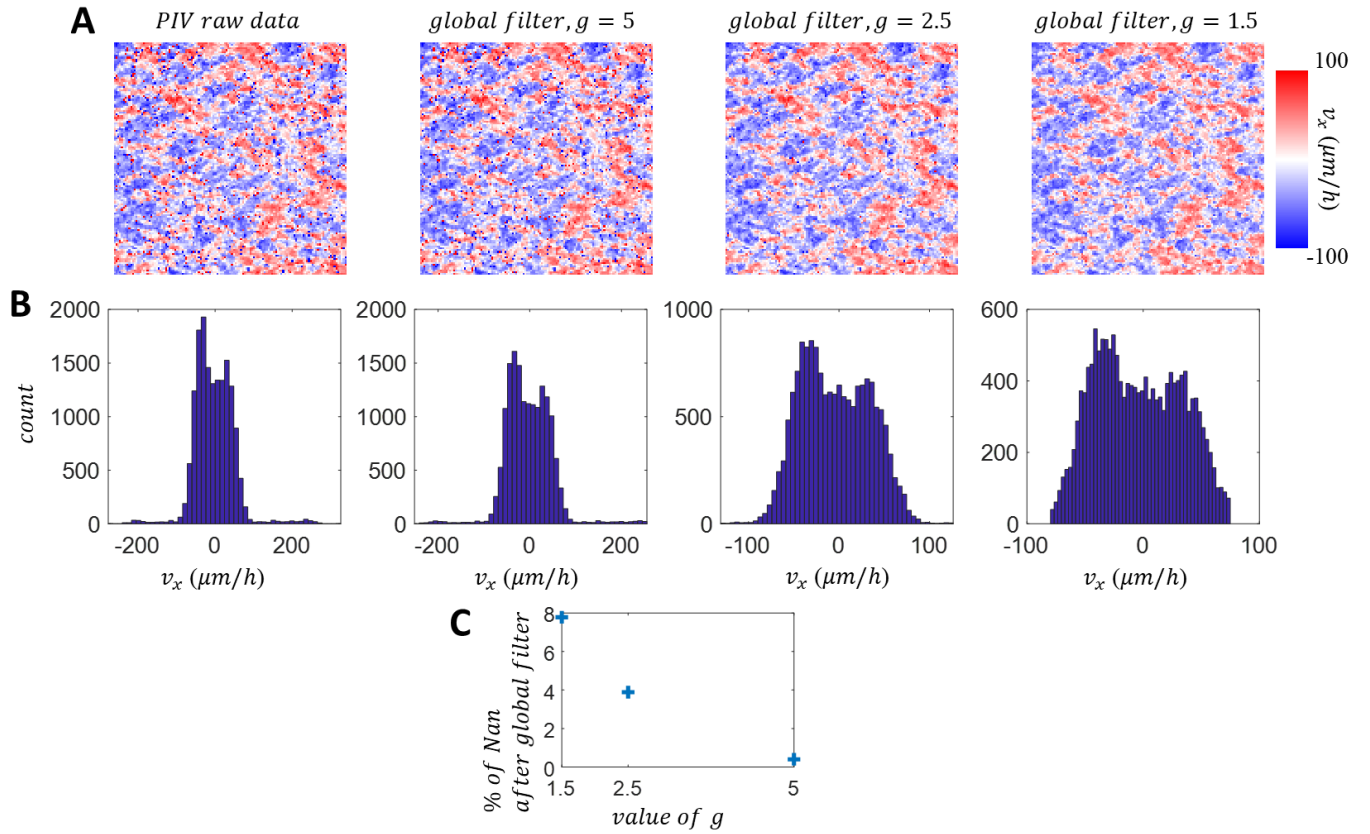


Figure 6.2 : Impact of global filter strength g on PIV results.

A: Color maps of the x velocity component; global filter strength increases (g decreases) from left to right; FOV is 3.3 mm X 3.3 mm. PIV measurements were performed between two images separated by 5 min, with a PIV sub window 52 μm wide and 50% overlap.

B: Corresponding histograms of the x velocity component.

C: evolution with g of the percentage of NaN values after performing the global filter on raw PIV measurements.

After performing the global filter, we time average the PIV results with a certain number of successive frames. The sliding time average window, i.e., the number of frames averaged, has an impact on the PIV results. Figure 6.3.A shows the map of the velocity x component after performing the global filter and the sliding time average for different sliding time average window: 5, 15, 30, 60 minutes (i.e., we average 1, 3, 6 or 12 successive frames). As the time window is increased, outliers and details in the x component of the velocity field are lost. Without time average, outlier values and discontinuities are still observed in the FOV. However, it seems that the large-scale features of the velocity field are conserved regardless of the size of the time average window.

To characterize quantitatively the effect of the time average window, the energy spectrum of the velocity field is calculated. The energy spectrum $E(q)$ of the velocity field is defined as the spectrum of the kinetic energy per unit mass density $E = \int \frac{1}{2} v^2 d^2\mathbf{r}$. Then, $E(q) \propto q \langle |\tilde{v}_q|^2 \rangle$, q being a wave vector amplitude⁵¹. Figure 6.3.B shows the normalized energy spectrum of the velocity fields obtained with different time average windows. The large-scale (small wavenumber) behavior of the spectra is not affected by the time average window. Increasing the time window for time average increases the slope of the energy spectrum decay at large q , as it smoothes out small scale details. With this quantitative analysis, one can confidently say

that the spectrum, and thus the structure of the velocity field obtained by PIV, are really close until $q \sim 6 \cdot 10^{-3} \mu\text{m}^{-1}$ (length scale above $150 \mu\text{m}$).

In our analysis, we chose to average 6 successive PIV results, i.e, we chose a sliding time average window of 30 min, because we keep the same structure at large scale and lose only small details that are outliers and can introduce discontinuities in the velocity field obtained.

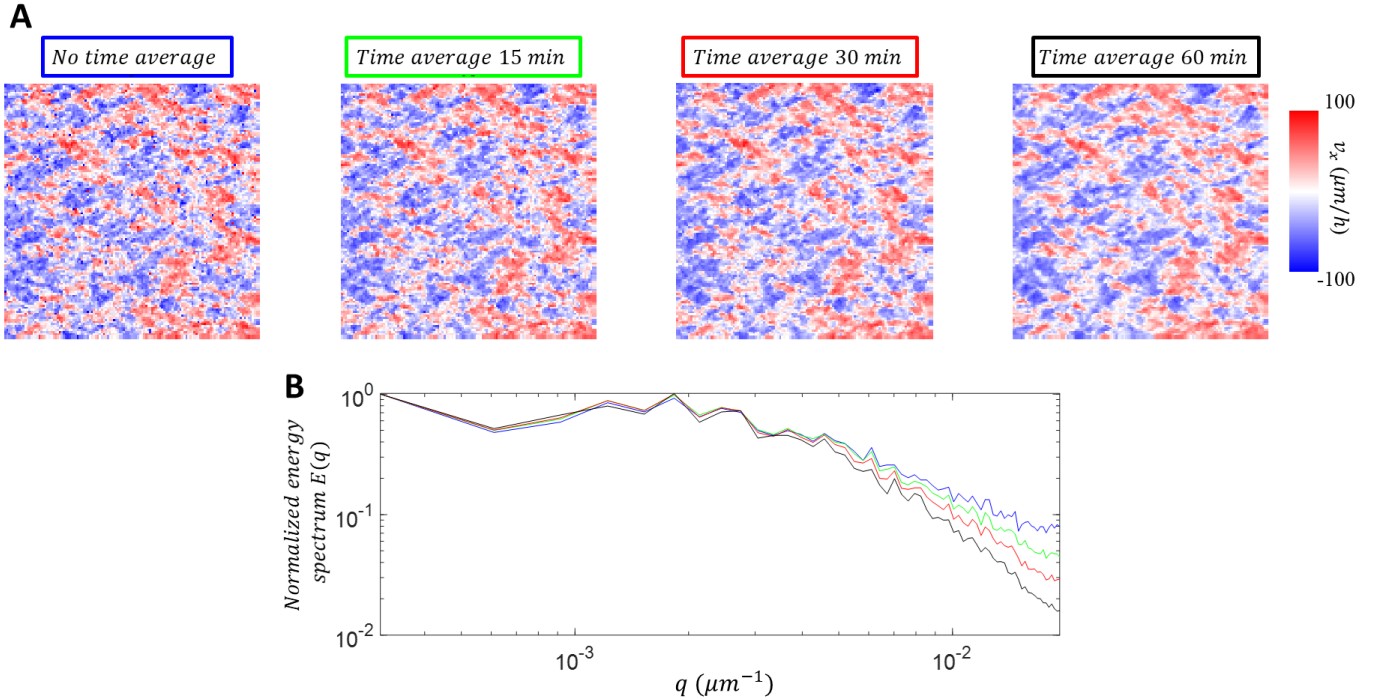


Figure 6.3 : Impact of sliding time average on PIV measurements.

A: Color maps of the x velocity component; sliding time average window increases from left to right; FOV is $3.3\text{mm} \times 3.3\text{mm}$. PIV measurements were performed between images separated by 5 min, with a PIV sub window $52 \mu\text{m}$ wide with a 50% overlap. A global filter with $g=2.5$ was performed before time averaging.

B: Energy spectrum of velocity fields obtained with different sliding time average time window. Colors of the curves correspond to the box colors in A.

6.2.3. Impact of sub window size

To assess the impact of the sub window size, a sequence of images separated by 5min were analyzed with PIV using different PIV sub window sizes (26, 52 and $104 \mu\text{m}$, shown in Figure 6.1.B), keeping a 50% overlap. The results were filtered with a global filter with $g=2.5$ and time averaged over a 30 min time window. As the PIV sub window size is increased, details in the x component of the velocity field are lost (Figure 6.4.A). However, it seems that the large-scale features of the velocity field are equal for all sub window sizes tested. To compare quantitatively the velocity fields obtained with different PIV window sizes, the energy spectrum of the velocity field is calculated. Figure 6.4.B shows the normalized energy spectrum of the velocity fields computed with different PIV sub window sizes. The large-scale (small wavenumber) behavior of the spectra is not affected by the PIV subwindow size. Increasing the sub window size increases the slope of the energy spectrum decay at large q , as it smoothes out small scale details. With this quantitative analysis, one can confidently say that the spectrum are similar until $q \sim 6 \cdot 10^{-3} \mu\text{m}^{-1}$ (length scale above $150 \mu\text{m}$).

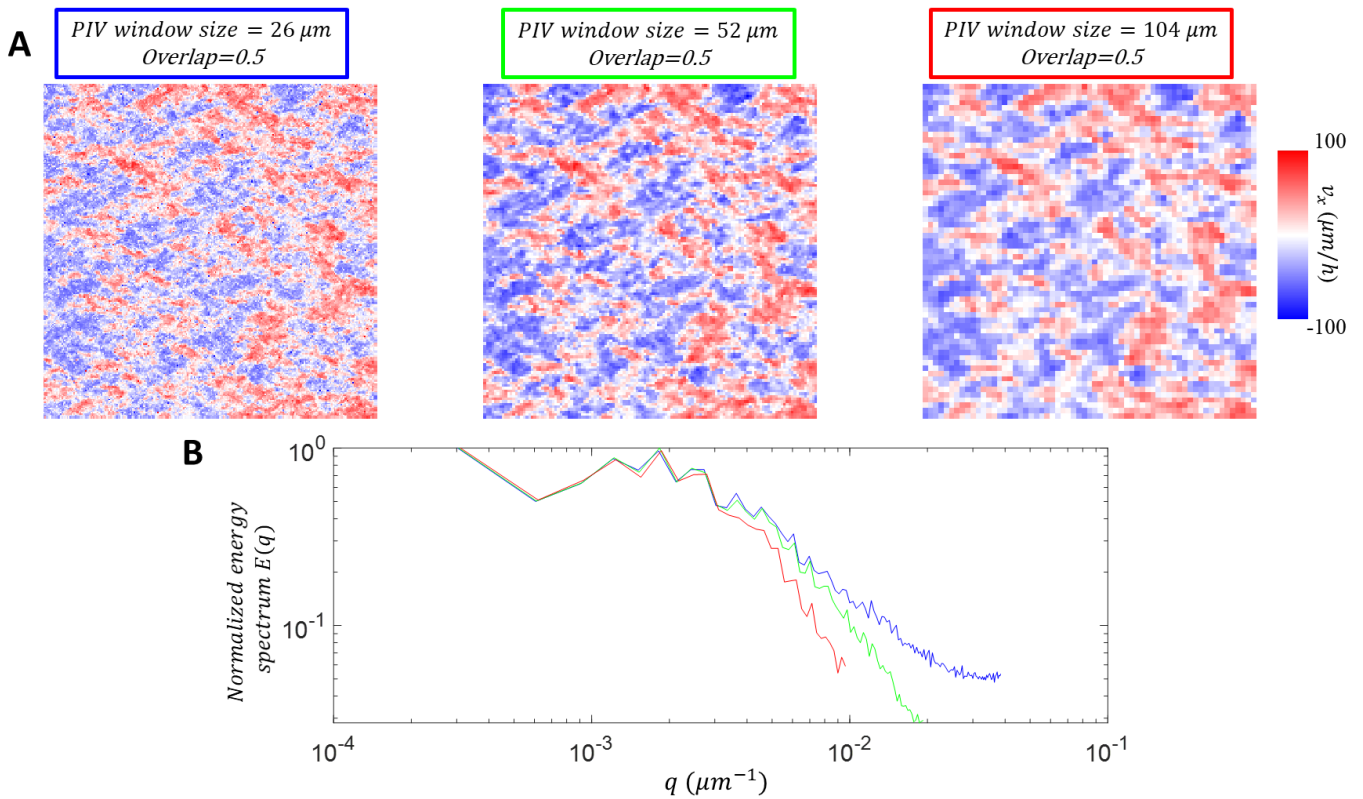


Figure 6.4 : Impact of PIV sub window size on PIV results.

A: Color map of the x velocity component; PIV sub window size increases from left to right, the overlap being kept at 50%; FOV is 3.3 mm X 3.3 mm. A global filter with $g=2.5$ was performed and the results were averaged over a 30 min time window.

B: Energy spectrum of the three measured velocity field. PIV measurements were performed between images separated by 5 min.

The conclusion of these analyses is that PIV gives robust results at large scale but that small scale details are sensitive to the choice of parameters. For the analysis of confluent HBECs monolayers in Chapter 3, a 52 μm sub window has been chosen as it seems a good compromise to scan local variations of the velocity field without introducing too much noise.

6.3. Continuum theory of an active polar fluid with anisotropic friction

To better understand the mechanism underlying the chaotic dynamics to laning transition in HBEC monolayers on anisotropic substrates (see Chapter 3), I worked in close collaboration with theoreticians from the team “Physical approach of biological problems” at Physico Chimie Curie. Carles Blanch Mercader, Samuel Bell and Jacques Prost proposed a hydrodynamic description in which a HBEC monolayer on a micro-grooved substrate is modeled as an active polar fluid with anisotropic friction. The main insights their work provides to our experimental system are presented section 3.4 of the main text. In this annex, I present in more details the continuum model and the analysis performed by our collaborators to describe our experimental observations.

6.3.1. Conservation and constitutive equations

To describe our experimental system, our collaborators used a coarse-grained hydrodynamic approach with two main degrees of freedom: the velocity field \mathbf{v} and the polarization field \mathbf{p} , which capture respectively the local cell velocity and cell polarization. The polarization field might reflect the orientation of active traction forces or the orientation of cellular migratory structures such as lamellipodia.

We first write the conservation equations. By considering the system incompressible, the conservation of mass reads:

$$\partial_\gamma(v_\gamma) = 0 \quad (6.1)$$

where γ represents the cartesian coordinates in the substrate plane (x, y) . We adopt the Einstein convention such that summation over repeated indices is tacitly assumed.

Next, we consider momentum conservation, which, as the Reynolds number is low, is expressed through force balance. In a thin-film approximation, well-adapted to describe cell monolayers, the force balance is captured by

$$\partial_\beta \sigma_{\alpha\beta}^{tot} = \Lambda_{\alpha\beta} v_\beta - T_0 p_\alpha \quad (6.2)$$

Here, $\sigma_{\alpha\beta}^{tot}$ are the cartesian components of the in-plane total mechanical stress tensor obtained after averaging with respect to the material height. $\Lambda_{\alpha\beta} v_\beta$ describes friction between the cell monolayer and the substrate, and $T_0 p_\alpha$ is the active polar traction forces of cells.

To describe the effect of the anisotropic structure of subcellular grooves on cells, we consider an anisotropic friction coefficient $\Lambda_{\alpha\beta}$.

$$\Lambda_{\alpha\beta} = \lambda_{\parallel} \mathbf{H} + \lambda_{\perp} (\mathbf{I} - \mathbf{H}) \quad (6.3)$$

where \mathbf{I} is the identity matrix, $\mathbf{H} = \begin{pmatrix} 1 & 0 \\ 0 & 0 \end{pmatrix}$ and λ_{\parallel} (respectively λ_{\perp}) is an effective friction coefficient when the local velocity is parallel (respectively perpendicular) to the orientation of the grooves. Hereon, we consider that the orientation of the grooves is in the x direction. As cells are guided by the grooves, we typically impose $\lambda_{\parallel} \leq \lambda_{\perp}$. How does increasing groove depth modify λ_{\parallel} and λ_{\perp} is not obvious and this point will be further discussed in the next subsection.

We then follow the standard approaches of non-equilibrium thermodynamics to constraint the constitutive equations of our active polar fluid (see 1.2.4.1), and in particular, to specify the total stress σ^{tot}

and the time evolution of the polarization field $\frac{Dp_\alpha}{Dt}$. In the incompressible limit and ignoring terms that are subdominant for the linear dynamics around the disordered state, the constitutive relations read:

$$\sigma_{\alpha\beta}^{tot} \approx 2\eta \left(v_{\alpha\beta} - \frac{1}{2} v_{\gamma\gamma} \delta_{\alpha\beta} \right) - P \delta_{\alpha\beta} \quad (6.4)$$

$$\frac{Dp_\alpha}{Dt} = \partial_t p_\alpha + v_\beta \partial_\beta p_\alpha + \omega_{\alpha\beta} p_\beta \approx \frac{h_\alpha}{\gamma} + k v_\alpha \quad (6.5)$$

where:

- $v_{\alpha\beta} = (\partial_\alpha v_\beta + \partial_\beta v_\alpha)/2$ is the strain rate tensor
- η is the shear viscosity
- P is an effective pressure field which acts as a Lagrange multiplier to ensure incompressibility
- $\omega_{\alpha\beta} = (\partial_\alpha v_\beta - \partial_\beta v_\alpha)/2$ is the vorticity tensor
- $\frac{h_\alpha}{\gamma}$ captures the relaxation of the polarization field with γ being a rotational viscosity and h_α the molecular field computed from the equilibrium free energy. We consider that the part of the free energy associated with distortions of the polarization field reads

$$\mathcal{F} = \int_{\mathcal{A}} \left\{ \frac{\chi}{2} p_\alpha^2 + \frac{\beta}{4} p_\alpha^4 + \frac{\mathcal{K}}{2} (\partial_\alpha p_\beta)^2 \right\} da \quad (6.6)$$

We choose the elastic parameters $\chi > 0$ and $\beta > 0$, meaning that the preferred bulk equilibrium state is disordered with $\mathbf{p} = 0$ and $\mathbf{v} = 0$ (see 1.2.5.3). The energy cost associated with gradients of polarization is accounted for by the final term, which is the Frank free-energy in the one-constant approximation with elastic modulus \mathcal{K} . The general expression for the molecular field in Cartesian coordinates reads

$$h_\alpha = -\frac{\delta\mathcal{F}}{\delta p_\alpha} = -\chi p_\alpha - \beta(p_x^2 + p_y^2)p_\alpha + \mathcal{K}\nabla^2 p_\alpha \quad (6.7)$$

- the parameter k represents a velocity-polarization coupling, which describes the re-orientation of the polarization field by the velocity field. Polarization alignment in uniform flows is allowed by symmetries in the presence of a substrate and has already been experimentally observed in cell monolayers (see 1.2.5.3).

$\Lambda, T_0, \eta, \gamma, \chi, \beta, \mathcal{K}$ and k are phenomenological parameters to be determined by experiments. Note that, conversely to what is usually done in hydrodynamic descriptions of active ordered fluids, the active anisotropic nematic stresses $-\zeta\Delta\mu(p_\alpha p_\beta - \frac{p_\gamma^2 \delta_{\alpha\beta}}{2})$ are ignored here and the activity is captured by polar traction forces in the force balance. In our case, this is a reasonable assumption as we experimentally showed that inhibiting cell contractility did not prevent the emergence of a laning pattern. Moreover, flow gradient-polarity couplings are also ignored here. Indeed, we showed experimentally that flows are uniform in lanes, which suggests that, in our system, polarization alignment in shear flows are subdominant compared to polarization alignment in uniform flows. These two contributions (active anisotropic stresses and flow gradient-polarity couplings) are indeed second order contributions near the disorder to polar laning transition, because \mathbf{p} and \mathbf{v} are small variables close to this transition.

6.3.2. Velocity fluctuations response to anisotropic friction

In this subsection, we compute the velocity fluctuations in the disordered phase. These expressions are compared to the experimental observations. From this comparison, we propose that the friction coefficients λ_{\parallel} and λ_{\perp} can be varied using a single parameter h representing friction anisotropy and having an effect similar than microgroove depth in experiments.

A steady state solution of the equations presented before is the uniform disordered phase defined by the conditions $\mathbf{v} = \mathbf{p} = 0$ and $P = P_0$. Note here that the disordered state does not capture the local complexity of the nematic chaotic state observed in HBEC monolayers on flat substrate but has the same characteristics at large length scales. We can introduce a perturbation of small amplitude to the previous solution $\mathbf{v} = \epsilon \delta \mathbf{v}$, $\mathbf{p} = \epsilon \delta \mathbf{p}$ and $P = P_0 + \epsilon \delta P$, where $\epsilon \ll 1$ is a small dimensionless parameter. Linearizing the equations and including the fluctuations ζ^v in the force balance and ζ^p in the dynamical equation of the polarization field, we obtain the following equations:

$$\partial_{\gamma}(\delta v_{\gamma}) = 0 \quad (6.8)$$

$$\eta \partial_{\gamma\gamma}(\delta v_{\alpha}) - \partial_{\alpha} \delta P = \Lambda_{\alpha\beta} \delta v_{\beta} - T_0 \delta p_{\alpha} + \zeta_{\alpha}^v \quad (6.9)$$

$$\partial_t \delta p_{\alpha} = \frac{-\chi \delta p_{\alpha} + \mathcal{K} \nabla^2 \delta p_{\alpha}}{\gamma} + k \delta v_{\alpha} + \zeta_{\alpha}^p \quad (6.10)$$

where the fluctuations obey the relations:

$$\begin{aligned} \langle \zeta_{\alpha}^{p,v}(r, t) \rangle &= 0 \\ \langle \zeta_{\alpha}^{p,v}(r, t) \zeta_{\beta}^{p,v}(r', t') \rangle &= 2D^{p,v} \delta(r - r') \delta(t - t') \delta_{\alpha\beta} \\ \langle \zeta_{\alpha}^{p,v}(r, t) \zeta_{\beta}^{v,p}(r', t') \rangle &= 0 \end{aligned} \quad (6.11)$$

The coefficients D^v and D^p correspond to fluctuation amplitudes, which we consider isotropic, δ corresponds to the Dirac delta function and the operator $\langle \rangle$ denotes an average over independent realizations.

Solving those equations in Fourier space allows to calculate $\langle v_x(r, t)^2 \rangle$ and $\langle v_y(r, t)^2 \rangle$ close to the disordered state. In general, the integrals in their expressions cannot be calculated explicitly. However, when the polarization fluctuations amplitude vanishes ($D^p = 0$),

$$\langle v_x(r, t)^2 \rangle = \frac{D^v}{4\pi\eta\tau(\lambda_{\parallel} + \sqrt{\lambda_{\perp}\lambda_{\parallel}})} \quad (6.12)$$

$$\langle v_y(r, t)^2 \rangle = \frac{D^v}{4\pi\eta\tau(\lambda_{\perp} + \sqrt{\lambda_{\perp}\lambda_{\parallel}})} \quad (6.13)$$

where τ is a cut-off for small time scales. Note that these expressions are valid in the disordered phase when we neglect D^p .

As presented in 3.2.1.2, we measured $\langle v_x(r, t)^2 \rangle$ and $\langle v_y(r, t)^2 \rangle$ for our experimental case of HBEC monolayers and varying groove depth. We observed that $\langle v_x^2 \rangle$ increases with groove depth and $\langle v_y^2 \rangle$ decreases with it, while $v_{rms} = \sqrt{\langle v_x(r, t)^2 + v_y(r, t)^2 \rangle}$ is approximately independent on the groove depth (blue points in Figure 3.25.A-C). This effect is also observed for HT1080 cells that stay disordered even on 1.75 μm deep grooves (red points in Figure 3.25.A-C).

To match the experimental data, one must find a single parameter increasing friction anisotropy and modifying λ_{\parallel} and λ_{\perp} in such a way that the root mean square velocity stays constant while $\langle v_x(r, t)^2 \rangle$ increases

and $\langle v_y(r, t)^2 \rangle$ decreases. To impose that, we set $\lambda_\perp \lambda_\parallel = \lambda^2$ and $\lambda_\perp = h \lambda_\parallel$ with $h \geq 1$. With this definition and using the relations (6.12) and (6.13), one finds:

$$v_{rms}^2 = \langle v_x(r, t)^2 \rangle + \langle v_y(r, t)^2 \rangle = \frac{D^v}{4\pi\eta\tau\lambda} \quad (6.14)$$

$$\frac{\langle v_x(r, t)^2 \rangle}{v_{rms}^2} = \frac{1}{\left(\frac{1}{\sqrt{h}} + 1\right)} \quad (6.15)$$

$$\frac{\langle v_y(r, t)^2 \rangle}{v_{rms}^2} = \frac{1}{(\sqrt{h} + 1)} \quad (6.16)$$

Figure 3.25 shows the variation of v_{rms} , $\sqrt{\langle v_x(r, t)^2 \rangle} / v_{rms}$ and $\sqrt{\langle v_y(r, t)^2 \rangle} / v_{rms}$ with the friction anisotropy h . Increasing h in the model has qualitatively the same effect as increasing groove depth in experiments. We checked that these dependences are also satisfied when D^p is non-vanishing (Figure 3.25).

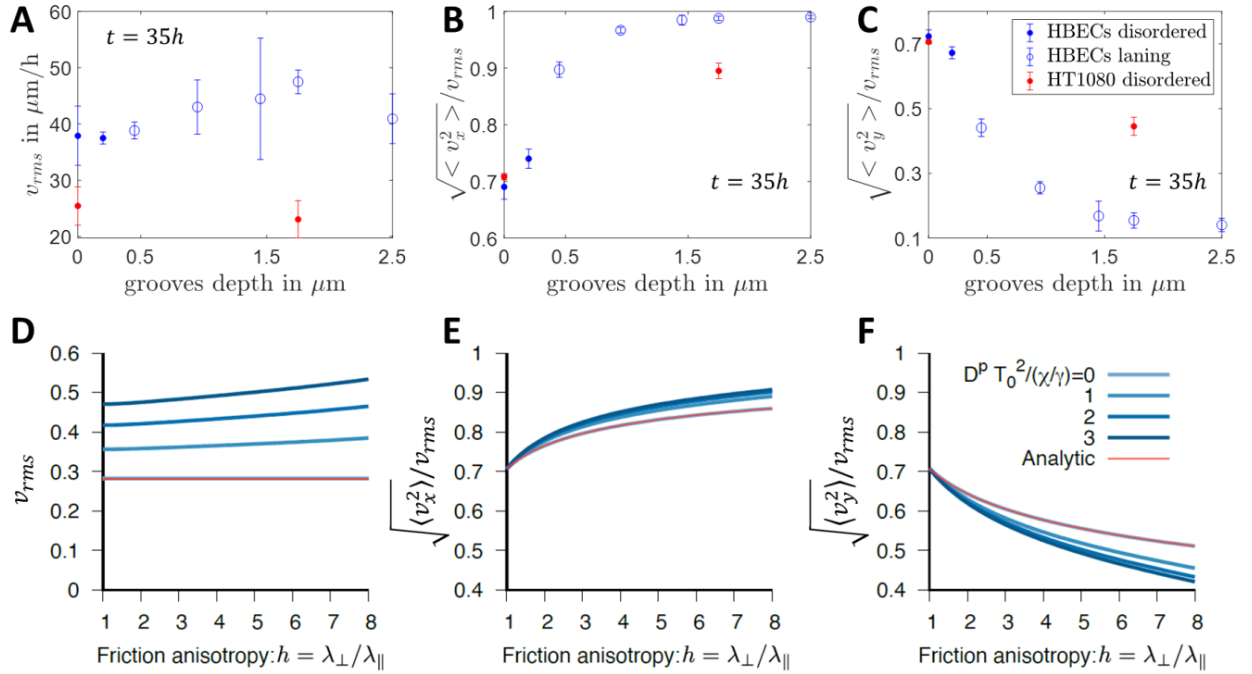


Figure 6.5 : The effects of increasing groove depth in experiments (A-C) are well-captured by increasing the friction anisotropy

$h = \frac{\lambda_\perp}{\lambda_\parallel}$ while maintaining the friction scale $\lambda = \sqrt{\lambda_\parallel \lambda_\perp}$ constant in the hydrodynamic description (D-F).

A-C: In experiments, 35 hours after cell seeding, v_{rms} does not show a clear dependence with groove depth (A) while $\sqrt{\langle v_x(r, t)^2 \rangle} / v_{rms}$ increases (B) and $\sqrt{\langle v_y(r, t)^2 \rangle} / v_{rms}$ decreases (C) when groove depth increases for both HBEC and HT1080 monolayers. Note that higher values of $\sqrt{\langle v_x(r, t)^2 \rangle} / v_{rms}$ and lower values of $\sqrt{\langle v_y(r, t)^2 \rangle} / v_{rms}$ are obtained when laning has emerged in HBEC monolayers compared to the disordered HT1080 for the same groove depth 1.75 μm . Error bars correspond to standard deviation to the mean (for HBECs $n = 10, 5, 7, 6, 16, 7, 4$ FOVs for groove depth equal to 0, 0.2, 0.45, 0.95, 1.45, 1.75, 2.5 μm and for HT1080, $n = 3, 5$ for groove depth equal to 0, 1.75 μm).

D-F: Similarly, the theoretical description of the disordered state predicts that v_{rms} does not vary dramatically (D), $\sqrt{\langle v_x(r, t)^2 \rangle} / v_{rms}$ increases (E) and $\sqrt{\langle v_y(r, t)^2 \rangle} / v_{rms}$ decreases (F) when friction anisotropy h increases. The values of $\frac{D^p T_0^2}{\chi/\gamma}$ for the blue curves in panels D-F change as indicated in the legend of panel F. The solid red curves correspond to the analytical expressions in the case $D^p = 0$ and are in perfect agreement with the numerical resolutions in the case $D^p = 0$ (lighter blue curves). The units were set as $D^p / \tau = \mathcal{K} / \chi = \eta = 1$ and the parameter value is set $kT_0 = 0.3$.

One can note that the highest values of $\sqrt{\langle v_x^2 \rangle} / v_{rms}$ and lowest values of $\sqrt{\langle v_y^2 \rangle} / v_{rms}$ are obtained for grooves deep enough to be in the laning regime in HBEC monolayers compared to both disordered HT1080 and theoretical predictions. Let's remind here that the theoretical predictions presented in this subsection are valid in the disordered state. The emergence of collective laning in HBECs reinforces cell guidance along grooves. This justifies that $\sqrt{\langle v_x^2 \rangle} / v_{rms}$ is higher and $\sqrt{\langle v_y^2 \rangle} / v_{rms}$ is lower for HBECs laning compared to HT1080 and theoretical predictions for large substrate anisotropy.

Therefore, this analysis suggests that the effect of increasing microgroove depth is well captured by changing the friction anisotropy $h = \frac{\lambda_{\perp}}{\lambda_{\parallel}}$ while maintaining the friction scale $\lambda = \sqrt{\lambda_{\parallel}\lambda_{\perp}}$ constant.

6.3.3. Linear stability of the disordered state

In this subsection, we study the disordered to polar laning transition in our hydrodynamical description. To do that, we investigate the stability of the disordered phase to linear perturbations, in the absence of fluctuations. Like in the previous subsection, the perturbation of the disordered state follows the linearized equations:

$$\partial_{\gamma}(\delta v_{\gamma}) = 0 \quad (6.17)$$

$$\eta \partial_{\gamma\gamma}(\delta v_{\alpha}) - \partial_{\alpha} \delta P = \Lambda_{\alpha\beta} \delta v_{\beta} - T_0 \delta p_{\alpha} \quad (6.18)$$

$$\partial_t \delta p_{\alpha} = \frac{-\chi \delta p_{\alpha} + \mathcal{K} \nabla^2 \delta p_{\alpha}}{\gamma} + k \delta v_{\alpha} \quad (6.19)$$

with $\Lambda_{\alpha\beta} = \frac{\lambda}{\sqrt{h}} \mathbf{H} + \sqrt{h} \lambda (\mathbf{I} - \mathbf{H})$ and $h \geq 1$.

In Fourier space, those equations reduce to a linear system, which after diagonalization reads:

$$\begin{aligned} \partial_t e_1 &= \omega_1 e_1 \\ \partial_t e_2 &= \omega_2 e_2 \end{aligned} \quad (6.20)$$

in which e_1 and e_2 are the two independent modes given by

$$\begin{aligned} e_1 &= q_x \widetilde{\delta p}_x + q_y \widetilde{\delta p}_y \\ e_2 &= -q_y \widetilde{\delta p}_x + q_x \widetilde{\delta p}_y \end{aligned} \quad (6.21)$$

The corresponding growth rates ω_1 and ω_2 associated with each mode are given by

$$\omega_1 = -\frac{\chi + \mathcal{K} q^2}{\gamma} \quad (6.22)$$

$$\omega_2 = -\frac{\chi + \mathcal{K} q^2}{\gamma} + \frac{k T_0 q^2}{\frac{\lambda}{\sqrt{h}} q_y^2 + \sqrt{h} \lambda q_x^2 + \eta q^4} \quad (6.23)$$

where $\mathbf{q} = (q_x, q_y)$ is the wave vector and $\widetilde{\delta p}_{\alpha}$ denotes the Fourier transform of the perturbation of the polarization field. The perturbations of the velocity field and the pressure field can be expressed as a function of the perturbations in the polarization field.

Because $\omega_1 < 0$ for all values of the wavevector \mathbf{q} , perturbations of the mode e_1 are always stable. However, $\omega_2(\mathbf{q})$ can be positive which corresponds to unstable perturbations of the mode e_2 . Because ω_2 decreases monotonically as the amplitude of the wave vector \mathbf{q} increases, the maximal value of ω_2 is found

for vanishing \mathbf{q} . Note that ω_2 is ill-defined at $\mathbf{q} = 0$ and thus to study the limit of vanishing \mathbf{q} , we should specify a direction. The limits in the main direction $q_x = 0$ and $q_y = 0$ are given by:

$$\omega_{2,x}^{max} = \lim_{q_x \rightarrow 0} \omega_2(q_x, q_y = 0) = -\frac{\chi}{\gamma} + \frac{kT_0}{\sqrt{h}\lambda} \quad (6.24)$$

$$\omega_{2,y}^{max} = \lim_{q_y \rightarrow 0} \omega_2(q_x = 0, q_y) = -\frac{\chi}{\gamma} + \frac{kT_0\sqrt{h}}{\lambda} \quad (6.25)$$

As $h \geq 1$, $\omega_{2,y}^{max} \geq \omega_{2,x}^{max}$. Thus ω_2 is maximal for $q_x = 0$ and $q_y \rightarrow 0$ and its maximal value is:

$$\omega_2^{max} = -\frac{\chi}{\gamma} + \frac{kT_0\sqrt{h}}{\lambda} \quad (6.26)$$

When $kT_0 = 0$, one finds that the disordered phase is always stable as $\omega_2^{max} < 0$. As kT_0 increases, there is a critical threshold $(kT_0)_c$ above which $\omega_2^{max} \geq 0$ and consequently ω_2 is positive for certain values of \mathbf{q} , meaning that some perturbations grow exponentially. Figure 6.6 shows the phase diagram in the plane (h, kT_0) and the regions in the wavevector-space whereby $\omega_2(\mathbf{q})$ is positive for varying values of h and fixed kT_0 . The value of the critical threshold plotted in Figure 6.6.a is given by:

$$(kT_0)_c = \frac{\chi\lambda}{\gamma\sqrt{h}} \quad (6.27)$$

This result shows that the interplay between the velocity-polarization coupling k and the polar traction forces T_0 can destabilize the disordered phase via a long-wavelength instability at $\mathbf{q} = 0$.

When the disordered phase becomes unstable for $h > 1$ and $kT_0 > (kT_0)_c$, the regions in the wavevector-space whereby $\omega_2(\mathbf{q})$ is positive is asymmetric in the plane (q_x, q_y) (Figure 6.6.b-d). The most unstable perturbation corresponds to $q_x = 0$ and $q_y \rightarrow 0$ in the y-direction. This perturbation is characterized by stable δp_y and δv_y that decay to zero, and by unstable δp_x and δv_x that grow with time. Altogether, this shows that at the onset of the instability, the dynamics of small perturbations around the disordered phase selects a laning pattern with stripes oriented in the x direction in which the friction is the smallest and spatial modulation in the y-direction. Because the most unstable mode corresponds to $\mathbf{q} = 0$, no characteristic finite wavelength is selected by the linear dynamics.

Interestingly, the critical threshold decreases sub linearly with h : $(kT_0)_c \sim h^{-\frac{1}{2}}$ (Figure 6.6.a). It means that for a given value of kT_0 below the critical threshold for $h = 1$, the system can cross the polar laning threshold by increasing the friction anisotropy h (dashed line in Figure 6.6.a). Similarly, in HBEC monolayers, laning is triggered by an increase in groove depth. For such a fixed value of kT_0 , which depends on the material properties of the cell monolayer, and for sufficiently small values of h , $\omega_2 < 0$ for all values of \mathbf{q} and thus the disordered state is linearly stable. When h is increased enough, the critical threshold $(kT_0)_c$ eventually becomes smaller than kT_0 and a region of the (q_x, q_y) space in which $\omega_2 > 0$ appears progressively (Figure 6.6.b-d). All perturbations of the mode e_2 with a wave vector in this region will grow exponentially and thus the disordered state is not stable anymore.

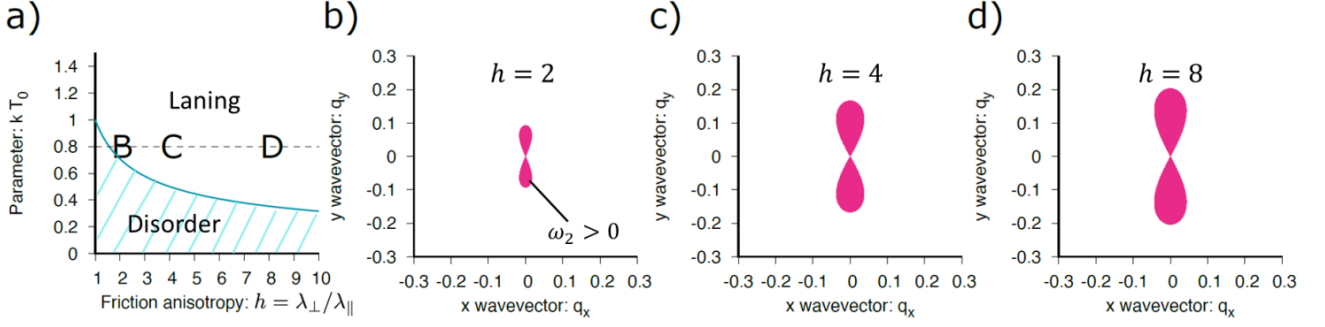


Figure 6.6 : Linear stability of the disordered phase. a) Phase-diagram in the plane kT_0 and h . The solid line corresponds to the critical threshold $(kT_0)_c$. The letter denotes the conditions for panels b, c and d. b-d) Region whereby the growth rate ω_2 is positive in the (q_x, q_y) plane for a fixed $kT_0=0.8$ and varying h from 2, 4 and 8, respectively. The other material parameters are set to $\chi = \lambda = \gamma = \mathcal{K} = 1, \eta = 10$.

When we simulate the linear dynamics above threshold, we found that from an initial random perturbation of the polarization field, a laning pattern is indeed selected by the linear dynamics (Figure 6.7). This laning pattern presents similar features than the HBECs laning patterns observed experimentally. At long timescales, the asymptotic state achieved by the linear dynamics depends on boundary conditions. For periodic boundary conditions, we expect the system to achieve asymptotically a polar flocking state.

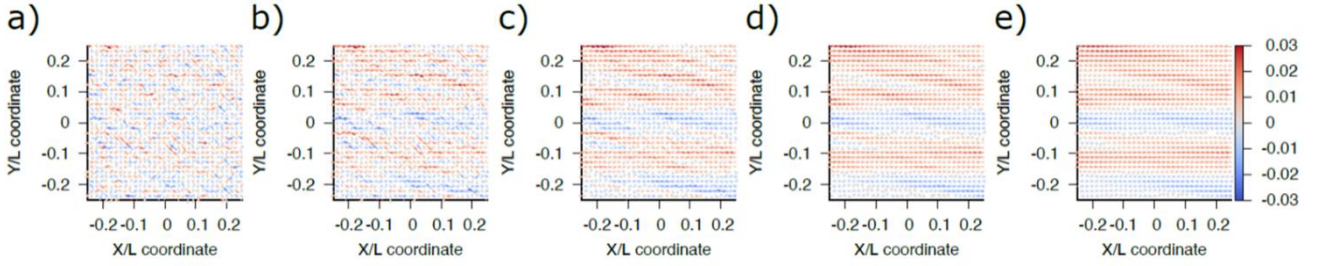


Figure 6.7 : Linear dynamics above threshold. a-e) Snapshots at different time points ($t=0.4, 0.8, 1.2, 1.6$ and 2 , respectively) of the linear dynamics of the polarization field from an initial random perturbation. The scale of the arrow length is normalized at each snapshot for visualization purposes. The parameters are set to $\chi = \lambda = \gamma = \mathcal{K} = 1, \eta = 10, kT_0 = 2$ and $h = 4$. The position coordinates are normalized by the system size $L=800$ and modes with $\max(q_x, q_y) < 2\pi \frac{60}{L}$ were used to simulate the linear dynamics. The color bar indicates the normalized value of p_x .

6.3.4. Summary of the active polar fluid theory contributions

We have shown that the laning transition in HBEC monolayers can be interpreted by a large wavelength instability of an active polar fluid in a disordered state mediated by the interplay between active traction forces and velocity-polarization coupling. Anisotropy in the system that we introduced through anisotropic friction lowers the threshold of the transition from a disordered state to a polar laning state, and thus, the transition can be triggered by an increase in friction anisotropy. Moreover, when the friction is anisotropic, the most unstable perturbations above threshold correspond to a laning pattern with no finite wavelength selection.

Note that anisotropy could have been introduced in other ways. For example, introducing anisotropy in other material parameters like the velocity-polarization coupling k or in the elastic parameter χ . We found that these modifications do not change qualitatively the instability scenario that was described above. One

can imagine introducing anisotropy in other terms such as in fluctuations or in the traction forces. We expect that the bifurcation scenario will not change dramatically aside from nonlinear corrections to the shape and dynamics of the laning patterns with these modifications.

The polar active fluid model captures well the principal features of the laning transition observed experimentally:

- The transition can be triggered by an increase in microgroove depth modeled by friction anisotropy that effectively lowers the critical threshold
- In the ordered state, a laning pattern is selected with no characteristic finite wavelength
- The transition is not dependent on anisotropic nematic active stresses (cell contractility) but is mediated by polar contributions (active traction and polarity-velocity coupling).

However, this linear instability analysis has some limits. First, this linear continuum approach is valid close to the disordered state and at the onset of the instability. Thus, it cannot describe the final state of the system when the instability is well developed. In HBECs laning, the velocity profiles have plug flow structures in the lanes and the shear flows are localized within one cell size between two lanes. This discontinuity in the velocity profile is not captured by this continuum description. Moreover, our hydrodynamical theory relies on phenomenological parameters and the dependence of these parameters with more microscopic parameters is not explicit. This limits our understanding of the instability mechanism and the dynamics of the polar laning pattern for varying cell-related parameters.

6.4. Equations for self-propelled particle-based simulations

To investigate the microscopic mechanisms leading to laning in HBEC monolayers, we collaborated with Bart Smeets from the “BIOSYST-MeBioS” group at KU Leuven that developed self-propelled particle-based simulations. Simulation results and comparison with the experiments are described in the main text section 3.5. In this annex, I present in more details the equations underlying the numerical model proposed by Bart Smeets and the quantification of the laning transition in simulations.

6.4.1. Equations describing single particle trajectory

We first write equations governing the trajectory of a single particle freely moving on an isotropic substrate with a constant particle-substrate friction λ_s . In this case, the velocity and the polarity are directly coupled through $\mathbf{v} = v_0 \mathbf{p}$. The polarity is governed by the equation:

$$d\mathbf{p} = [\alpha \mathbf{v} - \beta \|\mathbf{v}\|^2 \mathbf{p}] dt + \sqrt{2D} d\mathbf{W} \quad (6.28)$$

In this equation, α represents the coupling that causes the polarity of the particle to align with the current migration velocity \mathbf{v} . β is a restoring parameter that limits the polarity (which is bounded by constraints in cell geometry, limitations in cell activity, and active restoring mechanisms). Finally, to consider the stochastic nature of the cell repolarization, the polarity also undergoes a 2-dimensional Wiener process $d\mathbf{W}$ with diffusivity D .

We ensure that the velocity distribution of a freely moving particle is centered around a fixed value v_0 by imposing $\beta = \frac{D + \alpha v_0}{v_0^2}$. This condition is found by analytically expressing the probability distribution for $\|\mathbf{v}\|$ and computing from that the most probable velocity in terms of the parameters α , β and D . We can then rewrite the equation for the polarization as:

$$d\mathbf{p} = [k_s \hat{\mathbf{v}} - (k_s + 1) \|\hat{\mathbf{v}}\|^2 \mathbf{p}] dt + \sqrt{2D} d\mathbf{W} \quad (6.29)$$

where we have used the normalized cell velocity $\hat{\mathbf{v}} = \frac{\mathbf{v}}{v_0}$. k_s is an adimensional parametrization of the velocity-polarization coupling and is the dimensionless equivalent in the simulations of the parameter k introduced in the continuum model. Note that $k_s = \frac{\alpha v_0}{D}$. Also note that, by design, the normalized cell velocity distribution of a single particle is centered around 1.

6.4.2. Equations including interactions between neighboring particles

We now propose a set of equations to describe the evolution of a system composed of many particles. As previously, we introduce anisotropy in the friction to model the effect of the grooves. Each particle i is governed by the previous polarization equation and an overdamped force balance:

$$d\mathbf{p}_i = [k_s \hat{\mathbf{v}}_i - (k_s + 1) \|\hat{\mathbf{v}}_i\|^2 \mathbf{p}_i] dt + \sqrt{2D} d\mathbf{W}_i \quad (6.30)$$

$$\hat{\Lambda} \cdot \hat{\mathbf{v}}_i = \mathbf{p}_i + \sum_{j \neq i} \hat{\mathbf{F}}_{ij}^c \quad (6.31)$$

- $\hat{\Lambda} = \mathbf{H} + h_s(\mathbf{I} - \mathbf{H})$ in a normalized anisotropic friction with $h_s \geq 1$. When $h_s = 1$, the friction is isotropic, whereas for higher h_s , the friction is anisotropic, and the particles flow preferentially in the x direction in which they experience lower friction. Note that h_s is an adimensional parameter controlling friction anisotropy, like h introduced in the continuum model.

- $\hat{\mathbf{F}}_{ij}^c = \frac{\mathbf{F}_{ij}^c}{\lambda_s v_0}$ is a normalized interaction force. Interactions with neighbors are excluded volume interactions and are modeled through a repulsive soft potential:

$$\mathbf{F}_{ij}^c = -\nabla U_{ij}$$

$$U_{ij} = \begin{cases} \frac{k_c \lambda_s v_0}{2} \delta_{ij}^2 & \text{if } \delta_{ij} > 0 \\ 0 & \text{if } \delta_{ij} \leq 0 \end{cases} \quad (6.32)$$

with k_c being the adimensionalized contact stiffness between particles and δ_{ij} the distance between particles. Note that the interactions are purely repulsive, and no adhesion has been included in the model. This is reasonable as we experimentally showed that cell-cell adhesion is not necessary for HBEC laning.

This model is minimal in the sense that the system dynamics is controlled by only four parameters:

- h_s the friction anisotropy
- k_s the strength of the polarization-velocity coupling
- k_c the contact stiffness between close particles
- ρ the density of particles.

As we are interested in systems at confluence, we set the density of particles to 1.2, a value that ensures that particles are in close contact with their neighbors. Note that the density is slightly larger than 1, meaning that small overlaps between particles are allowed. Then, the system is governed by only three parameters: h_s , k_s and k_c .

Additionally, particles are chosen to be disks of diameter “20 μm ” and evolve in a system “10 mm” long and “2 mm” wide. Note that these sizes are scaled to be close to experimental sizes but what matters for simulations is the ratio between system size and particle size. Periodic boundary conditions are imposed. Particles are initially homogeneously distributed in the system and their initial condition is $\mathbf{p}_i = 0$ and $\mathbf{v}_i = 0$. Simulations are run until the systems reach a steady state. To analyze simulation results, we first coarse-grain single particle velocities. The analyses are then performed on the locally averaged normalized velocity field $\hat{\mathbf{v}}(\mathbf{r}, t)$.

Note that we also simulated systems in which anisotropy was introduced in other terms of the governing equations such as in the polarization-velocity coupling or in the noise. As similar results were obtained, we focused on particle-based simulations encapsulating anisotropy in the friction term.

6.4.3. Quantifying the laning transition in simulations

In simulations, for fixed values of k_s and k_c , there is a transition from disorder to laning when h_s increases (Figure 6.8.A). To characterize this laning transition in simulations and obtain a phase diagram in the parameter space (h_s, k_s) , we need to define a quantity which values allow to identify the transition. To do that, we measure $C_x(dx)$, the \hat{v}_x correlation function along x , defined as for the experimental measures by equation (3.1). For given values of k_s and k_c , $C_x(dx)$ increases when the friction anisotropy h_s is increased (Figure 6.8.B), similarly to experimental data when groove depth is increased (Figure 3.12). Moreover, the characteristic length over which this correlation decays seems to increase with h_s . For simulations, we approximate the characteristic length of velocity correlation decay in an idealized ‘infinite’ system using the initial decay of the curves:

$$L_{x,s} \approx - \left(\min_{dx>0} \frac{dC_x(dx)}{ddx} \right)^{-1} \quad (6.33)$$

$L_{x,S}$ increases with h_s and is a good quantitative characterization of the laning transition in simulated systems (Figure 6.8.C). Indeed, the value of $L_{x,S}$ increases sharply at the transition between $h_s = 1.25$ and $h_s = 1.5$.

Note that we do not use the same definition than L_x chosen for the experimental measures (see 3.2.1.2). This is because, when laning emerges, the laning pattern is “perfect” in simulations due to periodic boundary conditions, and thus C_x decays quickly towards a large constant finite value. Simulated systems’ size is close to the FOVs’ size in experiments. However, in experiments, FOVs are a subpart part of a larger system, thus the laning is never “perfect” and C_x decays toward lower values. We then use in simulations only the initial decay of the curves which is independent from the system size. Since simulation data are very consistent, this ‘derivative’-type estimate is well adapted and very robust. We use this indicator in the phase diagram of the main text to quantify the laning transition (Figure 3.30).

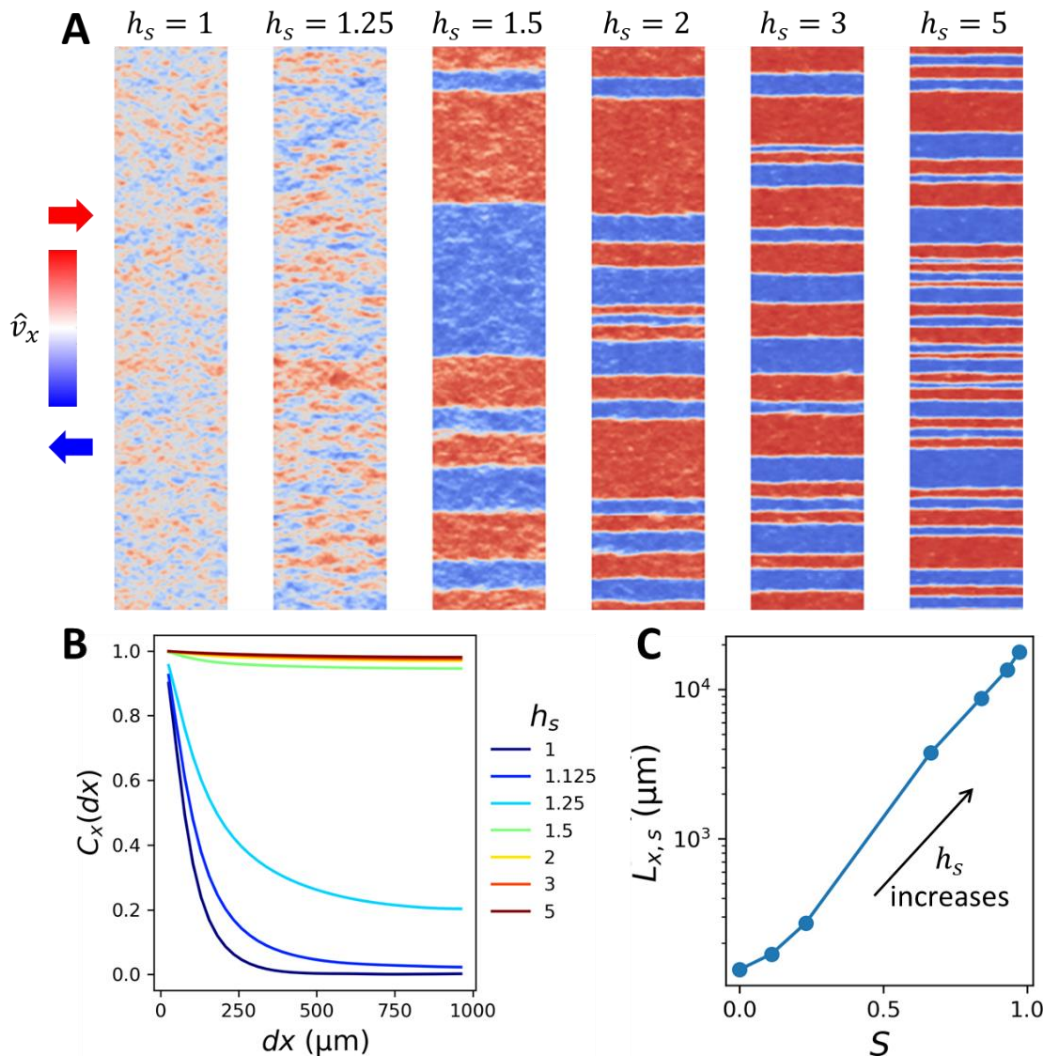


Figure 6.8 : In self-propelled particle-based simulations, the transition from disorder to laning mediated by an increase in friction anisotropy h_s is well characterized using the characteristic length of the \hat{v}_x correlation function initial decay along x .

A: A transition from disorder to laning is observed between $h_s = 1.25$ and $h_s = 1.5$. From left to right, \hat{v}_x is displayed for systems simulated until a steady state is reached for $k_s = 6, k_c = 2.5$ and $h_s = 1 - 5$.

B: C_x , the \hat{v}_x correlation function along x , decreases less and less sharply toward increasing final values as h_s is increased. $C_x(dx)$ initial decay allows to extract a characteristic length in the x direction $L_{x,S}$. Curves are obtained for $k_c = 2.5$ and $k_s = 6$.

C: $L_{x,S}$ increases with S , the guidance along x . The points are obtained for $k_c = 2.5, k_s = 6$ and $h_s = 1; 1.125; 1.25; 1.5; 2; 3; 5$ from left to right. The transition from disorder to laning between $h_s = 1.25$ and $h_s = 1.5$ is well captured by a large increase in $L_{x,S}$.

6.5. Impact of surface chemistry on bilayering

In Chapter 4, I present a way to trigger the self-formation of orthogonal bilayers of myoblasts, by seeding C2C12 cells at high density on PDMS micro-grooved substrates designed with a perpendicular interface geometry. To obtain this behavior, I first optimized the substrate treatment. Indeed, the long-term fate of the system was found to depend on the PDMS substrate's treatment performed. In this annex, I present how the substrate treatment impact the C2C12 monolayer evolution.

6.5.1. Cells dewet and form aggregates on non-treated PDMS substrates

Non-treated PDMS is hydrophobic and consequently cells do not spread easily on this substrate. They tend to dewet and regroup into rounded aggregates that migrate and grow over time by accumulating cells and merging with other aggregates (Figure 6.9). That dynamic is rich and could be the subject of later studies.

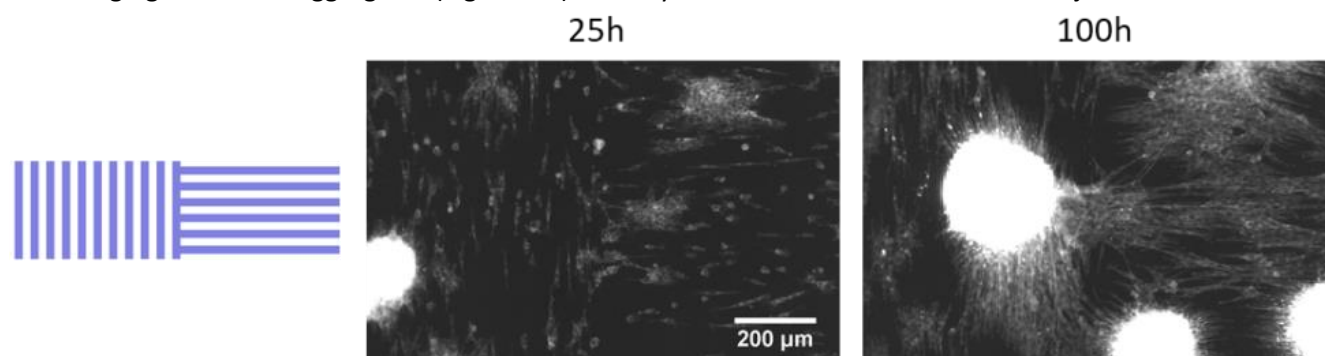


Figure 6.9 : Formation of cellular aggregates on non-treated PDMS substrate. From left to right: schematic of the substrate and fluorescent images 25 and 100 hours after seeding cells at high density.

However, for the project presented in Chapter 4, we were interested in triggering the spontaneous formation of a bilayer from an initial monolayer. Therefore, I first optimized PDMS substrate's treatment to trigger the desired long-term behavior.

6.5.2. PDMS activation and coating contribute to stable bilayering at a perpendicular interface

Conversely to cells on non-treated substrates, cells successfully spread and form a confluent monolayer on PDMS plasma activated for 30 seconds and/ or coated with fibronectin before cell seeding (Figure 6.10. top images). Cells orient along the grooves in both sides of the interface and the orientation sharply changes from 90° to 0° at the interface. Depending on the nature of surface treatment, the evolution of the monolayer is different. Here, I qualitatively compare fluorescent movies for different substrate's treatment (Figure 6.10):

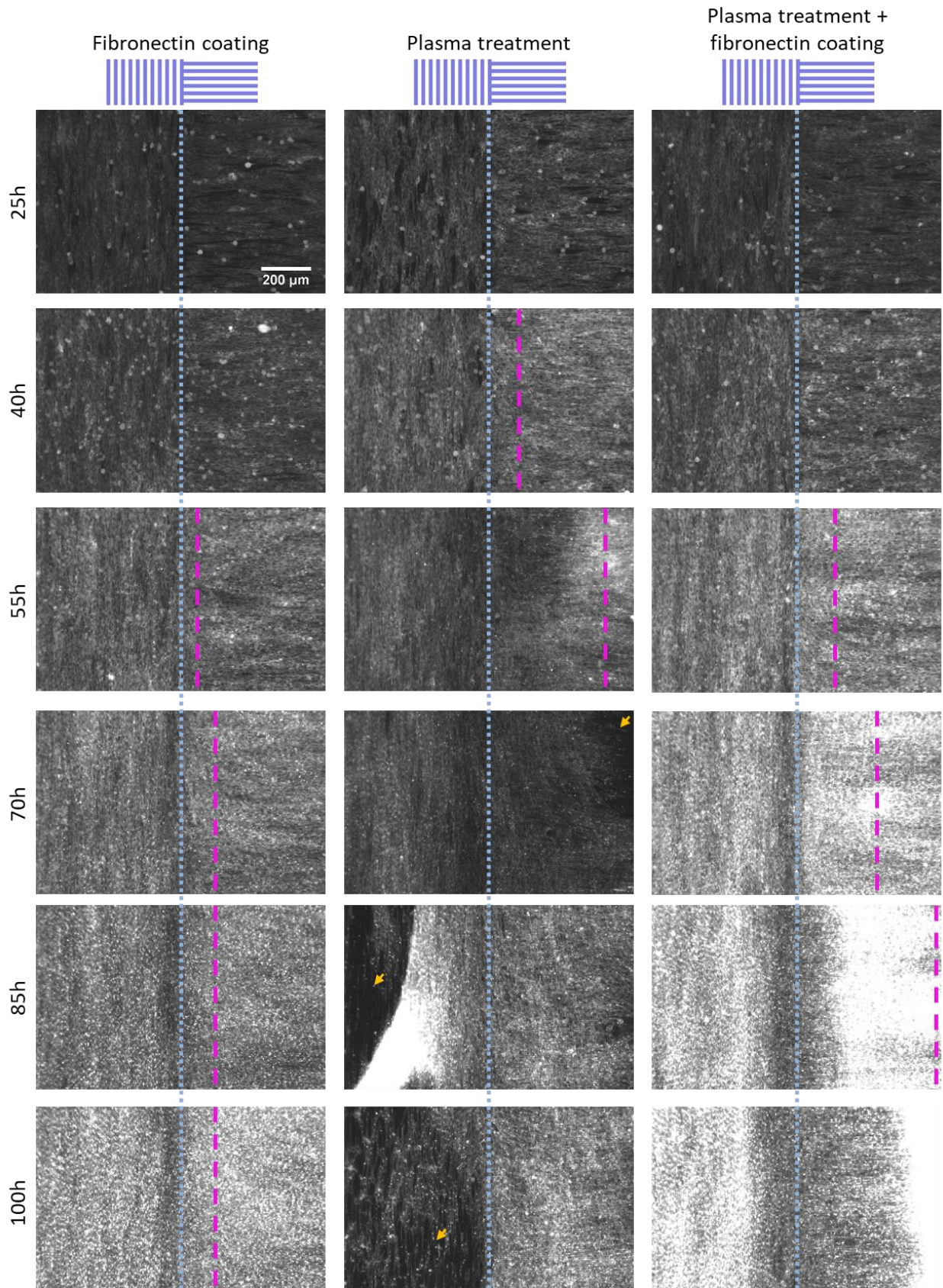


Figure 6.10 : Evolution of a C2C12 monolayer on a perpendicular interface coated with fibronectin (left), plasma treated (middle) and both plasma treated and fibronectin coated (right). From top to bottom, fluorescent images are displayed for different times, indicated in hours after cell seeding. Schematics of the underlying substrate are shown at the top. Blue dotted lines indicate substrate interface position. Magenta dashed lines show the bilayering front. The bilayering front corresponds to the zone of high density

separating the top layer east of the interface in two parts: a west part in which cells are N/S-oriented and an east part in which cells are W/E-oriented. Here, the bilayering front position is qualitatively estimated while slowly playing the movies. Note that a second layer appears between 40 to 55 hours after cell seeding depending on the condition. Note also that detachment events, highlighted by orange arrows, are observed in the absence of fibronectin coating. The top layer formation and progression from the interface towards the right is observed with plasma treatment.

- Fibronectin coating (Figure 6.10.left): over time, the images get increasingly brighter. Thus, we conclude that density increases in both sides of the interface leading eventually to a multilayered structure. The qualitative analysis of time lapse movies reveals that:
 - Cells in the top layer away from the interface stay aligned with the bottom cells in both sides
 - From 55 hours after cell seeding, the top layer in a small zone near and east of the interface is formed by cells that are extruded at the interface and migrate eastward. This can explain that the cell density in the west zone near the interface is lower than in other locations 55 hours post seeding and later.
 - There is an orientation mismatch between the bottom and the top layers in the zone delimited by the interface (blue dotted line) and the “bilayering front”, defined here qualitatively as the line around which cells reorient from N/S to W/E in the top layer (magenta dashed line) (see Figure 6.10.left at 70h).
 - However, this top layer zone with an angle mismatch does not propagate significantly away from the interface as the bilayering front is approximately fixed from 70h to 100h after cell seeding (Figure 6.10.left).
- Plasma activation (Figure 6.10.middle): compared to the previous condition, a collective migration from the interface eastward is observed on a much larger scale. It corresponds to the formation of a new layer on top of the bottom layer initiating from the interface and progressing eastward. Notably, cells in this newly formed top layer are N/S-oriented west of the bilayer front (Figure 6.10.middle 55 h and 70 h post cell seeding) and thus perpendicular to bottom cells. The bilayer front that propagates eastward becomes increasingly brighter, suggesting an increase over time of cell density at this location (see magenta dashed lines in Figure 6.10.middle). 70 hours after cell seeding, the bilayering front has propagated through the whole FOV. However, detachment events, in which the tissue detaches either in some parts or completely from the substrate, are also observed at random times and places in this substrate condition (see orange arrows in Figure 6.10.middle).
- Plasma activation + fibronectin coating (Figure 6.10.right): a similar bilayering dynamics is observed but rather the bilayer progression is qualitatively slower and more stable. Indeed, cells eventually detach from the substrate but at much longer time scales, meaning after the bilayer front has propagated at least through the whole FOV.

6.5.3. PDMS plasma activation decreases fibronectin absorption

To better understand the observed differences, I measured the relative amount of fibronectin absorption on the PDMS substrate with and without plasma activation. To do that, both a non-treated and a plasma activated substrate, deposited in the same glass bottom dish, were coated with fluorescently labeled fibronectin. These substrates were imaged with super resolution confocal microscopy (Figure 6.11.A-B).

The relative amount of fibronectin on both substrates is measured by comparing the maximal value of the normalized fluorescence intensity (Figure 6.11.C). I observed that the absorption of fibronectin is higher in the absence of plasma treatment (Figure 6.11.D). This result suggests that in the absence of plasma treatment, fibronectin absorption is too large and cell-substrate adhesion is so strong that cell extrusions at the interface are much slower and do not lead to a clear progression of a bilayering front (Figure 6.10.left). Conversely, without any fibronectin coating, cell substrate adhesion is too small to balance collective cell contraction forces and lead to precipitated tissue detachment (Figure 6.10.middle). A combination of plasma treatment and fibronectin coating leads to intermediate fibronectin absorption and thus intermediate strength of cell-substrate adhesion. This allows for cell extrusions at the interface while ensuring strong anchoring of the cell monolayer on the substrate.

The effect of plasma on surface activation is known to fade out with time. Therefore, as fibronectin absorption is maximal in the absence of plasma treatment, we hypothesize that increasing the delay between PDMS plasma activation and fibronectin coating increases fibronectin absorption. We thus decided to plasma activate for 30s the substrates and allow them to rest for approximately 8 hours before fibronectin coating, to obtain intermediate fibronectin absorption. In this condition, we observe the stable formation of a top layer that originates at the interface and propagates eastward on top of the bottom layer. The quantitative description of the dynamics and structure of this bilayered system can be found in Chapter 4.

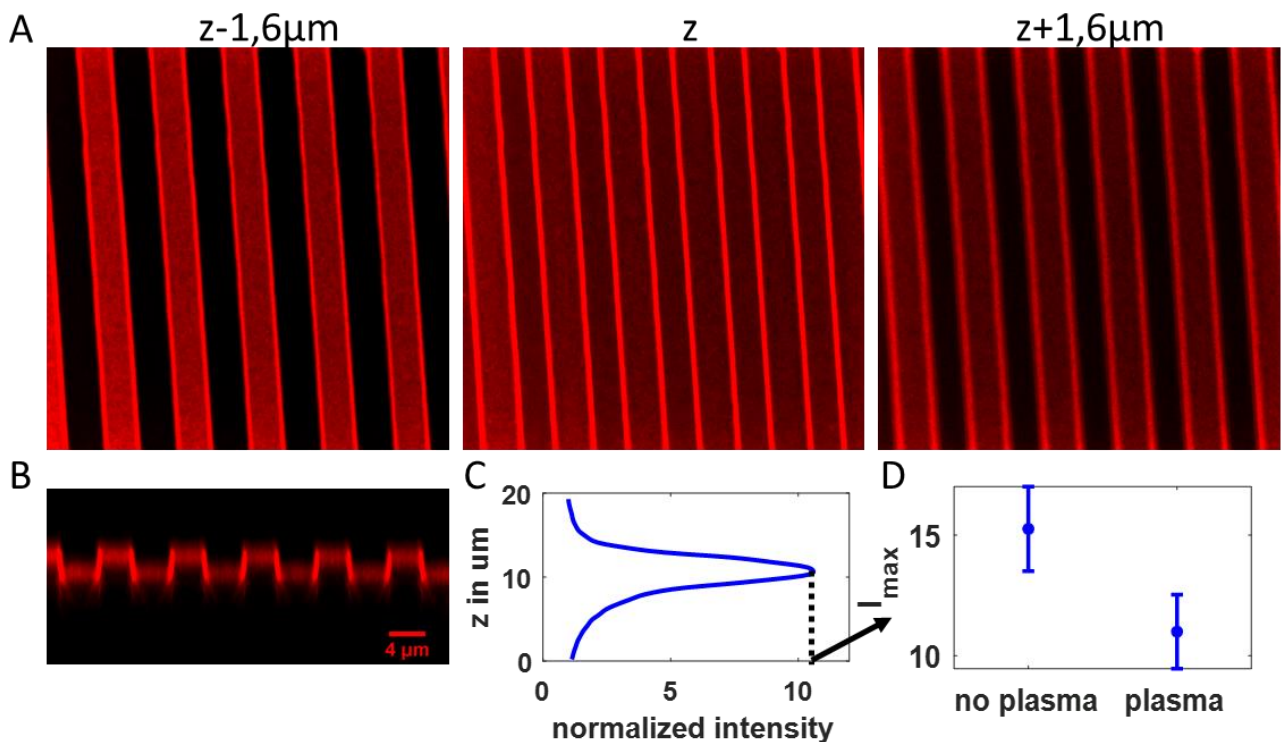


Figure 6.11 : Fibronectin absorption is higher on non-treated substrates than on plasma-activated substrate.

A: Confocal fluorescent images of a fluorescent fibronectin coated grooved substrate.

B: Orthogonal view of the same substrate. Scale bar, $4\mu\text{m}$, common to A and B.

C: Averaged FOV intensity normalized with background intensity (intensity of the first z slice) for each z slice.

D: Maximal intensity for substrate with and without plasma activation. Error bars represent standard deviation to the mean ($N=5$ FOVs per condition)

7. Bibliography

1. Alberts, B. *et al. Essential Cell Biology*. (2014).
2. Vicente-Manzanares, M., Webb, D. J. & Horwitz, A. R. Cell migration at a glance. *J. Cell Sci.* **118**, 4917–4919 (2005).
3. Blanchoin, L., Boujemaa-Paterski, R., Sykes, C. & Plastino, J. Actin dynamics, architecture, and mechanics in cell motility. *Physiol. Rev.* **94**, 235–263 (2014).
4. Friedl, P. & Gilmour, D. Collective cell migration in morphogenesis, regeneration and cancer. *Nature Reviews Molecular Cell Biology* **10**, 445–457 (2009).
5. Scarpa, E. & Mayor, R. Collective cell migration in development. *J. Cell Biol.* **212**, 143–155 (2016).
6. Rørth, P. Collective cell migration. *Annual Review of Cell and Developmental Biology* **25**, 407–429 (2009).
7. Ladoux, B. & Mège, R. M. Mechanobiology of collective cell behaviours. *Nat. Rev. Mol. Cell Biol.* **18**, 743–757 (2017).
8. Hakim, V. & Silberzan, P. Collective cell migration: A physics perspective. *Reports on Progress in Physics* **80**, 076601 (2017).
9. Alert, R. & Trepap, X. Physical Models of Collective Cell Migration. *Annual Review of Condensed Matter Physics* **11**, 77–101 (2020).
10. Jain, S., Ladoux, B. & Mège, R. M. Mechanical plasticity in collective cell migration. *Current Opinion in Cell Biology* **72**, 54–62 (2021).
11. Pinheiro, D. & Heisenberg, C. P. Zebrafish gastrulation: Putting fate in motion. *Curr. Top. Dev. Biol.* **136**, 343–375 (2020).
12. Keller, P. J., Schmidt, A. D., Wittbrodt, J. & Stelzer, E. H. K. Reconstruction of zebrafish early embryonic development by scanned light sheet microscopy. *Science (80-.)*. **322**, 1065–1069 (2008).
13. Gurtner, G. C., Werner, S., Barrandon, Y. & Longaker, M. T. Wound repair and regeneration. *Nature* **453**, 314–321 (2008).
14. Alexander, S., Koehl, G. E., Hirschberg, M., Geissler, E. K. & Friedl, P. Dynamic imaging of cancer growth and invasion: A modified skin-fold chamber model. *Histochem. Cell Biol.* **130**, 1147–1154 (2008).
15. Liu, R. *et al.* Diversity of collective migration patterns of invasive breast cancer cells emerging during microtrack invasion. *Phys. Rev. E* **99**, 062403 (2019).
16. Garcia, S. *et al.* Physics of active jamming during collective cellular motion in a monolayer. *Proc. Natl. Acad. Sci. U. S. A.* **112**, 15314–15319 (2015).
17. Poujade, M. *et al.* Collective migration of an epithelial monolayer in response to a model wound. *Proc. Natl. Acad. Sci. U. S. A.* **104**, 15988–15993 (2007).
18. Doxzen, K. *et al.* Guidance of collective cell migration by substrate geometry. *Integr. Biol.* **5**, 1026–1035 (2013).
19. Weber, G. F., Bjerke, M. A. & DeSimone, D. W. A Mechanoresponsive Cadherin-Keratin Complex Directs Polarized Protrusive Behavior and Collective Cell Migration. *Dev. Cell* **22**, 104–115 (2012).
20. Dumortier, J. G., Martin, S., Meyer, D., Rosa, F. M. & David, N. B. Collective mesendoderm migration relies on an intrinsic directionality signal transmitted through cell contacts. *Proc. Natl. Acad. Sci. U. S. A.* **109**, 16945–16950 (2012).
21. Khalil, A. A. *et al.* Collective invasion induced by an autocrine purinergic loop through connexin-43 hemichannels. *J. Cell Biol.* **219**, (2020).
22. Tambe, D. T. *et al.* Collective cell guidance by cooperative intercellular forces. *Nat. Mater.* **10**, 469–475 (2011).
23. Trepap, X. *et al.* Physical forces during collective cell migration. *Nat. Phys.* **5**, 426–430 (2009).
24. Petitjean, L. *et al.* Velocity fields in a collectively migrating epithelium. *Biophys. J.* **98**, 1790–1800 (2010).
25. Peyret, G. *et al.* Sustained Oscillations of Epithelial Cell Sheets. *Biophys. J.* **117**, 464–478 (2019).
26. Desai, R. A., Gopal, S. B., Chen, S. & Chen, C. S. Contact inhibition of locomotion probabilities drive

- solitary versus collective cell migration. *J. R. Soc. Interface* **10**, (2013).
27. Carmona-Fontaine, C. *et al.* Contact inhibition of locomotion in vivo controls neural crest directional migration. *Nature* **456**, 957–961 (2008).
 28. Mayor, R. & Carmona-Fontaine, C. Keeping in touch with contact inhibition of locomotion. *Trends in Cell Biology* **20**, 319–328 (2010).
 29. Rupp, P. A. & Kulesa, P. M. A role for RhoA in the two-phase migratory pattern of post-otic neural crest cells. *Dev. Biol.* **311**, 159–171 (2007).
 30. Szabó, A., Theveneau, E., Turan, M. & Mayor, R. Neural crest streaming as an emergent property of tissue interactions during morphogenesis. *PLoS Comput. Biol.* **15**, (2019).
 31. Bain, N. & Bartolo, D. Dynamic response and hydrodynamics of polarized crowds. *Science (80-.)*. **363**, 46–49 (2019).
 32. Marchetti, M. C. *et al.* Hydrodynamics of soft active matter. *Rev. Mod. Phys.* **85**, 1143–1189 (2013).
 33. Jain, S. *et al.* The role of single-cell mechanical behaviour and polarity in driving collective cell migration. *Nat. Phys.* **16**, 802–809 (2020).
 34. Bricard, A., Caussin, J. B., Desreumaux, N., Dauchot, O. & Bartolo, D. Emergence of macroscopic directed motion in populations of motile colloids. *Nature* **503**, 95–98 (2013).
 35. Guillamat, P., Ignés-Mullol, J. & Sagués, F. Taming active turbulence with patterned soft interfaces. *Nat. Commun.* **8**, 1–8 (2017).
 36. Ramaswamy, S. The Mechanics and Statistics of Active Matter. *Annu. Rev. Condens. Matter Phys.* **1**, 323–345 (2010).
 37. Doostmohammadi, A., Ignés-Mullol, J., Yeomans, J. M. & Sagués, F. Active nematics. *Nature Communications* **9**, (2018).
 38. Shankar, S., Souslov, A., Bowick, M. J., Marchetti, M. C. & Vitelli, V. Topological active matter. *arXiv* (2020).
 39. Gompper, G. *et al.* The 2020 motile active matter roadmap. *J. Phys. Condens. Matter* **32**, 193001 (2020).
 40. De Gennes, P.-G. & Prost, J. *The Physics of Liquid Crystals*. (1993).
 41. Frank, F. C. I. Liquid crystals: On the theory of liquid crystals. *Discuss. Faraday Soc.* **25**, 19–28 (1958).
 42. Duclos, G., Garcia, S., Yevick, H. G. & Silberzan, P. Perfect nematic order in confined monolayers of spindle-shaped cells. *Soft Matter* **10**, 2346–2353 (2014).
 43. Duclos, G., Erlenkämper, C., Joanny, J. F. & Silberzan, P. Topological defects in confined populations of spindle-shaped cells. *Nat. Phys.* **13**, 58–62 (2017).
 44. Surrey, T., Nédélec, F., Leibler, S. & Karsenti, E. Physical properties determining self-organization of motors and microtubules. *Science (80-.)*. **292**, 1167–1171 (2001).
 45. Duclos, G. Active Cellular Nematics. (Université Pierre et Marie Curie, 2015).
 46. Prost, J., Jülicher, F. & Joanny, J. F. Active gel physics. *Nat. Phys.* **11**, 111–117 (2015).
 47. Jülicher, F., Grill, S. & Salbreux, G. Hydrodynamic Theory of Active Matter. *Reports Prog. Phys.* **81**, 076601 (2018).
 48. Kruse, K., Joanny, J. F., Jülicher, F. & Prost, J. Contractility and retrograde flow in lamellipodium motion. *Phys. Biol.* **3**, 130–137 (2006).
 49. Duclos, G. *et al.* Spontaneous shear flow in confined cellular nematics. *Nat. Phys.* **14**, 728–732 (2018).
 50. Chen, T., Saw, T. B., Mege, R. M. & Ladoux, B. Mechanical forces in cell monolayers. *J. Cell Sci.* **131**, (2018).
 51. Alert, R., Casademunt, J. & Joanny, J.-F. Active Turbulence. *Annu. Rev. Condens. Matter Phys.* **13**, 143–170 (2022).
 52. Blanch-Mercader, C. *et al.* Turbulent Dynamics of Epithelial Cell Cultures. *Phys. Rev. Lett.* **120**, 208101 (2018).
 53. Sarkar, T. *et al.* Crisscross multilayering of cell sheets. *bioRxiv* 2021.06.22.449403 (2021).
 54. Voituriez, R., Joanny, J. F. & Prost, J. Spontaneous flow transition in active polar gels. *Europhys. Lett.* **70**, 404–410 (2005).
 55. Yashunsky, V. *et al.* Chiral edge currents in confined fibrosarcoma cells. *arXiv* (2020).
 56. Szabó, B. *et al.* Phase transition in the collective migration of tissue cells: Experiment and model. *Phys.*

- Rev. E - Stat. Nonlinear, Soft Matter Phys.* **74**, 1–5 (2006).
57. Vicsek, T., Czirak, A., Ben-Jacob, E., Cohen, I. & Shochet, O. Novel type of phase transition in a system of self-driven particles. *Phys. Rev. Lett.* **75**, 1226–1229 (1995).
 58. Toner, J. & Tu, Y. Long-range order in a two-dimensional dynamical XY model: How birds fly together. *Phys. Rev. Lett.* **75**, 4326–4329 (1995).
 59. Toner, J. & Tu, Y. Flocks, herds, and schools: A quantitative theory of flocking. *Phys. Rev. E - Stat. Physics, Plasmas, Fluids, Relat. Interdiscip. Top.* **58**, 4828–4858 (1998).
 60. Notbohm, J. *et al.* Cellular Contraction and Polarization Drive Collective Cellular Motion. *Biophys. J.* **110**, 2729–2738 (2016).
 61. Kim, J. H. *et al.* Propulsion and navigation within the advancing monolayer sheet. *Nat. Mater.* **12**, 856–863 (2013).
 62. Blanch-Mercader, C. & Casademunt, J. Hydrodynamic instabilities, waves and turbulence in spreading epithelia. *Soft Matter* **13**, 6913–6928 (2017).
 63. Kumar, N., Soni, H., Ramaswamy, S. & Sood, A. K. Flocking at a distance in active granular matter. *Nat. Commun.* **5**, 4688 (2014).
 64. Brotto, T., Caussin, J. B., Lauga, E. & Bartolo, D. Hydrodynamics of confined active fluids. *Phys. Rev. Lett.* **110**, 1–5 (2013).
 65. Basan, M., Elgeti, J., Hannezo, E., Rappel, W. J. & Levine, H. Alignment of cellular motility forces with tissue flow as a mechanism for efficient wound healing. *Proc. Natl. Acad. Sci. U. S. A.* **110**, 2452–2459 (2013).
 66. George, M., Bullo, F. & Campàs, O. Connecting individual to collective cell migration. *Sci. Rep.* **7**, 1–10 (2017).
 67. Smeets, B. *et al.* Emergent structures and dynamics of cell colonies by contact inhibition of locomotion. *Proc. Natl. Acad. Sci. U. S. A.* **113**, 14621–14626 (2016).
 68. Harrison, R. G. The reaction of embryonic cells to solid structures. *J. Exp. Zool.* **17**, 521–544 (1914).
 69. Weiss, P. Nerve Patterns: the Mechanics of Nerve Growth. in *Dynamics of Development: Experiments and Inferences* (1941).
 70. Friedl, P. & Alexander, S. Cancer invasion and the microenvironment: Plasticity and reciprocity. *Cell* **147**, 992–1009 (2011).
 71. Petrie, R. J., Doyle, A. D. & Yamada, K. M. Random versus directionally persistent cell migration. *Nature Reviews Molecular Cell Biology* **10**, 538–549 (2009).
 72. Clark, A. G. & Vignjevic, D. M. Modes of cancer cell invasion and the role of the microenvironment. *Current Opinion in Cell Biology* **36**, 13–22 (2015).
 73. Alexander, S., Weigelin, B., Winkler, F. & Friedl, P. Preclinical intravital microscopy of the tumour-stroma interface: Invasion, metastasis, and therapy response. *Curr. Opin. Cell Biol.* **25**, 659–671 (2013).
 74. Sarna, M., Wybieralska, E., Miekus, K., Drukala, J. & Madeja, Z. Topographical control of prostate cancer cell migration. *Mol. Med. Rep.* **2**, 865–871 (2009).
 75. Conklin, M. W. *et al.* Aligned collagen is a prognostic signature for survival in human breast carcinoma. *Am. J. Pathol.* **178**, 1221–1232 (2011).
 76. Chanrion, M. *et al.* Concomitant Notch activation and p53 deletion trigger epithelial-to-mesenchymal transition and metastasis in mouse gut. *Nat. Commun.* **5**, 5005 (2014).
 77. Erdogan, B. *et al.* Cancer-associated fibroblasts promote directional cancer cell migration by aligning fibronectin. *J. Cell Biol.* **216**, 3799–3816 (2017).
 78. Daley, W. P. & Yamada, K. M. ECM-modulated cellular dynamics as a driving force for tissue morphogenesis. *Current Opinion in Genetics and Development* **23**, 408–414 (2013).
 79. Sherwood, D. R. Basement membrane remodeling guides cell migration and cell morphogenesis during development. *Curr. Opin. Cell Biol.* **72**, 19–27 (2021).
 80. Latimer, A. & Jessen, J. R. Extracellular matrix assembly and organization during zebrafish gastrulation. *Matrix Biol.* **29**, 89–96 (2010).
 81. Winklbauer, R. & Nagel, M. Directional mesoderm cell migration in the *Xenopus* gastrula. *Dev. Biol.* **148**, 573–589 (1991).

82. Haigo, S. L. & Bilder, D. Global tissue revolutions in a morphogenetic movement controlling elongation. *Science (80-.)*. **331**, 1071–1074 (2011).
83. Paul, C. D., Mistriotis, P. & Konstantopoulos, K. Cancer cell motility: Lessons from migration in confined spaces. *Nature Reviews Cancer* **17**, 131–140 (2017).
84. Cetera, M. *et al.* Epithelial rotation promotes the global alignment of contractile actin bundles during *Drosophila* egg chamber elongation. *Nat. Commun.* **5**, 5511 (2014).
85. Cetera, M. & Horne-Badovinac, S. Round and round gets you somewhere: Collective cell migration and planar polarity in elongating *Drosophila* egg chambers. *Curr. Opin. Genet. Dev.* **32**, 10–15 (2015).
86. Nguyen, A. T., Sathe, S. R. & Yim, E. K. F. From nano to micro: Topographical scale and its impact on cell adhesion, morphology and contact guidance. *J. Phys. Condens. Matter* **28**, 183001 (2016).
87. Leclech, C. & Villard, C. Cellular and Subcellular Contact Guidance on Microfabricated Substrates. *Front. Bioeng. Biotechnol.* **8**, 551505 (2020).
88. Li, Y. *et al.* Engineering cell alignment in vitro. *Biotechnol. Adv.* **32**, 347–365 (2014).
89. Clark, P., Connolly, P., Curtis, A. S. G., Dow, J. A. T. & Wilkinson, C. D. W. Topographical control of cell behaviour: II. multiple grooved substrata. *Development* **108**, 635–644 (1990).
90. Teixeira, A. I., Abrams, G. A., Bertics, P. J., Murphy, C. J. & Nealey, P. F. Epithelial contact guidance on well-defined micro- and nanostructured substrates. *J. Cell Sci.* **116**, 1881–1892 (2003).
91. Ray, A. *et al.* Anisotropic forces from spatially constrained focal adhesions mediate contact guidance directed cell migration. *Nat. Commun.* **8**, 14923 (2017).
92. Londono, C. *et al.* Nonautonomous contact guidance signaling during collective cell migration. *Proc. Natl. Acad. Sci.* **111**, 1807–1812 (2014).
93. Buskermolen, A. B. C. *et al.* Cellular Contact Guidance Emerges from Gap Avoidance. *Cell Reports Phys. Sci.* **1**, 100055 (2020).
94. Leclech, C. & Barakat, A. I. Is there a universal mechanism of cell alignment in response to substrate topography? *Cytoskeleton* **78**, 284–292 (2021).
95. Kubow, K. E., Shuklis, V. D., Sales, D. J. & Horwitz, A. R. Contact guidance persists under myosin inhibition due to the local alignment of adhesions and individual protrusions. *Sci. Rep.* **7**, 14380 (2017).
96. Lou, H. Y., Zhao, W., Zeng, Y. & Cui, B. The Role of Membrane Curvature in Nanoscale Topography-Induced Intracellular Signaling. *Acc. Chem. Res.* **51**, 1046–1053 (2018).
97. Uttayarat, P., Toworfe, G. K., Dietrich, F., Lelkes, P. I. & Composto, R. J. Topographic guidance of endothelial cells on silicone surfaces with micro- to nanogrooves: Orientation of actin filaments and focal adhesions. *J. Biomed. Mater. Res. - Part A* **75**, 668–680 (2005).
98. Lou, H. Y. *et al.* Membrane curvature underlies actin reorganization in response to nanoscale surface topography. *Proc. Natl. Acad. Sci. U. S. A.* **116**, 23143–23151 (2019).
99. Grigola, M. S., Dyck, C. L., Babacan, D. S., Joaquin, D. N. & Hsia, K. J. Myoblast alignment on 2D wavy patterns: Dependence on feature characteristics and cell-cell interaction. *Biotechnol. Bioeng.* **111**, 1617–1626 (2014).
100. Clark, P., Connolly, P., Curtis, A. S. G., Dow, J. A. T. & Wilkinson, C. D. W. Cell guidance by ultrafine topography in vitro. *J. Cell Sci.* **99**, 73–77 (1991).
101. Nam, K. H. *et al.* Multiscale Cues Drive Collective Cell Migration. *Sci. Rep.* **6**, 29749 (2016).
102. Lee, G. *et al.* Contact guidance and collective migration in the advancing epithelial monolayer. *Connect. Tissue Res.* **59**, 309–315 (2018).
103. Dalton, B. A. *et al.* Modulation of epithelial tissue and cell migration by microgrooves. *J. Biomed. Mater. Res.* **56**, 195–207 (2001).
104. Lawrence, B. D., Pan, Z. & Rosenblatt, M. I. Silk Film Topography Directs Collective Epithelial Cell Migration. *PLoS One* **7**, (2012).
105. Haga, H., Irahara, C., Kobayashi, R., Nakagaki, T. & Kawabata, K. Collective movement of epithelial cells on a collagen gel substrate. *Biophys. J.* **88**, 2250–2256 (2005).
106. Duclos, G. *et al.* Controlling confinement and topology to study collective cell behaviors. in *Methods in Molecular Biology* **1749**, 387–399 (Humana Press, New York, NY, 2018).
107. Preibisch, S., Saalfeld, S. & Tomancak, P. Globally optimal stitching of tiled 3D microscopic image

- acquisitions. *Bioinformatics* **25**, 1463–1465 (2009).
108. Rezakhaniha, R. *et al.* Experimental investigation of collagen waviness and orientation in the arterial adventitia using confocal laser scanning microscopy. *Biomech. Model. Mechanobiol.* **11**, 461–473 (2012).
 109. Püspöki, Z., Storath, M., Sage, D. & Unser, M. Transforms and operators for directional bioimage analysis: A survey. *Adv. Anat. Embryol. Cell Biol.* **219**, 69–93 (2016).
 110. Aryaksama, T. Confined cell nematics submitted to an orientation field. Application to differentiation. (2021).
 111. Mardia, K. V. & Jupp, P. E. *Directional Statistics*. (1999).
 112. Deforet, M. *et al.* Automated velocity mapping of migrating cell populations (AVeMap). *Nat. Methods* **9**, 1081–1083 (2012).
 113. Garcia, S. Maturation et mise en compétition de monocouches cellulaires.
 114. Sveen, J. K. An introduction to MatPIV v. 1.6.1. (2004).
 115. Szabó, A. *et al.* Collective cell motion in endothelial monolayers. *Phys. Biol.* **7**, 046007 (2010).
 116. Czirók, A., Varga, K., Méhes, E. & Szabó, A. Collective cell streams in epithelial monolayers depend on cell adhesion. *New J. Phys.* **15**, (2013).
 117. Sepúlveda, N. *et al.* Collective cell motion in an epithelial sheet can be quantitatively described by a stochastic interacting particle model. *PLoS Comput. Biol.* **9**, e1002944 (2013).
 118. Henkes, S., Kostanjevec, K., Collinson, J. M., Sknepnek, R. & Bertin, E. Dense active matter model of motion patterns in confluent cell monolayers. *Nat. Commun.* **11**, 1405 (2020).
 119. Leclech, C. *et al.* Topography-induced large-scale anti-parallel collective migration in vascular endothelium. *bioRxiv* 2021.07.05.451106 (2021).
 120. Guillamat, P., Ignés-Mullol, J. & Sagués, F. Control of active liquid crystals with a magnetic field. *Proc. Natl. Acad. Sci. U. S. A.* **113**, 5498–5502 (2016).
 121. Thijssen, K., Metselaar, L., Yeomans, J. M. & Doostmohammadi, A. Active nematics with anisotropic friction: The decisive role of the flow aligning parameter. *Soft Matter* **16**, 2065–2074 (2020).
 122. Deforet, M., Hakim, V., Yevick, H. G., Duclos, G. & Silberzan, P. Emergence of collective modes and tri-dimensional structures from epithelial confinement. *Nat. Commun.* **5**, 3747 (2014).
 123. Krause, M. & Gautreau, A. Steering cell migration: Lamellipodium dynamics and the regulation of directional persistence. *Nat. Rev. Mol. Cell Biol.* **15**, 577–590 (2014).
 124. Rotty, J. D., Wu, C. & Bear, J. E. New insights into the regulation and cellular functions of the ARP2/3 complex. *Nat. Rev. Mol. Cell Biol.* **14**, 7–12 (2013).
 125. Tlili, S. *et al.* Collective cell migration without proliferation: density determines cell velocity and wave velocity. *R. Soc. Open Sci.* **5**, (2018).
 126. Killeen, A., Bertrand, T. & Lee, C. F. Polar Fluctuations Lead to Extensile Nematic Behavior in Confluent Tissues. *Phys. Rev. Lett.* **128**, 78001 (2022).
 127. Vafa, F., Bowick, M. J., Shraiman, B. I. & Marchetti, M. C. Fluctuations can induce local nematic order and extensile stress in monolayers of motile cells. *Soft Matter* **17**, 3068–3073 (2021).
 128. Park, J. A. *et al.* Unjamming and cell shape in the asthmatic airway epithelium. *Nat. Mater.* **14**, 1040–1048 (2015).
 129. Rhodin, J. A. G. Architecture of the Vessel Wall. in *Vascular smooth muscle* 1–31 (1980).
 130. Holzapfel, G. A., Gasser, T. C. & Ogden, R. W. A new constitutive framework for arterial wall mechanics and a comparative study of material models. *J. Elast.* **61**, 1–48 (2000).
 131. Kier, W. M. The diversity of hydrostatic skeletons. *Journal of Experimental Biology* **215**, 1247–1257 (2012).
 132. Huycke, T. R. *et al.* Genetic and Mechanical Regulation of Intestinal Smooth Muscle Development. *Cell* **179**, 90-105.e21 (2019).
 133. Maroudas-Sacks, Y. *et al.* Topological defects in the nematic order of actin fibres as organization centres of Hydra morphogenesis. *Nat. Phys.* **17**, 251–259 (2021).
 134. Gilbert, R. J., Napadow, V. J., Gaige, T. A. & Wedeen, V. J. Anatomical basis of lingual hydrostatic deformation. *Journal of Experimental Biology* **210**, 4069–4082 (2007).

135. Hirt, M. N., Hansen, A. & Eschenhagen, T. Cardiac tissue engineering : State of the art. *Circulation Research* **114**, 354–367 (2014).
136. Liu, J. *et al.* Current Methods for Skeletal Muscle Tissue Repair and Regeneration. *BioMed Research International* **2018**, (2018).
137. Saba, I., Jakubowska, W., Bolduc, S. & Chabaud, S. Engineering Tissues without the Use of a Synthetic Scaffold: A Twenty-Year History of the Self-Assembly Method. *BioMed Research International* **2018**, (2018).
138. Takahashi, H. & Okano, T. Thermally-triggered fabrication of cell sheets for tissue engineering and regenerative medicine. *Advanced Drug Delivery Reviews* **138**, 276–292 (2019).
139. Haraguchi, Y. *et al.* Fabrication of functional three-dimensional tissues by stacking cell sheets in vitro. *Nat. Protoc.* **7**, 850–858 (2012).
140. Williams, C., Xie, A. W., Yamato, M., Okano, T. & Wong, J. Y. Stacking of aligned cell sheets for layer-by-layer control of complex tissue structure. *Biomaterials* **32**, 5625–5632 (2011).
141. Jiao, A. *et al.* Thermoresponsive nanofabricated substratum for the engineering of three-dimensional tissues with layer-by-layer architectural control. *ACS Nano* **8**, 4430–4439 (2014).
142. Elsdale, T. & Foley, R. Morphogenetic aspects of multilayering in Petri dish cultures of human fetal lung fibroblasts. *J. Cell Biol.* **41**, 298–311 (1969).
143. Jiao, A. *et al.* Regulation of skeletal myotube formation and alignment by nanotopographically controlled cell-secreted extracellular matrix. *J. Biomed. Mater. Res. - Part A* **106**, 1543–1551 (2018).
144. Conrad, G. W., Hart, G. W. & Chen, Y. Differences in vitro between fibroblast-like cells from cornea, heart, and skin of embryonic chicks. *J. Cell Sci.* **26**, 119–137 (1977).
145. Guillemette, M. D. *et al.* Surface topography induces 3D self-orientation of cells and extracellular matrix resulting in improved tissue function. *Integr. Biol.* **1**, 196–204 (2009).
146. Elsdale, T. & Bard, J. Cellular interactions in morphogenesis of epithelial mesenchymal systems. *J. Cell Biol.* **63**, 343–349 (1974).
147. Elsdale, T. & Bard, J. Cellular interactions in mass cultures of human diploid fibroblasts. *Nature* **236**, (1972).
148. Kawaguchi, K., Kageyama, R. & Sano, M. Topological defects control collective dynamics in neural progenitor cell cultures. *Nature* **545**, 327–331 (2017).
149. Copenhagen, K., Alert, R., Wingreen, N. S. & Shaevitz, J. W. Topological defects promote layer formation in *Myxococcus xanthus* colonies. *Nat. Phys.* **17**, 211–215 (2021).
150. Saw, T. B. *et al.* Topological defects in epithelia govern cell death and extrusion. *Nature* **544**, 212–216 (2017).
151. Sarkar, T. Criss-cross bilayering of cell sheets. (Université PSL, 2021).
152. Uroz, M. *et al.* Traction forces at the cytokinetic ring regulate cell division and polyploidy in the migrating zebrafish epicardium. *Nat. Mater.* **18**, 1015–1023 (2019).
153. Mohammed, D. *et al.* Substrate area confinement is a key determinant of cell velocity in collective migration. *Nat. Phys.* **15**, 858–866 (2019).
154. Da Costa, A. D. S. *et al.* Fibroblasts close a void in free space by a purse-string mechanism. *bioRxiv* 2020.08.15.250811 (2020).
155. Chaturvedi, V. *et al.* Interactions between skeletal muscle myoblasts and their extracellular matrix revealed by a serum free culture system. *PLoS One* **10**, e0127675 (2015).
156. Guillamat, P., Blanch-Mercader, C., Pernolet, G., Kruse, K. & Roux, A. Integer topological defects organize stresses driving tissue morphogenesis. *Nat. Mater.* 1–10 (2022).
157. Blanch-Mercader, C., Guillamat, P., Roux, A. & Kruse, K. Integer topological defects of cell monolayers: Mechanics and flows. *Phys. Rev. E* **103**, 012405 (2021).

RÉSUMÉ

Les flux cellulaires collectifs au sein des tissus jouent un rôle central dans les processus biologiques tels que la morphogenèse, la cicatrisation ou la progression du cancer. *In vivo*, la migration cellulaire est influencée par des structures orientées telles que les fibres de matrice extracellulaire, qui peuvent être imitées *in vitro* par des topographies rainurées. Bien que le "guidage par contact" de cellules individuelles ait été étudié de manière approfondie, on en sait moins sur la réponse d'ensembles de cellules à ces signaux anisotropes. Dans cette thèse, nous utilisons le guidage par contact pour induire des comportements collectifs dans des monocouches de cellules confluentes.

Nous nous concentrons tout d'abord sur les cellules épithéliales HBEC qui ont une dynamique chaotique sur des substrats non structurés. Lorsqu'elles sont déposées sur des rainures subcellulaires, ces cellules s'organisent spontanément en larges bandes supra cellulaires, alternantes, non périodiques, de plusieurs millimètres de long, et migrant dans des directions antiparallèles. En combinant des expériences avec une description hydrodynamique des fluides polaires actifs et des simulations de particules, nous montrons que notre système subit une transition d'un état désordonné à un état ordonné contrôlée par des forces de traction polaires et un couplage polarité-vitesse. Augmenter la profondeur des sillons favorise cette transition et stabilise le motif de migration en bandes via l'anisotropie de la friction.

Nous étudions ensuite la formation de couches de cellules empilées orthogonalement. Nous avons conçu des substrats rainurés juxtaposés orthogonalement pour imposer d'importants gradients d'orientation le long d'une interface. Grâce à cette géométrie, nous avons réussi à contrôler la formation spontanée de bicouches orthogonales de myoblastes à grande échelle. En combinant les expériences avec une description hydrodynamique des fluides nématiques actifs, nous montrons que l'interaction entre des gradients abrupts d'orientation et des forces de traction nématiques actives conduit à des flux complexes et déclenche l'initiation et la progression de bicouches.

MOTS CLÉS

Matière active - Comportements cellulaires collectifs - Guidage par contact – Migration en bandes polaires - Formation de bicouches orthogonales - Auto-organisation

ABSTRACT

Collective cell flows within tissues are central in biological processes such as morphogenesis, wound healing, or cancer progression. *In vivo*, cell migration is influenced by oriented structures such as extracellular matrix bundles, which can be mimicked *in vitro* by grooved topographies. Although "contact guidance" of single cells has been thoroughly studied, less is known on the response of cell assemblies to such anisotropic cues. In this thesis, we use contact guidance to drive collective behaviors in confluent cell monolayers.

We focus first on HBEC epithelial cells that have a chaotic dynamic on unpatterned substrates. When seeded on subcellular grooves, these cells spontaneously organize into wide supracellular, alternating, non-periodic, millimeter-long lanes that migrate in antiparallel directions. Combining experiments with a hydrodynamic description of active polar fluids and particle-based simulations, we show that our system undergoes a disorder-to-order transition mediated by polar traction forces and polarity-velocity coupling. Increasing the groove depth favors this transition and stabilizes a laning pattern via friction anisotropy.

We then study the formation of stacked orthogonal layers of cells. We designed orthogonal juxtaposed grooved substrates to impose large gradients of orientation along an interface. With this geometry, we succeeded in controlling the spontaneous formation of large-scale orthogonal bilayers of myoblasts. Combining experiments with a hydrodynamic description of active nematic fluids, we show that the interplay between steep orientation gradients and active nematic traction forces leads to complex flows and triggers bilayering initiation and progression.

KEYWORDS

Active matter – Collective cell behaviors - Contact guidance - Polar laning – Crisscross bilayering – Self-organization